To the Graduate Council:

I am submitting herewith a dissertation written by Gary L. Haag entitled "Application of the Carbon Dioxide–Barium Hydroxide Hydrate Gas-Solid Reaction for the Treatment of Dilute Carbon Dioxide-Bearing Gas Streams." I recommend that it be accepted in partial fulfillment of the requirements for the degree of Doctor of Philosophy, with a major in Chemical Engineering.

Joseph J. Perona, Major Professor

We have read this dissertation and recommend its acceptance:

M. N. Liebman

Edward S. Clark

J. A. Watson

Accepted for the Council:

L. Evans Reed

Vice Chancellor
Graduate Studies and Research

APPLICATION OF THE CARBON DIOXIDE-BARIUM HYDROXIDE HYDRATE GAS-SOLID REACTION FOR THE TREATMENT OF DILUTE CARBON DIOXIDE—BEARING GAS STREAMS

A Dissertation

Presented for the

Doctor of Philosophy

Degree

The University of Tennessee, Knoxville

Gary L. Haag

August 1982

3063269

ACKNOWLEDGMENTS

This research was sponsored by the Division of Waste Products, the U.S. Department of Energy, under contract W-7405-eng-26 with the Union Carbide Corporation. The research is part of the National Airborne Waste Management Program. The author gratefully acknowledges the support and guidance of R. A. Brown, J. D. Christian, and T. R. Thomas of the Airborne Waste Management Program Office.

The experimental studies were performed within the Experimental Engineering Section of the Chemical Technology Division at the Oak Ridge National Laboratory. To acknowledge all those who have been called upon for help and expertise during this research effort would be impossible. However, the author desires to extend special acknowledgments to D. E. Ferguson, Division Director; C. D. Scott, Associate Division Director; Section Heads R. E. Leuze and W. W. Pitt; and immediate supervisors W. D. Bond and A. D. Ryon. D. F. Green and W. G. Chapman were instrumental in the obtaining and the initial analyzing of the data. Drafting and editing support were provided by the Chemical Tecnology Division Support Services Section. A special thank you to editors Cathy Shappert and Luci Bell. Special appreciation is extended to Bobbie Hoyle, Donna Snow, and Wanda Gilliam, who have toiled for many hours in the typing and retyping of this manuscript and the original research proposal.

Support services consisting of scanning electron micrographs, x-ray diffraction analyses, and mercury porosimetry data were provided by experts in the Analytical Chemistry Division. The author thanks L. M. Ferris, Chemistry Division, and L. E. Fuller, formerly of the Chemistry Division and now of the Y-12 Product Certification Division at the Y-12

plant, for their support during the microbalance studies. The information, guidance, and expertise provided by Dr. Fuller were invaluable in the design, construction, operation, and analysis of data from the microbalance system. Discussions with ORNL consultant, Dr. Paul H. Emmett of Oregon State University, were both educational and inspirational.

I wish to thank the following educational institutions: Bartley Elementary and High School, McCook College, University of Nebraska, Iowa State University, and the University of Tennessee. They, like my parents, have opened my eyes to the wonders of this world.

In particular, I would like to acknowledge the Chemical Engineering faculty at the University of Tennessee and the members of my committee: Chairman J. J. Perona, J. S. Watson, E. S. Clark, and M. H. Lietzke (Chemistry Department). These people are true craftsmen of their trade, Thank you for your guidance and direction.

To my wife, Cindy, I extend a very special thank you, for you as much as I have paid the price. To my children, Blaine and Jessica, thank you for the little things, and may this work be of benefit to yours and to all generations. And to my parents, thank you for everything.

ABSTRACT

The removal of trace components from gas streams via irreversible gas-solid reactions is an area of interest to the chemical engineering profession. This research effort addresses the use of fixed beds of $Ba(OH)_2$ hydrate flakes for the removal of an acid gas, CO_2, from air that contains ~330 ppm_v CO_2. Areas of investigation encompassed (1) an extensive literature review of $Ba(OH)_2$ hydrate chemistry, (2) microscale studies on 0.150-g samples to develop a better understanding of the reaction, (3) process studies at the macroscale level with 10.2-cm-ID fixed-bed reactors, and (4) the development of a model for predicting fixed-bed performance.

Experimental studies indicated fixed beds of *commercial* $Ba(OH)_2 \cdot 8H_2O$ flakes at ambient temperatures to be capable of high CO_2-removal efficiencies (effluent concentrations <100 ppb), high reactant utilization (>99%), and an acceptable pressure drop (1.8 kPa/m at a superficial gas velocity of 13 cm/s). $Ba(OH)_2 \cdot 8H_2O$ was determined to be more reactive toward CO_2 than either $Ba(OH)_2 \cdot 3H_2O$ or $Ba(OH)_2 \cdot 1H_2O$. A key variable in the development of this fixed-bed process was relative humidity. Operation at conditions with effluent relative humidities >60% resulted in significant recrystallization and restructuring of the flake and subsequent pressure-drop problems. This phenomenon was attributed to capillary condensation of water at V-shaped contact points within the solid. For influent gas streams with water vapor pressures less than the dissociation vapor pressures of $Ba(OH)_2 \cdot 8H_2O$, the activity of the bed decreased to essentially zero as the lower hydrates were formed. Based upon these constraints, an

operating window for optimum bed operation for the isothermal treatment of an air-based (330-ppm_v CO_2) gas stream was determined.

Modeling studies indicated the rate of mass transfer to be limited by the gas-film mass transfer coefficient, K_F. The rate-limiting species was the reactant, CO_2. Because of nonuniformities in the thickness and size of the *commercial* $Ba(OH)_2 \cdot 8H_2O$ flakes, the area available for mass transfer was modeled semiempirically as a function of reactant conversion, $A = A_o(1-X)$, where A_o is the initial area and X is the extent of conversion. Numerical solutions to the controlling partial differential equations were obtained. Data analyses of the breakthrough profiles indicated excellent correlation between the data and model when the exponent, n, in the area correlation was equal to 1. Values for K_FA_o obtained from the breakthrough profiles were correlated as a function of system parameters, most notably relative humidity, temperature, and gas velocity. Little correlation existed for either relative humidity or temperature, the latter case being indicative of gas-film control. K_FA_o was found to be proportional to $V_o^{1.11}$, where V_o is the superficial velocity at reference conditions (101.3 kPa, 294.3°K). Based upon published correlations for heat and mass transfer, one would expect $K_F \propto V_o^{0.3} \rightarrow V_o^{0.8}$. Thus the velocity exponent for K_FA_o was greater than expected and was attributed to result from a functional dependency of the initial area available for mass transfer, A_o, upon gas velocity. For this system that is composed of randomly packed flakes, increases in gas velocity appear to reallign the flakes slightly, thus reducing the number of planar contact points and increasing the surface area available for mass transfer. Observed bed expansion was nominal. Pressure drop studies indicated the pressure drop or

shear force to be a strong function of gas velocity, $\alpha V^{1.4}$. Hence a correlation appears to exist between the shear force exerted upon the particles and the increase in surface area resulting from the slight realignment of the flakes and a reduction in the number of planar contact points.

TABLE OF CONTENTS

CHAPTER		PAGE
1.	INTRODUCTION	1
	Background and Process Application	1
	$Ba(OH)_2$ Hydrate—$BaCO_3$ Literature Review	8
	Similar Systems — The Reaction of $Ca(OH)_2$ and $LiOH \cdot H_2O$ with CO_2	15
2.	EXPERIMENTAL EQUIPMENT, INSTRUMENTATION, AND COMPUTER SUPPORT	19
	Microbalance System	19
	Fixed-Bed Experimental System	30
	Reactant and Product Characterization Instrumentation	33
	Computer Support	34
3.	EXPERIMENTAL STUDIES AND DATA ANALYSES	35
	$Ba(OH)_2$ Hydrate Reactant Characterization	36
	Surface Morphology and Microscale Studies	43
	Sorption morphology studies	43
	Introduction	43
	Nitrogen adsorption isotherms — commercial $Ba(OH)_2 \cdot 8H_2O$ and $Ba(OH)_2 \cdot 8H_2O$	49
	Nitrogen adsorption isotherms — $BaCO_3$	56
	Nitrogen adsorption isotherms — conversion profile studies	57
	Single-point BET analyses of $BaCO_3$ products	61
	Mercury porosimetry studies	66
	Photographs and scanning electron micrographs of $BaCO_3$ Product	69
	The reactivity of $Ba(OH)_2$ hydrates toward CO_2	73

CHAPTER PAGE

$Ba(OH)_2 \cdot 8H_2O$ vapor pressure, dehydration, and rehydration studies 74

Conclusions — Surface Morphology and Microscale Studies 86

Fixed-Bed Macroscale Studies 88

Modeling of fixed-bed processes 88

Introduction 88

Model formulation 91

Experimental studies 102

Data analyses and modeling studies 105

Introduction 105

Determination of the $K_F A_o$ Coefficient - Technique No. 1 105

Determination of the $K_F A_o$ Coefficient - Technique No. 2 117

Determination of $K_F A_o$ via the conversion profile . . 132

Pressure drop during fixed-bed operation 132

Introduction 132

Pressure drop - operational characteristics 136

The friction factor method for pressure drop correlation 139

The Ergun equation for pressure drop correlation . . 143

Application of the Chilton-Colburn analogy 146

Conclusion — fixed-bed studies 150

4. CONCLUSIONS AND RECOMMENDATIONS 156

Conclusions 156

Recommendations 160

LIST OF REFERENCES 162

PAGE

APPENDIXES 171

APPENDIX A. THE VAPOR PRESSURE OF $Ba(OH)_2$ HYDRATES 172

APPENDIX B. THE BINARY WATER—$Ba(OH)_2$ HYDRATE SYSTEM 179

APPENDIX C. THERMAL STUDIES ON $Ba(OH)_2$ HYDRATES 182

APPENDIX D. CRYSTAL PROPERTIES OF $Ba(OH)_2$ HYDRATES AND $BaCO_3$. 187

APPENDIX E. SPECIFICATIONS FOR *COMMERCIAL* $Ba(OH)_2 \cdot 8H_2O$ 190

APPENDIX F. CALCULATION OF CORRECTION FOR THE BUOYANCY EFFECT IN MICROBALANCE STUDIES 191

APPENDIX G. SORPTION THEORY 197

The BET Adsorption Theory 197

Analysis of Porous Solids 206

Polarization Theory and The Sorption Potential Model 215

Conclusion 219

APPENDIX H. ADSORPTION ISOTHERMS, BET PLOTS, AND SORPTION POTENTIAL PLOTS 220

APPENDIX I. MERCURY POROSIMETRY DATA SHEET 229

APPENDIX J. GAS ROTAMETER CALIBRATION AND CORRECTION FACTORS . 230

APPENDIX K. FINITE DIFFERENCE SOLUTION TO THE FIXED-BED PARTIAL DIFFERENTIAL EQUATIONS 233

APPENDIX L. FITTED VALUES IN ERGUN EQUATION 237

APPENDIX M. MASS TRANSFER MODELS FOR SHRINKING CORE SYSTEMS . . 238

APPENDIX N. EXPERIMENTAL AND MODEL-PREDICTED BREAKTHROUGH CURVES FROM FIXED-BED STUDIES 255

APPENDIX O. INFRARED SPECTROMETER CALIBRATION CURVES 272

VITA 275

LIST OF TABLES

TABLE		PAGE
1.1.	Approximate production and release rates of carbon-14 in the nuclear fuel cycle	2
1.2.	Solubility and decomposition properties of Group 1 (alkali metal) and Group 2 (alkaline earth) carbonates at low CO_2 partial pressures	5
1.3.	Molar volume relationships among some possible carbon dioxide absorbents	7
1.4.	Thermodynamic properties of the CO_2-$Ba(OH)_2$ reaction at 298.15 K	12
1.5.	Equilibrium values for the CO_2-$Ba(OH)_2$ hydrate reaction	13
1.6.	Thermodynamic properties of the $Ca(OH)_2$ and $LiOH \cdot H_2O$ gas-solid carbonation reactions at 298.15 K	15
3.1.	X-ray diffraction analyses of $Ba(OH)_2$ hydrate samples	38
3.2.	Reactant analyses of two drums of *commercial* $Ba(OH)_2 \cdot 8H_2O$ obtained from the same batch number	38
3.3.	Particle size analysis of *commercial* $Ba(OH)_2 \cdot 8H_2O$ flakes obtained from two different batch numbers	42
3.4.	Cross-sectional area of adsorbed molecules	46
3.5.	Pore classification	48
3.6.	$Ba(OH)_2 \cdot 8H_2O$ and *commercial* $Ba(OH) \cdot 8H_2O$ densities	50
3.7.	Relative strength of the hydration bonds in $Ba(OH)_2$ hydrates	51
3.8.	Nitrogen adsorption isotherm surface area analyses	54
3.9.	Conversion-profile surface areas per gram of $BaCO_3$	60
3.10.	Comparison of single- and multi-point BET surface areas using nitrogen as an adsorbate	62
3.11.	The dehydration of *commercial* $Ba(OH)_2 \cdot 8H_2O$ to $Ba(OH)_2 \cdot 3H_2O$ and subsequent rehydration to $Ba(OH)_2 \cdot 8H_2O$	82

TABLE		PAGE
3.12.	Experimental and literature values for the equilibrium water vapor pressure of $Ba(OH)_2 \cdot 8H_2O$ and the experimental rate constant, K_{ov}	83
3.13.	Rate constants as determined via Equation (3.12)	86
3.14.	Experimental $K_F A_o$ values obtained via two techniques	110
3.15.	Particle shape factors for uniform packing	112
3.16.	Application of model, $\Delta P/L = 0.01BV^n$ (kPa/m), for correlating pressure drop across converted beds of *commercial* $Ba(OH)_2 \cdot 8H_2O$ flakes	140
3.17.	Application of model, $\Delta P/L = 0.01BV^n$ (kPa/m), for correlating pressure drop across fixed beds of $Ba(OH)_2 \cdot 8H_2O$ flakes	143
3.18.	Comparison of the calculated area availability factor, f', with experimental data	155
A.1.	$Ba(OH)_2$ hydrate vapor pressure data	172
A.2.	Vapor pressure analysis for thermodynamic consistency	177
A.3.	Published dissociation vapor pressures for $Ba(OH)_2$ hydrates	178
G.1.	Pore classification	207
G.2.	Thickness of adsorbed layer at various relative pressures	213
I.1.	Mercury porosimetry data sheet	229
L.1.	Fitted values in Ergun equation, $\Delta P/L = A'V + B'V^2$, and calculated values of ε and ϕd_p	237
M.1.	Shrinking core model predictions for limited mass transfer of gaseous reactant	254

LIST OF FIGURES

FIGURE		PAGE
1.1.	Dissociation vapor pressures for $Ba(OH)_2$ hydrates	10
2.1.	Schematic of the microbalance system	20
2.2.	Photograph of microbalance system	21
2.3.	Photograph of sample of *commercial* $Ba(OH)_2 \cdot 8H_2O$ flakes suspended in the sample hang-down tube	22
2.4.	Close-up photograph of gas transfer and pressure control portion of the microbalance system	26
2.5.	Microbalance situated in stainless steel vacuum enclosure .	27
2.6.	Schematic of the fixed-bed experimental equipment	29
3.1.	Photograph of potential $Ba(OH)_2$ hdyrate reactants for CO_2 removal	37
3.2.	Top and bottom views of a *commercial* $Ba(OH)_2 \cdot 8H_2O$ flake (Original photograph: 7.3 by 9.5 cm; magnification, 12.8X)	40
3.3.	Top and bottom scanning electron micrograph (SEM) of *commercial* $Ba(OH)_2 \cdot 8H_2O$ flake. (Original photograph: 8.9 by 11.4 cm, magnification, 5000X)	41
3.4.	Top and bottom views of a *commercial* $Ba(OH)_2$ octahydrate flake subjected to relative humidity >60%. (Original photograph: 2.85 by 3.75 in.; magnification, 16.5 and 13X, respectively.)	55
3.5.	Conversion profile obtained via two analytical techniques .	59
3.6.	Single-point BET surface area analyses using argon (P/P_0 = 0.6) as an adsorbate	64
3.7.	Mercury porosimetry results on *commercial* $Ba(OH)_2 \cdot 8H_2O$ flakes from two different batch numbers	67
3.8.	Mercury porosimetry results on two $BaCO_3$ samples	70
3.9.	Photograph of *commercial* $Ba(OH)_2 \cdot 8H_2O$ flakes and $BaCO_3$ flake product. The product was obtained at a process relative humidity <60%. (Original photograph: 7.3 by 9.5 cm, magnification, 16.5 and 13X, respectively.)	71

FIGURE		PAGE
3.10.	Scanning electron micrographs of top and bottom surfaces of $BaCO_3$ product from COM-40. (Original photograph, 8.9 by 11.4 cm; magnification, 5000X)	72
3.11.	The dehydration or dissociation of *commercial* $Ba(OH)_2 \cdot 8H_2O$ flakes to $Ba(OH)_2 \cdot 3H_2O$ as a function of time and water vapor pressure	76
3.12.	The rehydration of $Ba(OH)_2 \cdot 3H_2O$ to $Ba(OH)_2 \cdot 8H_2O$ as a function of time and water vapor pressure	77
3.13.	Rates of dehydration and rehydration as a function of water vapor pressure at 304.9 K	78
3.14.	Rates of dehydration and rehydration as a function of water vapor pressure at 294.8 K	79
3.15.	Cross-sectional view of $Ba(OH)_2 \cdot 8H_2O$—$BaCO_3$ flake. Note the sharp product-reactant interface	94
3.16.	A typical breakthrough curve and the change in pressure drop across the bed presented as functions of time . . .	104
3.17.	Logarithm of the experimental breakthrough profile and the change in pressure across the bed presented as function of times	106
3.18.	Correlation of $K_F A_o$ data obtained via technique No. 1 with model, $K_F A_o = K_1 P_o V^{1.16/P}$	115
3.19.	Residuals of model correlation of data obtained via technique No. 1	116
3.20.	Development of the concentration and the natural logarithm of the concentration profile as a function of Θ and S . .	119
3.21.	Development of the conversion and the natural logarithm of the conversion profile as a function of Θ and S . . .	120
3.22.	Developed concentration or conversion and natural logarithm of development concentration or conversion profile as a function of the $K_F A_o$ coefficient and S . . .	121
3.23.	Developed breakthrough and the logarithm of the developed breakthrough profile as a function of the $K_F A_o$ coefficient and time	123
3.24.	Natural logarithm of the developed conversion profile as a function of the $K_F A_o$ coefficient and axial distance for a superficial gas velocity of 13 cm/s	124

FIGURE PAGE

3.25. The effect and the natural logarithm of the effect of the exponent in the area (A) term upon the developed breakthrough profile 125

3.26. The effect and the natural logarithm of the effect of temperature upon the developed breakthrough profile . . . 128

3.27. The effect and the natural logarithm of the effect of pressure upon the developed breakthrough profile 129

3.28. The effect and the logarithm of the effect of reactant molecular weight upon the developed breakthrough profile . 131

3.29. Correlation of $K_f A_o$ data obtained via technique No. 2 with model, $K_f A_o = K_1 P_o V^{1.11}/P$ 133

3.30. Residuals from model correlation of data obtained via technique No. 2 134

3.31. Conversion and model-predicted conversion profiles 135

3.32. Pressure drop as a function of relative humidity during fixed-bed studies on *commercial* $Ba(OH)_2 \cdot 8H_2O$ flakes, reference superficial gas velocity of ~13 cm/s 137

3.33. The effects of effluent relative humidity on the "B" term in the pressure-drop model, $\Delta P/L = 0.01 B V_0^{1.4}$ (kPa/m) 141

3.34. Operating window for the contacting of a 330 ppm_v CO_2 gas stream with fixed beds of *commercial* $Ba(OH)_2 \cdot 8H_2O$ flakes 159

A.1. Dissociation vapor pressures for $Ba(OH)_2$ hydrates 175

B.1. H_2O-$Ba(OH)_2$ liquid-solid phase diagram 180

C.1. Thermogravimetric study of $Ba(OH)_2 \cdot 8H_2O$ samples prepared by different techniques 184

F.1. Adsorption isotherm data obtained with a balance-beam microbalance 194

G.1. Representative adsorption isotherms and associated sorption phenomenom 208

G.2. Representative adsorption isotherms for porous solids with differing pore geometries 212

FIGURE		PAGE
H Series.	Adsorption isotherms, BET plots, and sorption potential plots	221
K.1.	Grid schematic for finite-difference solution of the controlling partial differential equations and their respective boundary conditions	235
K.2.	Computer program flowchart	236
N Series.	Experimental and model-predicted breakthrough curves for the fixed-bed studies	256
O.1.	Calibration curve for IR No. 1	273
O.2.	Calibration curve for IR No. 2	275

LIST OF SYMBOLS

A = surface area, either internal or external depending upon usage, per unit volume

A_o = initial surface area per unit volume available for mass transfer

A_p = particle area/particle

A' = arbitrary constant

B = arbitrary constant

B' = arbitrary constant

b = stoichiometry coefficient
= position of reaction interface from surface of flake

b_0 = thickness of flaked particle

$\overline{b}$ = average flake thickness

C = reactant concentration

C_o = initial reactant concentration

C_p = specific heat

$c1$ = arbitrary constant

c_2 = arbitrary constant

$\overline{C}$ = C/C_o, normalized reactant concentration

c = constant in BET equation

D = dispersion coefficient
= diffusion coefficient (as defined in text)

D_n = diffusion coefficient for species n

DELS = finite difference increment in S domain

DELT = finite difference increment in Θ domain

d = mean pore diameter

d_p = mean pore diameter
= particle diameter, effective particle diameter

E_A = activation energy in Arrhenius equation

f = friction factor

f_p = particle friction factor

f' = area availability factor

G = mass flow rate/unit cross-sectional area

h = heat transfer coefficient

j = j factor

j_H = j factor for heat transfer

j_M = j factor for mass transfer

K_{EQ-n} = equilibrium constant for species n

K_F = film mass transfer coefficient

K_K = kinetic rate constant

K_n = rate constant for reaction n

K_o = frequency factor in Arrhenius equation

K_1 = arbitrary constant

L = bed length parameter

ℓ = pore depth

MW = molecular weight

n = arbitrary exponent

P = pressure, subscript refers to vapor pressure of given species

P_o = reference pressure of 101.2 kPa (1 atm)
= saturation vapor pressure

R = gas constant

$\overline{R}$ = rate of reaction per unit volume

$\overline{R}'$ = normalized rate of reaction, % conversion/time

Re = Reynolds number

Re_M = modified Reynolds number, $G/(\Psi A\mu)$

r = pore radius

S = $\frac{z}{V}$

Sc = Schmidt number

Sh = Sherwood number

T = absolute temperature

t = time

V = volume of gas adsorbed
= superficial velocity at system conditions

V_M = volume of gas adsorbed at monolayer coverage

V_0 = superficial gas velocity at reference conditions of 101.3 kPa, 294.3 K (1 atm, 70°F

$\bar{V}$ = velocity of the mass transfer zone

$\langle V \rangle$ = average stream velocity or free stream velocity (dependent upon definition as cited in text).

X = fraction of solid reacted

z = bed depth

Γ = amount sorbed at given P/P_o

Γ_M = amount sorbed at monolayer coverage

Δ_G = Gibbs free energy change

Δ_H = enthalpy change

Δ = entropy change

ε = voidage (either inter-or intraparticle depending upon usage)

Θ = $t - \frac{\varepsilon z}{V}$

μ = viscosity

ρ = solid density

ρ_G = gas or fluid density

σ = standard deviation

σ = standard deviation

T = time required for complete conversion of solid
= tortuosity
= shear force

ψ = shape factor

CHAPTER I

INTRODUCTION

Background and Process Application

In the radiation field that exists within a nuclear reactor, radioisotope ^{14}C is produced by neutron interactions with ^{14}N, ^{15}N, ^{16}O, ^{17}O, and ^{13}C that are present in the fuel, the cladding, and the primary cooling system.[1–9] Although it is a weak beta emitter, ^{14}C poses a long-term health hazard because of its long half-life of 5730 years and the ease with which it may be assimilated into living matter.[10–15]

An appreciable fraction of the ^{14}C produced would be expected to be converted to gaseous effluent during normal operation of a light-water reactor, extensive fuel element failure, storage of spent fuel, and upon fuel reprocessing. The ^{14}C would exist as either CO_2 or low-molecular-weight hydrocarbons, with the most probable method of treatment being the oxidation of the hydrocarbons to CO_2 and subsequent fixation of the CO_2. Likely CO_2 gas concentrations containing traces of ^{14}C would range from 10 to 330 ppm_v, with gas flow rates of up to 20 m^3/min (700 ft^3/min) anticipated. Expected release rates from various nuclear facilities are presented in Table 1.1.

For the removal and fixation of ^{14}C in selected off-gas streams at nuclear facilities, the following criteria have been established with respect to process development. First, the process removal efficiency must be consistent with or greater than the anticipated release criteria from the Nuclear Regulatory Commission. Second, the final product must be in an acceptable form for final waste disposal. Third, the process must possess excellent on-line reliability characteristics. Fourth, it is

Table 1.1. Approximate production and release rates of carbon-14 in the nuclear fuel cycle

Nuclear reactors	Ci/Gw(e)year
LWR	8–10
CANDU	500
Reprocessing plant	
LMFBR	6
LWR	18
HTGR	200

Source: W. Davis, Jr., *Carbon-14 Production in Nuclear Reactors*, ORNL/NUREG/TM-12 (February 1977).

desirable that the process operate at ambient conditions. Fifth, process costs must be reasonable.

Suggested technologies for ^{14}C control have generally followed commercially available technology for CO_2 control.[16,17] The processes range from CO_2 absorption in amine-bearing solutions to physical adsorption on molecular sieves to chemical reaction with a NaOH solution and carbonate interchange with $Ca(OH)_2$, the double alkali process. However, absorption, adsorption, and reaction with NaOH solution share a common trait in that they are CO_2 removal processes, but they do not chemically fix the $^{14}CO_2$ for final disposal — a requisite for the disposal of nuclear waste. Therefore, suggested technologies for the treatment of dilute CO_2-bearing gases have generally employed a removal or an enrichment step to increase the CO_2 gas concentration, followed by a final fixation step whereby the CO_2 is reacted with $Ca(OH)_2$ slurry.[16–21] The product, $CaCO_3$, possesses excellent thermal and chemical stability that makes it suited for long-term waste disposal (thermal decomposition at 825°C and water solubility of 0.0153 g/L at 25°C).[22,23] However, for the treatment of

high-volumetric, low-CO_2-content gas streams, this process suffers severely because an enrichment step is required to restrict the overall size of the $Ca(OH)_2$ slurry reactor. Other areas of concern with this technology are the generation and recycle of aqueous wastes and the need for solid-liquid separation equipment.

For the treatment of a high-volumetric, dilute CO_2-bearing off-gas stream, many potential advantages could be realized if a suitable technology utilizing a gas-solid reaction for ^{14}C removal and fixation existed. However, such a technology would be required to meet the following criteria:

1. possess favorable reaction kinetics at desired process conditions (near ambient),
2. possess favorable thermodynamics to ensure low CO_2 vapor pressures at equilibrium,
3. produce a product that would achieve adequate thermal and chemical stability for the long-term disposal of ^{14}C, and
4. utilize a reactant that would undergo ~100% conversion in order to minimize the amount of reactant required and to avoid the presence of a potentially soluble reactant.

Generally, the Group I (alkali metal) and Group II (alkaline earth) hydroxides fulfill the first two requirements. However, widely acceptable CO_2 sorbents such as ascarite (NaOH on asbestos) and $LiOH \cdot H_2O$,[24-29] which have been used extensively for CO_2 control in life support systems, lack sufficient carbonate stability for final waste disposal. Studies in CO_2 removal have been conducted on soda lime [NaOH—$Ca(OH)_2$ mixture] and baralyme [$Ca(OH)_2$—$Ba(OH)_2$ mixture] with reasonable success.[29-34] However, the

solubility of Na_2CO_3 in the former and poor reactant utilization in the latter make the use of these reactants doubtful. An examination of the carbonate products of potential Group 1 hydroxides (Table 1.2) indicates that they may be classified categorically as possessing excessive solubility in water for long-term waste disposal. However, the higher-molecular-weight carbonates of the Group II elements are considerably more stable. As shown in Table 1.2, the carbonates of calcium, strontium, and barium possess excellent solubility charcteristics and furthermore, decompose at greater temperatures.[22,23]

It has been suggested in the literature, and confirmed experimentally in our laboratory, that at ambient conditions a carbonate coating forms about the $Ca(OH)_2$ reactant, thereby resulting in severe diffusional limitations.[35] Greater conversion has been reported by increasing the humidity or operating at higher temperatures. A German patent was issued in which thermal ramping was used to enhance the reactivity and conversion of the $Ca(OH)_2$ reactant. Process temperatures were 100 to 200°C.[36] Personnel at Ontario Hydro-Canada have indicated reactant conversions of 60% to be possible at 400°C. Furthermore, conversions of 60 to 80% have been reported[5] at ambient temperatures and extremely high relative humidities (i.e., >90%). In the latter case, this author speculates that surface water plays an active role in the overall mechanism.

The alkaline earth hydroxides of strontium and barium differ from the other alkaline earth hydroxides in that they may exist in a hydrated form. The most commonly reported coordination numbers are 1 and 8, although 2 and 3 waters of hydration have been reported for $Ba(OH)_2$. Because of the previously cited diffusional limitation in the $Ca(OH)_2$ system, one might

Table 1.2. Solubility and decomposition properties of Group 1 (alkali metal) and Group 2 (alkaline earth) carbonates at low CO_2 partial pressures

	Molal solubility		Decomposition temperature (°C)
	25°C	100°C	
Group 1 carbonates			
Li_2CO_3	0.18	0.10	1310
Na_2CO_3	2.80	4.26	--
K_2CO_3	8.10	4.41	--
Rb_2CO_3	19.48	--	740
Cs_2CO_3	8.00	--	610
Group 2 carbonates			
$MgCO_3$	0.00126[a]	--	350
$CaCO_3$	0.00013	0.000375	825
$SrCO_3$	0.000075	0.00044	1340
$BaCO_3$	0.000124	0.000332	1450

[a]Cold water.

Sources: *Handbook of Chemistry and Physics*, 52d ed., The Chemical Rubber Co., Cleveland, Ohio, 1972, pp. 13-70; W. F. Linke and A. Seidell, *Solubilities of Inorganic and Metal Organic Compounds*, 4th ed., American Chemical Society, Washington, D. C., 1958.

speculate that $Sr(OH)_2 \cdot 8H_2O$ and $Ba(OH)_2 \cdot 8H_2O$ are more reactive because of a more open crystal lattice since the waters of hydration would be removed upon the reaction of the hydroxide.

To determine the likelihood of a reactant being coated by a nonporous product that would result in severe diffusional limitations of the gaseous reactant, a comparison of the molar volume crystal ratios of the product and reactant, referred to as the Pilling-Bedworth ratio, is often beneficial. The Pilling-Bedworth ratios for several alkali and alkaline earth hydroxides and their carbonate products are presented in Table 1.3. With the exception of the $Ba(OH)_2$ and $Sr(OH)_2$ data, the table was taken

from a paper by Markowitz.[24] A Pilling-Bedworth ratio >1 indicates a high probability of diffusional limitations, and a value of <1 indicates that product porosity may exist. Apparent exceptions to this relationship may result for various mixtures where synergistic effects or physical changes of the solid such as sintering or melting may occur. From Table 1.3, one would anticipate that $LiOH \cdot H_2O$, $Sr(OH)_2 \cdot 8H_2O$, $Ba(OH)_2 \cdot H_2O$, and $Ba(OH)_2 \cdot 8H_2O$ would be efficient CO_2 absorbents if the chemical reactions were kinetically favored. Additionally, one might predict that $Ba(OH)_2 \cdot 8H_2O$ will be more efficient than $Ba(OH)_2 \cdot H_2O$ for CO_2 removal. The Pilling-Bedworth ratio of 1.18 for $Ca(OH)_2$ is consistent with the reported formation of an impervious shell about the $Ca(OH)_2$ particle, thus resulting in diffusional limitations. Similarly, work performed by Boryta and Maas[25] and the Naval Research Laboratory[26] have indicated $LiOH \cdot H_2O$ (Pilling Bedworth ratio of 0.64) to be the reactive species in CO_2 removal studies and LiOH (Pilling Bedworth ratio of 1.07), to be relatively unreactive. References concerning the reactivity of strontium and barium hydroxides are few. In the comprehensive treatise by Mellor in 1928, it was cited that care must be taken to avoid exposure of the hydroxides to CO_2 in moist air.[35] Many comparative studies have been conducted on lithium hydroxide, soda lime, and baralyme.[27–34] Baralyme has a 20/80 wt % mixture of $Ba(OH)_2 \cdot 8H_2O$ and $Ca(OH)_2$. Occasionally, the mixture may contain up to 5% potassium hydroxide. In two papers published in 1942 by physicians Adriani and Battern, experimental results regarding the potential use of baralyme as a replacement for soda lime in rebreathing appliances in hospitals were presented.[33–34] Although the results were promising because the system could remove CO_2 efficiently

Table 1.3. Molar volume relationships among some possible carbon dioxide absorbents

Substance	Formula weight	Density (g/cm^3)	Molar volume (cm^3/mol)	Pilling-Bedworth ratio
LiOH	23.95	1.43	16.75	1.07
$LiOH \cdot H_2O$	41.96	1.51	27.79	0.64
Li_2CO_3	73.89	2.07	35.70	
NaOH	40.01	2.13	18.78	1.47-$Na_2CO_3 \cdot H_2O$
				1.13-Na_2CO_3
Na_2CO_3	106.00	2.51	42.25	
$Na_2CO_3 \cdot H_2O$	124.02	2.25	55.12	
$Mg(OH)_2$	58.34	2.39	24.41	1.14
$MgCO_3$	84.33	3.04	27.77	
$Ca(OH)_2$	74.10	2.34	31.63	1.18
$CaCO_3$	100.09	2.71	36.92	
$Sr(OH)_2 \cdot 8H_2O$	265.76	1.90	139.87	0.29
$SrCO_3$	147.63	3.70	39.90	
$Ba(OH)_2 \cdot 8H_2O$	315.48	2.10	144.73	0.31
$Ba(OH)_2 \cdot 1H_2O$	189.48	3.65	51.8	0.86
$BaCO_3$	197.35	4.43	44.47	

from gas streams, little information concerning the overall reaction rate was provided or could be inferred. Work performed for the Navy, Air Force, and NASA on closed life-support systems was often of a comparative nature.[24–32] These studies indicated baralyme to be less reactive than either lithium hydroxide or soda lime, and the material had a lower utilization efficiency. No information on the use of barium hydroxide hydrates was presented. In the opinion of this investigator, such studies were not conducted because of the higher molecular weight of $Ba(OH)_2$ hydrates (i.e., less capacity per gram of material), the greater reactant cost, and the toxicity of the barium cation. Extrapolation of information from the baralyme data would be very difficult because of the possibility of synergistic effects.

Of the two elements, the $Ba(OH)_2$ hydrates were selected for additional studies.[37,38] The reasons for this are twofold. First, the $Ba(OH)_2$ hydrates are more stable than the $Sr(OH)_2$ hydrates. Second, $Ba(OH)_2$ hydrates are readily available in commercial quantities at reasonable costs. Such a market has not developed for the $Sr(OH)_2$ hydrates possibly because of (1) the smaller fraction of strontium in the earth's crust (0.018% as compared to 0.04% for the barium), and (2) the inaccessibility of strontium-rich minerals.[39] In comparison, calcium comprises 3.6 wt % of the earth's crust.

$Ba(OH)_2$ Hydrate–$BaCO_3$ Literature Review

An extensive literature review of $Ba(OH)_2$ hydrate vapor pressures, the binary water–$Ba(OH)_2$ system, thermal studies on $Ba(OH)_2$ hydrates, the thermodynamics of the CO_2–$Ba(OH)_2$ hydrate reaction, and the crystal properties of $Ba(OH)_2$ hydrates and $BaCO_3$ are presented in this section and

Appendixes A, B, C, and D. As no similar compilation was found in the open literature, this review is presented in its entirety such that it may be an aid to future researchers. The intent of this section will be to highlight information of special significance to this study.

Although hydrates of $Ba(OH)_2$ have been cited in the literature as being reactive toward CO_2 in ambient air,[35] the extent of this reactivity had not been examined until this research. The stoichiometry of the overall reaction may be represented by

$$Ba(OH)_2 \cdot xH_2O(s) + CO_2(g) \rightarrow BaCO_3(s) + (x+1)H_2O(g), \qquad (1.1)$$

where x is the initial degree of hydration.

In the opinion of this author, the most credible study conducted to date on the dissociation vapor pressures of $Ba(OH)_2$ hydrates was that of Kondakov, Kovtunenko, and Bundel.[40] The results were published in 1964. In this study, the water vapor pressure of $Ba(OH)_2 \cdot xH_2O$ samples with x values of 0.3896, 1.342, 2.260, 3.282, 4.196, 5.042, 5.882, and 6.763 were determined. When the results were plotted (log P vs 1/T), three distinct lines were obtained, as shown in Fig. 1.1. The lines correspond to $Ba(OH)_2$ hydrate samples in which $Ba(OH)_2 \cdot H_2O$, $Ba(OH)_2 \cdot 3H_2O$, and $Ba(OH)_2 \cdot 8H_2O$ were the contributing species to the water vapor pressure within the system. The controlling decomposition reactions and their respective dissociation vapor pressure equations were found to be the following:

$$Ba(OH)_2 \cdot 1H_2O(s) \rightarrow Ba(OH)_2(s) + H_2O(g), \qquad (1.2)$$

$$\log P = -\frac{61353}{19.155T} + 12.421 \; ;$$

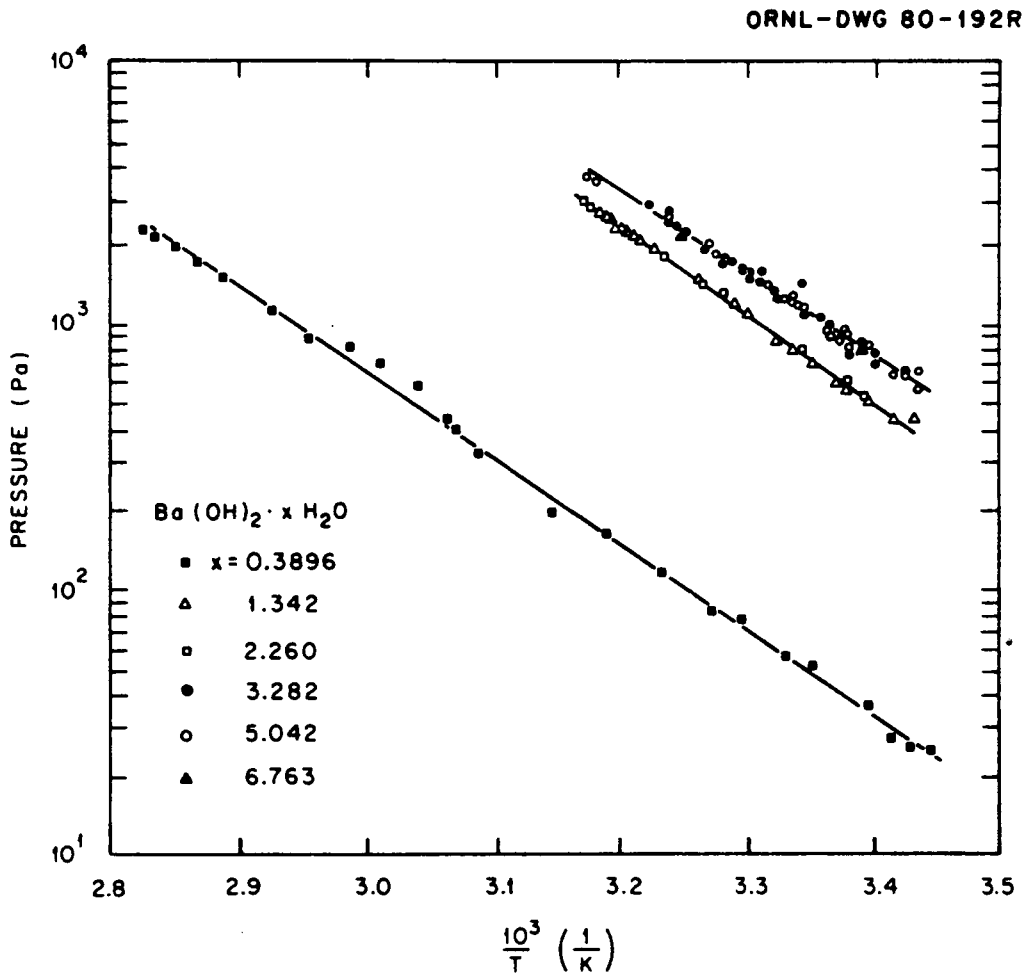


Figure 1.1. Dissociation vapor pressures for $Ba(OH)_2$ hydrates. Source: B. A. Kondakov, P. V. Kovtunenko, and A. A. Bundel, "Equilibria Between Gaseous and Condensed Phases in the Barium Oxide — Water System," *Russ. J. Phys. Chem.* 38(1), 99-102 (1964).

$$Ba(OH)_2 \cdot 3H_2O(s) \rightarrow Ba(OH)_2 \cdot 1H_2O(s) + 2H_2O(g), \quad (1.2)$$

$$\log P = -\frac{62618}{19.155T} + 13.823 ;$$

$$Ba(OH)_2 \cdot 8H_2O(s) \rightarrow Ba(OH)_2 \cdot 3H_2O(s) + 5H_2O(g), \quad (1.4)$$

$$\log P = -\frac{58230}{19.155T} + 13.238 ;$$

where

P = vapor pressure, Pa or $nt \cdot m^{-2}$,

T = temperature, K.

Using the Van't Hoff equation, the data were analyzed for thermodynamic consistency. Based upon the entropy change for the formation of the trihydrate, they concluded that the trihydrate may be less stable than the other crystalline hydrates. However, other investigators under highly controlled conditions have reported $Ba(OH)_2 \cdot 2H_2O$ and amorphous compounds to exist. Attributing to the difficulties in the analysis of vapor pressure data may be the presence of a $Ba(OH)_2 \cdot 3H_2O$—$Ba(OH)_2 \cdot 8H_2O$ eutectic. The existence of this eutectic, consisting of 10 mol % $Ba(OH)_2 \cdot 3H_2O$ or a stoichiometric composition of $Ba(OH)_2 \cdot 7.19\ H_2O$, was reported by Michand in 1968 (see Appendix B).[41,42]

With the exception of $Ba(OH)_2 \cdot 3H_2O$, the thermodynamics of the CO_2—barium hydroxide hydrate gas-solid reaction may be calculated from published values.[40,43–48] Several sources were consulted for enthalpy and entropy of formation values at 298.15 K. With the exception of $Ba(OH)_2$ and its hydrates, the values were extremely consistent. The thermodynamic values presented by Kondakov for $Ba(OH)_2$, $Ba(OH)_2 \cdot 1H_2O$, $Ba(OH)_2 \cdot 3H_2O$ and $Ba(OH)_2 \cdot 8H_2O$ were chosen so as to ensure internal consistency. The

enthalpy of formation values for $Ba(OH)_2 \cdot 1H_2O$ and $Ba(OH)_2 \cdot 8H_2O$ differed from the values of the National Bureau of Standards by <0.7%. Table 1.4 shows the thermodynamic values for the following reactions:

$$Ba(OH)_2(s) + CO_2(g) \rightarrow BaCO_3(s) + H_2O(g), \quad \Delta H = -115 \text{ kJ/mol}; \quad (1.5)$$

$$Ba(OH)_2 \cdot H_2O(s) + CO_2(g) \rightarrow BaCO_3(s) + 2H_2O(g), \quad \Delta H = -53 \text{ kJ/mol}; \quad (1.6)$$

$$Ba(OH)_2 \cdot 3H_2O(s) + CO_2(g) \rightarrow BaCO_3(s) + 4H_2O(g), \quad \Delta H = +73 \text{ kJ/mol}; \quad (1.7)$$

$$Ba(OH)_2 \cdot 8H_2O(s) + CO_2(g) \rightarrow BaCO_3(s) + 9H_2O(g), \quad \Delta H = 364 \text{ kJ/mol}. \quad (1.8)$$

Table 1.4. Thermodynamic properties of the CO_2—$Ba(OH)_2$ hydrate reaction at 298.15 K

Reaction	ΔG kJ/mol	ΔH kJ/mol	ΔS $J \cdot mol^{-1} \cdot K^{-1}$	K_{eq}
(1.5)	-103.5	-114.6	-37.2	$1.42 \cdot 10^{18}$
(1.6)	- 84.1	-52.9	104.6	$5.50 \cdot 10^{14}$
(1.7)	- 59.3	+72.6	442.3	$2.47 \cdot 10^{10}$
(1.8)	-2.3	364.4	1230.0	2.55
(1.9)	-79.8	-31.8	161.3	$9.80 \cdot 10^{13}$
(1.10)	-103.8	-113.3	-31.7	$1.58 \cdot 10^{18}$

At conditions of 298 K and 1 atm, the fugacities of the gas species (assuming gas ideality) may be approximated by their partial pressures (atm), and the fugacities of the crystalline species, with respect to their reference states, are equal to ~1. If the water product is present as vapor, the equilibrium constant, K_{eq}, is equal to $[P(H_2O)]^{x+1}/[P(CO_2)]$, where x is the hydration number of the reacting species and $P(H_2O)$ and $P(CO_2)$ are the partial pressures of water and carbon dioxide that exist within the system. The maximum water vapor partial pressure within the

system at a fixed temperature is that at complete saturation. At 25°C, this value is 3.165 kPa (23.75 mm Hg). Therefore, based upon the previously calculated equilibrium constants for the speculated reactions, the corresponding CO_2 partial pressure at equilibrium can be calculated for the possible carbonation reactions (Table 1.5). This analysis

Table 1.5. Equilibrium values for the CO_2—$Ba(OH)_2$ hydrate reaction

Reaction	K_{eq}	Reactant hydration	P_{CO_2}	
			Pa	mm Hg
(1.5)	$1.42 \cdot 10^{18}$	0	$2.2 \cdot 10^{-15}$	$1.7 \cdot 10^{-17}$
(1.6)	$5.50 \cdot 10^{14}$	1	$1.8 \cdot 10^{-13}$	$1.3 \cdot 10^{-15}$
(1.7)	$2.47 \cdot 10^{10}$	3	$3.9 \cdot 10^{-12}$	$2.9 \cdot 10^{-14}$
(1.8)	2.55	8	$1.1 \cdot 10^{-9}$	$8.5 \cdot 10^{-12}$
(1.9)	$1.58 \cdot 10^{18}$	aqueous	$2.0 \cdot 10^{-15}$	$1.5 \cdot 10^{-17}$
(1.10)	$9.80 \cdot 10^{13}$	8	$1.0 \cdot 10^{-9}$	$7.8 \cdot 10^{-12}$

assumes that (1) the transformation to a higher hydrate is slow, and (2) the maximum water vapor pressure is that at saturation. If the kinetics of the hydration steps are rapid, the maximum water vapor for the hydrates will be lowered and will correspond to that of the next higher hydrate, resulting in a lower-than-calculated CO_2 equilibrium concentration. With respect to the preceding analysis, if any of the speculated reaction processes were equilibrium-controlled, the effluent CO_2 concencentration would be less than 1 part per trillion. Also presented in Tables 1.4 and 1.5 are the thermodynamic and equilibrium values for the reaction of CO_2 with soluble $Ba(OH)_2$. The reaction may be represented by

$$Ba(OH)_2\ (aq) + CO_2(g) \rightarrow BaCO_3(s) + H_2O(l), \quad \Delta H = -113\ kJ/mol. \quad (1.9)$$

Again the reaction will become equilibrium-controlled only for very low CO_2 partial pressures.

Based upon a dissociation pressure for $Ba(OH)_2 \cdot 8H_2O$ of 1.1 kPa (8.26 mm Hg) at 298 K, any water vapor pressure greater than this value would override the thermodynamic constraints for formation of $Ba(OH)_2 \cdot 8H_2O$. However, the kinetics of this exothermic transformation are unknown. If the gas surrounding the particle is water saturated, the excess water of reaction (nine molecules of water per molecule of CO_2 reacted) must remain as a liquid in the pore structure and may have a deleterious effect on the overall reaction. Thermodynamic and equilibrium values for this reaction sequence are also presented in Tables 1.4 and 1.5 for the following reaction:

$$Ba(OH) \cdot 8H_2O(s) + CO_2(g) \rightarrow BaCO_3(s) + 9H_2O(l), \quad \Delta H = -32 \text{ kJ/mol.} \quad (1.10)$$

Again, the effluent CO_2 concentration will be limited by equilibrium considerations only at very low CO_2 partial pressures.

When no work is being performed on or by the system, the enthalpy change for a system with fluid flow is a measure of the endo- or exothermicity of the reaction at 298 K. Although hydroxide-carbonate reactions are generally regarded as exothermic, as reflected by the stability of the carbonate product, the waters of reaction (when released as a vapor) tend to make the reaction less exothermic. If the surrounding gas is water saturated and heat is not removed from the system by vaporization of the released waters of hydration, the reaction becomes more exothermic. Therefore, for situations in which the feed gas is rich in CO_2, the gas become saturated rapidly with water. In this case, part of the column may operate under endothermic conditions [Reaction (1.8)] and another section under exothermic conditions [Reaction (1.10)].

Similar Systems—The Reaction of $Ca(OH)_2$ and $LiOH \cdot H_2O$ with CO_2

Presented in Table 1.6 for the purpose of comparison are thermodynamic values for the analogous calcium and lithium hydroxide gas-solid systems. The overall reactions are the following:

$$Ca(OH)_2(s) + CO_2(g) \rightarrow CaCO_3(s) + H_2O(g), \ \Delta H = -69 \text{ kJ/mol}; \quad (1.11)$$

$$2LiOH(s) \cdot H_2O + CO_2(g) \rightarrow Li_2CO_3(s) + 3H_2O(g), \ \Delta H = +32 \text{ kJ/mol}. \quad (1.12)$$

Table 1.6. Thermodynamic properties of the $Ca(OH)_2$ and $LiOH \cdot H_2O$ gas-solid carbonation reactions at 298.15 K

Reaction	ΔG kJ/mol	ΔH kJ/mol	ΔS $J \cdot mol^{-1} \cdot K^{-1}$	K_{eq}	P_{CO2} (Pa)
(1.11)	-63.5	-69.4	-19.6	$1.3 \cdot 10^{11}$	$2.4 \cdot 10^{-8}$
(1.12)	-45.1	-32.1	258.7	$8.0 \cdot 10^{7}$	$3.8 \cdot 10^{-8}$

The reaction of $Ca(OH)_2$ with CO_2. It has been reported that when $Ca(OH)_2$ reacts with CO_2, a protective $CaCO_3$ coating is formed about the $Ca(OH)_2$ particles which creates severe diffusional resistances and causes the reaction to essentially cease.[35] In our studies, this observation was verified. Improved solid reactivity has been noted when temperature ramps are used to crack the surrounding $CaCO_3$ coating,[36] and when the temperature is raised to 400°C or where the relative humidity is increased to >90%.[5] Reactant conversions are still limited. When $Ca(OH)_2$ is incorporated with NaOH (soda lime), an acceptable CO_2—removal process is possible. However, the efficiency of the process is closely coupled to the amount of excess water.[29-32] A typical composition for high-moisture soda lime is 4.5 wt % NaOH, 17.5 wt % H_2O, and 78 wt %

$Ca(OH)_2$. It has been speculated that the reaction proceeds via the following mechanism:

$$\begin{aligned} CO_2 + H_2O &\rightarrow HCO_3^- + H^+ \\ Ca(OH)_2 + HCO_3^- &\rightarrow CaCO_3 + OH^- \\ 2NaOH + HCO_3^- &\rightarrow Na_2CO_3 + OH^- \\ OH^- + H^+ &\rightleftarrows H_2O \end{aligned} \qquad (1.13)$$

The extent of carbonate-hydroxyl interchange between Na_2CO_3 and $Ca(OH)_2$ is not known.

The $Ca(OH)_2$ reactant has shown excellent CO_2 scrubbing capabilities when present in aqueous solutions. Because of the low solubilities of $Ca(OH)_2$ (pH, 12.5) and $CaCO_3$ at ambient conditions, the solution is often in slurry form with an accompanying solution-dissolution mechanism. The reaction is ionic in nature, taking place in the aqueous solution. Because the water reaction product is liquid, the reaction is more exothermic than the gas-solid reaction. The overall carbonation reaction is

$$CO_2 + 2OH^- \rightarrow CO_3^{2-} + H_2O. \qquad (1.14)$$

This reaction in aqueous solution is usually broken into two steps, the formation of the bicarbonate ion and the formation of the carbonate ion.[49] The first step may be accomplished by one of two mechanisms:

$$CO_2 + OH^- \rightarrow HCO_3^- \qquad (1.15)$$

$$CO_2 + H_2O \rightarrow HCO_3^- + H^+ \qquad (1.16)$$

The rate constant for reaction (1.15) is given by

$$\log K_{OH^-} = 13.635 - \frac{2895}{T}, \qquad (1.17)$$

where T is the temperature in degrees Kelvin. At 20°C and infinite dilution, K_{OH^-} is equal to 6000 L/mol-OH^-•s. Reaction (1.16) is first order, with a rate constant of approximately 0.02 s^{-1} at 20°C. Therefore, if the solution has a hydroxyl ion concentration in excess of 10^{-4} mol/L ion (pH >10), reaction (1.15) will be controlling. As the hydroxyl ion concentration is decreased, the contribution from reaction (1.16) will increase and finally become controlling. Also, reaction (1.16) can be catalyzed by certain anions. The formation of the carbonate ion may be represented by the following equation:

$$HCO_3^- + OH^- \rightarrow CO_3^{2-} + H_2O. \qquad (1.18)$$

Since this reaction is ionic in nature, in alkaline solutions it is assumed to be instantaneous. Therefore, in alkaline solutions, reaction (1.15) is the rate controlling step in the overall mechanism.

The reaction of LiOH with CO_2. Lithium hydroxide is a widely accepted solid reactant for CO_2 removal.[24-26] At near ambient temperatures, anhydrous LiOH is unreactive toward CO_2. However, when the water vapor pressure is raised and the monohydrate ($LiOH•H_2O$) becomes stable, the reaction is quite rapid. It has been reported that care must be taken to avoid the formation of a saturated LiOH solution, which occurs at sufficiently high water vapor pressures. The saturated solution has been observed to glaze over the outside of the particle, causing the reactant to become inactive. Therefore, the partial pressure of the water vapor within the bed must be maintained between the dissociation vapor pressure of $LiOH•H_2O$ and the vapor pressure of a saturated LiOH

solution. The contribution of the water reaction product must be included in the total water vapor pressure as three molecules of H_2O are released per molecule of CO_2 reacted. Thus by having the water vapor pressure data available for saturated LiOH solutions and $LiOH \cdot H_2O$ dissociation, one may predict acceptable operating conditions for a given CO_2 concentration, system pressure, and temperature. Inherent in the preceding logic is the assumption that certain physical changes such as melting, sintering, etc., do not occur.

CHAPTER 2

EXPERIMENTAL EQUIPMENT, INSTRUMENTATION, AND COMPUTER SUPPORT

Microbalance System

To aid in the development of a model for the fixed-bed macrosystem, an understanding or at least an awareness of phenomena that occur at the microscale is required. Therefore, with the guidance of E. L. Fuller, Research Scientist at the Union Carbide Y-12 Plant, a microbalance analytical system was designed, constructed, and successfully operated. This system is particularly well suited for experimental studies in which mass, pressure, and temperature are key parameters. Such situations often occur during thermodynamic, kinetic, and surface studies on reacting solids.[50–54] A schematic and a photograph of the experimental system are presented in Figures 2.1 and 2.2.

The heart of the microbalance system is a Cahn Model RG automatic electrobalance. The balance is sensitive to 0.1 μg and has an upper capacity of 2.5 g. The microbalance was calibrated over the 100- to 200-mg range with U.S. National Bureau of Standards Class M weights manufactured by Ainsworth Weights. The tolerance on these weights is 0.0054 mg. The calibration was performed by placing the reference weights and the counterbalance weights in quartz or glass pans that were suspended from the ends of the microbalance beam by 25-μm-diam tungsten wire (Figure 2.3). System calibration was performed at a system pressure of $<10^{-4}$ Pa ($<10^{-6}$ torr) to avoid buoyancy effects (Appendix F). The output from the microbalance was monitored with a Keithly Model 177 digital multimeter and recorded with a Linear Instrument Corp. Model 485 strip chart

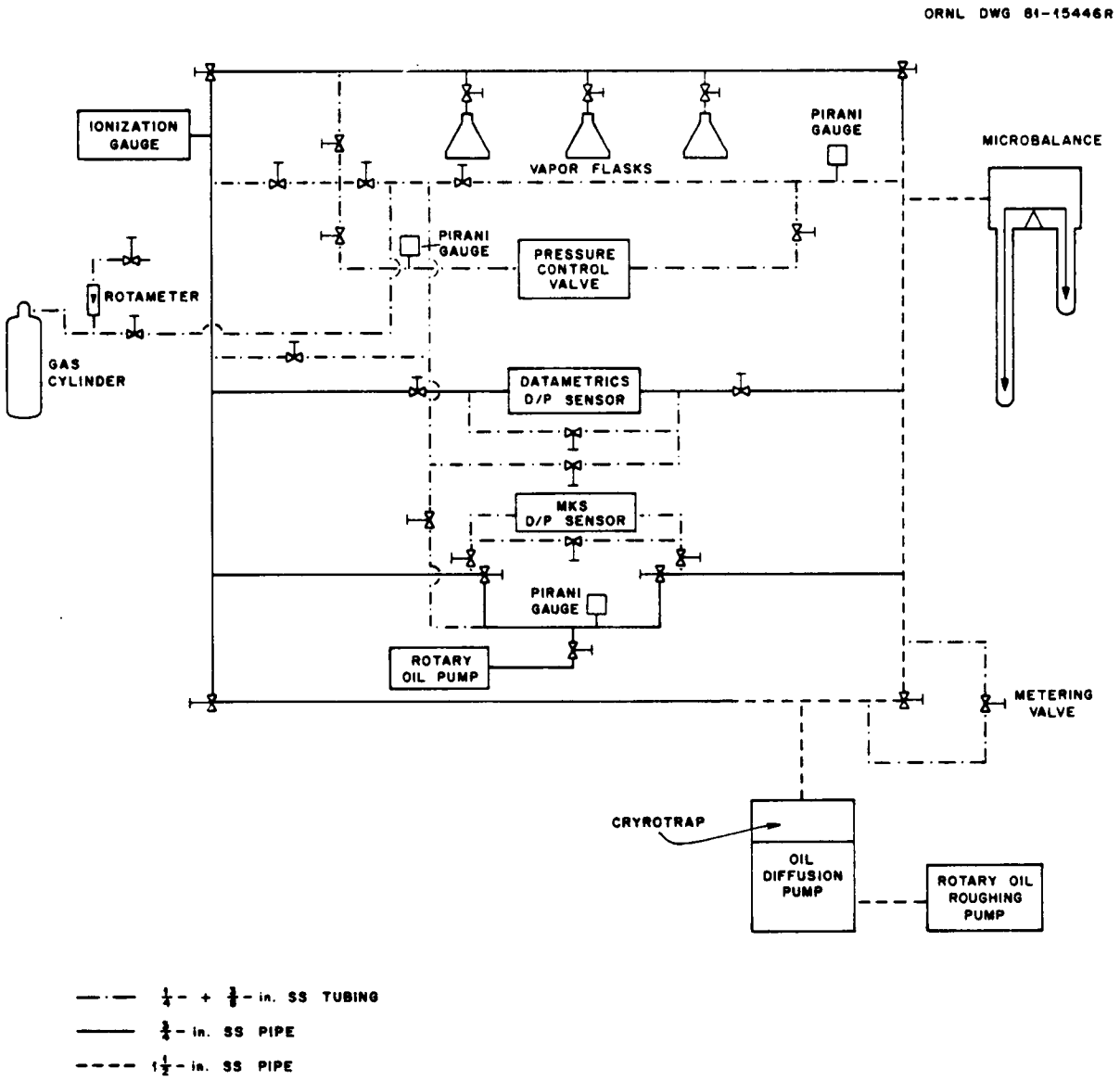


Figure 2.1. Schematic of the microbalance system.

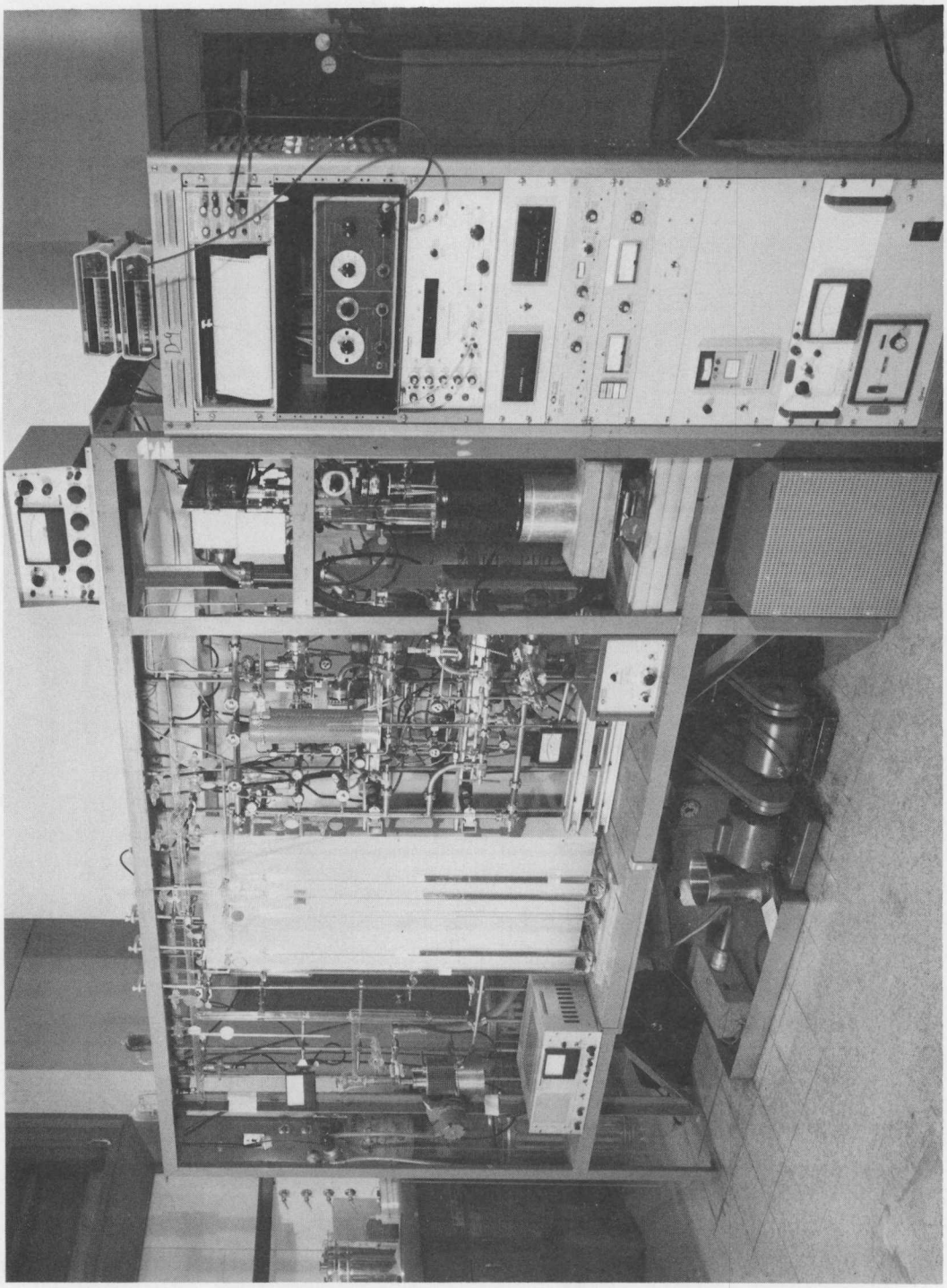


Figure 2.2. Photograph of microbalance system.

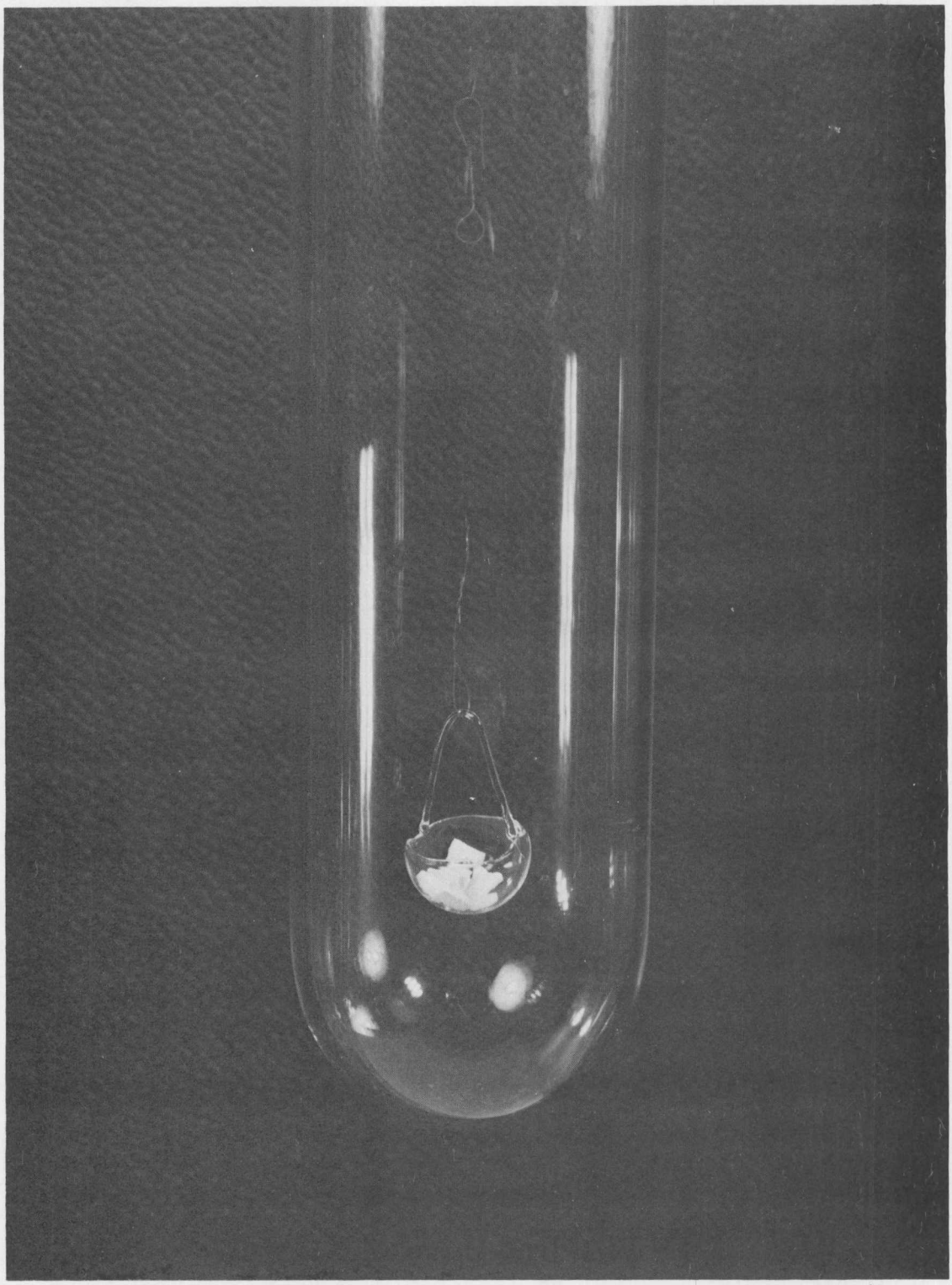


Figure 2.3. Photograph of sample of *commercial* $Ba(OH)_2 \cdot 8H_2O$ flakes suspended in the sample hang-down tube.

recorder. Baseline noise and drift were problems during the initial calibration of the system. However, the severity of these problems was greatly reduced by (1) maintaining a more uniform room temperature; (2) obtaining electrical power for the microbalance and other key components from a Elgar AC Line Conditioner thus minimizing the effects of line voltage fluctuations, (3) applying antistatic solution to the quartz hangdown tubes; and (4) applying a small time-dependent linear correction factor. The accuracy of the overall microbalance system was determined to be ±3μg.

Pressure within the system is controlled by one of two pressure sensors and a pressure control valve. Since both pressure sensors measure differential pressure, an absolute pressure reading is obtained by connecting the reference side to a 10^{-4} Pa vacuum. A Datametric Model Type 1018 electronic manometer equipped with a Model Type 1045 offset adapter or null pot was used for monitoring pressures in this study. Accuracy of the instrument is 0.07% of the reading plus 0.003% of the operating scale. For a 4.0-kPa (30-torr) reading, accuracy would then be ±4.0 Pa (±0.031 torr). Although not used in this study, the system is also equipped with a MKS Baratron electronic manometer that is capable of operating over pressure ranges of 0 to 1.33 kPa (0.01 torr) up to 0 to 4.0 kPa (30 torr). For digital output, accuracy is 0.02% of the full range plus 0.15% of the dial reading taken from the null pot. Both sensors are of the capacitance type and are thermostated to avoid drift from fluctuations in the ambient temperature. During operation, the desired system pressure is dialed at the electronic manometer and a nulled or error output signal is produced and sent to a Granville-Phillips Series

216 pressure controller. The pressure controller then actuates a servodriven valve.

Temperature control is possible over the continuous range of -35 to 1100°C. Ethylene glycol—water or water baths in vacuum Dewars flasks may be used at the lower temperatures. Refrigeration is supplied by a Polyscience Model KR50 refrigeration unit, and heating is by a regulated thermostated Hallikainen Instruments Thermotrol equipped with an immersion heater. An electric stirrer is situated in the bath to ensure temperature uniformity. For operation at higher temperatures, a Marshall furnace is used. Previous studies by Fuller have indicated this furnace to exert a negligible magnetic inductance force on the tungsten hangdown wire and sample. This force, if appreciable, would result in erroneous microbalance readings. Control for furnace temperatures over the ambient to 300°C range is provided by a Barber Coleman Series 527Z temperature controller. Temperature control over the 200 to 1100°C range is provided by a Varian Model 901-2060 temperature controller. System temperature is monitored with a calibrated Omega Trendicator temperature indicator connected to a Type K thermocouple. Liquid nitrogen and dry ice baths may be used for isotherm studies at -196°C and -78.5°C, respectively.

Vacuum is provided in the system by either a standard rotary oil vacuum pump capable of evacuating the system to <1.33 Pa (<10 μm Hg) or a Varian Model H2S diffusion pump, equipped with a Model 0325 Cryo-baffle liquid nitrogen trap, connected to a roughing pump (standard rotary oil pump). The system has a maximum pumping speed of 22.7 kPa L/s. Using the trap as a baffle to prevent backstreaming, an adequate vacuum of 10^{-4} Pa ($<10^{-6}$ torr) was possible. Vacuum pressures within the system

are monitored via an independent Hastings DV-6 gauge, and two Granville-Phillips Thermo-Gauges and one Bayard-Alpert ionization gauge connected to a Granville-Phillips Series 260 gauge controller. In the event of rapid system pressurization, an alarm signal from the gauge controller actuates a relay that in turn shuts off the diffusion pump, thus avoiding system contamination by the polyphenylether pump oil.

As indicated in Figure 2.1, the vacuum system was constructed of stainless steel tubing, having diameters of 1 1/2, 3/4, 3/8, and 1/4 in. Stainless steel was chosen in lieu of copper as the material of construction because of its greater inertness and rapid outgassing properties.[55] Joints within the system were constructed with commercially available Varian Conflat flanges and copper gaskets, Cajun fittings and gaskets, or they were welded or silver soldered. With the exception of one vacuum valve, all valves were constructed of stainless steel, monel, or inconel with metal bellows seals. The 3/4-in. valves were Varian Model 951-5014, bakeable to 400°C. The 3/8-in. valves were either Hoke Model 4611N4M or Model 4628N4M, bakeable to 180°C. The 1/4-in. valves were Nupro Model 4H-TSW, bakeable to 485°C, and the 1 1/2-in. valve was a Varian Model 951-5092 valve with a stainless steel body and a polyimide bellows. This valve is capable of a 300°C bakeout temperature. The pressure control valve, upon minor disassembly of key electrical components, may be subjected to temperatures as great as 450°C. Thus in the event of system contamination, much of the system may be thermally outgassed. A close-up photograph of this portion of the system is presented in Figure 2.4. A unique aspect of the microbalance system is the high vacuum microbalance enclosure shown in Figure 2.5. The standard vacuum enclosure supplied by

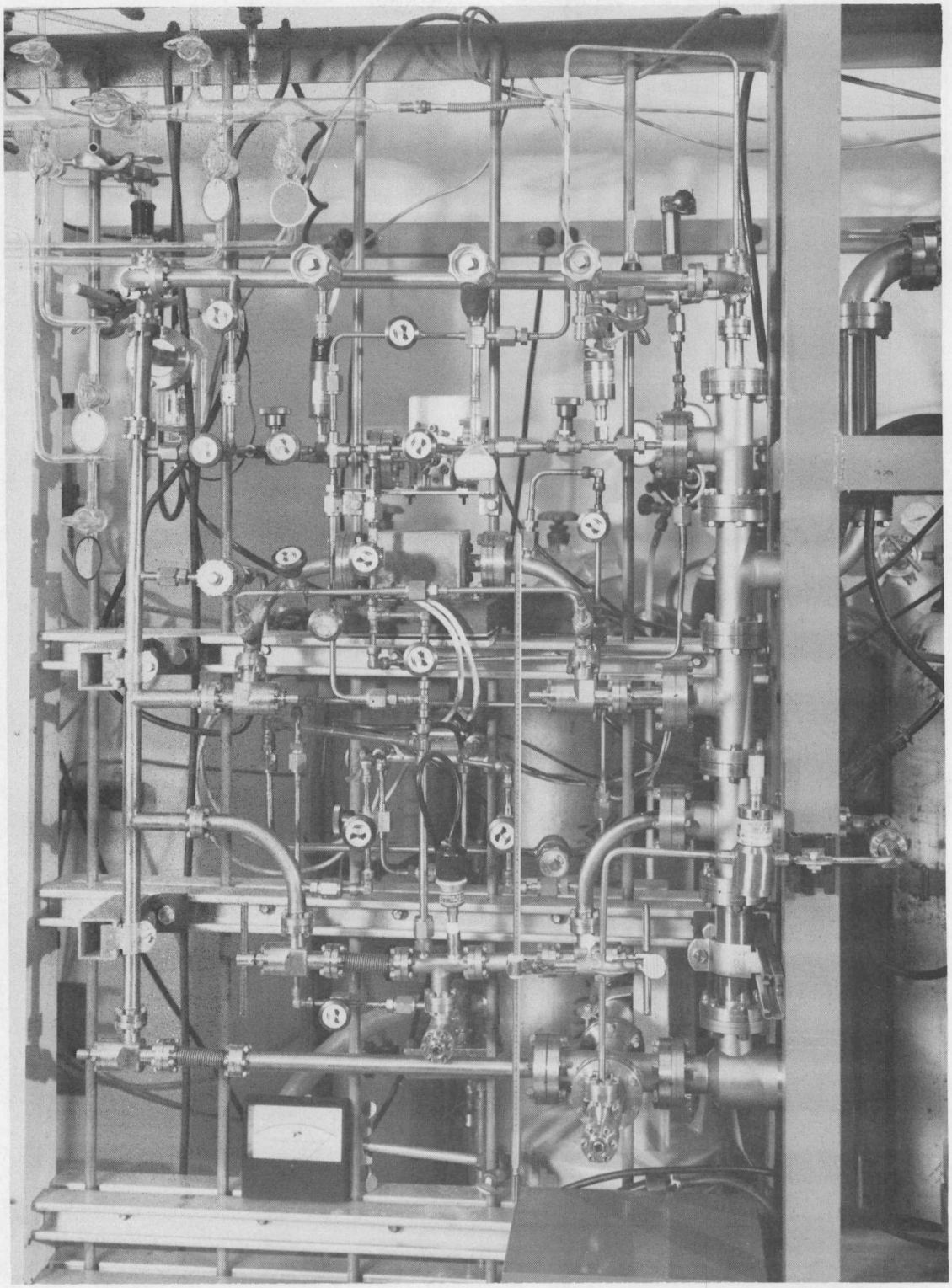


Figure 2.4. Close-up photograph of gas transfer and pressure control portion of the microbalance system.

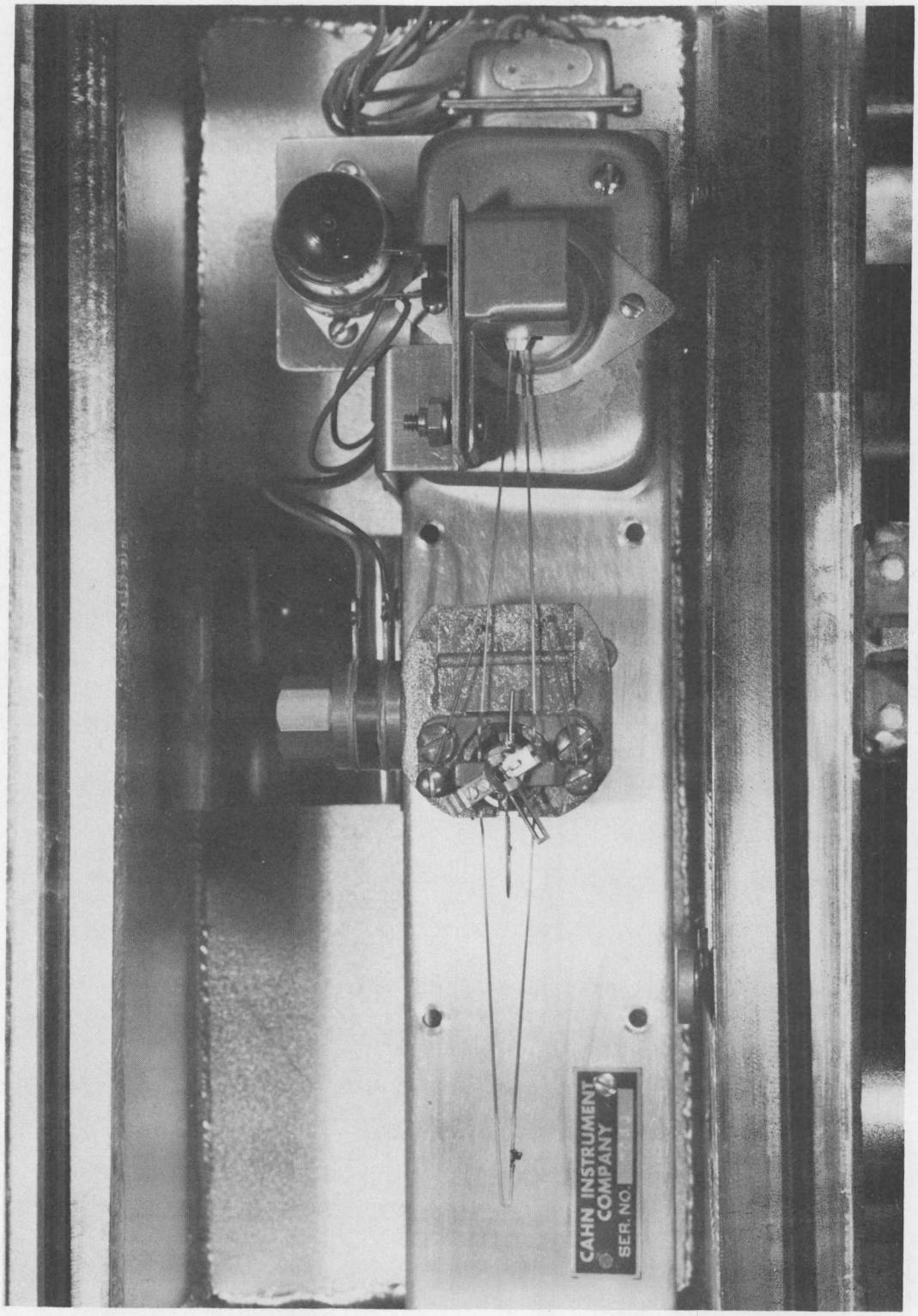


Figure 2.5. Microbalance situated in stainless steel vacuum enclosure.

Cahn is constructed of glass, and access to the balance for adjustment or repairs is difficult. The enclosure, designed for this study, is constructed of stainless steel that has been electropolished to minimize outgassing. Access to the balance is made possible by a 3/4-in. safety glass plate that may be removed for repairs and adjustments. A seal between the glass plate and flange is provided by a 1/4-in. neoprene O-ring situated in a machined groove. When under vacuum, a force of 3.36 kN (750 lb) is exerted by atmospheric pressure on the O-ring surface, thus providing an excellent seal. Standard tie-downs enable the system to be operated at a slightly positive pressure.

Upon the suggestion of Fuller, the microbalance beam is oriented in a north/south direction. This precaution was taken to reduce the possibility of strain being induced on the balance by thermal expansion of the building because the building is heated in an east to west manner during the day. For highly accurate work, it is important that the temperature of the laboratory be uniform so as to avoid possible strains in the system due to thermal expansion and to minimize instrument drift. The microbalance analytical system was firmly attached to a rigid metal rack that was bolted to the floor. Building vibrations were occasionally monitored by the balance; when severe, they caused the suspended sample to oscillate in a pendulumlike manner. At a pressure of 10^{-4} Pa (10^{-6} torr), the damping out of these oscillations by the dilute gas present in the system was extremely slow. Under certain conditions, the oscillations were observed to increase in amplitude. Precautions were also taken with respect to the amount of line noise in the electrical circuits that were used. As previously mentioned, an AC line conditioner

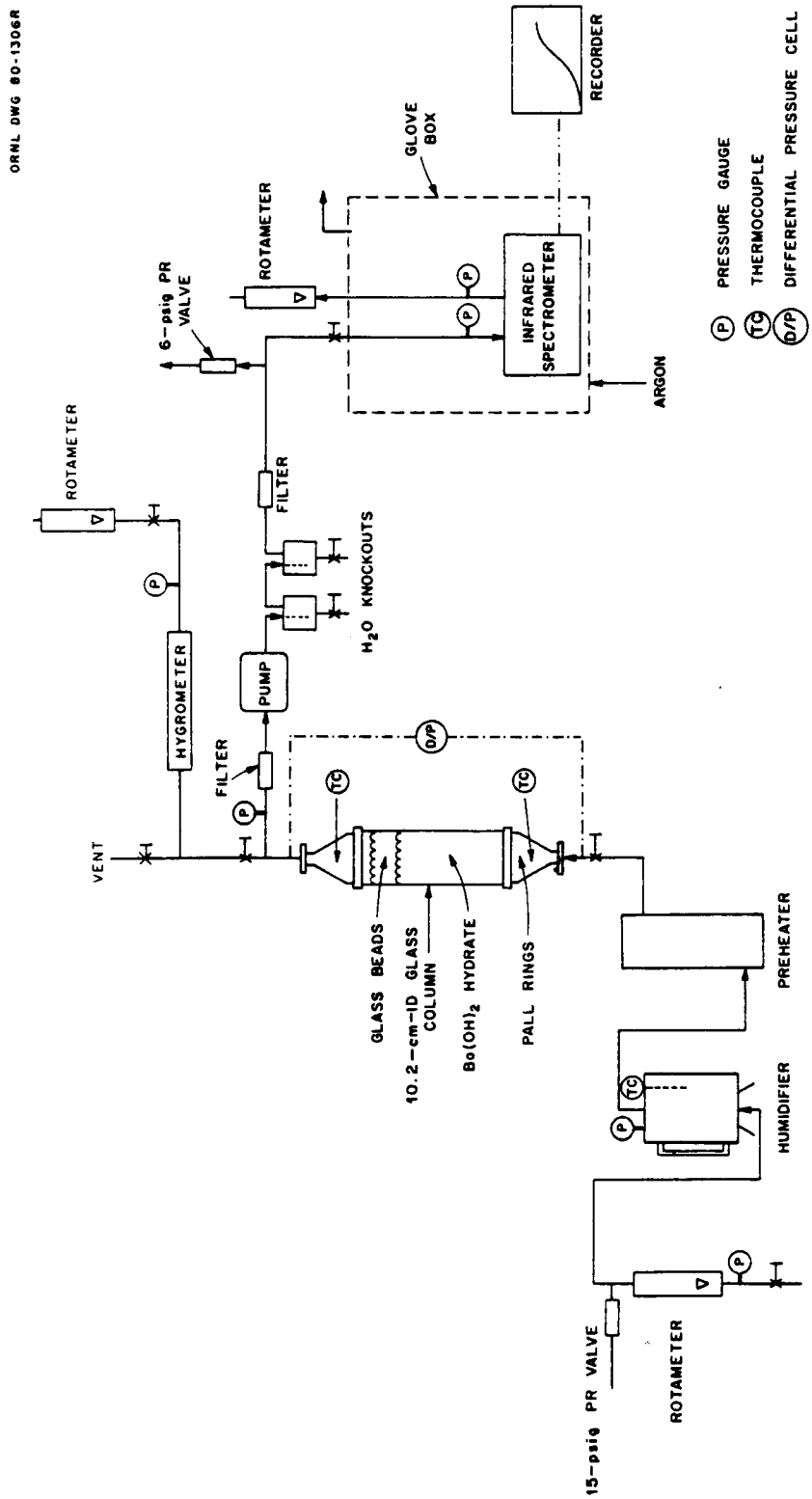


Figure 2.6. Schematic of the fixed-bed experimental equipment.

was used to supply electrical power to crucial instrumentation. Static electricity was a problem, particularly during the dry winter months. This problem was reduced by the routine use of an antistatic solution on glass and quartz surfaces.

Fixed Bed Experimental System

Studies have indicated that the most likely mode of gas-solid contact is a fixed bed. A schematic of the fixed-bed experimental equipment for this study is presented in Figure 2.6. Two identical systems were constructed, and the equipment may be used for either differential-bed or extended-length fixed-bed studies. The feed gas, dry air containing ~330 ppm_v CO_2, is metered through calibrated rotometers and to a humidifier. The extent of humidification is controlled by the temperature and pressure of the humidifier. Operation of the humidifier at subambient temperatures is possible with a refrigeration system. The gas is then passed through a preheater and to the reactor. Because of the endothermic nature of the reaction, 364 kJ/mol CO_2, the reactor is jacketed with a Glascol heating mantle to insure near-isothermal operating conditions. Calibrated thermocouples are inserted at the top and bottom of the reactor and are monitored on an Omega Trendicator digital temperature indicator. Temperature control to the electric heaters in the humidifier and preheater and to the heating mantle is provided by Barber-Coleman Series 527 temperature controllers. At the base of the 10.2-cm (4-in.)-ID glass reactor, the gas is dispersed by pall rings before passing through the fixed bed. The fixed bed is supported by 100 mesh wire screen. The minimal bed depth for differential reactor studies is 6 mm (1/4-in.).

The common length for the extended-length fixed-bed studies is 51 cm (20 in.). Five centimeters of glass or ceramic beds are placed on top of the reactant to ensure packed-bed flow continuity (minimize end effects) and to minimize bed expansion in the upper section. For these studies, a calibrated Foxboro Model E13DH differential pressure cell was used to monitor the pressure drop across the column. The gauge pressure at the top of the column was also determined by referencing the low-pressure-side to atmospheric pressure. An absolute pressure value was then obtained by a knowledge of the barometic pressure. Generally, the pressure at the top of the column was maintained at ~105 kPa (0.6 psig). A small portion of the effluent gas is filtered and fed to a Metal Bellows Corp. metal bellows pump for pressurization to 145 kPa (7 psig). Following pressurization, the gas flows through two knockout vessels for water removal and then to the CO_2 analytical system. A second off-gas stream is routed to the water vapor analysis system.

The CO_2 analytical system consists of two flowthrough Wilks-Foxboro Miran 1A infrared analyzers (IR) that are located in a glove box. Because the window to the flow cell and IR light source in the analyzer are separated by the surrounding gas, it was necessary to place the analyzers in a controlled environment because of fluctuations in the ambient CO_2 concentration and hence, the drifting of the baseline. The glove box is continuously purged with argon. The infrared spectrometer wavelength is set at 4.25 μm and the pathlength is set at 20.25 m. The cell pressure is maintained at 136 kPa (5 psig), and the cell is jacketed and maintained at 50°C to avoid water condensation within the cell. A sample gas flow rate of 1 L/min to the 5.6-L cell ensures rapid instrument

response. The instrument was calibrated over the concentration range 100 ppb_v to 330 ppm_v CO_2, using calibration gases obtained from the Bureau of Mines Helium Operations Plant in Amarillo, Texas, and from commercial vendors. Calibration curves are presented in Appendix N. The calibration gases obtained from the Bureau of Mines are excellent sub-ppm_v standards because they have been analyzed by a freeze-out preconcentration technique followed by mass spectroscopic analysis. The system is recalibrated on a routine basis. The voltage output from the IR is monitored on a Keithly Model 177 digital multimeter and is recorded on a Linear Instruments strip chart recorder. No interference from high water concentration was observed at extremely low CO_2 concentrations.

A small portion of the total effluent gas is routed to the H_2O analytical system that consists of a EG&G Model 660 dewpoint hygrometer and ancillary equipment. This instrument directly determines the temperature at which water in the off-gas stream condenses on a mirror surface, thus providing a true dewpoint measurement for a given sensor pressure. As liquid condensation is a function of temperature and pressure, a precise knowledge of the sensor pressure is required. These measurements are obtained with a Magnahelix differential pressure gauge referenced to ambient atmosphere. An absolute pressure value is then obtained via knowledge of the then current barometric pressure. The original hygrometer calibration is traceable to the National Bureau of Standards. Instrument specifications indicate a dewpoint accuracy of ±0.2°C. The calibration was routinely checked by recombining an O_2-H_2 gas mixture under reducing conditions over an Air Products and Chemicals Houdry Nixox HSC-205 catalyst maintained at 200°C. For a gas containing 0.544% O_2 and

excess H_2, a resulting dewpoint of 8.4°C should be monitored at a sensor pressure of 101 kPa (1 atm). Using this technique, no significant deviation from the factory calibration was observed in the course of the experimental work.

Reactant and Product Characterization Instrumentation

Reactant and product analysis of $Ba(OH)_2$ hydrate/$BaCO_3$ samples were performed on a Brinkmann Model E536-535-549 automatic titrator using a standard acid/base titration procedure. Special care was taken to avoid sample contamination from CO_2 in the ambient air during sample preparation. To increase the sharpness of the $BaCO_3$ peak when operating in the derivative mode on the automatic titrator, the samples were either soaked for several days or magnetically stirred in a sealed vessel for several hours. In either case, a definite improvement in the resolution of the analysis was obtained. This problem was most severe for samples that were predominantly $BaCO_3$. A typical titration consisted of placing 1.24 g of solid in 40 mL of distilled H_2O. The titration required 20 mL of 1.0 *N* HCl and was conducted under a nitrogen cover gas. The titration rate was 0.1 mL/min of titrate for a total titration time of 200 min.

Using the single-point BET adsorption theory, the surface area of the $BaCO_3$ product was routinely determined with a Quantachrome Monosorb. Typical sample size was 1.0 g. Sample preparation consisted of thermally outgassing the sample while under an inert gas purge. The adsorption point was obtained with a 15% argon-helium gas mixture at 77 K. The amount of sorbed gas was determined by raising the sample temperature from 77 K to ambient and integrating the change in argon concentration (i.e., thermoconductivity) in the purge gas. However, this procedure was

not applicable to $Ba(OH)_2 \cdot 8H_2O$ samples, even when the outgassing step was omitted, because of the high water vapor pressure of the hydrate.

Computer Support

Data analyses and modeling studies were performed via the use of three computer systems. Least-squares analyses of the data were performed using an IBM 375/3330 system and an Apple Plus II computer. Software for the former case was the Statistical Analysis System (SAS) Library, Version 79.5, which was developed by the SAS Institute, Raleigh, North Carolina.[56] Software for the Apple computer was a program and plotting routine entitled "Curve Fitter," which was developed by Paul K. Warme, Interactive Microware, Inc., State College, Pa.[57] A second program by Warme, "Scientific Plotter," was used for the overlaying and plotting of data.[58] For process modeling, numerical solutions using a finite difference technique were obtained with a Digital Equipment Company PDP 10 computer.

CHAPTER 3

EXPERIMENTAL STUDIES AND DATA ANALYSES

The interpretation of experimental data is often a tedious and difficult endeavor. For many cases, it may be likened to the famous tale of five blind men burdened with the task of describing an elephant, each being placed in contact with a unique, but different part. True, the whole is equal to the sum of its parts, but how many parts are required before one can predict the whole with adequate confidence? Such is the case with the experimental data to be presented and their subsequent interpretation. No piece of data and its interpretation can really stand alone. Rather, information available in the literature and from other experimental data obtained as part of this study was often required for successful interpretation and theorizing. Where such information was required, the author will attempt to cite it explicitly.

For the sake of nomenclature and consistancy, the raw reactant used in these studies will be designated as "*commercial* $Ba(OH)_2 \cdot 8H_2O$." Analyses have indicated the material to be substoichiometric in water. Discussions with the vendor indicated that the flake reactant was purposely prepared in this manner to ensure a free-flowing solid (i.e., to avoid particle agglomeration and sticking problems). Typically, water hydrations of 7.0 to 7.9 per molecule of $Ba(OH)_2$ are likely. Where the hydration stoichiometry is important, it will be reported in parenthesis, such as *commercial* $Ba(OH)_2 \cdot 8H_2O$ (7.1 H_2O). The term "$Ba(OH)_2 \cdot 8H_2O$" will be used to designate the stable $Ba(OH)_2$ crystalline species with 8 waters of hydration.

$Ba(OH)_2$ Hydrate Reactant Characterization

Studies were conducted on analytical-grade $Ba(OH)_2 \cdot 8H_2O$ and commercially designated $Ba(OH)_2 \cdot 1H_2O$, $Ba(OH)_2 \cdot 5H_2O$, and $Ba(OH)_2 \cdot 8H_2O$. A photograph of these materials is presented in Figure 3.1. X-ray diffraction patterns were obtained for each material form, and the results are presented in Table 3.1. For reasons to be discussed in a later section, the bulk of the experimental work was conducted on flakes of *commercial* $Ba(OH)_2 \cdot 8H_2O$.

Titriometric analysis of flakes of *commercial* $Ba(OH)_2 \cdot 8H_2O$ indicated them to be substoichiometric in water. As indicated in Table 3.2, the analysis of samples from two separate drums, but of the same batch number, indicated little variation in the reactant stoichiometry. Hydration stoichiometries of 7.54 and 7.47 were obtained with respective standard deviations of 0.0966 and 0.0830. The standard deviation attributed to the experimental technique was 0.077. This value was obtained by repetitive titration of analytical grade $Ba(OH)_2 \cdot 8H_2O$. Therefore, with considerable confidence, the bulk of the deviation about the mean that was observed for the two drums of *commercial* $Ba(OH)_2 \cdot 8H_2O$ may be attributed to the analytical technique and not to the sample position in the drum or the drum number. Analyses performed on subsequent shipments indicated that the stoichiometry varied between batches. Vendor specifications for the *commercial* $Ba(OH)_2 \cdot 8H_2O$ indicate that the reactant composition falls between $Ba(OH)_2 \cdot 7.0H_2O$ and $Ba(OH)_2 \cdot 7.9H_2O$. The product sheet specifications are presented in Appendix E. In no shipment was there appreciable $BaCO_3$. It is interesting to note that Michaud reported a $Ba(OH)_2 \cdot 3H_2O$—$Ba(OH)_2 \cdot 8H_2O$ eutectic to exist during solubility studies

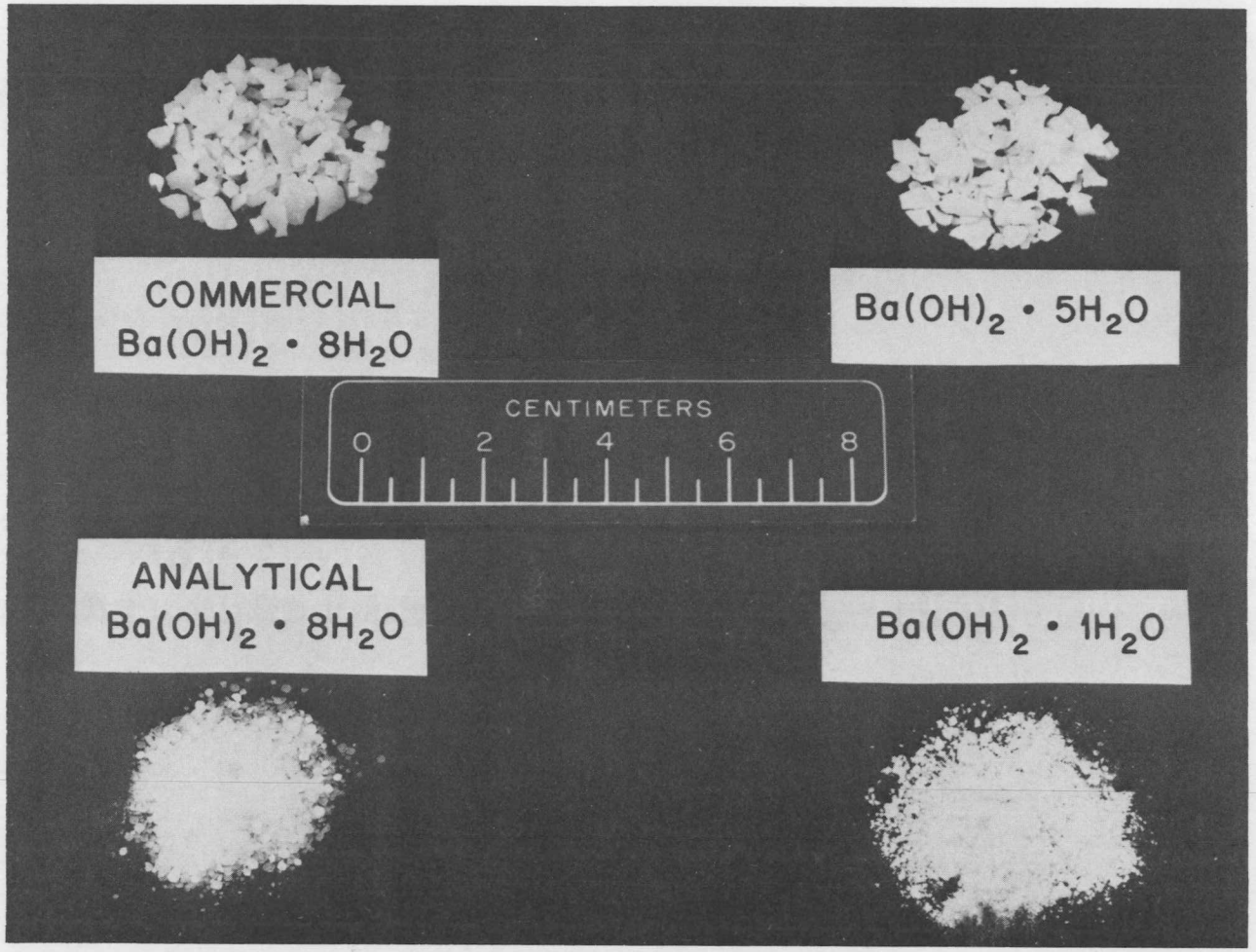


Figure 3.1. Photograph of potential $Ba(OH)_2$ hdyrate reactants for CO_2 removal.

Table 3.1. X-ray diffraction analyses of $Ba(OH)_2$ hydrate samples

Sample	Observed line intensities
$Ba(OH)_2 \cdot H_2O$	$Ba(OH)_2 \cdot H_2O$ - strongest
	$Ba(OH)_2 \cdot 3H_2O$
$Ba(OH)_2 \cdot 5H_2O$	$Ba(OH)_2 \cdot H_2O$, $\cdot 3H_2O$, $\cdot 8H_2O$ - same intensity
$Ba(OH)_2 \cdot 8H_2O$ — *commercial* (Hydration stoichiometry of 7.0 and 7.5)	$Ba(OH)_2 \cdot 8H_2O$
$Ba(OH)_2 \cdot 8H_2O$ - analytical	$Ba(OH)_2 \cdot 8H_2O$

Table 3.2. Reactant analyses of two drums of *commercial* $Ba(OH)_2 \cdot 8H_2O$ obtained from the same batch number

Drum No.	Average composition	Standard deviation	Number of samples
1	$Ba(OH)_2 \cdot 7.54H_2O$	0.0966	12
2	$Ba(OH)_2 \cdot 7.47H_2O$	0.0830	20

on the $Ba(OH)_2$ hydrate-water system (Appendix B).[41,42] The stoichiometric composition of the eutectic corresponds to $Ba(OH)_2 \cdot 7.19H_2O$, and consists of 16 mol % $Ba(OH)_2 \cdot 3H_2O$. Therefore, for a hydration stoichiometry of 7.5, the reactant would consist of 61 mol % eutectic and 39 mol % $Ba(OH)_2 \cdot 8H_2O$. The total amount of $Ba(OH)_2 \cdot 3H_2O$ would then be 10 mol %. It is also interesting to note that x-ray diffraction analysis of *commercial* $Ba(OH)_2 \cdot 8H_2O$ samples failed to confirm the presence of $Ba(OH)_2 \cdot 3H_2O$, although it was present in sufficient concentrations to be detected under normal conditions with the available instrumentation (>5%). The author speculates that the $Ba(OH)_2 \cdot 3H_2O$ crystallites are extremely small and well-dispersed. Failure to observe the compound via standard x-ray diffraction analysis would then be analogous to difficulties in analyzing amorphous compounds.[59,60]

Discussions with the vendor have indicated that the flakes are prepared by distributing a hot magma of $Ba(OH)_2$ hydrate (~1.0 mm thick) on a conveyer belt that is cooled on the underside by a water bath.[61] As shown in Figure 3.2, the two sides of the resultant flake are quite different — the side next to the belt is very smooth; the outer side, somewhat rough. However, when the flakes are magnified 5000X with an electron microscope (Figure 3.3), the flakes appear to be porous, and little difference is observed between the top and bottom of the flakes. Mercury porosimetry studies were conducted on samples of *commercial* $Ba(OH)_2 \cdot 8H_2O$ flakes obtained from two different batch numbers, hydration stoichiometries of 7.0 and 7.5. Results indicated flake porosities of 11.8 and 13.3%, respectively, and flake densities upon mercury penetration of 2.18 g/cm^3. This density value is also the reference density of $Ba(OH)_2 \cdot 8H_2O$.[22]

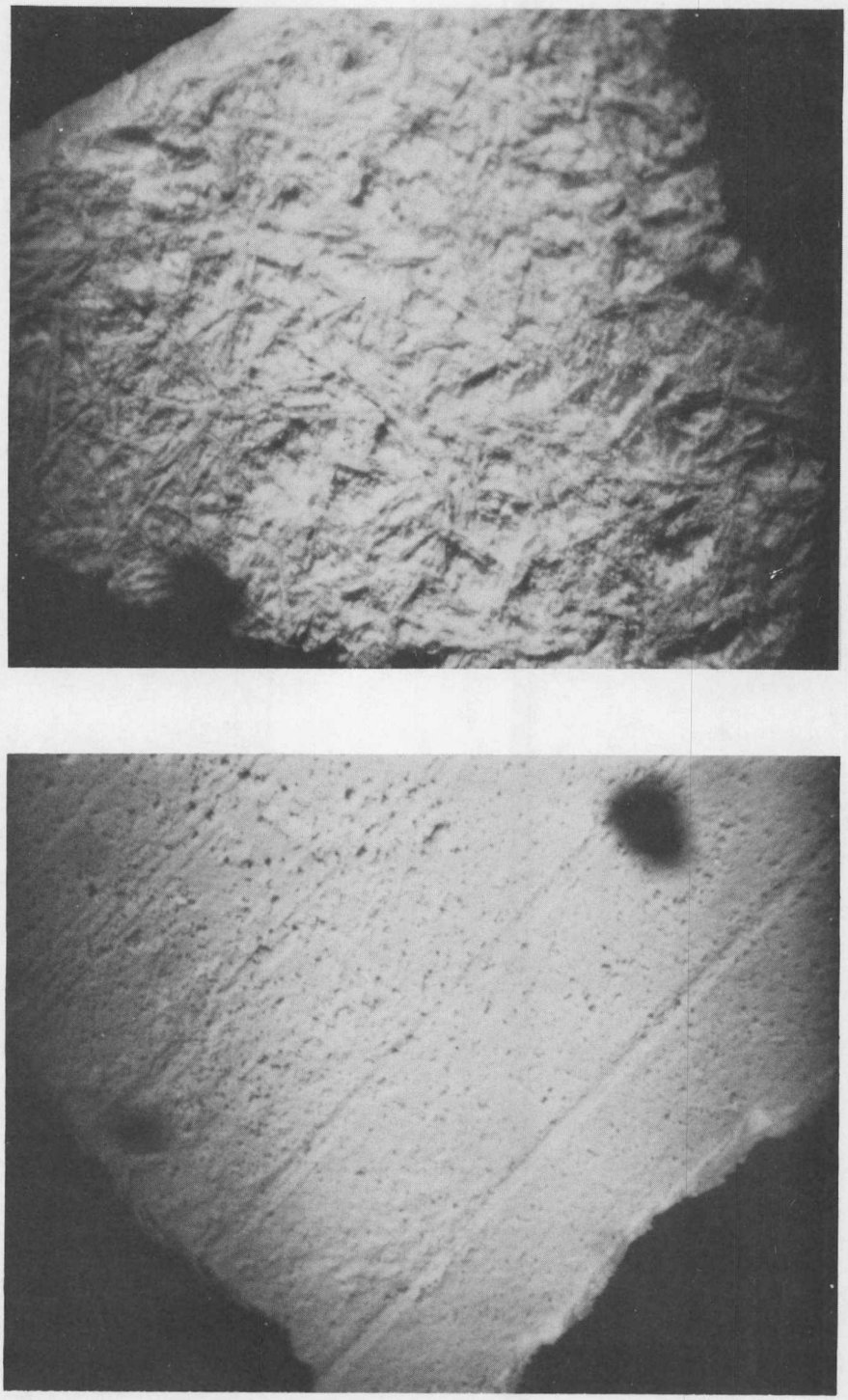


Figure 3.2. Top and bottom views of a *commercial* $Ba(OH)_2 \cdot 8H_2O$ flake (Original photograph: 7.3 by 9.5 cm; magnification, 12.8X).

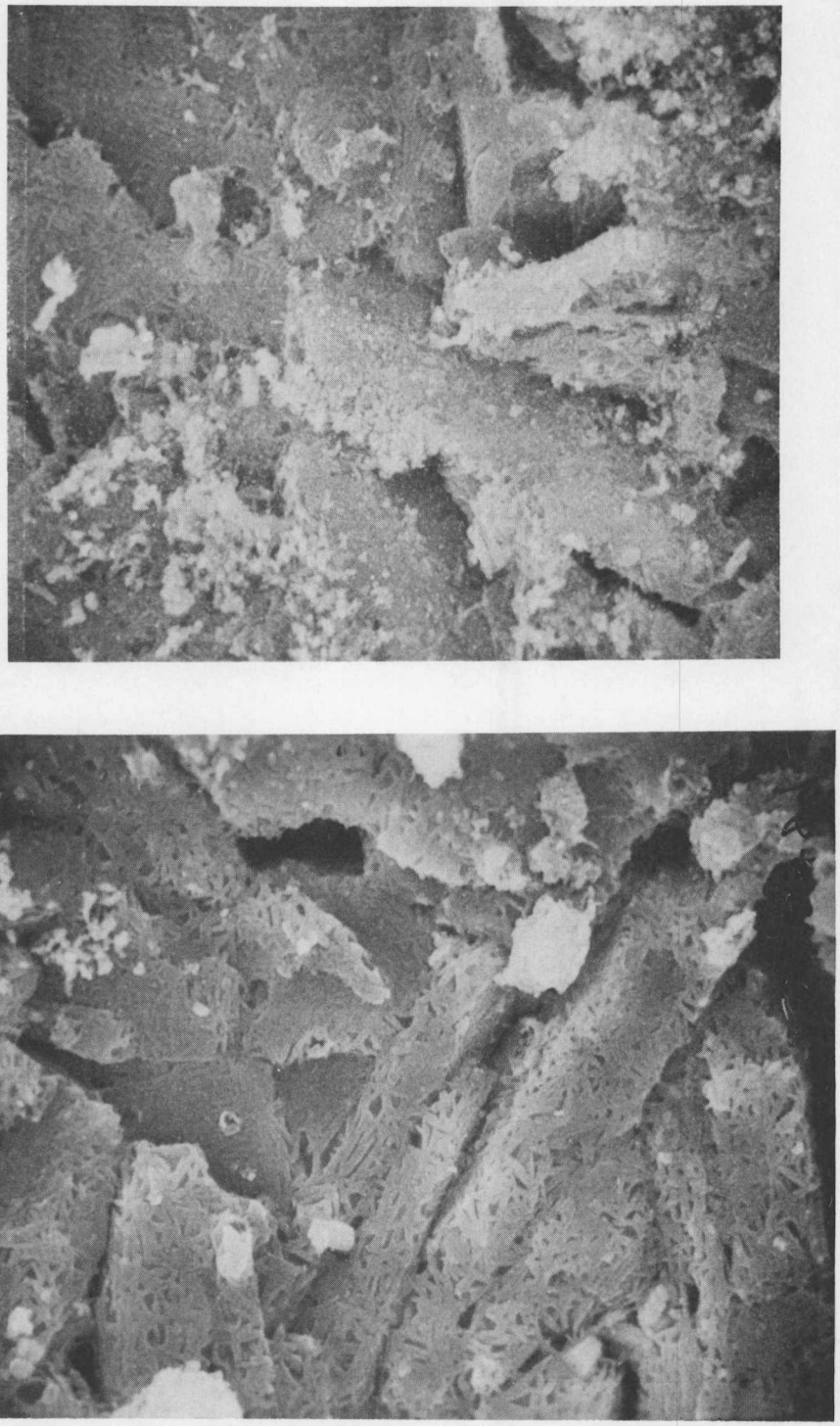


Figure 3.3. Top and bottom scanning electron micrograph (SEM) of *commercial* $Ba(OH)_2 \cdot 8H_2O$ flake. (Original photograph: 8.9 by 11.4 cm, magnification, 5000X).

Although no published density data were found for the $Ba(OH)_2 \cdot 3H_2O$—$8H_2O$ eutectic (overall stoichiometry of 7.19 H_2O), the author speculates that (1) the density is similar to that of $Ba(OH)_2 \cdot 8H_2O$, and (2) very little internal or locked-up voidage exists that is unavailable to mercurcy penetration. Similar flake density values were obtained, ρ = 2.16 g/cm^3, from the volumetric displacement of acetone, a liquid in which $Ba(OH)_2 \cdot 8H_2O$ is insoluble. The acetone displacement studies and overall bulk density studies indicated a bed porosity of ~48%. Therefore, a representative fixed bed would consist of ~52 vol % $Ba(OH)_2$ hydrate, ~45.5 vol % interparticle voids, and ~6.5 vol % intraparticle voids.

Although the flaked form of $Ba(OH)_2 \cdot 8H_2O$ is more ideally suited for fixed-bed operations than the particulate form, the characterization of flakes for modeling studies is very difficult because of variations in flake size and thickness. Presented in Table 3.3 are the results of a particle size analysis performed on flake samples obtained from two batch numbers. From a process development perspective, one would desire to use

Table 3.3 Particle size analysis of *commercial* $Ba(OH) \cdot 8H_2O$ flakes obtained from two different batch numbers

Particle size		Weight %	
Mesh	mm	Batch No. 1	Batch No. 2
4 →	4.75 →	18.5	5.8
8 → 4	2.36 → 4.75	46.9	33.0
20 → 8	0.850 → 2.36	31.6	54.5
50 → 20	0.300 → 0.850	2.0	4.9
120 → 50	0.125 → 0.300	0.4	1.2
→ 120	→ 0.125	0.6	0.6

all size fractions of reactant, and such was the case in the studies to be discussed. The manner in which the flakes were characterized for modeling studies will be covered in the latter portion of Chapter 3, "Fixed-Bed Macroscale Studies."

Attempts were made to make spheres, tablets, and cylinders of $Ba(OH)_2 \cdot 8H_2O$. However, upon conversion to $BaCO_3$, these geometries were extremely unstable. Furthermore, from a mass transfer perspective, the flake geometry does offer some unique advantages with respect to packing density, particle thickness or diameter, and total particle surface area. For systems in which reactant conversion may be represented by a shrinking-core-type model, the area available for mass transfer for a flake of uniform thickness is a function of conversion. This factor is particularly important when significant mass transfer resistance is associated with either diffusion through the product layer or the kinetic rate at the reaction interface.

Surface Morphology and Microscale Studies

Sorption Morphology Studies.

Introduction. The use of various sorbates as molecular probes to elucidate the surface properties of solids has been the topic of many investigations. These studies are generally conducted by measuring the sorption properties of a solid (sorbent) as a function of the partial pressure of the sorbing gas or vapor (sorbate) at isothermal conditions. From the shape of sorption isotherms, information concerning chemisorption, surface area, and porosity properties of the solid may be obtained. Numerous chemical species at various temperatures have been used as sorbates; the

choice of the sorbate is often dependent upon the solid and phenomenon being studied.

The use of adsorption isotherm data for determination of the surface area of a sorbent has been an area of great importance.[50–54,62–66] For the determination of surface area, initial information concerning the cross section or area covered by a sorbing molecule and the number of molecules at monolayer coverage was published in 1937 by Emmett and Brunauer. The procedure attempted to identify the point, "Point B," on the adsorption isotherm at which the affinity of the molecule for the surface changed most rapidly (i.e., from adsorbate-sorbent interactions to adsorbate-adsorbate interactions). The Point B method was later replaced by the classical Brunauer, Emmett, and Teller (BET) adsorption method published in 1938. This method was to become the cornerstone of surface area determination because it provided a simple, easily reproducible technique for adsorption analyses. The technique has become universal, and although the reported values are relative, they are usually within 30% of the absolute area. A derivation of the BET equation and the associated assumptions are presented in Appendix G. The working equation is

$$\frac{P}{(P_o-P)V} = \frac{1}{V_m c} + \frac{(c-1)}{V_m c}\frac{P}{P_o} \quad , \tag{3.1}$$

where

P = adsorbate vapor pressure,

P_o = adsorbate saturation vapor pressure,

V = volume of gas sorbed,

V_m = volume of gas for monolayer formation,

c = constant.

For nitrogen adsorption at liquid nitrogen temperatures, the range of validity of the BET equation is usually $0.05 \leq P/P_o \leq 0.35$, where P is the adsorbate vapor pressure and P_o is the adsorbate vapor pressure at saturation. The range of validity is affected by the assumptions implicated in the development of Equation (3.1) (see Appendix G). The adsorption isotherm range must include the point of monolayer formation. Factors indicating a more limited range of validity are a negative value of c and the failure of Equation (3.1) to be linear when plotted as

$$\frac{P}{(P_0-P)V} \text{ vs } P/P_0. \tag{3.2}$$

The range of application may also be reduced by the presence of micropores (diameter <2 nm), whose existence may be confirmed by obtaining an adsorption isotherm with a larger diameter adsorbate; or the existance of strong chemical bonding between the sorbate and sorbent, chemisorption. The sorbed volume terms, V and V_M, may be converted to mass terms, Γ and Γ_M, via the information presented in Table 3.4. With respect to the formation of a nitrogen monolayer, a weight increase of 280 μg per square meter of surface area would be predicted.

Surface area determination may also be performed via application of the sorption potential theory. This method, based upon thermodynamic principles, has unique advantages over the BET because the entire sorption isotherm is used.[50–54,62–65] However, its application has not been as universal. The derivation is presented in Appendix G, and the resulting working equation is

$$\Gamma_m = 2.0[\Gamma_2(P/P_o = 0.6065) - \Gamma_1(P/P_o = 0.3678)] \tag{3.3}$$

Table 3.4. Cross-sectional area of adsorbed molecules

Adsorbate	Bath	Bath temperature (K)	Saturation vapor pressure (torr)	Saturation vapor pressure (Pa)	Cross-sectional area factors $a_M \cdot 10^{18}$ (m^2/molecule)	Φ (m^2/g)	$\Phi \cdot 10^{-6}$ (m^2/m^3)
N_2	Liq. nitrogen	77.4	760.0	$1.01 \cdot 10^5$	0.162	3480	4.35
A	Liq. nitrogen	77.4	193.7	$2.58 \cdot 10^4$	0.138	3970	3.71
A	Liq. oxygen	90.19	1000.4	$1.33 \cdot 10^5$	0.138	3970	3.71
Kr	Liq. nitrogen	77.4	1.95	$2.66 \cdot 10^2$	0.202	1450	5.43
Kr	Liq. oxygen	90.19	17.02	$2.27 \cdot 10^3$	0.214	1540	5.75
O_2	Liq. oxygen	90.19	760.0	$1.01 \cdot 10^5$	0.14	2630	3.76
Xe	Liq. oxygen	90.19	0.0686	8.00	0.232	1090	6.39
H_2O	Ice/water	273.2	4.579	$6.11 \cdot 10^3$	0.125	4180	3.36
CO_2	CO_2/acetone	195	792.7	$1.06 \cdot 10^5$	0.21	2870	5.64
Benzene	Ice/water	273.2	31.3	$4.17 \cdot 10^3$	0.43	3320	11.55
n-butane	Ice/water	273.2	770	$1.03 \cdot 10^5$	0.444	4610	11.93

Source: E. Robens and G. Walter, "Determination of Specific Surface Area and Porosity of Solids," p. 678 in *Analytical Methods (CB)*, Academic Press, New York, 1974.

where

Γ = amount sorbed at P/P_o,

Γ_m = amount sorbed on monolayer.

As previously cited, many different adsorbates have been used for sorption isotherm studies (Table 3.4). Historically, nitrogen adsorption at liquid nitrogen temperatures has been the preferred method. However, in an extensive study by Rouquerol,[62] argon was determined to be a more ideal absorbate than nitrogen (N_2) because of the following:

1. a greater range of validity for application of the BET equation (i.e., more consistent with assumptions in the derivation of the BET equation),
2. reduced chemisorption,
3. the spherical form of the molecule, and
4. the absence of an electric quadrapole moment.

Another area of applicability of adsorption isotherm data is in the evaluation of sorbent porosity. A detailed review of the theory and the methods of evaluation of pores and pore size distributions are presented in Appendix G. Generally, porosity is broken into three regimes that are based upon the mean pore width, d(nm), (Table 3.5). Micropores are responsible for the mechanical properties of the solid, and because of the small diameter, pore areas cannot be determined. However, pore diameters may be measured via adsorption studies with molecules of differing sizes. Mesopores contribute significantly to the internal surface area and generally play an important role in chemical surface reactions. Pore sizes are usually determined via adsorption studies and application of the Kelvin equation for desorption. Macropores are visible under an

Table 3.5. Pore classification

Pore type	Pore width, d (nm)	Relative pressure range for adsorption (P/P_o)
Macropore	>50	>0.95
Mesopore	2—50	0.35—0.95
Micropore	<2	<0.35

Source: E. Robens and G. Walter, "Determination of Specific Surface Area and Porosity of Solids," *Analtyical Methods 1(B)*, Academic Press, New York, 1974.

optical microscope and determine the bulk density of the solid. As the pore size increases, the use of adsorption-desorption data and the Kelvin equation becomes progressively more difficult. For pore diameters >50 nm, the technique of mercury penetration is the standard method of pore size characterization.[65]

Specific studies were conducted to determine and develop an awareness of the surface characteristics of *commercial* $Ba(OH)_2 \cdot 8H_2O$, $Ba(OH)_2 \cdot 8H_2O$, $BaCO_3$, and partially converted samples of $Ba(OH)_2 \cdot 8H_2O$. With the exception of the mercury porosimetry studies, the results were performed on equipment described in Chapter 2. The mercury porosimetry studies were performed by the Analytical Chemistry Division at Oak Ridge National Laboratory. To keep this section as brief as possible, experimental results and their interpretation are presented. Other information such as adsorption isotherms, BET plots, data analysis techniques, etc., are presented in the cited appendixes.

Nitrogen adsorption isotherms — *commercial* $Ba(OH)_2 \cdot 8H_2O$ and $Ba(OH)_2 \cdot 8H_2O$. Using the microbalance analytical system described in a preceding section, nitrogen adsorption isotherms were obtained on *commercial* $Ba(OH)_2 \cdot 8H_2O$ flakes, *commercial* flakes dehydrated to ~$Ba(OH)_2 \cdot 6.4H_2O$, and *commercial* flakes hydrated at low and high humidities to $Ba(OH)_2 \cdot 8H_2O$. Typical sample sizes were 150 to 200 mg and consisted of several flakes (Figure 2.3). Because of the high water vapor pressure of the hydrated samples, outgassing to remove sorbed water from the surface was not possible. In fact for $Ba(OH)_2 \cdot 8H_2O$ at room temperature, the dissociation vapor pressure corresponds to a relative humidity that would result in ~1.65 layers of sorbed water on the solid surface.[64] Because of the volatility of the sample, a reproducible method for changing the temperature and pressure of the sample environment from 101 kPa (760 torr) and 295 K to 10^{-4} Pa (10^{-6} torr) and 77 K was developed. The procedure consisted of the rapid room temperature evacuation of the sample to a pressure of 4 kPa (~30 torr) over a 2-min period, followed by placement of the hangdown tube and sample in a liquid nitrogen bath and subsequent evacuation to a pressure of 10^{-4} Pa (10^{-6} torr). Typically, the sample weight would decrease by ~0.4% (~0.6 mg for 150-mg sample). Upon conclusion of the isotherm analysis, the stoichiometry was determined by sample decomposition to $Ba(OH)_2$ and a subsequent mass balance.

Nitrogen adsorption studies were conducted on $Ba(OH)_2 \cdot 8H_2O$ prepared from *commercial* $Ba(OH)_2 \cdot 8H_2O$(~$7.0H_2O$) which was hydrated at a relative humidity <60% and *commercial* $Ba(OH)_2 \cdot 8H_2O$(~$7.0H_2O$). Before buoyancy corrections, the isotherms displayed negligible curvature, thus indicating extremely low surface areas. From the observed weight changes that

were assumed to result solely from buoyancy effects, solid densities were determined (Appendix F). However, as presented in Table 3.6, the measured density for $Ba(OH)_2 \cdot 8H_2O$ at liquid nitrogen temperatures (77 K) was considerably less than that expected based upon literature values. Using a weighted average based upon the crystal densities of $Ba(OH) \cdot H_2O$ and $Ba(OH)_2 \cdot 8H_2O$, a corrected density was calculated for the *commercial* $Ba(OH)_2 \cdot 8H_2O$ (~7.0 H_2O). Ideally, a density value for $Ba(OH)_2 \cdot 3H_2O$ or the $Ba(OH)_2 \cdot 3H_2O Ba(OH)_2 \cdot 8H_2O$-eutectic ($H_2O$ stoichiometry of 7.19) would have been more rigorous, but such values were not found in the literature. In both cases as presented in Table 3.6, the experimental density values were roughly 12% less than the anticipated values based upon crystal densities at room temperature. Because the transition of the sample from

Table 3.6. $Ba(OH)_2 \cdot 8H_2O$ and *commercial* $Ba(OH)_2 \cdot 8H_2O$ densities

	Observed density at 77 K	Predicted density	% of prediction
$Ba(OH)_2 \cdot 8H_2O$	1.90	2.18	87.2
Commercial $Ba(OH)_2 \cdot 8H_2O$ (7.0 H_2O)	2.12	2.39	88.7

room temperature to 77 K was not instantaneous, the author speculates that crystal expansion occurred in a manner very similar to freezing of water, for which the solid density is ~9% less than the liquid density.[22] The author feels that one may view the $Ba(OH)_2 \cdot 8H_2O$ solid as a semirigid water solution containing approximately 11 mol % $Ba(OH)_2$. The relative strength of the hydration bond may be evaluated by comparing the

enthalpy and entropy changes associated with the hydration of $Ba(OH)_2$ and its lower hydrates, the condensation of water vapor, and the freezing of water. As shown in Table 3.7, the greater decreases in enthalpy and entropy, on a per mole water basis, indicate that considerable bonding strength is associated with the hydration step.[40]

Table 3.7. Relative strength of the hydration bonds in $Ba(OH)_2$ hydrates

Reaction[a]	Temperature (K)	Δ_H kJ/mol-H_2O	Δ_S J/mol-H_2O K
$Ba(OH)_2(s) + H_2O(g) \rightarrow Ba(OH)_2 \cdot H_2O$	298.15	-61.35	-141.8
$Ba(OH)_2 \cdot H_2O(s) + 2H_2O(g) \rightarrow Ba(OH)_2 \cdot 3H_2O$	298.15	-62.62	-138.8
$Ba(OH)_2 \cdot 3H_2O(s) + 5H_2O(g) \rightarrow Ba(OH)_2 \cdot 8H_2O$	298.15	-58.23	-157.7
$H_2O(g) \rightarrow H_2O(l)$	298.15	-44.02	-117.5
$H_2O(l) \rightarrow H_2O(s)$	273.15	-6.12	-22.4

[a]Thermodynamic values for $Ba(OH)_2$ hydrates were taken from B. A. Kondakov, P. V. Kovtunenko, and A. A. Bundel, "Equilibria Between Gaseous and Condensed Phases in the Barium Oxide - Water System," *Russ. J. Phys. Chem.* 38(1), 99-102 (1964).

With respect to the entropy of formation values for $Ba(OH)_2 \cdot 3H_2O$, Kondakov questioned the stability of this species. As discussed earlier in this chapter, mercury porosimetry and acetone displacements studies on *commercial* $Ba(OH)_2 \cdot 8H_2O$ (7.0 and 7.5) at ambient temperatures have indicated crystal densities of ~2.18 g/cm^3. However, as shown in Table 3.6, the predicted densities based upon the weighted average of $Ba(OH)_2 \cdot H_2O$

and $Ba(OH)_2 \cdot 8H_2O$ are much greater. Therefore, this analysis indicates the molar volume of $Ba(OH)_2 \cdot 3H_2O$ or the $Ba(OH)_2 \cdot 3H_2O$ — $Ba(OH)_2 \cdot 8H_2O$ eutectic is much greater than expected. Little information exists concerning $Ba(OH)_2 \cdot 3H_2O$. It does possess a distinct x-ray diffraction pattern and was routinely prepared in the course of this study by the room-temperature, vacuum dehydration of *commercial* $Ba(OH)_2 \cdot 8H_2O$ flakes. The author speculates the greater than anticipated entropy of formation for $Ba(OH)_2 \cdot 3H_2O$ results from the larger than expected molar volume. Unlike $Ba(OH)_2 \cdot 8H_2O$, no in-depth study of the crystal structure has been conducted. It is unfortunate in the course of this study that sorption isotherms with differing sorbates were not conducted because molecular voids may exist within the structure of $Ba(OH)_2 \cdot 3H_2O$. These molecular voids would then account for the smaller than anticipated change in volume between the experimentally determined density of *commercial* $Ba(OH)_2 \cdot 8H_2O$ and the same material at liquid nitrogen temperatures.

Manohar and Ramaseshan, in determining the crystal structure of $Ba(OH)_2 \cdot 8H_2O$ via x-ray analysis, noted considerable mobility of the OH^- ions and considerable hydrogen bonding in the $Ba(OH)_2 \cdot 8H_2O$ crystal structure.[67] Therefore, the formation of crystalline linkages and expansion upon exposure to sub-zero temperatures would seem highly plausible. One might view $Ba(OH)_2 \cdot 8H_2O$ at sub-zero temperatures as a clathrate compound with Ba^+ and OH^- occupying voids in the H_2O crystal structure.[68,69]

Although *commercial* $Ba(OH)_2 \cdot 8H_2O$ was determined to possess negligible surface area, room temperature dehydration to a stoichiometry of 6.4 waters of hydration resulted in considerable curvature of the adsorption isotherm. The isotherm is presented in Appendix H along with the BET and

sorption potential plots. As the isotherm displayed no hysteresis and the upper adsorption pressure (P/P_o) was >0.99, few mesopores (2 nm < d < 50 nm) and macropores of diameters <150 nm likely exist. Furthermore, from the shape of the adsorption isotherm and the extremely weak energy of the interaction (E_o) of 3.20 kJ/mol obtained from the sorption potential model, very few micropores (d < 2 nm) appear to exist. For the condensation of nitrogen at saturation conditions, the energy of interaction should equal the heat of liquifaction (E_L) which is 5.65 kJ/mol. Hence the physical system and the postulated model are in slight conflict as $E_o > E_L$. From the value of the energy of interaction and the BET "c" value of 21.0, the sorbate-sorbent bond appears to be comparable in strength to the sorbent-sorbent bond. The BET and sorption potential surface areas correlated quite well, indicating areas of 0.99 and 1.35 m^2/g respectively (Table 3.8, Sample 1).

The information in the preceding paragraph may be used as a check with respect to the sample evacuation procedure for $Ba(OH)_2$ hydrates. For a typical weight loss upon sample evacuation of 0.6 mg (~0.4% of sample mass) and assuming a linear relationship between weight loss and surface area formation, an increase in BET surface area of only 0.11 m^2/g would be predicted. Because of kinetic limitations, the true number is likely less since the sorbed water (minimum of ~1.65 layers) would probably be released first. For 1.65 monolayers of water on a surface area of 1 m^2, 0.40 mg of water would be lost upon total desorption. Hence this analysis indicates that little additional surface area may be attributed to the evacuation procedure.

Table 3.8. Nitrogen adsorption isotherm surface area analysis

Sample	Composition	BET Surface area (m^2/g)	BET c Value	Sorption potential Surface area (m^2/g)	Sorption potential Energy of interaction kJ/mol
1	$Ba(OH)_2 \cdot 6.4H_2O$	0.99	21	1.35	3.20
2	$Ba(OH)_2 \cdot 8H_2O$	0.98	1825	0.95	7.27
3	$BaCO_3$	7.52	180	6.16	9.43
4	$BaCO_3$	8.70	511	6.58	11.40
5	2.7% $Ba(OH)_2 \cdot 8H_2O$	5.46	123	4.03	11.51
6	15.4% $Ba(OH)_2 \cdot 8H_2O$	4.44	263	3.56	8.53
7	50.5% $Ba(OH)_2 \cdot 8H_2O$	1.67	350	0.93	19.95
8	59.6% $Ba(OH)_2 \cdot 8H_2O$	1.48	-97	0.91	20.77
9	76.4% $Ba(OH)_2 \cdot 8H_2O$	<0.5	——	<0.35	——
10	87.0% $Ba(OH)_2 \cdot 8H_2O$	<0.5	——	<0.35	——
11-A	92.9% $Ba(OH)_2 \cdot 8H_2O$	<0.5	——	<0.35	——
11-B	97.5% $Ba(OH)_2 \cdot 8H_2O$	<0.5	——	<0.35	——

Studies have indicated that the hydration of *commercial* $Ba(OH)_2 \cdot 8H_2O$ may proceed in one of two regimes. For humidities of 60% or less, little or no physical change is observed upon hydration to $Ba(OH)_2 \cdot 8H_2O$. The actual rates of hydration and dehydration are discussed later in this chapter. However, for relative humidities in excess of ~60%, the flakes are observed to recrystallize and preferentially curl as shown in Figure 3.4. Although this curling results in a more active solid (greater

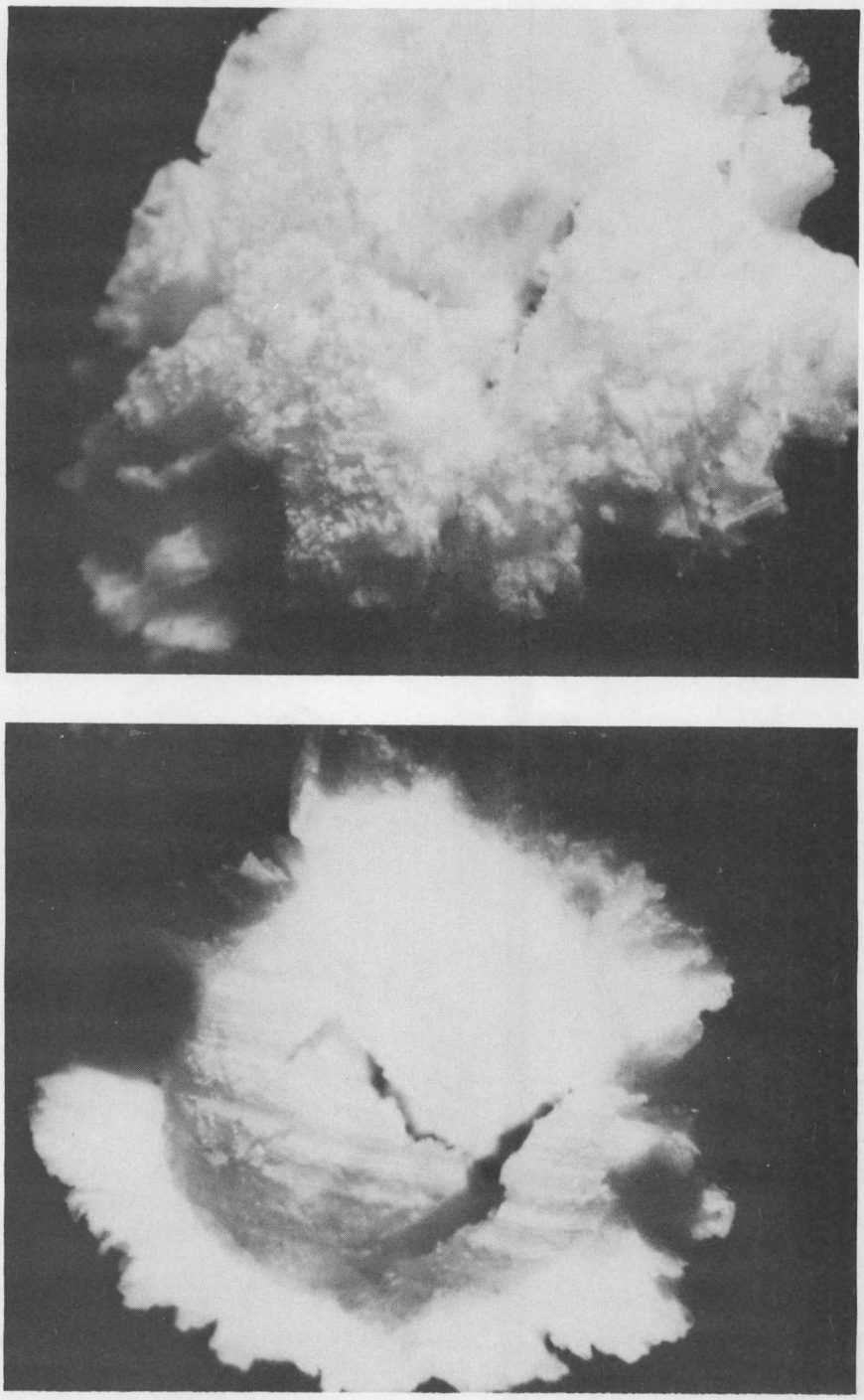


Figure 3.4. Top and bottom views of a *commercial* $Ba(OH)_2$ octahydrate flake subjected to relative humidity >60%. (Original photograph: 2.85 by 3.75 in.; magnification, 16.5 and 13X, respectively.)

surface area), the solid is also more fragile and degrades easily upon conversion to $BaCO_3$. Based upon this and other data to be presented in this chapter under the heading entitled "Fixed-Bed Macroscale Studies," the author believes that in the regime of 60% relative humidity and greater, sufficient sorbed water exists on the surface for rapid recrystallization to take place. This recrystallization and crystal growth proceeds very likely in capillaries or at contact points where water has condensed via a phenomenon referred to as capillary condensation (Appendix G). A contact point may be described as the meeting of two nonplanar surfaces. Therefore, as the adsorption isotherm was extremely linear for the *commercial* $Ba(OH)_2 \cdot 8H_2O$, the number of capillaries or contact points must be small. The BET and sorption potential surface areas, the BET c value, and the sorption potential energy of interaction for the *commercial* $Ba(OH)_2 \cdot 8H_2O$ sample hydrated at a humidity in excess of ~60% are presented in Table 3.8 as Sample 2. The BET analysis indicated a very large c value of 1825, thus indicating the energy of sorbent-sorbate interaction to be considerably greater than sorbent-sorbent interactions. The sorption potential energy of interaction was relatively weak for such interactions as it was 7.27 kJ/mol. It is interesting to note that although the two models predicted essentially the same surface area (0.98 vs 0.95 m^2/g), the strength of the sorbent-sorbate interactions are in conflict.

Nitrogen adsorption isotherms — $BaCO_3$. Nitrogen adsorption isotherm studies were conducted on a representative $BaCO_3$ product from a fixed-bed run (latter portion of this chapter). These samples were outgassed for several hours at room temperature and a pressure of 10^{-4} Pa until no

weight change was observed. Adsorption isotherms were obtained on two samples. Buoyancy corrections were made assuming a $BaCO_3$ density of 4.43 g/cm^3, and the isotherms displayed no hysteresis. The isotherms are presented in Appendix H. As the maximum value of P/P_0 during the adsorption experiment was in excess of 0.99, the absence of hysteresis would indicate few restrictive mesopores (2 nm < d < 50 nm) or macropores of diameters <150 nm. From the shape of the adsorption isotherms and the value of the sorption potential energy of interaction, 9.43 and 11.40 kJ/mol, few micropores (d < 2 nm) would be predicted. The energy of interaction is what would be expected for a moderately active surface. The BET and sorption potential surface areas were found to be reasonably consistant and are presented in Table 3.8, Samples 3 and 4. The surface areas from BET theory were 7.57 and 8.73 m^2/g, respectively, and those from the sorption potential model were 6.16 and 6.58. For each analysis technique, differences in surface areas for the two samples are relatively small and are attributed to both experimental techique and nonhomogenity of the samples.

Nitrogen adsorption isotherms - conversion profile studies. Adsorption studies were conducted on the conversion profile of a typical fixed bed run. This profile was obtained by terminating a fixed-bed experiment prior to the start of the CO_2 breakthrough. The 10.2-cm-diam bed was then partitioned in the axial (z-direction) into 2.54-cm increments for subsequent titriometric analyses. Because of the presence of $Ba(OH)_2 \cdot 8H_2O$ in the samples, sample out-gassing was not possible. The 150- to 200-mg samples were prepared for the adsorption study using the same procedure that was developed for $Ba(OH)_2 \cdot 8H_2O$ adsorption studies.

Sample weight loss between loading conditions, 101 kPa (760 torr) and 295 K, and adsorption conditions, 10^{-4} Pa (10^{-6} torr) and 77 K, were reasonably consistent at ~0.4 wt %. Based upon the experimental conditions of the fixed-bed run and the titriometric analysis, the reactant was assumed to be fully hydrated (i.e., $Ba(OH)_2 \cdot 8H_2O$). To correct for the buoyancy effect, the extent of sample conversion to $BaCO_3$ and the respective crystal densities at 77 K were required. The extent of conversion was obtained by the room temperature, vacuum dehydration (10^{-4} Pa) of the $Ba(OH)_2 \cdot 8H_2O$ to the stable species at these conditions, $Ba(OH)_2$. From a mass balance, the amount of $Ba(OH)_2 \cdot 8H_2O$ was determined, and the mass of $BaCO_3$ was calculated by mass differences. Experimental values obtained via this technique and acid-base titriometry are presented in Figure 3.5. As the surface adsorption samples were only ~150 mg, the titriometric samples were ~2.4 g, and the total weight of the 2.54-cm sample increment was ~200 g; the observed differences could easily result form the nonhomogeneity of the sample (i.e., was the analyzed sample characteristic of the top or bottom of the 2.54-cm increment?). The density values used in the buoyancy calculations were the 1.90 g/cm^3 for $Ba(OH)_2 \cdot 8H_2O$ obtained in the preceding section and the literature value of 4.43 g/cm^3 for $BaCO_3$.[22] A weighted average was then used to calculated a corrected density for the partially converted samples.

The sorption profiles and the subsequent analyses are presented in Appendix H. The lack of hysteresis for these profiles and the linear sorption potential plot indicate few mesopores of macropores of diameters <150 nm. The initial shape of the isotherms and the increase in the sorption potential theory energy of interaction with decreasing conversion,

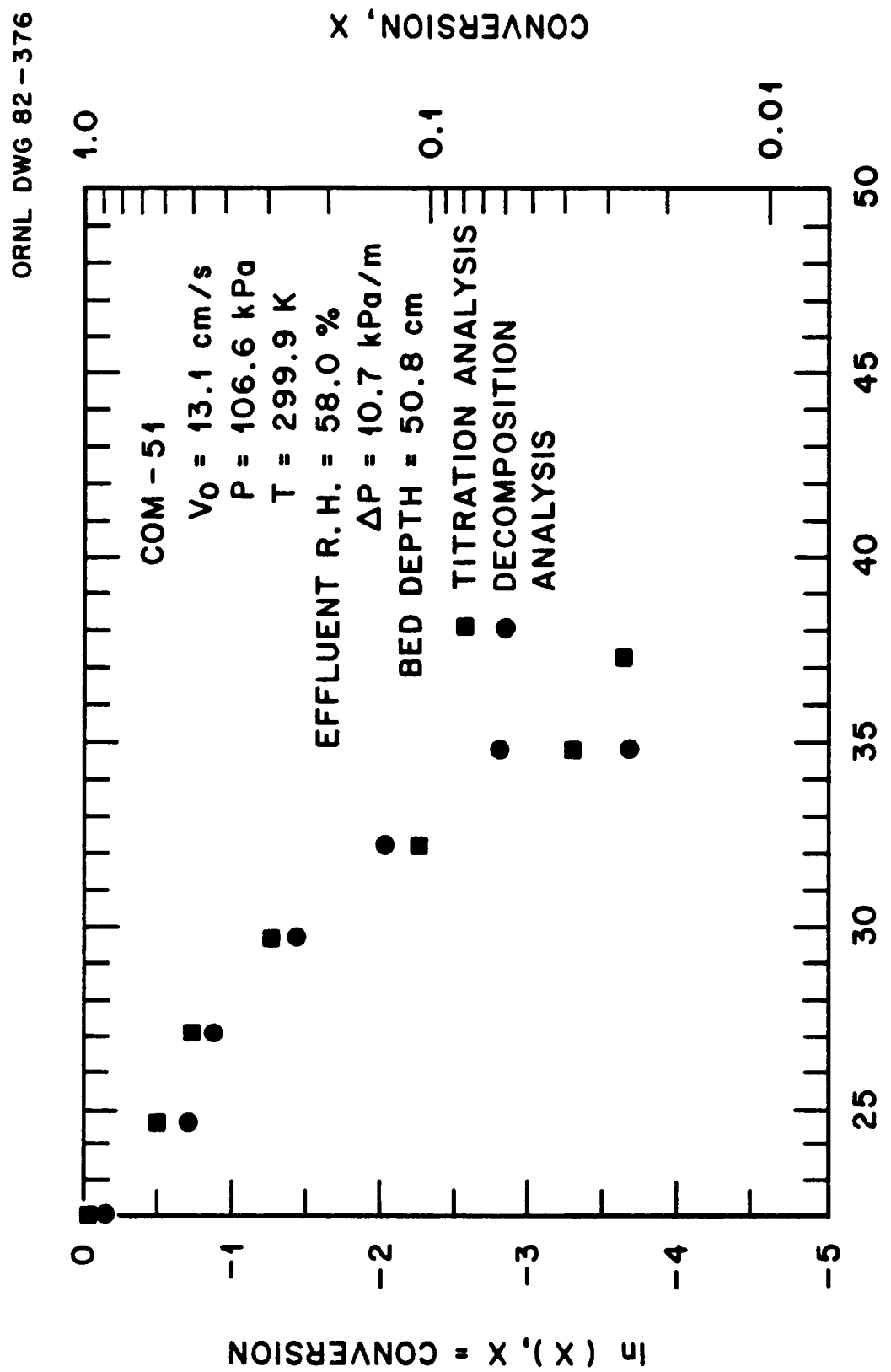


Figure 3.5. Conversion profile obtained via two analytical techniques.

8.53 to 20.77 kJ/mol, indicates that microporosity may exist in the less converted samples. The surface areas obtained via BET and sorption potential theories are presented in Table 3.8, Samples 5—11B. Since the relative humidity of the fixed-bed run was <60% (a value >60% would result in capillary condensation of H_2O and subsequent recrystallization and increased surface area), the surface area contribution from $Ba(OH)_2 \cdot 8H_2O$, was assumed negligible. The surface area per gram of $BaCO_3$ was calculated and is presented in Table 3.9. These studies indicated that a more rapid increase in surface area occurred for the more highly converted samples or those samples exposed to the greatest CO_2 concentration. Experimental data, obtained from fixed-bed studies

Table 3.9. Conversion profile surface areas per gram of $BaCO_3$

Sample	Composition	BET surface area (m^2/g-sample)	BET surface area (m^2/g-$BaCO_3$)
3	$BaCO_3$	7.57	7.57
4	$BaCO_3$	8.93	8.93
5	2.66% $Ba(OH)_2 \cdot 8H_2O$	5.46	5.61
6	15.43% $Ba(OH)_2 \cdot 8H_2O$	4.46	5.27
7	50.45% $Ba(OH)_2 \cdot 8H_2O$	1.67	3.37
8	59.55% $Ba(OH)_2 \cdot 8H_2O$	1.47	3.63
9	76.37% $Ba(OH)_2 \cdot 8H_2O$	<0.50	<2.12

and to be discussed later in this chapter, have indicated the specific reaction rate of unreacted material to be roughly proportional to

CO_2 concentration. Thus, the rapid specific rates coincide with a greater incremental increase in surface area per gram of product. This factor and its significance will be addressed in greater detail in a subsequent section entitled "Single-Point BET Analyses of $BaCO_3$ Products."

The BET "c" value for Sample 9 reported in Table 3.8 is slightly negative because of a negative BET intercept. Typically, this is an indication of a deviation from the assumptions in the BET theory. However, based upon the proximity of the intercept term to zero and the value of the slope term, the discrepancy was judged to be insignificant.

Single-point BET analyses of $BaCO_3$ products. Single-point BET surface areas were obtained using the Quantachrome Monosorb described in Chapter 2. These studies were conducted to determine the effects of fixed-bed parameters such as relative humidity, temperature, gas flow rate, etc., on the surface area of the $BaCO_3$ product. The merits and limitations of the single-point BET technique are described in detail in Appendix G. Basically, they require that the "c" term in the BET equation be of sufficient magnitude to ensure a zero or near-zero intercept on the BET plot. Furthermore, the single-point adsorption pressure must lie within the BET regime. Typically, this value is $0.05 < P/P_0 < 0.35$. However, the regime of applicability is dependent upon the sorbent and sorbate. Multipoint BET studies on $BaCO_3$ indicated appreciable sorbate-sorbent interaction, thus a large value of "c" and a near-zero intercept. Argon was chosen as the adsorbent for these studies as work performed by Roqueral indicated it to be a more ideal adsorbent than nitrogen.[62] The argon adsorbent pressure for the single-point method was 0.60. This value is outside the normal BET regime, and this factor was

investigated to determine the validity of such data. (The gas mixture was 15% argon and the balance helium. At liquid N_2 temperatures, the P/P_0 value is 0.60. If the adsorbent gas was nitrogen, the corresponding P/P_0 value would be 0.15, which is near the center of the BET regime. The choice of 15% argon was an oversight of the investigator.)

Using the nitrogen adsorption data presented in a previous section, a comparative study of surface areas using the multi- and single-point BET methods was conducted. For the latter case, a P/P_0 value of 0.60 was chosen. As may be seen in Table 3.10, the single-point surface area was approximately 80% of the value obtained from the multipoint analysis.

Table 3.10. Comparison of single- and multipoint BET surface areas using nitrogen as an adsorbate[a]

Sample	Composition	Multipoint BET surface area, X_{M-MP} (m^2/g)	Single-point BET surface area, X_{M-SP} (m^2/g)	$\frac{X_{M-SP}}{X_{M-MP}}$
1	$Ba)OH)_2 \cdot 6.4H_2O$	0.99	0.83	0.834
2	$Ba(OH)_2 \cdot 8.0H_2O$	0.98	0.84	0.856
3	$BaCO_3$	7.52	6.08	0.809
4	$BaCO_3$	8.70	6.97	0.801
5	2.66% $Ba(OH)_2 \cdot 8H_2O$	5.46	4.19	0.767
6	15.43% $Ba(OH)_2 \cdot 8H_2O$	4.44	3.36	0.757
7	50.45% $Ba(OH)_2 \cdot 8H_2O$	1.67	1.07	0.638
8	59.55% $Ba(OH)_2 \cdot 8H_2O$	1.48	1.02	0.689

[a] $P/P_0 = 0.60$ for single-point method.

Using the same bulk sample as used for Samples 3 and 4 in Table 3.8, a single-point BET surface area using argon as an adsorbate was obtained. The surface area was 9.24 m^2/g as compared to values of 7.57 and 8.93 m^2/g obtained from the multipoint analysis using nitrogen as an adsorbate. Thus reasonable consistency exists. A second area of concern regarding the validity of using argon (P/P_0 = 0.60) as an adsorbate was whether capillary condensation might occur, thus resulting in a calculated surface area greater than the actual area. Multipoint studies have indicated no hysteresis and thus negligible filling of circular or near-circular pores on any of the isotherms. Sorption potential studies indicated no appreciable capillary condensation for any samples. However, the mercury porosimetry data (next section) did indicate a possible decrease in pore size as the surface area increased for $BaCO_3$ product samples. However at P/P_0 = 0.60, only pores of diameter <5 nm would be filled. From the mercury porosimetry density function plots in the subsequent section, one may observe that ln (0.005) = -5.30 is far to the left of the experimentally determined maximas. Thus it was concluded that the single-point BET surface areas obtained with argon at a P/P_0 = 0.60 could be used, with reservation, for establishing possible data trends.

Presented as a function of relative humidity in Figure 3.6 are the single-point surface areas of $BaCO_3$ product samples. These samples were obtained from fixed-bed studies in which the dependent variables were relative humidity, temperature, and gas flow rate. An area of interest, previously cited earlier in this chapter and to be discussed in greater detail later, is the effect of water vapor upon the surface of the

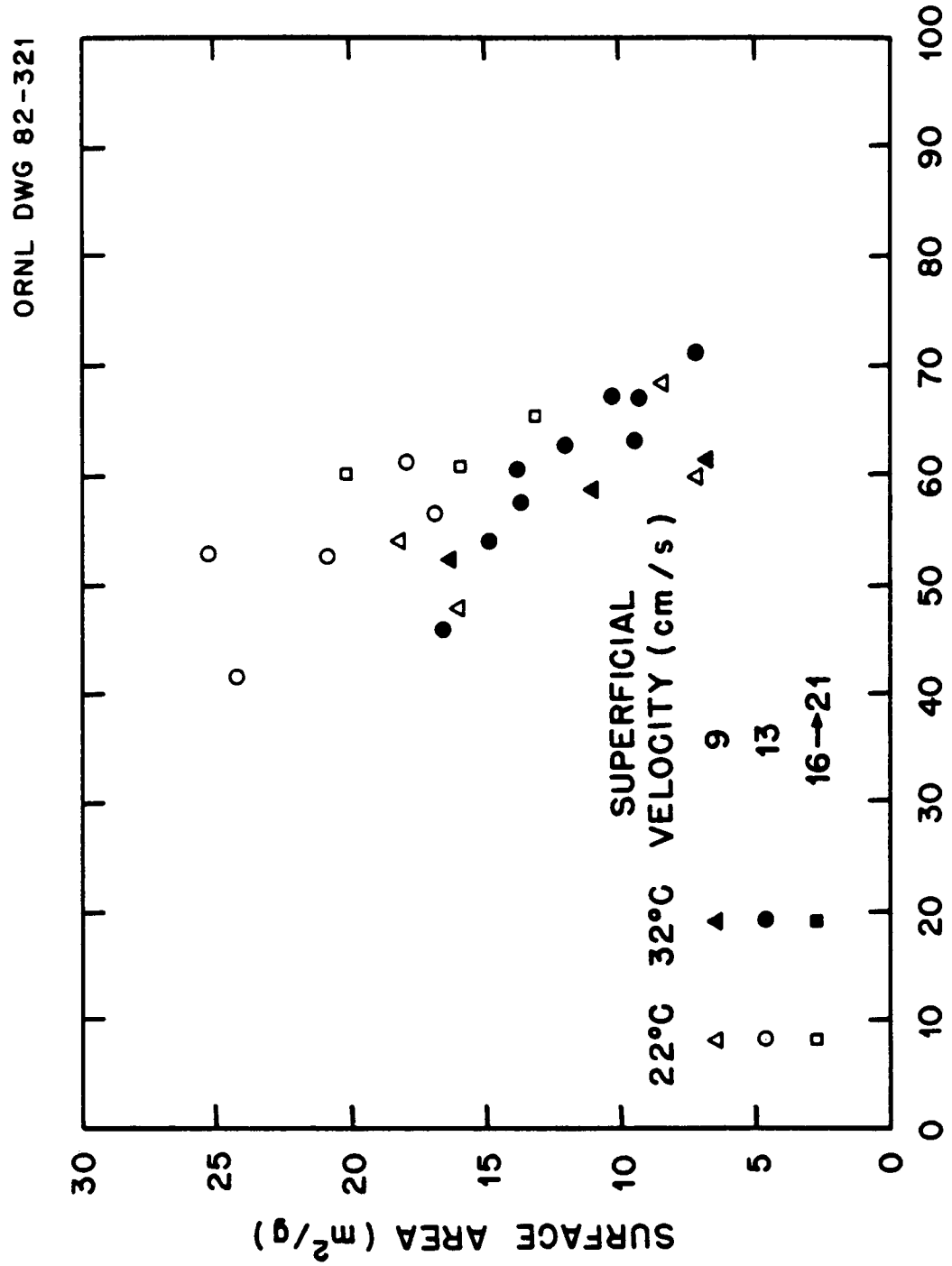


Figure 3.6. Single-point BET surface area analyses using argon ($P/P_0 = 0.6$) as an adsorbate.

reactant and product. The amount of water vapor on the surface is dependent upon the extent of saturation of the vapor in equilibrium with the sorbed liquid, the percent of saturation of water vapor being termed relative humidity. Adsorption processes are then a strong function of the percentage of vapor saturation, P/P_0, and are not a function of temperature. As shown in Figure 3.6, surface area data obtained at run temperatures of 22°C and 32°C correlate reasonably well when plotted as a function of relative humidity. For this temperature range, the saturation vapor pressure, P_0, increases from 2.64 kPa (19.8 torr) at 295.2 K to 4.76 kPa (35.7 torr) at 305.2 K. Futhermore, the surface area is observed to decrease as a function of relative humidity. It therefore appears that adsorbed water on the surface plays an active role in the transport of the Ba^{2+}, OH^-, and CO_3^{2-} ions; thus affecting the reaction and recrystallization process and resulting in larger crystallites and less surface area. Although the data are not conclusive, there are indications (as shown in Figure 3.6) that lower gas flow rates may result in lower surface areas. In the previous section, the observation was made that the increase in specific surface area was dependent upon the rate of reaction; the greater the specific rate of reaction, the greater the surface area per gram of product. It would, therefore, seem plausible that for a slow reaction, fewer sites of crystal nucleation and growth would exist and the presence of adsorbed water on the surface would aid in the transport of the Ba^{2+}, OH^-, and CO_3^{2-} ions to the existing $BaCO_3$ crystallites. The reaction process would then take place in a more orderly environment. In conclusion, the presence of sorbed water on the solid surface appears to take an active role in the overall mechanism.

Mercury porosimetry studies. Previous adsorption studies have indicated few capillaries of mean diameters <150 nm. Furthermore, density measurements presented earlier in this chapter indicated very little intraparticle porosity that was available for penetration. To obtain additional information concerning the surface morphology of *commercial* $Ba(OH)_2 \cdot 8H_2O$ and $BaCO_3$ product, mercury porosimetry tests were performed by the Analytical Chemistry Division at Oak Ridge National Laboratory. For data interpretation, the assumption of circular pores was made. The data, presented in Appendix I, were analyzed by the author and converted to density distribution plots. The density distribution is equivalent to $dV/d[\ln(d_p)]$, where V is the penetration volume and d_p is the capillary radius. The data for two *commercial* $Ba(OH)_2 \cdot 8H_2O$ samples, stoichiometry of 7.0 and 7.5, are presented in Figure 3.7. Little difference was observed to exist between the two samples. However, there are indications that the peak distribution may be bimodal, with maxima at ~1.0 μm and ~0.17 μm. Porosities for the two materials were determined to be 13.26 and 11.84%, respectively. As discussed previously, it is speculated that internal voids, which are not accessible to mercury porosimetry, contribute very little to the net voidage.

Similar studies were conducted on two different $BaCO_3$ product samples, each sample originating from the same *commercial* $Ba(OH)_2 \cdot 8H_2O$ batch number. Sample COM-35 was determined to have a BET single-point surface area of 18.3 m^2/g, whereas COM-40 had a surface area of 9.2 m^2/g. The data were analyzed in a similar manner as the preceding data to determine the density distribution (presented in Figure 3.8; the actual data are given in Appendix I). For COM-40, a bimodal distribution exists with a weak

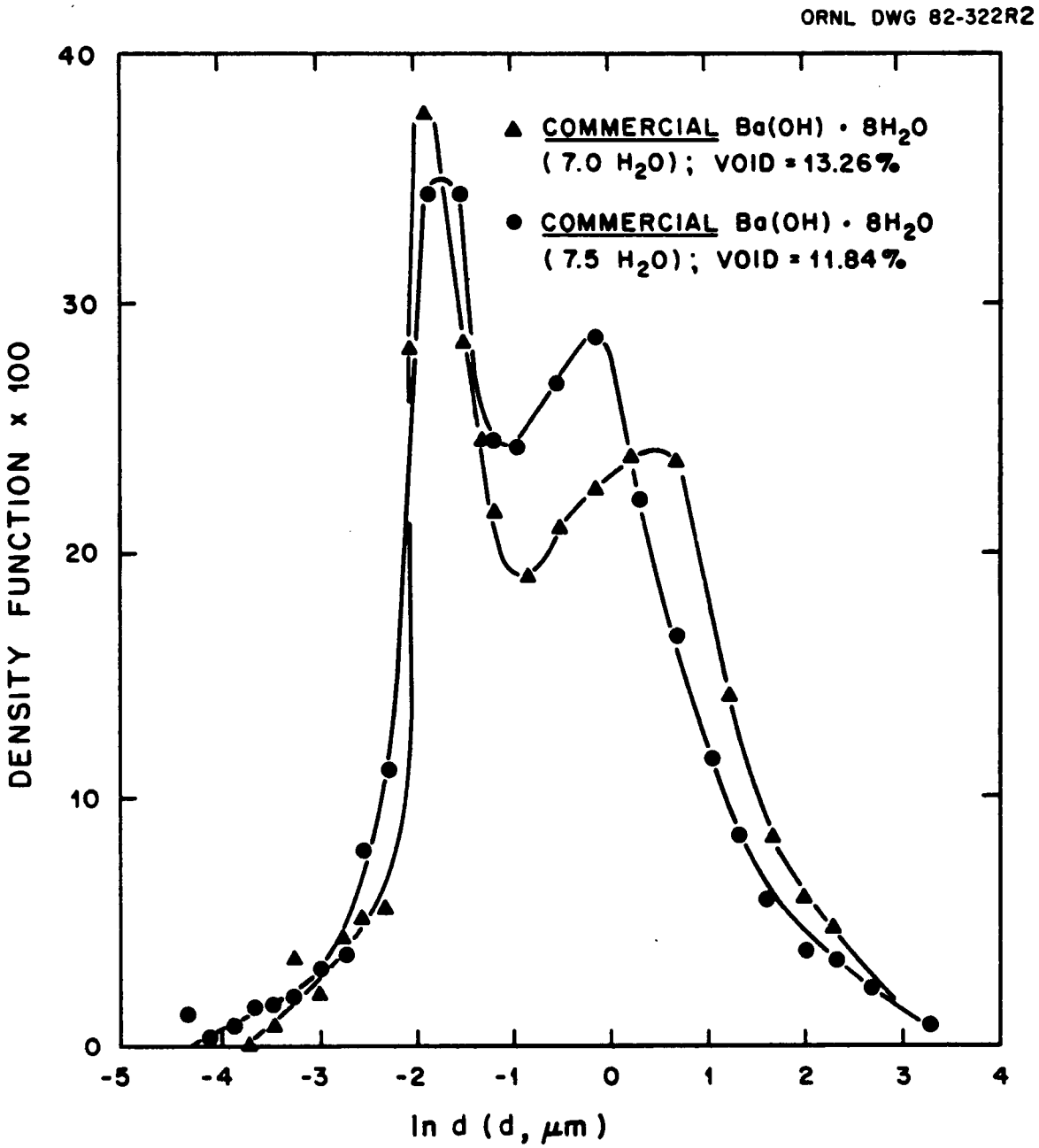


Figure 3.7. Mercury porosimetry results on *commercial* $Ba(OH)_2 \cdot 8H_2O$ flakes from two different batch numbers.

maxima at a diameter of ~3.50 μm and a strong maxima at ~15 μm. For COM-35, which possesses a greater surface area, the single maximum is downshifted and corresponds to a diameter of ~8.2 μm. The porosity of COM-40 was 72.05%, whereas the porosity of COM-35 was 66.49%. Based upon a Pilling-Bedworth ratio of 0.31 (molar volume of product/molar volume of reactant) and an initial flake porosity of 0.12, a final intraparticle void volume of 73% would have been predicted. Thus the results are reasonably consistant. Discrepancies could result from capillaries of such diameter that they are penetrated at very low mercury pressures.

Assuming negligible contribution to the total surface area from pores of <3.5 μm in diameter, the following analysis may be made. For cylindrical pores, the surface area per unit volume of pore is

$$A = \frac{2\pi r \ell}{\pi r^2 \ell} \qquad (3.4)$$

$$= \frac{2}{r} \quad ,$$

where

r = pore radius,

ℓ = pore depth.

Thus the ratio of surface areas per unit volume of sample for COM-35 to COM-40, R, would be the following:

$$R = \frac{A}{A}\Bigg|_{\text{COM-40}}^{\text{COM-35}}$$

$$R = \frac{\varepsilon}{r}\Bigg|_{\text{COM-35}} * \frac{r}{\varepsilon}\Bigg|_{\text{COM-40}} \qquad (3.5)$$

$$= \frac{0.665}{0.082} * \frac{0.15}{0.721} = 1.69 \ ,$$

where ε is the intraparticle voidage. The ratio obtained from the single-point BET analysis was 1.99. In light of the potential error in estimating the maxima from Figure 3.8 and other potential sources of error, the comparison is reasonably consistent with anticipated results.

As may be seen from the density distribution plots, the voidage contribution of pores with diameters <30 μm (ln(0.03) = 3.5) is very small. For a pore diameter of 30 μm, the Kelvin equation predicts a desorption P/P_0 of 0.993. Hence hysteresis during adsorption-desorption studies would not be observed with the present experimental system. As a point of reference, the desorption $P/P_0 \rightarrow 1.0$ as the pore diameter becomes progressively larger.

Photographs and scanning electron micrographs of $BaCO_3$ product. As previously discussed, the relative humidity of the system may greatly affect the surface morphology of the reactant, the product, or both. When operating at relative humidities in excess of 60%, the *commercial* $Ba(OH)_2 \cdot 8H_2O$ (Figure 3.4) is observed to recrystallize and curl. Upon conversion to $BaCO_3$, the particle degrades and operational problems become more severe. For humidities <60%, this phenomena is less apparent upon hydration to $Ba(OH)_2 \cdot 8H_2O$. The flake form is observed to remain essentially intact, even upon conversion to $BaCO_3$ (Figure 3.9). Scanning electron micrographs of the smooth and rough side of Sample COM-40 are presented in Figure 3.10. As predicted, considerable porosity is observed. Assuming negligible particle shrinkage, calculations indicate

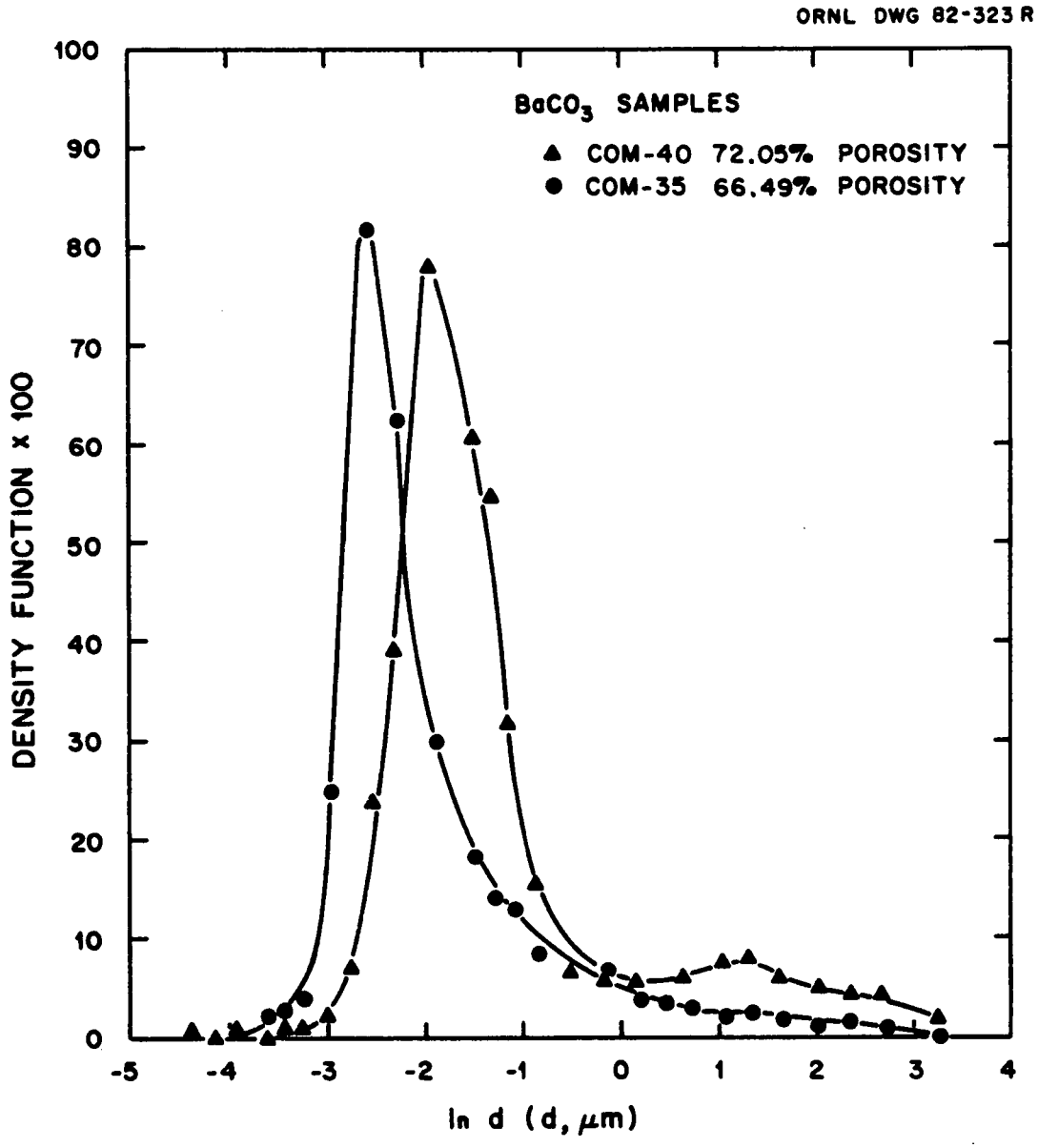


Figure 3.8. Mercury porosimetry results on two $BaCO_3$ samples.

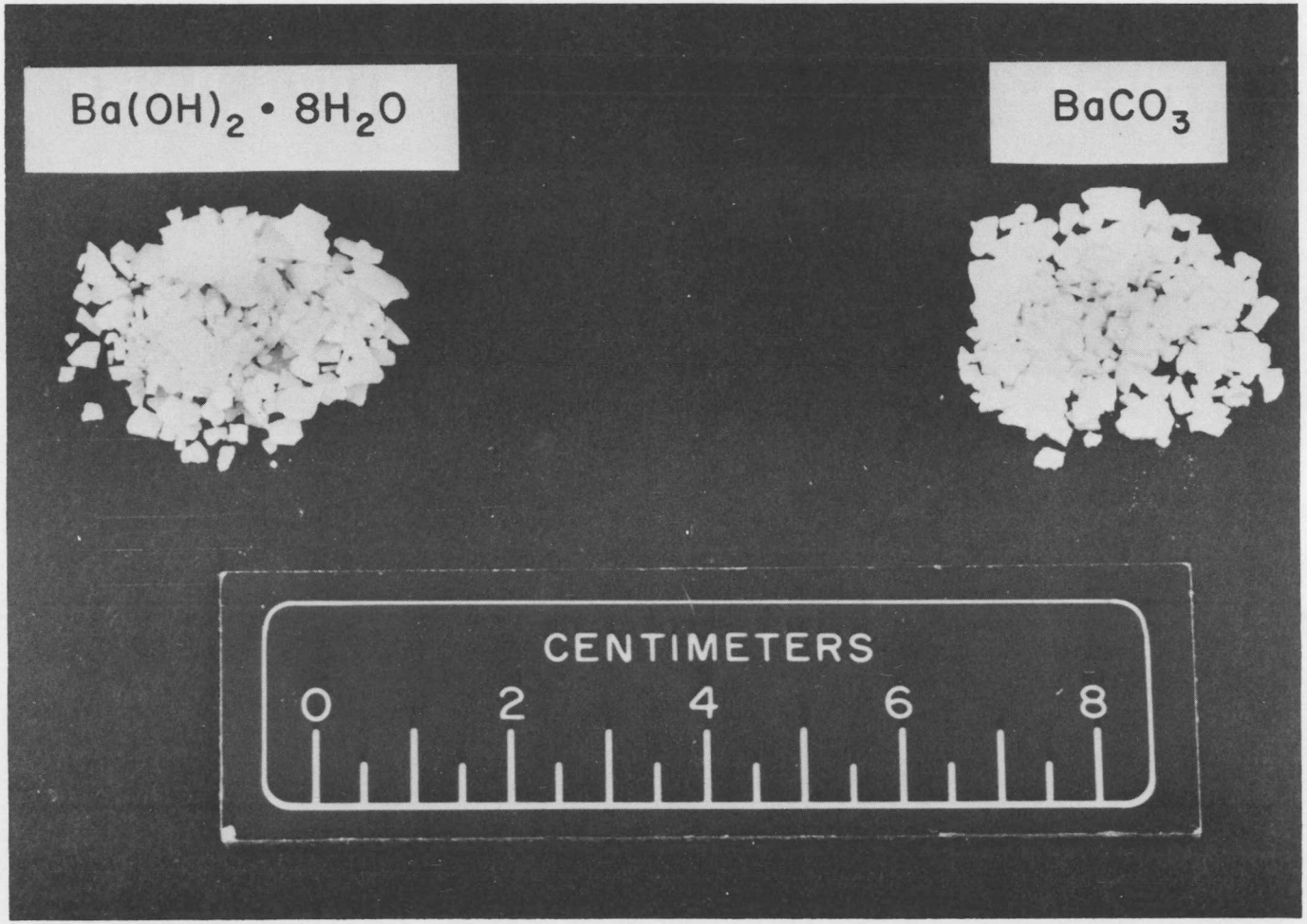


Figure 3.9. Photograph of *commercial* $Ba(OH)_2 \cdot 8H_2O$ flakes and $BaCO_3$ flake product. The product was obtained at a process relative humidity <60%. (Original photograph: 7.3 by 9.5 cm, magnification, 16.5 and 13X, respectively.)

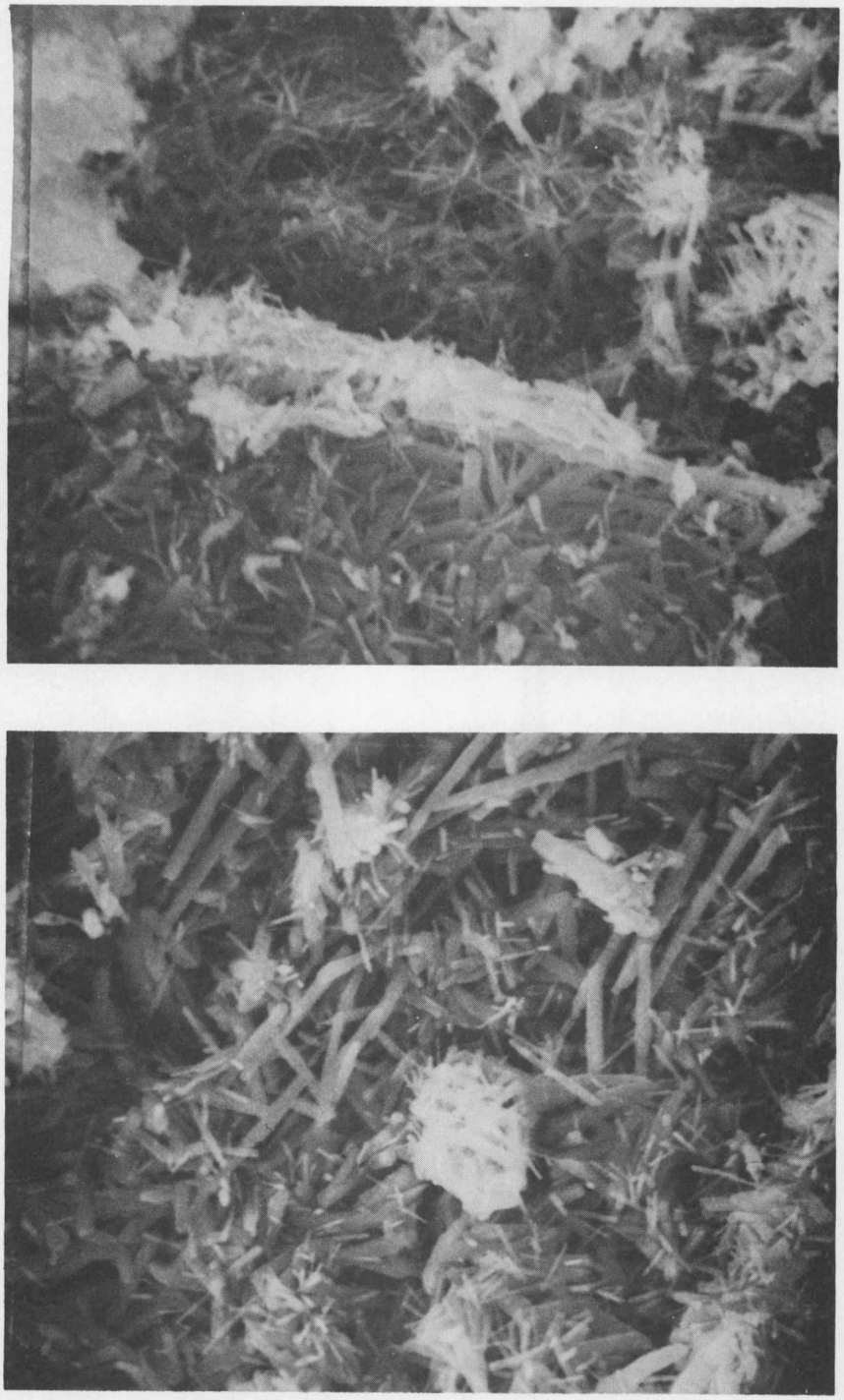


Figure 3.10. Scanning electron micrographs of top and bottom surfaces of $BaCO_3$ product from COM-40. (Original photograph, 8.9 by 11.4 cm; magnification, 5000X).

the particle should be ~73% void. Mercury porosimetry measurements indicated a voidage of 72.1% for this sample.

The reactivity of $Ba(OH)_2$ hydrates toward CO_2. Studies were conducted with the microbalance analytical system to determine the reactivity of $Ba(OH)_2 \cdot H_2O$, $Ba(OH)_2 \cdot 3H_2O$, and $Ba(OH)_2 \cdot 8H_2O$ toward CO_2. $Ba(OH)_2 \cdot H_2O$ was prepared by the room temperature, vacuum dehydration of *commercial* $Ba(OH)_2 \cdot 8H_2O$ to $Ba(OH)_2$ and subsequent quantitative rehydration at 294.8 K and 266.0 Pa (2 torr) water vapor pressure to $Ba(OH)_2 \cdot H_2O$. $Ba(OH)_2 \cdot 3H_2O$ was prepared by subjecting a sample of *commercial* $Ba(OH)_2 \cdot 8H_2O$ to a water vapor pressure of 480.0 Pa (3.6 torr) at 294.8 K. The validity of this technique will be established further in the next section. Finally, $Ba(OH)_2 \cdot 8H_2O$ was prepared by subjecting *commercial* $Ba(OH)_2 \cdot 8H_2O$ to a water vapor pressure of 1.28 kPa (9.6 torr) at 294.8 K. The relative humditiy for this step was 50%. Since this value was <60% relative humidity, curling of the flake during rehydration was avoided.

For the reaction of CO_2 with $Ba(OH)_2 \cdot H_2O$, $Ba(OH)_2 \cdot 3H_2O$, and $Ba(OH)_2 \cdot 8H_2O$, the respective relative humidities were 10%, 19%, and 50%. The first relative humidity corresponds to the approximate completion of the initial monolayer of water, whereas 50% relative humidity corresponds to the approximate completion of two layers of water or a water film thickness of ~0.7 nm. The pressure of each system was then raised from the respective water vapor pressure to a pressure that was 133.3 Pa (1.0 torr) greater by the addition of CO_2. The rate of reaction was then monitored by the resulting weight changes. Because of an accompanying increase in molecular weight (MW), the $Ba(OH)_2 \cdot H_2O$ sample increased in weight upon conversion to $BaCO_3$ (MW = 189 → MW = 197), whereas

$Ba(OH)_2 \cdot 3H_2O$ (MW = 225) and $Ba(OH)_2 \cdot 8H_2O$ (MW = 315) lost weight upon conversion to $BaCO_3$. At 5 mol % conversion, the relative rates of reaction were compared. The rates for $Ba(OH)_2 \cdot H_2O$ and $Ba(OH)_2 \cdot 3H_2O$ were roughly equivalent. However, the rate of the CO_2—$Ba(OH)_2 \cdot 8H_2O$ reaction was more than 3 orders of magnitude greater (~3000 times). To state whether the increase in reactivity results from the presence of $Ba(OH)_2 \cdot 8H_2O$ or the presence of increased surface water is difficult. Earlier in this chapter, it was shown that sorbed water does play an active role in the surface transport process. However, because of the small increase in surface water and the sharpness of the transition, the author speculates that the presence of the 5 additional waters of hydration in the crystal lattice near the reactive hydroxyl ions are largely responsible for the drastic increase in the kinetic rate.

$Ba(OH)_2 \cdot 8H_2O$ vapor pressure, dehydration, and rehydration studies. As previously discussed, the presence of $Ba(OH)_2 \cdot 8H_2O$ is very important for a rapid CO_2 reaction. Therefore, studies were conducted with the microbalance system on 150- to 200-mg samples of *commercial* $Ba(OH)_2 \cdot 8H_2O$ (7.0 H_2O) to determine (1) the validity of published vapor pressure data and correlations, and (2) the rates of dehydration of $Ba(OH)_2 \cdot 8H_2O$ to $Ba(OH)_2 \cdot 3H_2O$ and subsequent rehydration.

Static vapor pressure studies to determine the equilibrium vapor pressure of $Ba(OH)_2 \cdot 8H_2O$ were attempted. However, because of fluctuations in the ambient temperature of the room in which the equipment was housed (these fluctuations affected the pressure within the system) and

the slowness of the kinetics as equilibria was approached, these studies were abandoned.

Studies were conducted at 294.8 and 304.9 K and varying water vapor pressures to determine the rates of dehydration of *commercial* $Ba(OH)_2 \cdot 8H_2O$ flakes to $Ba(OH)_2 \cdot 3H_2O$ and the subsequent rehydration to $Ba(OH)_2 \cdot 8H_2O$. The presence of $Ba(OH)_2 \cdot 3H_2O$ was confirmed gravimetrically and by x-ray diffraction. As shown in Figures 3.11 and 3.12, the dehydration and rehydration conversion profiles were a linear function of time for up to 80% conversion. Furthermore, as shown Figures 3.13 and 3.14, the rate data for both dehydration and rehydration were linear functions of water vapor pressure. Mathematically, it was found that by assuming a shrinking-core model for a flat flake and a first-order kinetically controlled reaction (Appendix M), a suitable model applicable to both dehydration and rehydration could be developed. The conversion profile from such a shrinking-core model would be represented by

$$X_B = \frac{t}{\tau} , \qquad (3.6)$$

where

X_B = fraction converted,

$\tau = \dfrac{\rho \, b_o}{2b \, K_K \, C}$,

ρ = solid density,

b_o = particle thickness,

b = stoichiometry coefficient, molecules solid reactant/molecule gaseous reactant,

K_K = kinetic rate constant,

C = reactant gas concentration.

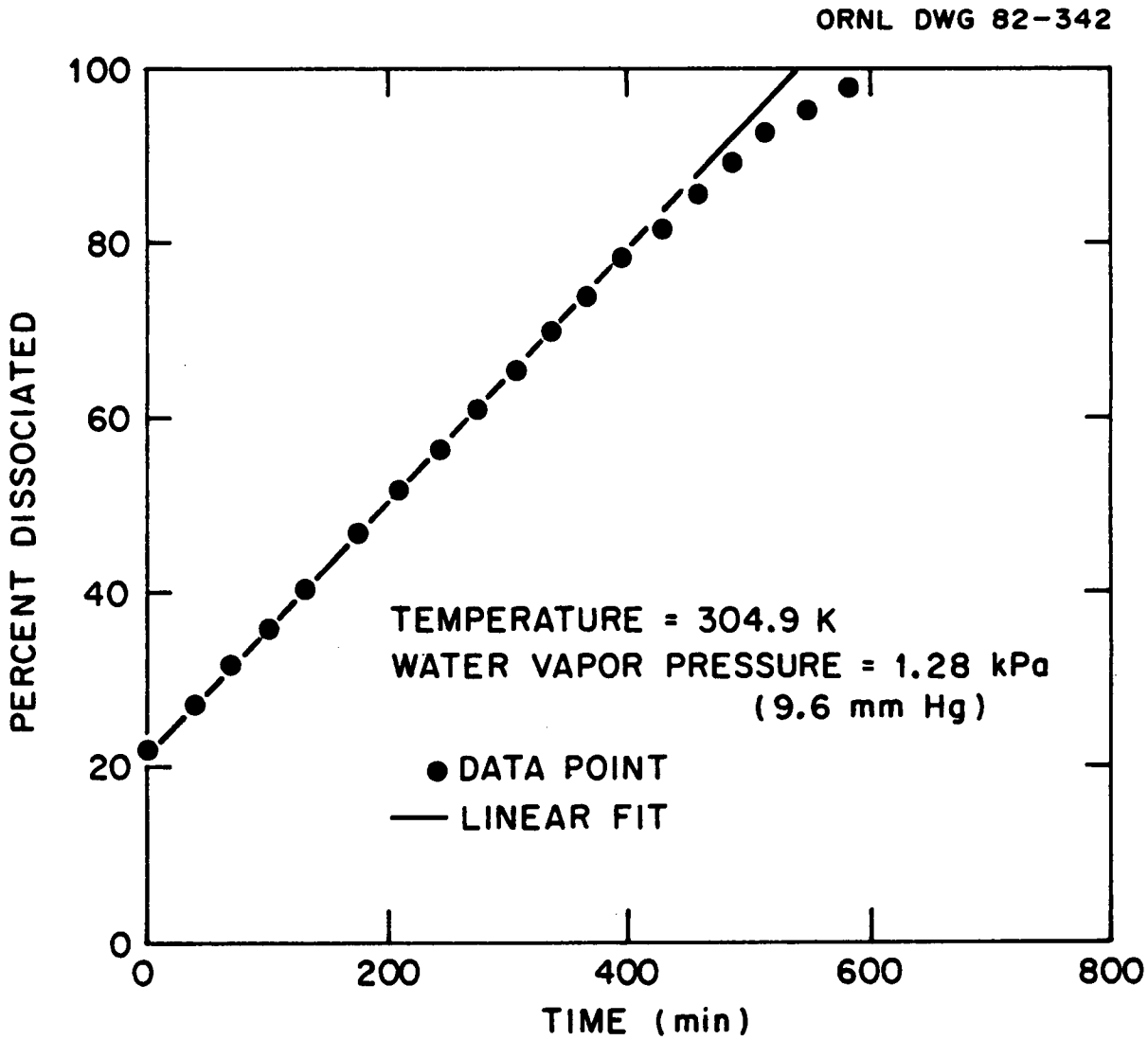


Figure 3.11. The dehydration or dissociation of *commercial* $Ba(OH)_2 \cdot 8H_2O$ flakes to $Ba(OH)_2 \cdot 3H_2O$ as a function of time and water vapor pressure.

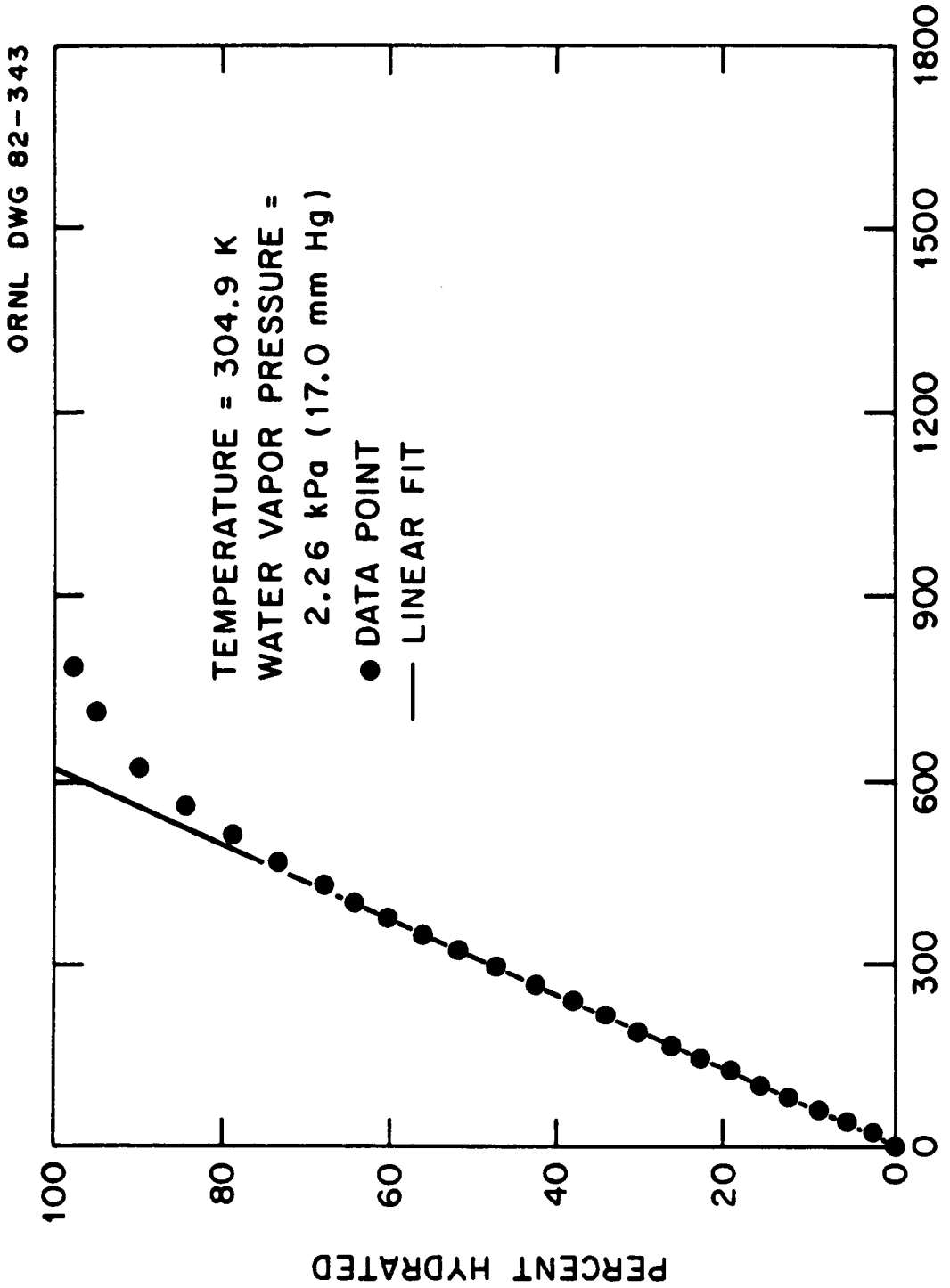


Figure 3.12. The rehydration of $Ba(OH)_2 \cdot 3H_2O$ to $Ba(OH)_2 \cdot 8H_2O$ as a function of time and water vapor pressure.

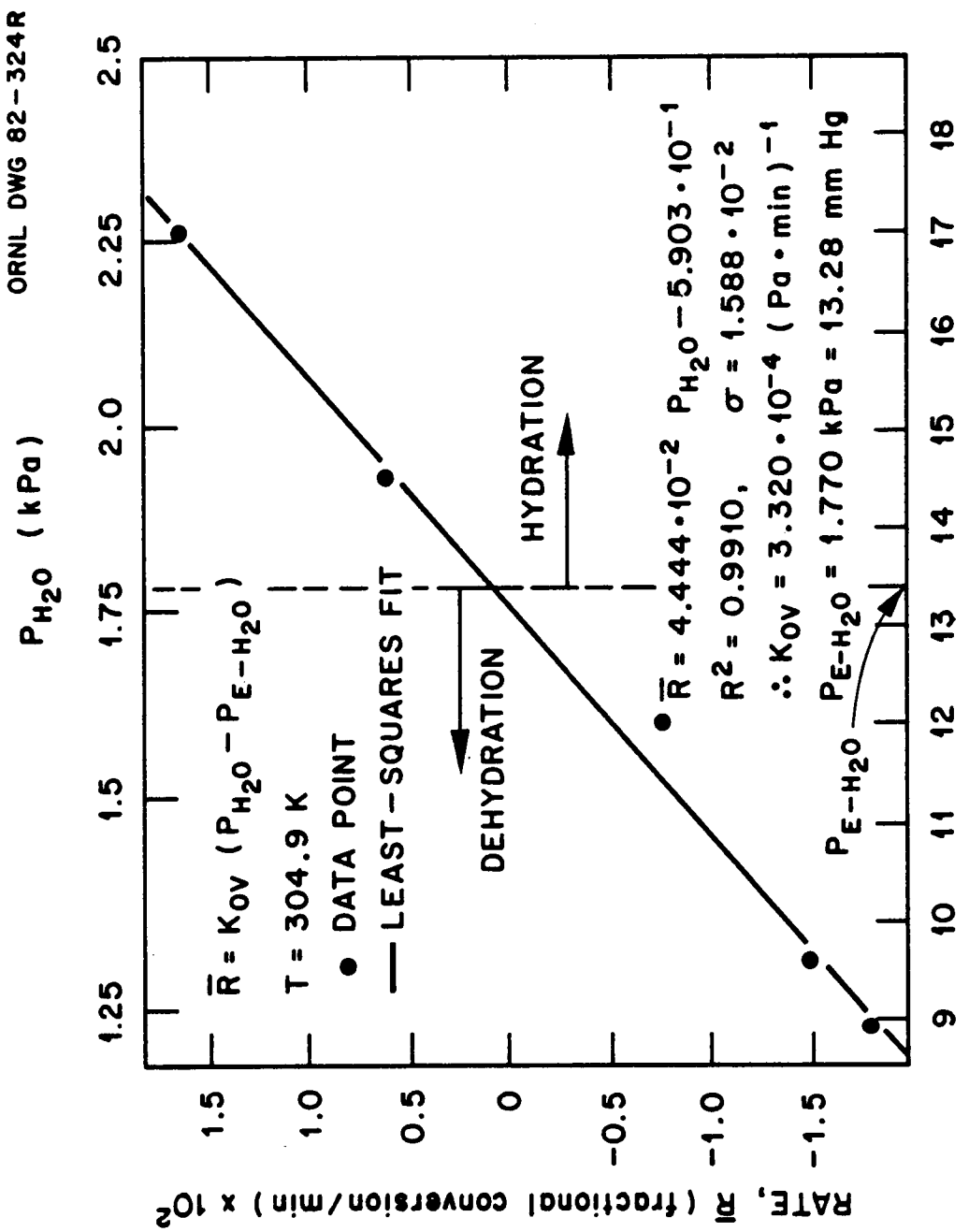


Figure 3.13. Rates of dehydration and rehydration as a function of water vapor pressure at 304.9 K.

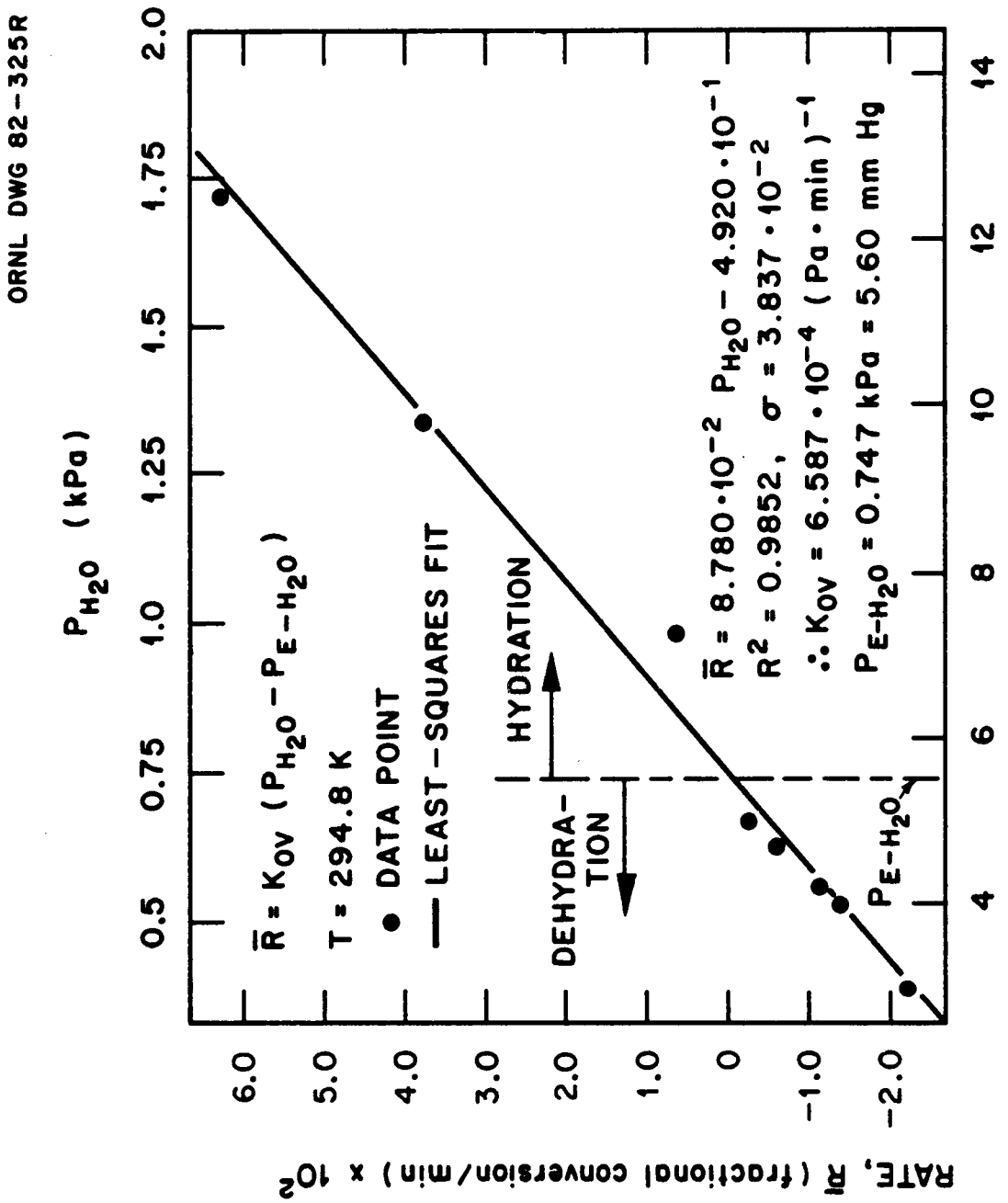


Figure 3.14. Rates of dehydration and rehydration as a function of water vapor pressure at 294.8 K.

The derivation of this equation and other shrinking-core models for kinetic, gas film, and diffusion control for flat plate, cylindrical, and spherical particle geometries and the associated assumptions are presented in Appendix M. The chosen rate expression for dehydration was of the form

$$\bar{R} = K_K C = \frac{K_K}{RT} \left(P_{E\text{-}H_2O} - P_{H_2O}\right) , \qquad (3.7)$$

where

R = gas constant,

T = absolute temperature,

$P_{E\text{-}H_2O}$ = equilibrium water vapor pressure of $Ba(OH)_2 \cdot 8H_2O$,

P_{H_2O} = water vapor pressure in system.

The driving force for the reaction was assumed to be the difference between the water vapor pressure and the dissociation vapor pressure. When the preceding equation is substituted into Equation (3.6), the following conversion expression is obtained:

$$X = \frac{2bKK}{\rho b_o RT} \left(P_{E\text{-}H_2O} - P_{H_2O}\right)t , \qquad (3.8)$$

$$= \bar{R}'t ,$$

where

$\bar{R}'$ = Fractional conversion per unit time.

For rehydration, the equation is the same except the driving force becomes $(P_{H_2O} - P_{E\text{-}H_2O})$.

From a plot of conversion versus time, the reaction rate R' was determined and is presented in Table 3.11 as a function of temperature and water vapor pressure. The least-squares correlation coefficient at 50% conversion is also presented. The change in correlation coefficients between 50 and 80% was small. However, since the flakes did vary in thickness by a factor of ~2, some nonlinearity in the conversion equation would be expected, and the $\bar{R}'$ values for 50% conversion were used.

Using the preceding assumptions, the kinetic rate terms and the dissociation vapor pressures were determined with Equation (3.8) via least-squares analyses (Figures 3.13 and 3.14). The calculated equilibrium vapor pressure and rate constant, K_{ov}, are presented in Table 3.12, where K_{ov} is defined as follows:

$$\bar{R}' = \frac{2b\ K_K}{\rho b_0\ RT} (P_{E\text{-}H_2O} - P_{H_2O}) \ , \qquad (3.9)$$

$$= K_{ov}(P_{E\text{-}H_2O} - P_{H_2O}) \ ,$$

where K_{ov} = overall rate constant. Also presented in Table 3.12 are the literature values for the dissociation vapor pressure at these temperatures and the least-squares correlation coefficients for the fitted equation. From Table 3.12, the experimental vapor pressure values correlate quite well with the published values, thus establishing a degree of validity to the preceding assumptions. These assumptions are (1) kinetically limited dehydration and rehydration reactions that may be modeled by a shrinking core within a flat plate, and (2) kinetic rate constants for dehydration and rehydration that are similar in magnitude. The consistency of the data is demonstrated by the fact that with the

Table 3.11. The dehydration of *commercial* $Ba(OH)_2 \cdot 8H_2O$ to $Ba(OH)_2 \cdot 3H_2O$ and subsequent rehydration to $Ba(OH)_2 \cdot 8H_2O$

Experimental conditions	Temperature (°C)	Water vapor pressure (torr)	(kPa)	Fractional conversion per (min x 10^2)	Least-squares correlation coefficient
Dehydration	21.6	3.0	0.40	2.219	0.9993
Dehydration	21.6	4.0	0.53	1.401	0.9999
Dehydration	21.6	4.25	0.56	1.134	0.9999
Dehydration	21.6	4.7	0.63	0.650	0.9995
Dehydration	21.6	5.0	0.66	0.268	0.9996
Rehydration	21.6	7.25	0.97	0.589	0.9988
Rehydration	21.6	9.8	1.31	3.777	0.9998
Rehydration	21.6	12.5	1.67	6.269	0.9999
Dehydration	31.7	9.4	1.25	1.786	0.9996
Dehydration	31.7	9.6	1.28	1.470	0.9999
Dehydration	31.7	12.0	1.60	0.761	0.9999
Rehydration	31.7	14.5	1.93	0.627	0.9967
Rehydration	31.7	17.0	2.27	1.655	0.9998

Table 3.12. Experimental and literature values for the equilibrium water vapor pressure of $Ba(OH)_2 \cdot 8H_2O$ and the experimental rate constant, K_{ov}

Temperature (K)	Rate constant, K_{ov} [Fraction converted /(Pa•min)]	Equilibrium water vapor pressure (kPa)			Correlation coefficient
		Experimental	Literature[a]	Literature[b]	
294.8	$6.59 \cdot 10^{-6}$	0.740	0.839	0.757	0.9956
304.9	$3.32 \cdot 10^{-6}$	1.770	1.845	1.635	0.9916

[a]Data obtained from B. A. Kondakov, P. V. Kovtunenko, and A. A. Bundel, "Equilibria Between Gaseous and Condensed Phases in the Barium Oxide–Water System," *Russ. J. Phys. Chem.* *38*(1), 99–102 (1964).

[b]Data obtained from S. Tamaru and K. Siomi, "Redetermination of Thermal Dissociation Equilibria of Inorganic Compounds," *V. Z. Phys. Chem., 171A,* 229 (1934).

exception of one data point, all hydration-dehydration data were used in the least-squares analyses. One rehydration data point obtained at 304.9 K and 2.53 kPa (19.0 torr) was not used because of the proximity of the vapor pressure to saturation at system conditions. (Ideally, one would desire to enclose the entire microbalance system in a thermal enclosure, thus eliminating this restriction.) A factor that is particularly noticeable in Figures 3.12 and 3.13 is the existence of a possible induction phenomenon or a slower-than-expected reaction rate as the equilibrium vapor pressure is approached. This phenomenon may result from a change in the extent of control of various steps in the overall mechanism.

However, a problem exists with the preceding mathematical model. Although the calculated vapor pressures correlate with the literature

values, the rate constant for the kinetic reaction at 21.6°C is 1.98 times greater than at 31.7°C. Although not rigorous, the Arrhenius equation usually provides an excellent means of estimating the effect of temperature upon the kinetic rate constant[70] and takes the following form:

$$K_K = K_o \exp[-E_A/RT] \ , \qquad (3.10)$$

where

K_o = frequency factor,

E_A = activation energy,

R = gas constant,

T = absolute temperature.

In the real world, the energy of activation for a rate-limited reaction is usually constrained to be a positive number. From the form of the equation for a given activation energy and frequency factor, one would expect the rate constant to increase with temperature (a positive activation energy) or for very low activation energies, to remain constant and to approach an asymtote very rapidly because there are no kinetic barriers. The calculated activation energy was -48 kJ/mol-H_2O. Although mathematically the developed model correlates the data quite well, an error appears to exist because the model gives a negative activation energy and thus violates the expected constraints of the real world.

To develop a more plausible model, we now turn to the physical system. Surface area measurements reported earlier indicated that sorbed surface water takes an active role in the recrystallization of the $BaCO_3$ product. Hence the assumption that sorbed water will play an active role in the dehydration and rehydration mechanisms would seem

appropriate. As may be observed from the adsorption isotherms in Appendix H, the increase in the amount of sorbate on the solid surface varies linearly over the range $0.15 < P/P_0 < 0.55$. Thus the assumption is made that water sorption may be modeled by a linear isotherm. This assumption is also commonly used in the modeling of adsorption studies on resins, as indicated by

$$\Gamma = K_E \frac{P}{P_0} , \tag{3.11}$$

where

Γ = H_2O sorbed, (g/g),

Γ_E = H_2O sorbed, (g/g), at P_{E-H_2O} for $Ba(OH)_2 \cdot 8H_2O$,

K_E = equilibrium constant,

P = water vapor pressure,

P_0 = saturation water vapor pressure.

Therefore, based upon the preceding analysis, the following rate equation was examined:

$$\bar{R}' = K_s[\Gamma_E - \Gamma] . \tag{3.12}$$

The preceding equation states that the rate of dehydration or rehydration is proportional to the difference in water sorbed on the solid surface and that present at equilibrium with $Ba(OH)_2 \cdot 8H_2O$. Values for the rate constant constant K_S based upon combined dehydration and rehydration data are presented in Table 3.13. From the data presented in Table 3.13, one may conclude that this model comes very close to both modeling the system and to being consistant with the physical constraints imposed upon the system by the real world. Since the rate constants are nearly equal,

Table 3.13. Rate constants as determined via Equation (3.12)

Temperature (K)	Rate constant, K_s (Fractional conversion/min)
294.8	$1.699 \cdot 10^{-2}$
304.9	$1.588 \cdot 10^{-2}$

a difference of <10%, this would indicate a very low activation energy. The activation energy for an exact fit was calculated to be -6 kJ/mol-H_2O added or removed. Considering the assumptions made in the model development, the fit is excellent. The proximity of the activation energy to zero indicates that near-equilibria must exist. Hence the author speculates that the actual system consists of two solids, $Ba(OH)_2 \cdot 8H_2O$ and $Ba(OH)_2 \cdot 3H_2O$, and a liquid, H_2O. The system strives to maintain the following equilibrium:

$$Ba(OH)_2 \cdot 8H_2O(s) \rightleftarrows Ba(OH)_2 \cdot 3H_2O(s) + 5H_2O(l) \qquad (3.13)$$

In striving to maintain equilibrium, the absence of sufficient amounts of sorbed water to stabilize the crystalline $Ba(OH)_2 \cdot 8H_2O$ causes $Ba(OH)_2 \cdot 8H_2O$ to decompose, thus attempting to reestablish the equilibrium concentration of sorbed water. Rehydration occurs in a similar but reversed manner. A phase diagram for the system is presented in Appendix B.

Conclusions — surface morphology and microscale studies. With regard to the surface morphology and microscale studies reported in this section, the conclusions may be highlighted in the following manner:

1. Methods of preparation of $Ba(OH)_2 \cdot H_2O$, $Ba(OH)_2 \cdot 3H_2O$, and $Ba(OH)_2 \cdot 8H_2O$ were developed, and the presence of said species was confirmed.

2. *Commercial* $Ba(OH)_2 \cdot 8H_2O$ flakes were found to display negligible surface area. Hydration to $Ba(OH)_2 \cdot 8H_2O$ was observed to proceed in one of two regimes. For relative humidities <60%, the increase in surface area was small and the flake form remained intact. For relative humidities >60%, the flake recrystallized in a manner which resulted in greater surface area, but the increase in activity also resulted in a more fragile product.

3. Dehydration of *commercial* $Ba(OH)_2 \cdot 8H_2O$ to $Ba(OH)_2 \cdot 3H_2O$ and subsequent rehydration to $Ba(OH)_2 \cdot 8H_2O$ at relative humidities <60% was modeled by a shrinking-core model. The relative rate was found to be dependent upon the difference between the water sorbed on the surface for a given P/P_0 value (i.e., relative humidity) and that required on the surface for $Ba(OH)_2 \cdot 8H_2O$ to exist in a stable form.

4. There was evidence of considerable hydrogen bonding within the $Ba(OH)_2 \cdot 8H_2O$ crystal. These results paralleled the crystallography studies of Monohar and Ramaseshan in which they cited difficulty in differentiating the location of the hydroxyl ions from the waters of hydration in the unit cells.[67]

5. The vapor pressure correlation for $Ba(OH)_2 \cdot 8H_2O$ cited in the previous section was indirectly verified at two temperatures.

6. At low CO_2 vapor pressures, $Ba(OH)_2 \cdot 8H_2O$ was observed to be three orders of magnitude more reactive toward CO_2 than either $Ba(OH)_2 \cdot 3H_2O$ or $Ba(OH)_2 \cdot H_2O$.

7. For relative humidities <60%, the increase in surface area with product conversion was found to be a very strong function of the specific rate of reaction and was not a linear function of conversion.

8. The surface area of $BaCO_3$ product was determined to be a function of relative humidity. In a manner analogous to the dehydration of *commercial* $Ba(OH)_2 \cdot 8H_2O$ and the rehydration of $Ba(OH)_2 \cdot 3H_2O$, surface water appears to aid in the transport of the reactant and product species, thus resulting in lower surface areas at higher values of P/P_0 (i.e., relative humidity). However, it is the opinion of the author that the increase in surface water could not account for the drastic difference in CO_2 reactivity observed for the various hydrate species. The difference in reactivity appears to result from the additional water in the crystal structure and the greater mobility of the hydroxyl ions.

9. Based upon the analysis of nitrogen sorption isotherm data, there were no indications of hysteresis. Therefore, if capillary condensation should occur, one would speculate it to result from the wall effects of noncircular pores (e.g., V-shaped points of intersurface contact).

Fixed-bed Macroscale Studies

Modeling of fixed-bed processes.

Introduction. The modeling of fixed-bed processes has been an area of much interest to the chemical engineering profession. However, with the exception of a few specific cases, analytical solutions of the governing differential equations are nonexistent. The intent of this section will be to review briefly the modeling approach for various fixed-bed systems

and to act as a starting point in the development of a model for the fixed-bed process of interest.

The starting point of most fixed-bed models is a differential mass balance performed upon the gas phase. Assuming that there is negligible radial dispersion and that axial dispersion can be modeled by a diffusion-type model, the differential mass balance equation takes the following form:

$$\varepsilon\frac{\delta C}{\delta t} - D\frac{\delta^2 C}{\delta z^2} + V\frac{\delta C}{\delta z} = \bar{R} \quad , \tag{3.14}$$

where

C = concentration of component of interest,

t = time,

z = axial distance,

ε = interparticle void fraction,

D = effective dispersion coefficient,

V = superficial velocity,

$\bar{R}$ = rate of reaction/unit volume.

Upon examining the preceding equation in a term-by-term manner, $\varepsilon\delta C/\delta t$ represents the nonsteady or transient change of concentration with time, $-D\delta^2 C/\delta z^2$ accounts for the effects of longitudinal dispersion (i.e., deviations from true plug flow of the gas phase), and $V\delta C/\delta z$ reflects the effects of net mass flow and the changes in the longitudinal concentration profile upon the differential mass balance. The rate of reaction, $\bar{R}$, is the specific rate at which the component of interest is being generated

(a positive value) or reacted (a negative value) within the element of differential volume.

As one might expect, the great diversity of the solutions to fixed-bed processes results from the many possible forms of the rate equation and the ways in which it is coupled to the capacity of the sorbent or reactant. For the case of sorption on resins, an expression often exists which relates sorbate concentration to sorbate loading on the sorbent. Because of this relationship and the widespread interest in separation processes based upon the sorption characteristics of various solids, considerable effort has been directed toward determining solutions to the mathematic equations of interest. Papers by Schumann, Furnas, Wilke, Rosen, and Rasmuson provide an excellent chronological review of the various stages of model development for these systems.[71-75] In the last paper, an exact solution of a fixed-bed model for diffusion and transient adsorption with longitudinal dispersion is presented. By assuming a linear sorption isotherm, Rasmuson's model accounts for the effects of both internal (intraparticle) and external (interparticle) diffusion of sorbate and longitudinal dispersion effects when represented by a diffusion-type model.

However, when the amount of reactant sorbed or reacted cannot be directly coupled to the solution phase, the following two differential equations must be solved simultaneously:

$$\varepsilon\frac{\delta C}{\delta t} - D\frac{\delta^2 C}{\delta z^2} + V\frac{\delta C}{\delta z} = \bar{R} \quad , \tag{3.15}$$

$$\frac{\delta X}{\delta t} = -(MW/\rho)\bar{R} \quad , \tag{3.16}$$

where

X = mole fraction of solid reacted,

MW = molecular weight of the reactant,

ρ = density of reactant.

The second differential equation results from a mass balance on the solid reactant. For a few cases, the rate equations are such that the two differential equations may be coupled and an analytic solution obtained. However, for most cases, exact solutions are possible only through the use of numerical techniques and a computer.

For gas-solid or liquid-solid reactions, the form of the rate equation is dependent upon (1) the resistances associated with various mass transfer steps, (2) the surface area available for mass transfer, and (3) the geometry and physical properties of the solid. For a shrinking-core-type model (a distinct reaction interface), resistance terms associated with mass transfer may result from reactant or product transfer across the gas film or boundary layer surrounding each particle, mass transfer through the product layer surrounding the unreacted core, and kinetic limitations at the reaction interface. For a porous solid with reaction occurring throughout the solid, the complexity of the rate equation is further increased. A review and derivations of shrinking-core models for various controlling resistances and particle geometries are presented in Appendix M. For additional information, excellent texts by Levenspiel or Szekely, Sohn, and Evans should be consulted.[76,77]

Model formulation. In the preceding section, the controlling partial differential equations for fixed-bed processes were presented. This

section is directed toward the formulation of a model for the CO_2—$Ba(OH)_2 \cdot 8H_2O$ fixed-bed process. Although the fixed-bed data will be presented in a subsequent section, knowledge of the trends in data is used in initial model formulation. The starting point in the model development is the gas-phase mass balance, shown by

$$\varepsilon\frac{\delta C}{\delta t} - D\frac{\delta^2 C}{\delta z^2} + V\frac{\delta C}{\delta z} = \bar{R} \ . \tag{3.17}$$

The extent to which dispersion will affect the removal efficiency of the fixed bed may be estimated. With respect to the preceding equation for a given z value within the bed, $\delta C/\delta t \sim 0.0$, and dispersion effects may be neglected if

$$-D\frac{\delta^2 C}{\delta z^2} << V\frac{\delta C}{\delta z} \ . \tag{3.18}$$

As an approximation, experimental data have indicated that the concentration profile within the fixed bed may be modeled by

$$\frac{C}{C_o} = \exp(-0.5z) \ , \tag{3.19}$$

where z has units of cm. If we were working with uniform, nearly spherical particles, one could calculate the Reynolds number, $d_p V\rho/\mu$, and from a correlation, determine the Peclet number, Vd_p/D. However, for a fixed-bed system of flakes, estimation of a suitable particle diameter is difficult. As pointed out by Carberry, the particle diameter is an estimate of the mixing length.[66] Hence for a fixed bed of flakes, the mixing length would likely be between the nominal and maximum flake dimensions, or 0.1 cm $< d_p <$ 1.2 cm for the system of interest. For an airlike gas stream at ambient conditions and superficial gas velocities of 8 to

21 cm/s, the Reynolds number for mixing lengths of 0.1 to 1.2 cm ranges from 5 to 100. Based upon the correlations of Wilhem as presented by Bischoff and Levenspiel or the study of Edwards and Richardson,[78,79] the Peclet number for these gas velocities would be ~2.0. The corresponding effective dispersion coefficients would then range from 0.40 to 12.6 cm/s. Upon substituting the preceding values into Equation (3.18) and rearranging, one obtains the following:

$$0.03 + 0.30 \ll 1.0 \ . \tag{3.20}$$

Hence this analysis indicates the dispersion contributions will likely be small and as an initial approximation, they are ignored. For the preceding conditions, the calculated effective dispersion coefficients were 6 to 200 times greater than the corresponding effective molecular diffusivity (εD_{CO_2}) for CO_2 in air.

A second area of interest is the form of the rate equation in the overall mass balance. As discussed in the preceding section, the form of the rate equation will be dependent upon (1) the resistances associated with the various mass transfer steps, (2) the external area available for mass transfer, and (3) the geometry and physical properties of the solid. As shown in Figures 3.1 and 3.15, the reactant used in this study is flakelike in nature and upon reacting with CO_2, a shrinking-core phenomenon is observed with respect to the product-reactant interface. The actual area available for mass transfer will be discussed in greater detail in a subsequent paragraph. Assuming that the flakes are of a uniform thickness and may be approximated by infinite-plate geometry, the mass transfer area can be separated from the mass transfer resistance terms in the derivation of the overall rate equations. Such is not the



Figure 3.15. Cross-sectional view of $Ba(OH)_2 \cdot 8H_2O$—$BaCO_3$ flake. Note the sharp product-reactant interface.

case for cylindrical or spherical geometry because the surface area and concentration are both functions of the particle radius. The mass transfer resistances result from component transfer through the gas film, the product layer, and kinetic limitations at the reaction interface. For the reaction of interest,

$$CO_2(g) + Ba(OH)_2 \cdot 8H_2O(s) \rightarrow BaCO_3(s) + 9H_2O(g), \qquad (3.21)$$

it will be assumed that the controlling component will be CO_2 and that the CO_2 concentration is negligible. Furthermore, experimental results have indicated the gas-phase water vapor pressure, hence the driving force for the removal of the water vapor product, does not appreciably affect the mass transfer properties of the process.

To determine the relative extent of control of the various resistances to mass transfer, they may be compared via dimensionless numbers. The corresponding rate equations and resistances for mass transfer are as follows:

Gas film controlling

$\bar{R} = K_F AC$

Ω (Film Control) $= 1/K_F$

K_F = gas film mass transfer coefficient

A = area for mass transfer

Ω = resistance

Diffusion controlled through product layer

$$\bar{R} = \frac{D_{CO_2} \varepsilon AC}{b}$$

$$\Omega \text{ (Diffusion control)} = \frac{b\tau}{D_{CO_2} \varepsilon}$$

D_{CO_2} = CO_2 diffusivity

ε = product porosity

τ = tortuosity

b = thickness of product layer

Kinetic controlled by first-order reaction

$\bar{R} = K_K AC$ $\qquad K_K$ = kinetic rate constant

$$\Omega(\text{Reaction Control}) = \frac{1}{K_K}$$

From a rigorous standpoint, the equation for reactant diffusion through the product layer is not correct. From the reaction stoichiometry, 9 water molecules are released for each molecule of CO_2 that reacts. Hence equimolal flow does not exist, but rather there is a net mass flow outward away from the reaction interface. However, because of the small CO_2 concentrations used in this study (a maximum value of 330 ppm_v), the overall rate and the resulting net mass flow will be extremely small and are therefore neglected.

From the preceding resistance terms, the following dimensionless numbers may be defined.[66]

$$\frac{\Omega\ (\text{Diffusion control})}{\Omega\ (\text{Film control})} = \frac{K_F b\tau}{D_{CO_2}\varepsilon} = \text{Biot number}$$

$$\frac{\Omega\ (\text{Film control})}{\Omega\ (\text{Reaction control})} = \frac{K_K}{K_F} = \text{Damkohler number}$$

$$\frac{\Omega\ (\text{Diffusion control})}{\Omega\ (\text{Reaction control})} = \frac{K_K b\tau}{D_{CO_2}\varepsilon} = (\text{Thiele modulus})^2$$

Experimental studies conducted at 22, 32, and 42°C indicated little (if any) change in reaction rates. If the process were kinetically controlled, a factor of ~2 to 4 increase in reaction rate would have been

predicted. Hence kinetic control does not appear to be a limiting step to mass transfer for this process.

The ratio of mass transfer resistance through the product layer to that through the gas film (in this case, the Biot number), should then provide an indication of the extent of control of each mechanism. Based upon the correlations of Gamson and the interpretation of fixed-bed data from this study in the regime of negligible product diffusional resistance (very low reactant conversion), a gas film mass transfer coefficient of ~0.2 → 1.0 cm/s would be predicted.[80] The diffusivity of CO_2 in air at ambient temperature and pressure is 0.16 cm^2/s.[81] The porosity of the product is 0.73, and because of the high porosity, the tortuosity is assumed to be 1.0. For these studies, the average particle thickness for the flakes is approximately 0.1 cm. Since we are interested in a comparison of the average resistances, the specific Biot number will be integrated over the flake half-thickness to determine the average Biot number.

$$\text{Average Biot Number} = \frac{\int_0^{0.05} (\text{Biot number})db}{\int_0^{0.05} db}$$

$$= \frac{\int_0^{0.05} \frac{K_F b \tau}{D_{CO_2} \varepsilon} db}{\int_0^{0.05} db} \qquad (3.22)$$

$$= \frac{K_F b \tau}{2D_{CO_2}} \Bigg|_0^{0.05}$$

$$= 0.042 \rightarrow 0.21$$

Hence the preceding analysis would indicate diffusion through the product layer to contribute from 4 to 17% of the total resistance. Therefore, this effect is ignored in initial model formulation.

Based upon the preceding analyses, one would predict the differential gas-phase mass balance to be the following:

$$\varepsilon\frac{\delta C}{\delta t} + V\frac{\delta C}{\delta z} = -K_F AC \ , \tag{3.23}$$

with the following boundary conditions:

$$\frac{C}{C_o} = 0 \quad t = 0 \quad z > 0$$

$$\frac{C}{C_o} = 1 \quad t > 0 \quad z = 0$$

The corresponding solid-phase mass balance differential equation and boundary conditions would be

$$\frac{\rho}{MW}\frac{\delta X}{\delta z} = K_F AC \ , \tag{3.24}$$

where

$$X = 0 \quad t = 0 \quad z > 0$$

However, for the system of interest, a major problem exists in predicting the area available to mass transfer because the flakes are of nonuniform thickness or size (Figure 3.9). Unlike spheres for which the contact area is extremely small, the contact area between nonhomogeneous flakes may reduce greatly the area available to mass transfer. Experimental data and correlations for heat and mass transfer with nonspherical particles, in particular for flakes, are limited. After a thorough review of the literature, the correlations of Gamson (1951) were deemed most

applicable. Gamson attempted to account for differences in particle geometry via use of the total external surface area and a shape factor.[82,83] However, because of the nonuniformity of the flakes in the present study and the difficulty in predicting external surface area, even this approach is impractical. Therefore, because of the complexity of the present system, an approximation of the surface area available for mass transfer as a function of conversion will be postulated. The postulated equation will be of the following form:

$$A = A_o(1 - X^n) \ , \tag{3.25}$$

where

A = area available for mass transfer,

A_o = initial area available for mass transfer,

X = average conversion of flakes,

n = exponent.

Precedence for reducing the complexity of a problem via a simple mathematical expression includes the velocity profile approximation by Von Karman in the development of boundary layer theory and the parabolic concentration profile assumed by Liaw, Wang, Greenkorn, and Chao in modeling radial dispersion.[84,85] Upon substituting Equation (3.25) into Equations (3.23) and (3.24), and dividing by the initial concentration, C_o, one obtains

$$\varepsilon\frac{\delta\bar{C}}{\delta t} + V\frac{\delta\bar{C}}{\delta z} = K_F A_o(1 - X^n)\bar{C} \tag{3.26}$$

and

$$\frac{\rho}{MW}\frac{\delta X}{\delta t} = K_F C_o A_o(1-X^n)\bar{C} \ , \tag{3.27}$$

with the boundary conditions:

$$\bar{C} = C/C_o = 1 \qquad z = 0 \qquad t > 0$$

$$X = 0 \qquad z > 0 \qquad t = 0$$

Since the preceding equations are nonlinear, an analytical solution is not possible. However, the equations with their respective boundary conditions may be solved numerically. To simplify the preceding equations, the following change of variables will be made:

$$\Theta = t - \frac{\varepsilon z}{V},$$

$$S = \frac{z}{V} \quad .$$

The equation may be transformed to the new coordinate system by using the following equations:

$$\frac{\delta Q}{\delta t} = \frac{\delta Q}{\delta \Theta}\frac{\delta \Theta}{\delta t} + \frac{\delta Q}{\delta S}\frac{\delta S}{\delta t}, \tag{3.28}$$

$$\frac{\delta Q}{\delta z} = \frac{\delta Q}{\delta \Theta}\frac{\delta \Theta}{\delta z} + \frac{\delta Q}{\delta S}\frac{\delta S}{\delta z}, \tag{3.29}$$

where

$Q = \bar{C}$ or X.

The transformed equations and corresponding boundary conditions are the following:

$$\frac{\delta \bar{C}}{\delta S} = -K_F A_o (1 - X^n)\bar{C}, \qquad \bar{C} = 1 \quad S = 0 \quad \Theta > 0; \tag{3.30}$$

$$\frac{\rho}{MW}\frac{\delta X}{\delta \Theta} = K_F A_o C_o (1 - X^n)\bar{C}, \qquad X = 0 \quad S > 0 \quad \Theta = 0. \tag{3.31}$$

Since the preceding nonlinear partial differential equations are hyperbolic in form, numerical solutions may be obtained via the method of characteristics or the use of a finite difference technique.[86] The finite difference technique was chosen, and the following substitutions were made:

$$\frac{\delta \bar{C}}{\delta S} = \frac{\bar{C}(S+1,\Theta)-\bar{C}(S,\Theta)}{DELS} , \tag{3.32}$$

$$\frac{\delta X}{\delta \Theta} = \frac{X(S,\Theta+1)-X(S,\Theta)}{DELT} , \tag{3.33}$$

where DELS and DELT are the respective finite difference increments in the S and Θ domains. Using the respective boundary conditions $\bar{C}(0,\Theta) = 1.0$ and $X(S,0) = 0.0$, the conversion and concentration profiles were solved as a function of S and Θ. The technique used in this study was to solve the equations for a given Θ value and to increase the S value until the concentration of the reacting species approached zero. The Θ value was then incremented and a new concentration and conversion profile were determined. The importance of the change in variables becomes apparent at this point. Initially, a very short Θ increment is required because of the step change in concentration at $\Theta = 0.0$. However, as this change is damped out, the change in concentration with Θ becomes much slower and the Θ increment may be increased, thus singificantly reducing computer time. Furthermore, as Θ becomes large, the value of $\varepsilon z/V$ will remain small and $\Theta \simeq$ time, t. Without the change in variables, stability problems would have prevented such an increase in the time increment, and the computer time required for a solution would have been increased by 3 to 5 orders of magnitude. A copy of the computer program, a list of

program nomenclature, and a program flowchart are located in Appendix K. Numerical solutions to the controlling partial differential equations will be presented later in this chapter.

Experimental studies. Using air as a feed gas (330 ppm_v CO_2), experimental studies were conducted on 10.2-cm-ID fixed beds of *commercial* $Ba(OH)_2 \cdot 8H_2O$ flakes. The studies were designed to evaluate the effect of water vapor pressure, temperature, and superficial gas velocity upon the operational properties of the bed (most notably, the shape of the CO_2 breakthrough profile and the change in pressure drop across the bed). The range of water vapor pressures corresponded to relative humidities of 25 to 70% at system conditions. Operating temperatures were varied from 294 to 315 K, and superficial gas velocities ranged from 8.5 to 20 cm/s. Due to the endothermic nature of the reaction (364 kJ/mol), the reactor is jacketed so as to ensure near-isothermal operation. For the treatment of an air-based (330-ppm_v-CO_2) gas stream under near-adiabatic conditions, a temperature drop in the gas stream of ~4°C would be predicted. This temperature drop has been experimentally verified. Bed depths were varied from 36 to 51 cm and were chosen to ensure the complete development of the conversion and concentration profiles. Because of the low CO_2 concentration in the influent gas and the time required to reach steady state, a typical run required ~300 h and ~680 to 1160 m^3 (24,000 to 41,000 ft^3) of air, depending upon the bed depth. In most cases, the runs were continued until the CO_2 breakthrough was complete. During the course of these studies, the influent CO_2 concentration was observed to vary. Further analyses indicated the variation to result from the air supply system at Oak Ridge National Laboratory. The system, designed to

supply instrument-grade air with a dewpoint <-40°C, uses sorption beds for water removal. Upon bed regeneration, the beds have an affinity for both H_2O and CO_2, and the CO_2 concentration of the effluent gas is decreased. Once the bed becomes loaded with CO_2, the CO_2 concentration of the effluent gas increases as more strongly sorbed water displaces CO_2 from the bed. Fluctuations in CO_2 concentration were observed. The problem was much more severe during the summer months when the increased water content of the outside air resulted in more frequent bed regenerations. The nominal peak-to-peak time was ~24 h. Therefore, prediction of the actual time of breakthrough was difficult. However, extremely valuable information was obtained based upon the shape of the breakthrough curve.

The existence of an initial induction period with respect to reactant reactivity is a point of debate. For the fixed-bed studies with bed lengths of 36 and 51 cm, the induction effect (if present) was effectively masked out by the bed length. However, differential bed studies with bed depths of 0.6, 1.3, and 2.5 cm were discontinued because of the effects of relative humidity on bed properties and difficulties in the interpretation of the experimental data, possibly a result of an induction phenomenon. Presented in Figure 3.16 is a typical breakthrough curve and pressure drop profile, cross-plotted as a function of time. The breakthrough curve is the familiar S-shaped curve which is characteristic of many fixed-bed processes and may be produced by a number of different mass transfer mechanisms. The change in pressure drop with time is a key parameter for fixed-bed operations and will be addressed in

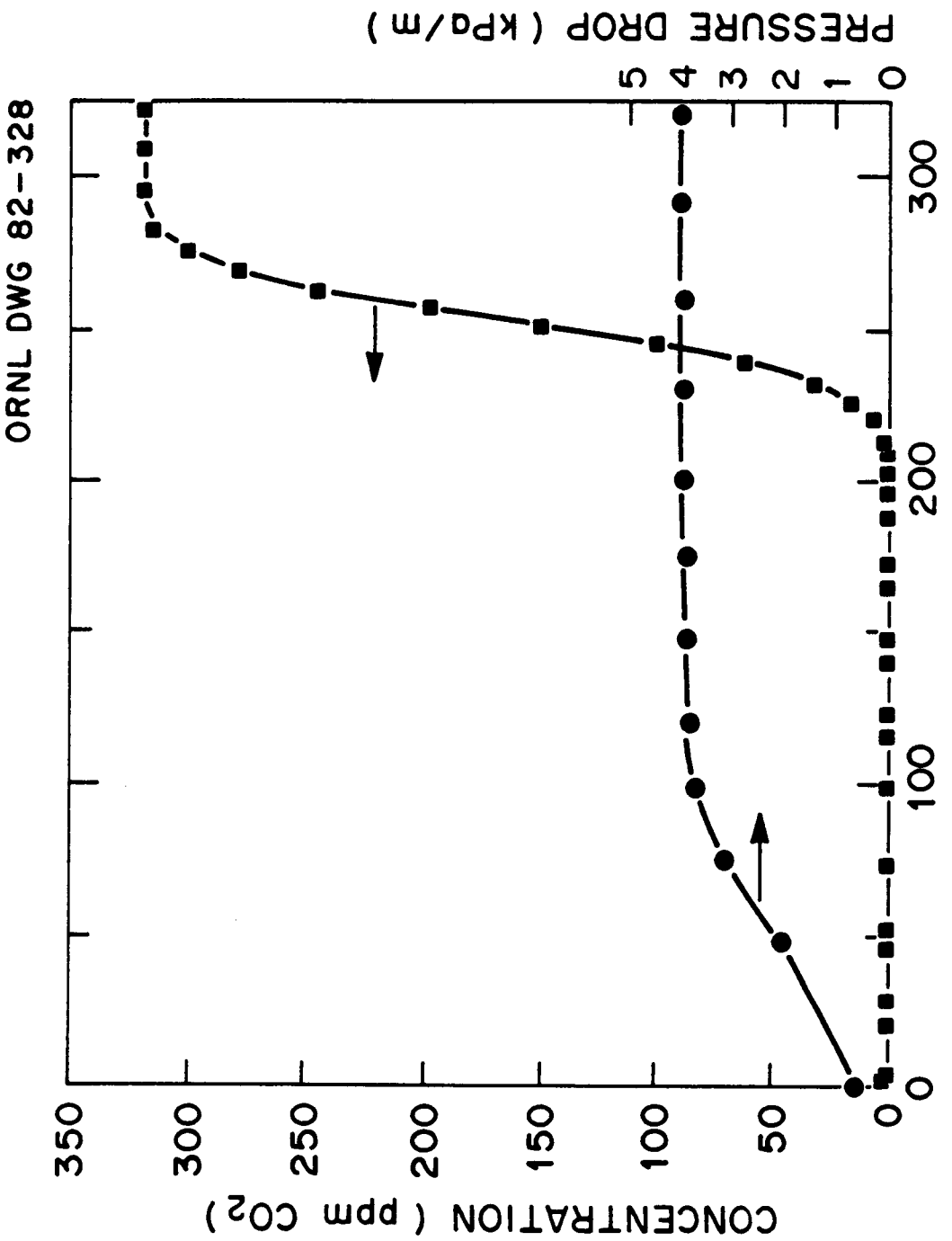


Figure 3.16. A typical breakthrough curve and the change in pressure drop across the bed presented as functions of time.

detail in a subsequent section. It should be noted that the pressure drop did not increase linearly with bed conversion or time.

As described in Chapter 2 under the section "Fixed Bed Experimental Equipment," accurate CO_2 analyses over the 100-ppb_v- to 330-ppm_v CO_2 concentration range were performed routinely. As shown in Figure 3.17, the data in the lower concentration regime may be better displayed by using the logarithm of concentration. Rather than being S-shaped, the breakthrough curve now consists of a linear section to ~80 ppm_v followed by a section of rapid curvature. The significance of these two regimes in analyzing fixed-bed data will be addressed in the next section.

Data analyses and modeling studies.

Introduction. A model for predicting the CO_2 removal properties of a fixed bed of $Ba(OH)_2 \cdot 8H_2O$ was developed earlier in this chapter. The analyses presented there indicated that mass transfer of the reactant through the gas film would likely be the controlling resistance. This discussion will address the applicability of the model. First, the K_FA_o coefficients will be determined from a section of the breakthrough curve. The numerical solutions associated with the controlling partial differential equations in the model will then be presented. The solutions, applicable over the entire breakthrough profile, will be tested against experimental data, and values for the K_FA_o coefficients will be obtained. These values will then be tested against those obtained in the first step.

Determination of the K_FA_o coefficient — Technique No. 1. The controlling partial differential equations were developed earlier in this

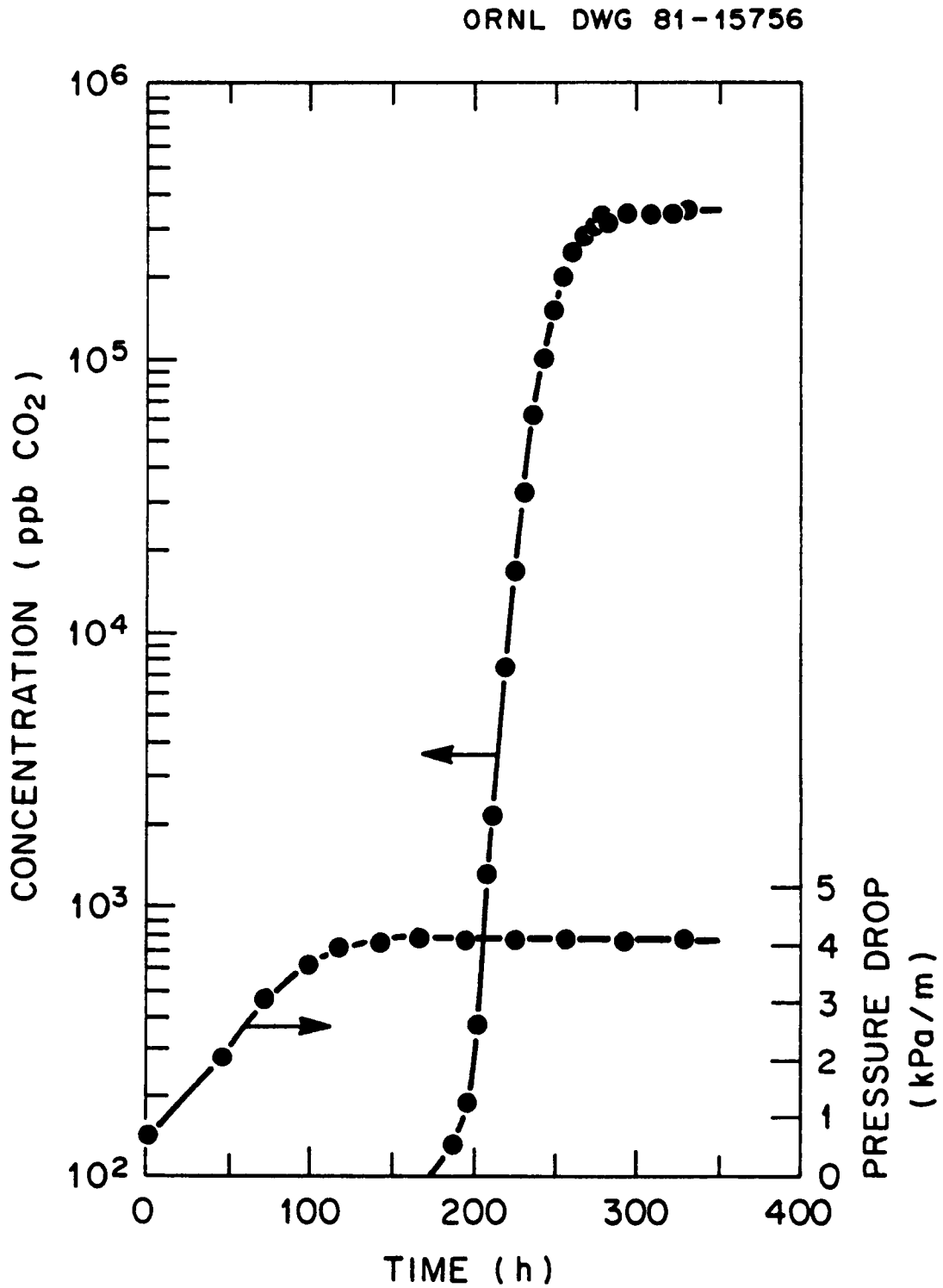


Figure 3.17. Logarithm of the experimental breakthrough profile and the change in pressure across the bed presented as function of times.

work. The corresponding gas and solid differential mass balances are the following:

$$\frac{\delta C}{\delta t} + V\frac{\delta \bar{C}}{\delta z} = -K_F A_o (1-X^n)\bar{C} , \tag{3.34}$$

$$\frac{\partial X}{\partial t} = \frac{MW}{\rho} K_F A_o (1-X^n)C , \tag{3.35}$$

with the boundary conditions:

$$C = C/C_o = 1.0 \qquad z = 0 \qquad t > 0$$

$$X = 0 \qquad z \geq 0 \qquad t = 0$$

In obtaining a solution to the fixed-bed problem, the two equations are coupled by the interfacial area, A, available for mass transfer, which is a function of conversion, X. In the model development, it was assumed that the area may be related to bed conversion as follows:

$$A = A_o(1-X^n) . \tag{3.36}$$

For small conversions, $X \sim 0$, the area becomes a constant, and the differential equations are no longer coupled. Furthermore, as the rate of movement of the mass transfer zone is much less than the superficial gas velocity, a pseudo-steady state exists and $\delta\bar{C}/\delta t = 0$. Therefore, $\bar{C}$ is no longer a function of time, and Equation (3.26) becomes

$$\frac{d\bar{C}}{dz} = -\frac{K_F A_o \bar{C}}{V} , \tag{3.37}$$

with boundary conditions of $C = C_o$ at $z = 0$. The solution to this equation is

$$\ln\bar{C} = \ln\frac{C}{C_o} = -\frac{K_F A_o z}{V} . \tag{3.38}$$

However, in evaluating the concentration profile during breakthrough, one is observing the change in concentration at a given position in the bed, z_o, as a function of time. At this point it will be assumed that upon formation of a developed concentration and conversion profile within the bed, the profile (the developed mass transfer zone) will then advance through the bed essentially unchanged. The validity of this assumption will be established in the next section where numerically derived exact solutions will be presented. Therefore, to determine the concentration profile within the bed from the breakthrough profile, one may define $\bar{V}$, the velocity of the steady state or developed mass transfer zone, in the following way:

$$\bar{V} = \frac{MWVC_o}{\rho}$$

One may then use the following equation to determine the concentration profile within the bed from breakthrough data or vice versa, starting at z_o and t_o:

$$z - z_o = \bar{V}(t-t_o) \ . \tag{3.39}$$

By rearranging and substituting the preceding equation into Equation (3.38), one obtains a model-predicted breakthrough curve for the regime of $X \sim 0.0$,

$$\ln \frac{C}{C_o} = \frac{K_F A_o \bar{V}}{V} t + Q \ , \tag{3.40}$$

where Q is a constant. Furthermore, for a given packing density and molecular weight for the solid reactant and a given inlet concentration

of the gas reactant, the $\bar{V}/V$ term will be a constant. Thus in the regime of low reactant conversion, a plot of the breakthrough curve, ln C/C_o versus t, should be linear. Hence the linear regime discussed in the preceding section may be used to determine the $K_F A_o$ coefficient.

The results of the fixed-bed analyses using this technique are presented in Table 3.14. The values of $K_F A_o$ were then correlated as a function of system parameters, most notably relative humidity or water vapor pressure, temperature, reactant batch number, and gas flow rate. The system pressure at the top of the fixed bed did vary between the runs by ~7 kPa (~1 psig) and was included in the correlation. Furthermore, as the pressure drop across the bed was often appreciable, the average pressure within the bed at the conclusion of the run was used as the system pressure. As may be seen in Table 3.14, little correlation was observed to exist between $K_F A_o$ and relative humidity. This observation was somewhat surprising as a correlation was noted to exist between pressure drop and relative humidity. This factor will be addressed in greater detail in a subsequent section. As would be predicted for gas film control, $K_F A_o$ is a weak function of temperature. No dependency upon reactant batch number was observed. The anticipated dependency of K_F upon system parameters will now be examined.

Based in principle upon the Chilton-Colburn analogy, Gamson used the following equation for correlating mass transfer coefficients obtained on particles of differing geometries in fixed and fluidized beds:[80]

$$j_M = \frac{K_F \rho_G}{G}\left[\frac{\mu}{\rho_G D}\right]^{2/3} = f(\Psi, Re_M) = \frac{A' \psi Re_M^{\ x}}{(1-\epsilon)^y} \quad , \tag{3.41}$$

Table 3.14. Experimental $K_F A_o$ values obtained via two techniques

COM Run No.	Superficial velocity at reference conditions (101.3 kPa, 294.3 K), V_o (cm/s)	Effluent relative humidity (%)	Average temperature (K)	Average pressure (kPa)	Reactant batch No.[a]	$K_F A_o$, s^{-1}	
						Technique No. 1	Technique No. 2
50	8.73	48.5	296.4	104.3	2	5.57	7.0
53	8.89	53.2	303.9	107.2	2	4.49	5.0
52	8.66	54.3	296.3	104.2	2	2.15	3.0
55	9.08	59.1	304.0	110.4	2	4.01	4.0
48	8.65	60.2	296.3	108.1	2	5.45	6.0
57	9.08	62.6	304.0	108.7	2	4.13	5.0
26	12.86	26.1	296.9	108.3	1	6.47	7.0
23B	12.86	34.0	296.6	104.1	1	8.08	9.0
29	12.86	35.2	296.9	102.0	1	6.83	8.0
23A	12.86	36.1	296.3	108.4	1	7.19	8.0
31	13.00	40.2	296.9	107.6	2	8.62	9.0
24	13.04	45.7	304.6	102.1	1	8.38	9.0
25	13.59	45.7	306.8	107.0	1	7.19	8.0
54	13.65	47.8	317.5	105.0	2	7.01	8.0
33	12.93	51.6	295.9	109.2	1	8.20	9.0
20	13.53	53.0	315.5	111.6	1	6.95	8.5
56	14.16	54.8	316.2	106.1	2	6.89	9.0
49	13.94	55.0	305.3	108.6	2	8.44	10.0
28	13.87	55.6	305.0	106.9	1	7.31	8.0
30	13.23	55.6	305.4	106.9	2	6.35	8.0
36	12.95	56.4	296.2	105.0	2	8.14	9.0
37	13.13	60.4	305.4	108.4	2	5.39	6.0
41	13.02	60.2	297.9	112.5	2	8.92	10.0
39	12.97	62.2	304.8	111.6	2	8.68	7.0
32	13.45	64.5	306.4	110.0	2	6.59	7.0
40	13.88	63.3	305.2	111.0	2	5.51	6.0
42	14.71	70.7	304.6	120.8	2	6.47	7.0
35	21.0	53.4	299.7	111.9	2	10.18	10.0
44	21.9	60.6	295.2	104.1	2	17.43	18.0
46	17.5	61.2	295.5	106.9	2	5.45	8.0
45	18.5	66.4	296.1	127.3	2	10.54	10.0

[a] Batch stoichiometry: No. 1 $Ba(OH)_2 \cdot 7.5H_2O$; No. 2 $Ba(OH)_2 \cdot 7.0H_2O$.

where

K_F = gas film mass transfer coefficient, length per unit time;

ρ_G = gas density;

G = mass flow rate/unit cross-sectional area;

μ = viscosity;

D = diffusivity;

ψ = shape factor;

Re_M = modified Reynolds Number, $G/(\Psi A\mu)$;

A = area/unit bulk volume;

A' = 17 for Re_M <10, = 1.46 for Re_M >100;

x = -1.0 for Re_M <10, = -.41 for Re_M >100;

ε = bed voidage;

y = 0.2.

Thus the form of the rate equation is

$$\overline{R} = K_F AC. \tag{3.42}$$

A more in-depth analysis of the analogy between momentum, heat, and mass transfer via the Reynolds and Chilton-Colburn analogies will be presented later. The preceding equation is unique in that it can be applied to systems of differing particle geometry. The shape factors for fixed and fluidized beds are presented in Table 3.15 and were determined from experimental data.

Frequently, the Reynolds number for j-factor correlations on spheres is defined as d_pG/μ, where d_p is the sphere diameter. It can be shown for spherical geometry and for equivalent bed voidage that this Reynolds number is proportional to Gamson's modified Reynolds number for spheres. Furthermore, Gamson's correlation predicts the functional dependency on

Table 3.15. Particle shape factors for uniform packing

Particle shape	Ψ
Spheres	1.00
Cylinders	0.91
Flakes	0.86
Raschig rings	0.79
Partition rings	0.67
Berl saddles	0.80

Source: B. W. Gamson, "Heat and Mass Transfer, Fluid-Solid System," *Chem. Eng. Prog.* 47(1), 19 (1951).

bed voidage to be weak. Hence j-factor correlations obtained on spheres may be used for predicting mass transfer coefficients on particles of differing geometries. With respect to the j-factor correlations, considerable variation in the magnitude of the various coefficients has been reported by experimental investigators. This variation will be addressed in greater detail later in this chapter.

An area of potential confusion are the terms effective diameter and sphericity, which are often used in the reaction of solids. The effective diameter, d_p, is defined as the diameter of a sphere with the same volume as the particle of interest. The sphericity factor, ϕ, is the ratio of the surface area of the sphere of diameter d_p to the surface area of the actual particle.[56,82,83] Hence

$$A = \frac{\text{Area of particle}}{\text{Volume of particle}}(1-\varepsilon) = \left[\frac{4\pi r_p^2}{\phi}\right]\left[\frac{3}{4\pi r_p^3}\right](1-\varepsilon) ,$$

$$= \frac{6(1-\varepsilon)}{\phi d_p} . \qquad (3.43)$$

Therefore, as cited in the previous paragraph (ϕ = 1 for spheres, and ε = constant),

$$Re_M = \frac{G}{A\mu} = \frac{d_p G}{6\mu(1-\varepsilon)} \alpha\ Re = \frac{d_p G}{\mu} \quad . \tag{3.44}$$

For particles that are nearly spherical, the use of the effective diameter and the sphericity factor enables solutions obtained for spherical reactants to be used as approximate solutions, thus reducing the complexity of the overall problem.

Assuming (1) $D \alpha T^{3/2}/P$, $\mu \alpha T$, and $\rho \alpha P/T$ where P and T are the absolute pressures and temperatures;[81] and (2) a relatively small change in the absolute temperature of the experimental data (~3%), the preceeding j-factor equation can be rearranged in the following manner:

$$K_F \alpha \frac{G}{\rho G}\left[\frac{\rho_G D}{\mu}\right]^{2/3} \left(\frac{G}{\mu}\right)^X$$

$$K_F \alpha A\frac{T}{P}\left[\frac{P}{T}\frac{T}{P}^{3/2}\frac{1}{T}\right]^{2/3}\left[\frac{G}{T}\right]^X \tag{3.45}$$

$$K_F \alpha \frac{GT}{P}^{1/3}\left[\frac{G}{T}\right]^X$$

$$K_F \alpha \frac{G^n}{P}\ T^m \approx \frac{G^n}{P} \alpha \frac{P_0}{P}\ V_0{}^n$$

where V_0 is the superficial velocity at reference conditions, 101.2 kPa and 294.3 K (1 atm, 70°F, noted by subscript 0). The functional effect of pressure is retained because of a variation of ~20% in the experimental pressures. The assumption is made that A_0, the area available for mass transfer, at zero conversion is a constant. Therefore,

$$K_F A_o \propto K_F \propto \frac{P_0 V_0^n}{P} \quad . \tag{3.46}$$

Assuming P to be the average system pressure, correlation of the preceding experimental data (Table 3.14, technique No. 1), for gas velocities up to 15 cm/s resulted in the following expression:

$$K_F A_o = K_1 \frac{P_0}{P} V_0^{1.16} \quad . \tag{3.47}$$

The data and the fitted model are presented in Figure 3.18. Data at greater flow rates were of limited quantity and displayed much greater variance in the $K_F A_o$ values. Therefore, these data were not used in the correlation. Presented in Figure 3.19 is the dispersion of the fitted values from the actual data. It is interesting to note that for these flow velocities, the dispersion was not a strong function of V_0, the superficial velocity at reference conditions.

For this study, the modified Reynolds number as defined by Gamson was varied from ~40 to 90. As cited by Gamson,[80] Carmon noted that for mass transfer in a fixed bed of spheres, a transition zone, from laminar to turbulent flow, existed for $20 < Re_M < 100$. A similar transition in the present system could help to account for the dispersion in the data. This dispersion phenomenon will be addressed in greater detail in the final section of this chapter.

From the $K_F A_o$ data presented in Table 3.14, an estimation of the gas film mass transfer coefficient, KF, may be made. Assuming infinite flat-plate geometry (negligible area from the sides of the flakes) and an interparticle porosity of 0.46, the transfer area-per-unit volume may be represented by the following equation:

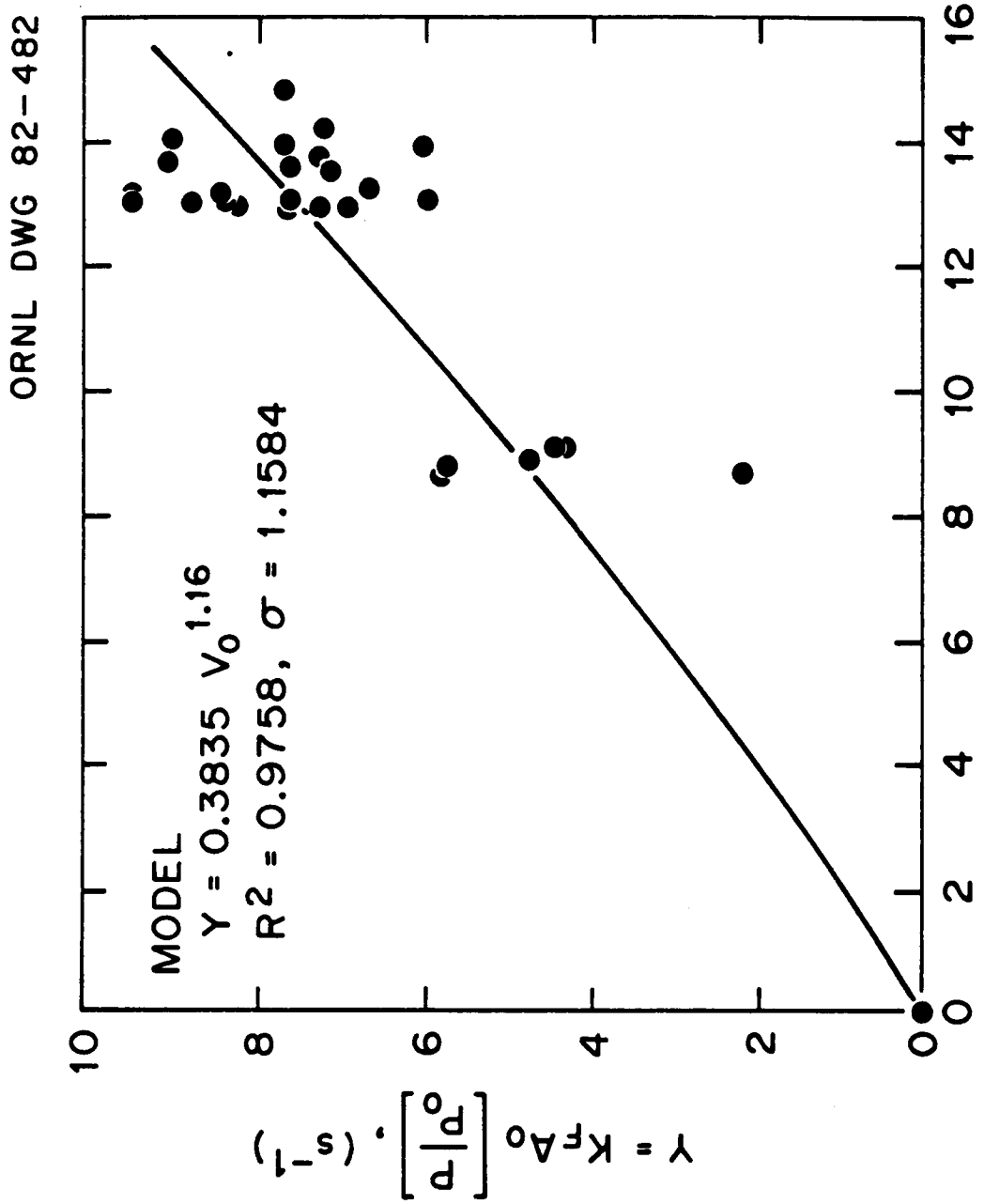


Figure 3.18. Correlation of $K_F A_o$ data obtained via technique No. 1 with model, $K_F A_o = K_1 P_o V^{1.16}/P$.

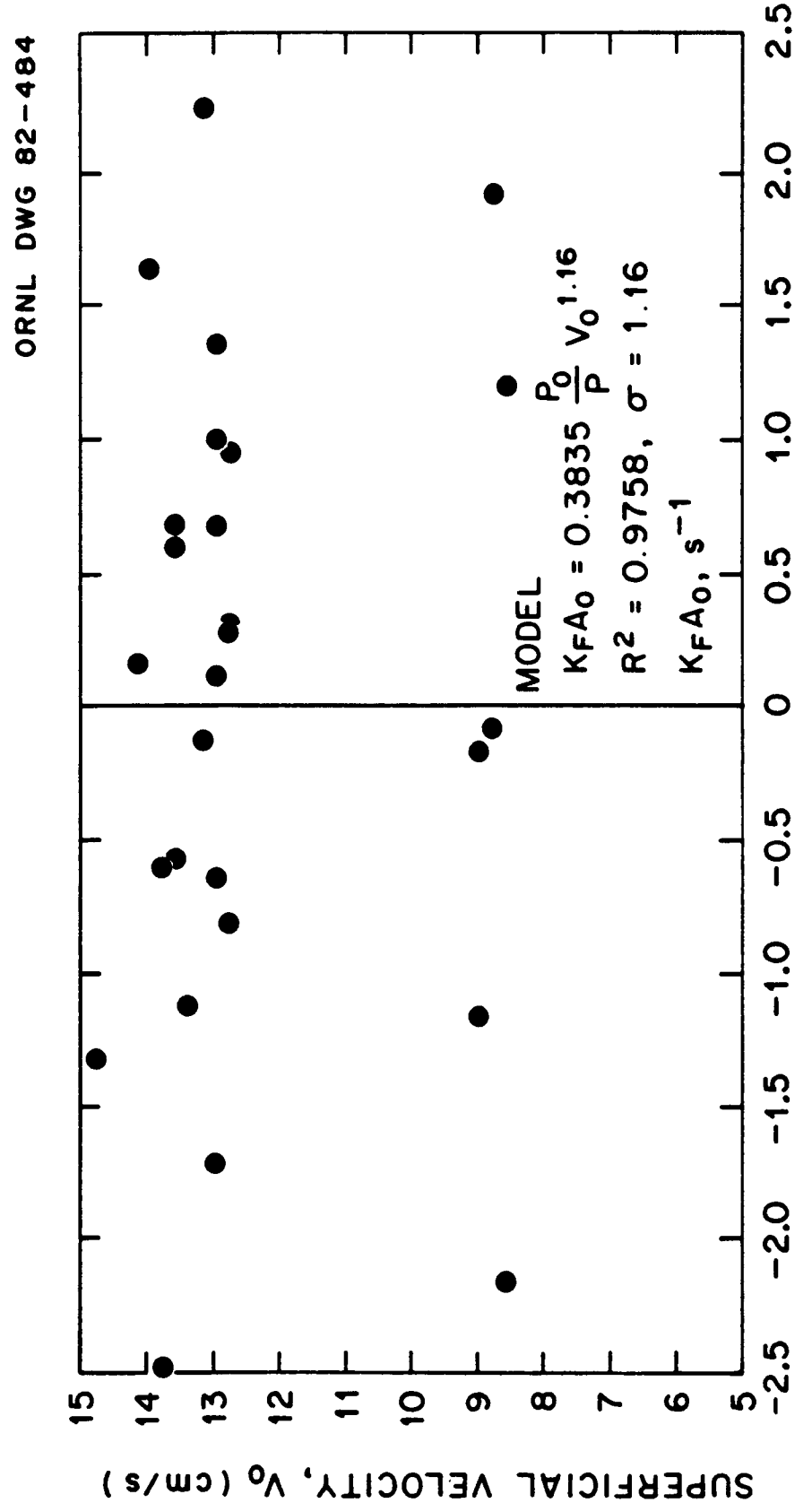


Figure 3.19. Residuals of model correlation of data obtained via technique No. 1.

$$A_o = \frac{\text{Area}}{\text{Bed volume}} = \frac{2(1-\varepsilon)}{b_0} , \qquad (3.48)$$

where

ε = interparticle porosity, ~0.46,

b_0 = flakes thickness.

Assuming an average particle thickness of 0.1 cm (0.05 in.), the predicted value of A_o is 10.8 cm^2/cm^3. Hence for a superficial velocity of ~13 cm/s, this order-of-magnitude calculation indicates a modified K_F value of ~0.7 cm/s. The correlation by Gamson predicted a modified K_F of 1.0 cm/s. Hence the experimental values are reasonable for film mass transfer coefficients at the conditions studied. Gamson's flake data were based upon the dissolution of flakes of 2-napthol in water.[87]

Determination of the $K_F A_o$ Coefficient — Technique No. 2. Using the finite difference equations developed earlier in this chapter, numerical solutions for the postulated model were obtained. Because of the form of the partial differential equations, stability was not a significant problem in obtaining solutions. Convergence to the correct values was assured by decreasing the step size in both planes, S and Θ, until there was negligible effect on the final solution. The ΔS increment ($S = z/V$) chosen for these studies was either 0.0035 or 0.0070 s, depending upon the value of the $K_F A_o$ coefficient. The development of the concentration profile as a function of Θ ($\Theta = t - \varepsilon z/V$) may be broken into two regimes. The first is the rapid development of a concentration profile within the bed, resulting from the step change in dimensionless concentration from 0 to 1 at $S = 0$ and $\Theta = 0$. Upon the development of this profile,

additional changes will be much slower and will be associated with the development of the conversion profile and subsequent advancement of the mass transfer zone as the bed is depleted. The initial $\Delta\Theta$ increment was 0.00015 s. Upon the development of the concentration profile within the bed resulting from the step change, the increment was increased to 10.0 s.

Subsequent analyses of breakthrough curves will indicate that excellent correlation between the model and the experimental data may be obtained when the area available for mass transfer is modeled as a linear function of conversion,

$$A = A_o(1-X) \quad . \tag{3.49}$$

Using this equation and assuming a $K_F A_o = 6.0 \ s^{-1}$ and a system temperature and pressure of 295.3°K and 1.04 atm, respectively, the development of the concentration and the logarithm of the concentration profile as a function of S and distinct values of Θ was determined and is presented in Figure 3.20. In a similar manner, the development of the conversion profiles is presented in Figure 3.21. In obtaining these solutions, the dimensionless concentration profile in the S-plane was determined to a lower concentration of $1 \cdot 10^{-6}$, whereupon it was assumed to be zero. Further reduction of this value had negligible effect upon the concentration or conversion profiles in the regimes of interest. Presented in Figure 3.22 are the developed concentration and conversion profiles for differing $K_F A_o$ coefficients. For large values of Θ, Θ reduces to t, the time. Therefore, upon the development of the dimensionless concentration and conversion profiles within the bed, the profiles then advance through the bed essentially unchanged. Furthermore, the concentration and conversion profiles within the bed are essentially identical.

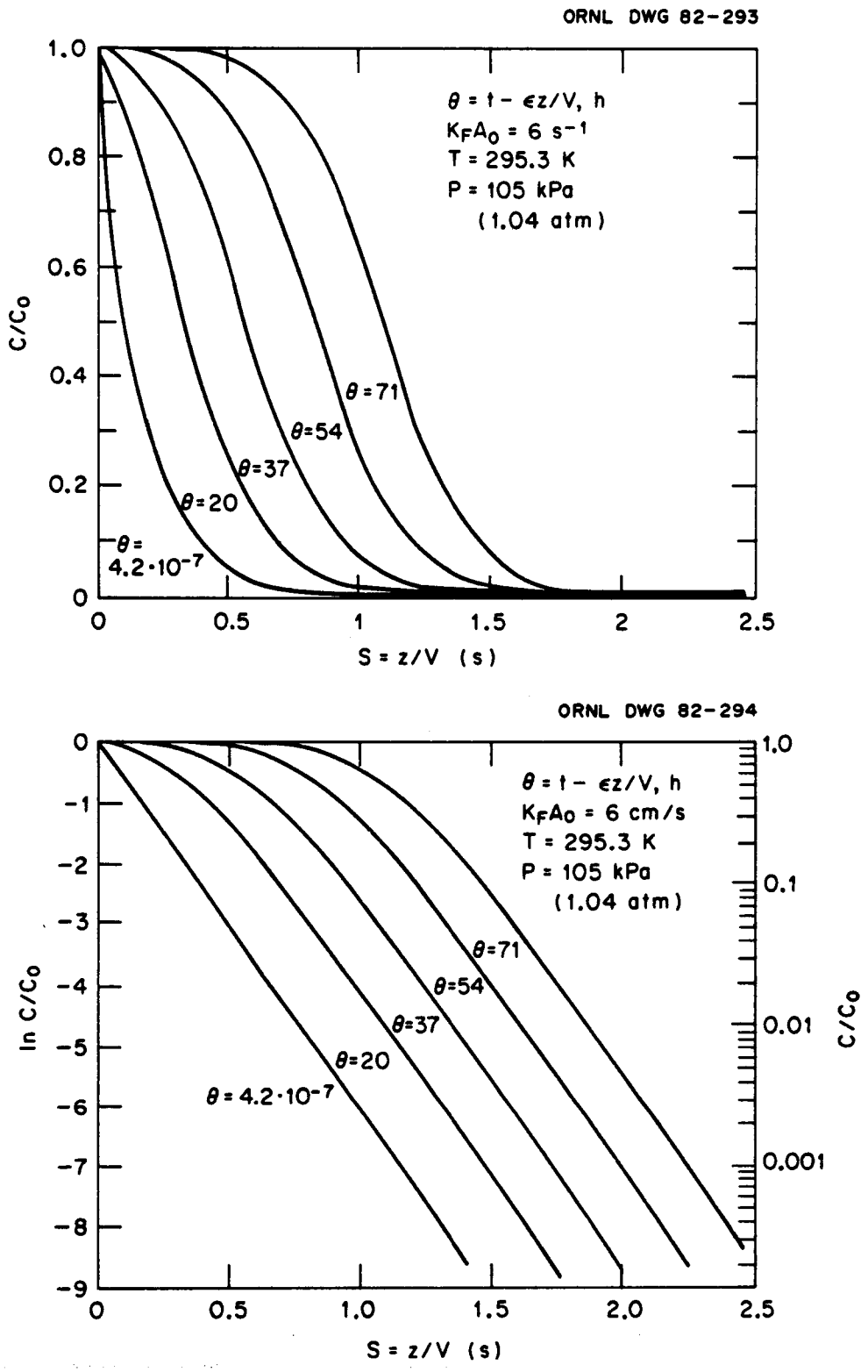


Figure 3.20. Development of the concentration and the natural logarithm of the concentration profile as a function of Θ and S.

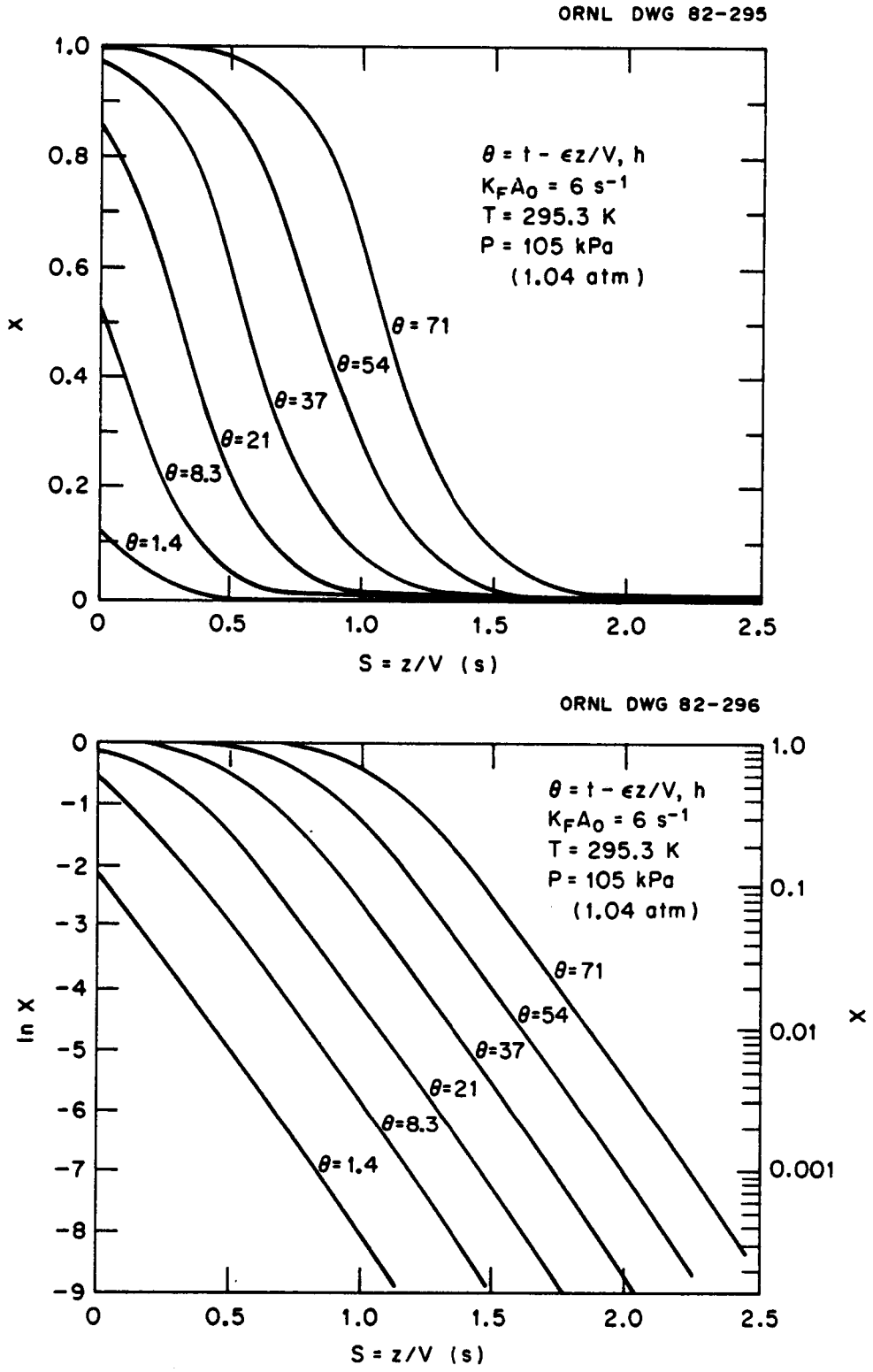


Figure 3.21. Development of the conversion and the natural logarithm of the conversion profile as a function of Θ and S.

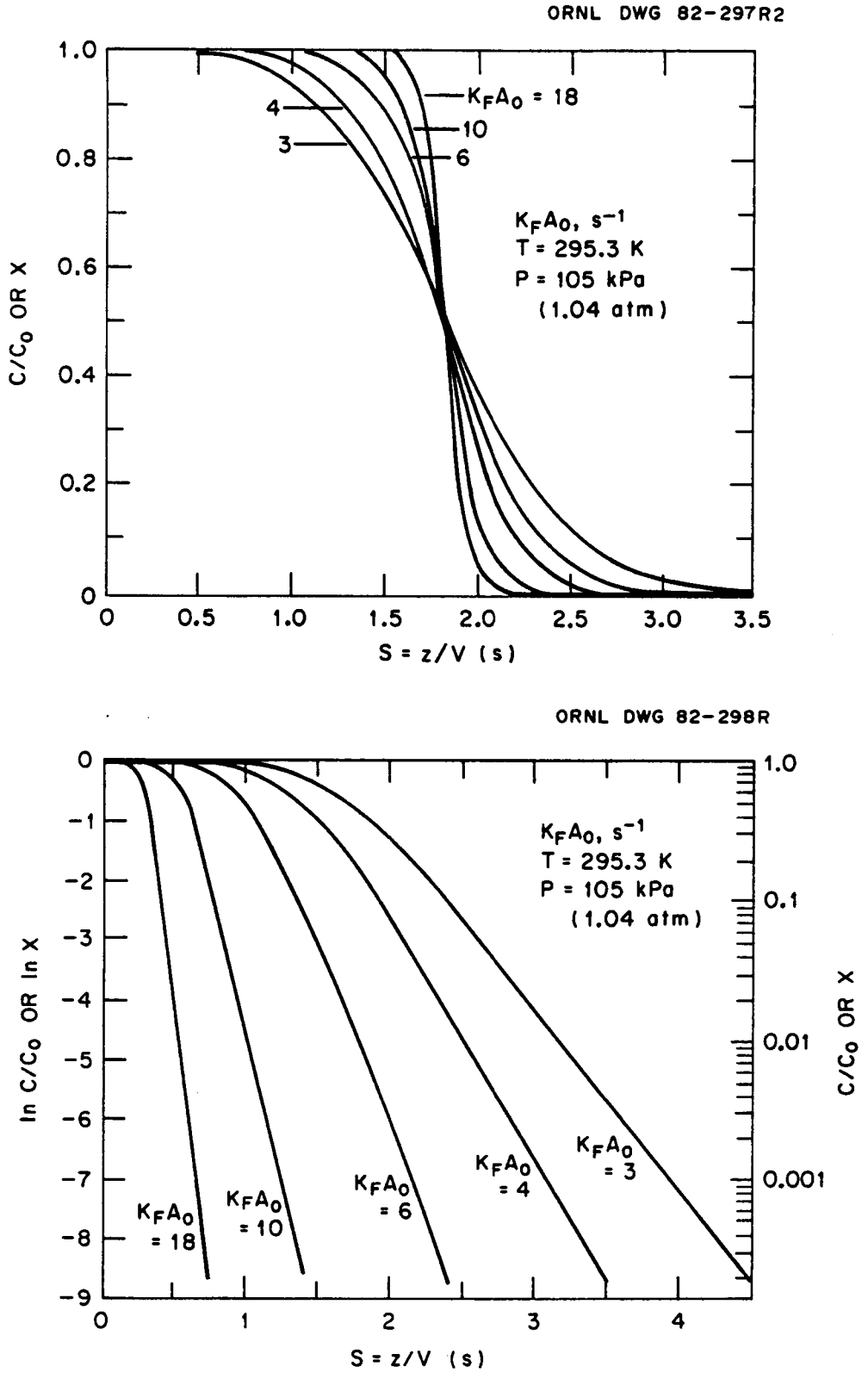


Figure 3.22. Developed concentration or conversion and natural logarithm of development concentration or conversion profile as a function of the $K_F A_0$ coefficient and S.

By transforming the developed concentration profile from the S-plane to the z-plane (multiplication by V) and using the relationship developed in the preceding section [Equation (3.35)] for converting a concentration profile within the bed to a breakthrough profile at a given z position, one can obtain a model-predicted breakthrough curve. Presented in Figure 3.23 are a series of model-predicted breakthrough curves for various K_FA_o coefficients. Because of the terms involved in the preceding transformation, the resulting shape of the breakthrough curve is independent of gas velocity for a given K_FA_o value. The functional dependancy of velocity appears only in the magnitude of the K_FA_o coefficient. For the case of transforming the conversion profile from the S- to z-plane, the resulting profile within the bed is a linear function of velocity because the S values are multiplied by velocity in the transformation. In essence, increasing the gas velocity will increase the length of the mass transfer zone, but if the K_FA_o coefficient is not a function of velocity (an invalid assumption), no change in the breakthrough curve is predicted. Figure 3.24 indicates the predicted conversion profiles under conditions for which the profile is fully developed and a superficial gas velocity of 13 cm/s.

Previously, the assumption was made that the area available for mass transfer was a linear function of conversion. Presented in Figure 3.25 are the results of a sensitivity analysis performed on the following equation:

$$A = A_o(1-X^n) \ , \qquad (3.50)$$

where n = arbitrary exponent. In general, the curvature of the breakthrough curve becomes sharper as $X \rightarrow 1.0$, and n becomes larger. The

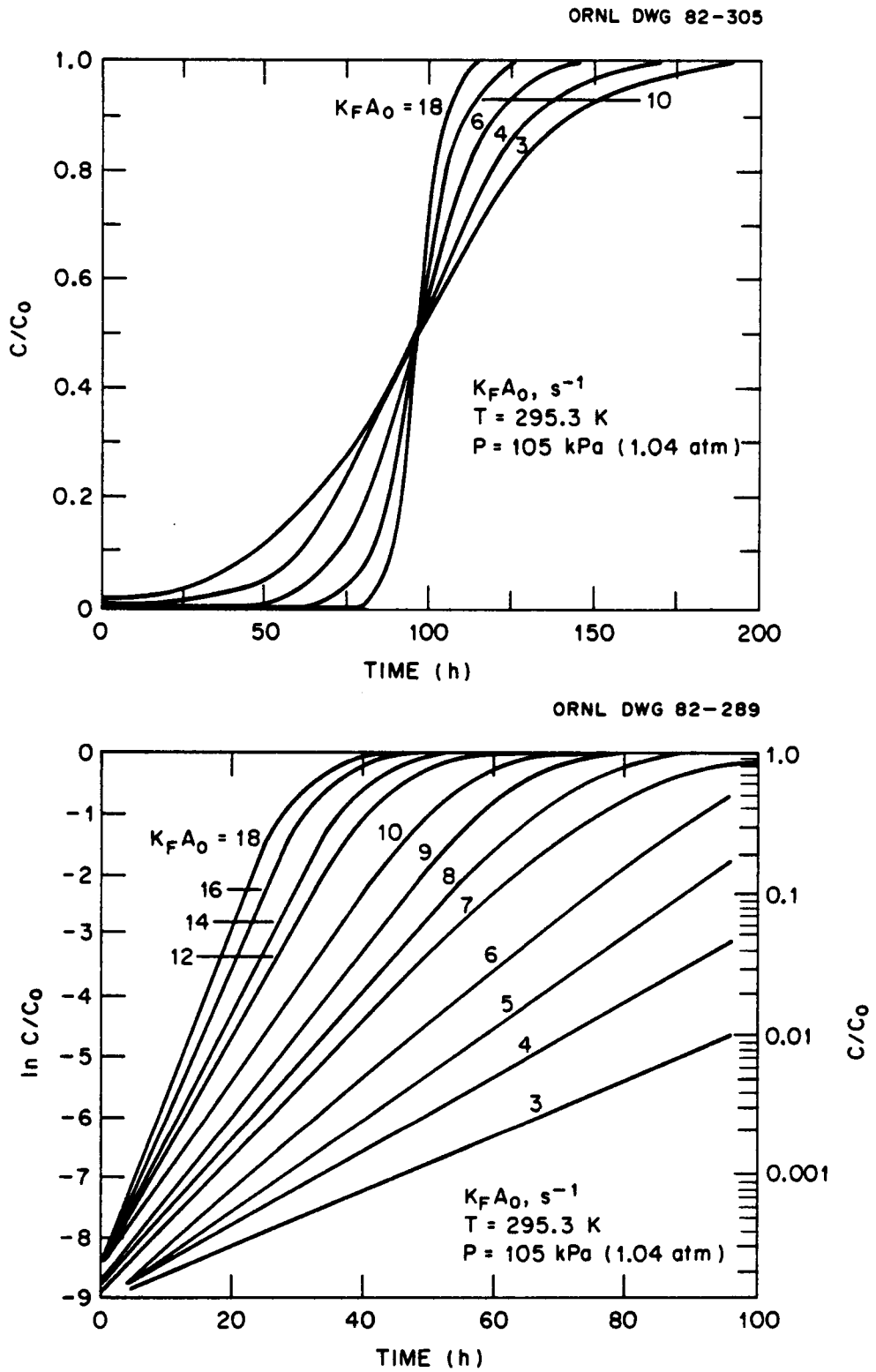


Figure 3.23. Developed breakthrough and the logarithm of the developed breakthrough profile as a function of the K_FA_0 coefficient and time.

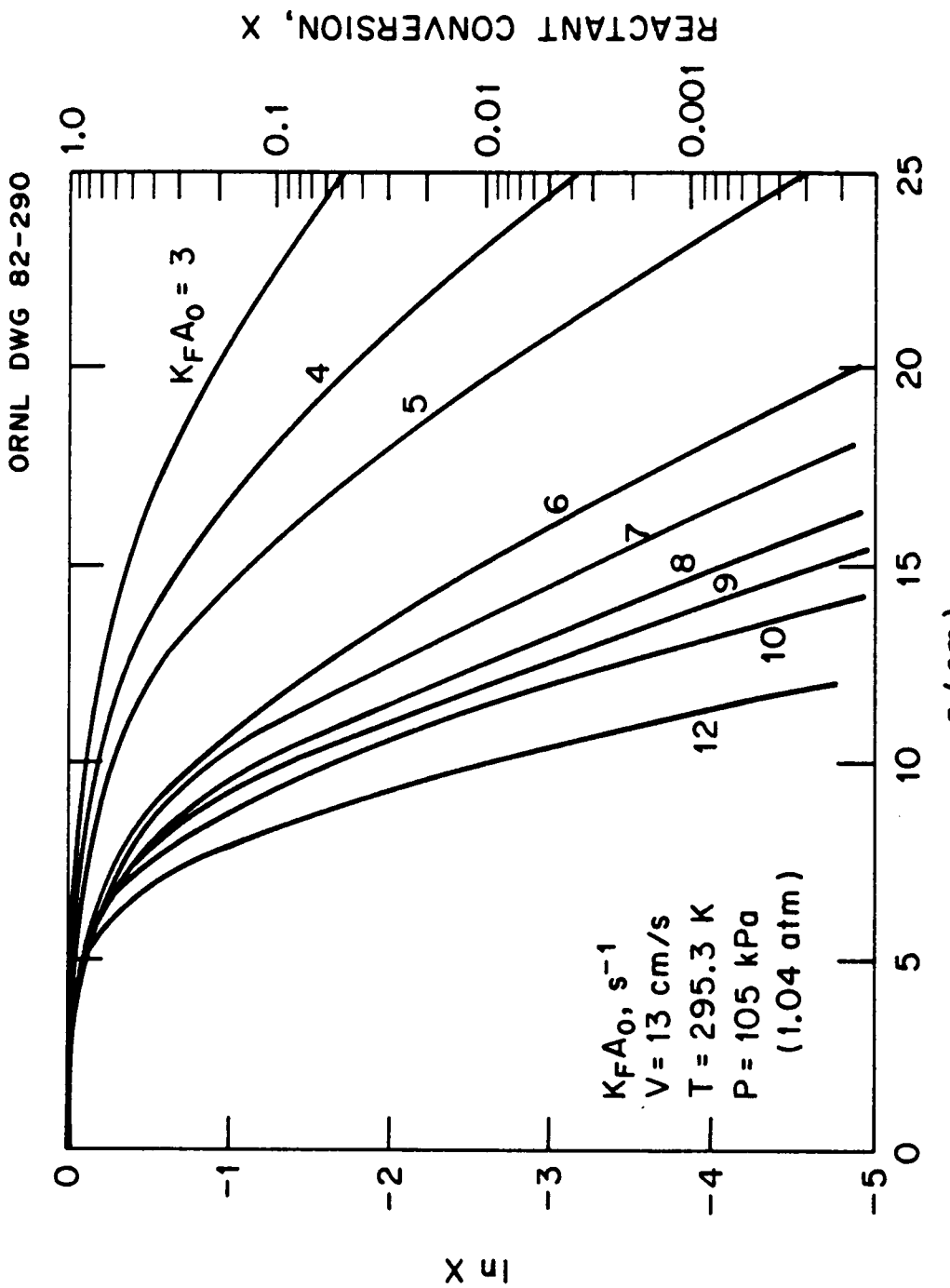


Figure 3.24. Natural logarithm of the developed conversion profile as a function of the K_FA_0 coefficient and axial distance for a superficial gas velocity of 13 cm/s.

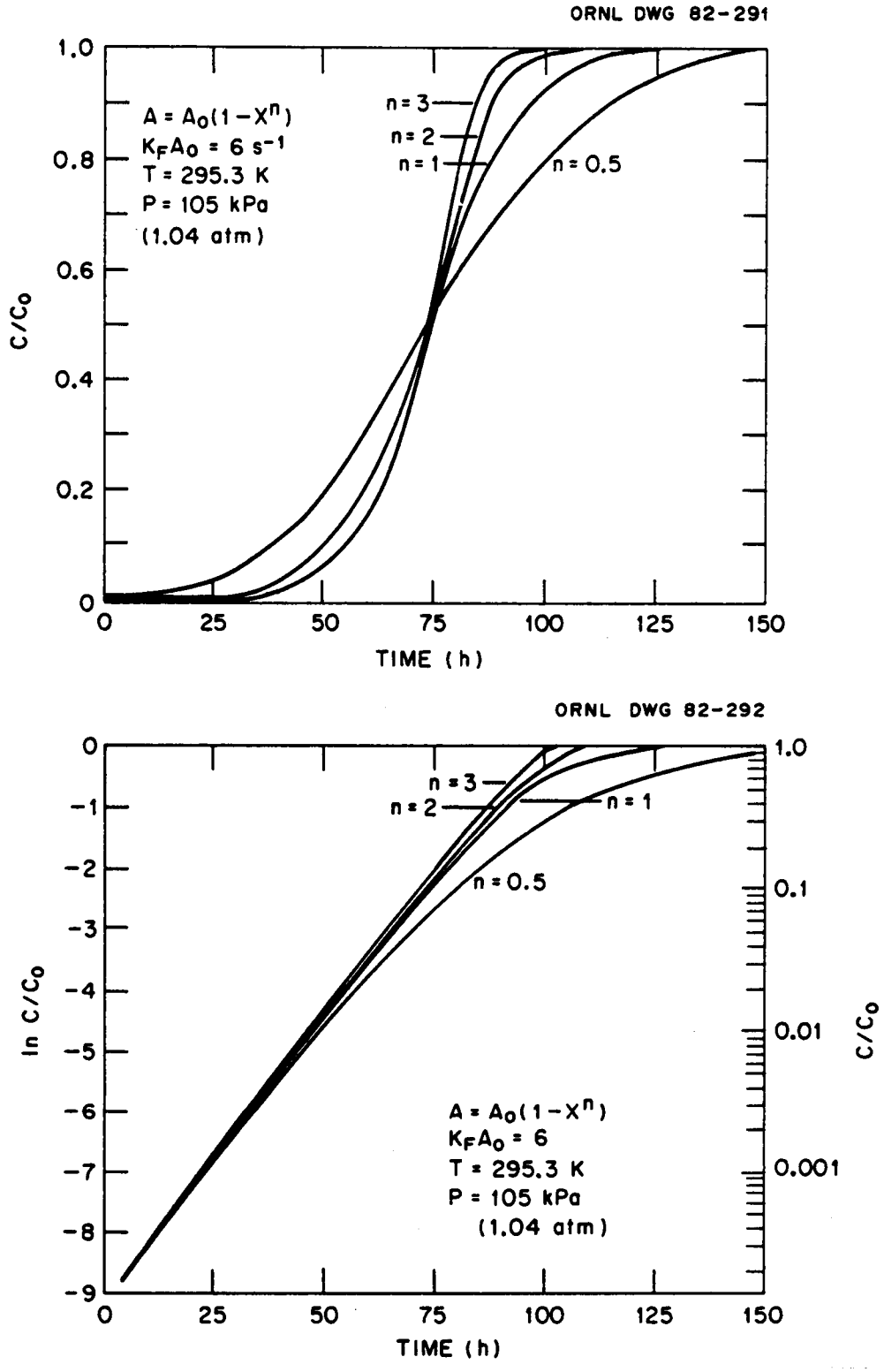


Figure 3.25. The effect and the natural logarithm of the effect of the exponent in the area (A) term upon the developed breakthrough profile.

choice of n = 1 provided the best correlation between the model and the experimental data.

Although the correlation for predicting mass transfer area as a function of conversion is empirical in nature, the question arises as to what physical significance can one attach to the correlation. It must be remembered that the correlation not only models the functional effect of conversion upon transfer area, but it also helps to account for deviations between the assumed model and the actual physical system. Most notable among the model assumptions are the lack of a resistance term associated with mass transfer through the porous product layer and the absence of significant amounts of axial dispersion and channeling. Assuming that these and other neglected effects contribute very little to the overall process mechanism, the correlation will not be examined to see if indeed physical significance can be attached to it.

Assuming that the flakes, which are of variable thickness, may be modeled by infinite flat-plate geometry, following the analysis for predicting the available area as a function of flake thickness, b_0, may be performed:

$$A = A_o(1 - X)$$

$$X = \frac{\int_0^{b_0} A db_0}{\int_0^{\infty} A db_0} \tag{3.51}$$

$$\frac{A}{A_o} = 1 - \frac{\int_0^{b} A db_0}{\int_0^{\infty} A db_0}$$

A solution to this equation is $A/A_o = \exp(-Kb)$, where K is a constant. Upon substitution into the preceding equation, an identity is obtained, thus validating the solution. That the area available for mass transfer can be modeled by an exponential function of flake thickness is not physically consistant and not too surprising since exponential functions are commonly observed in nature. However, it must be remembered that if the assumptions to this point are valid, the exponential dependancy of A with respect to b_0 may be only an approximation to the exact solution, which might be a function of a Gaussian distribution.

$$\frac{A}{A_o} = 1-C_2 \int_0^b \exp[-C_1(b_0-\bar{b})^2]db_0 \ , \qquad (3.52)$$

where b is the average particle thickness, and C_1 and C_2 are constants. The incorporation of such improper integrals and other complicated functions into the actual development of the model is often not justifiable because of the increased difficulty and complexity in extracting a solution. Such was judged to be the case for the present study.

Since temperature and to a lesser extent pressure were variables in this study, a sensitivity analysis of the effects of changes in these variables was conducted, and the results are presented in Figures 3.26 and 3.27. Although the breakthrough curves were off-set from one another, the general shapes were unchanged. Thus model-predicted breakthrough curves obtained for operating conditions of 295.3 K and 1.04 atm were used for the other temperatures and pressures encountered in this study.

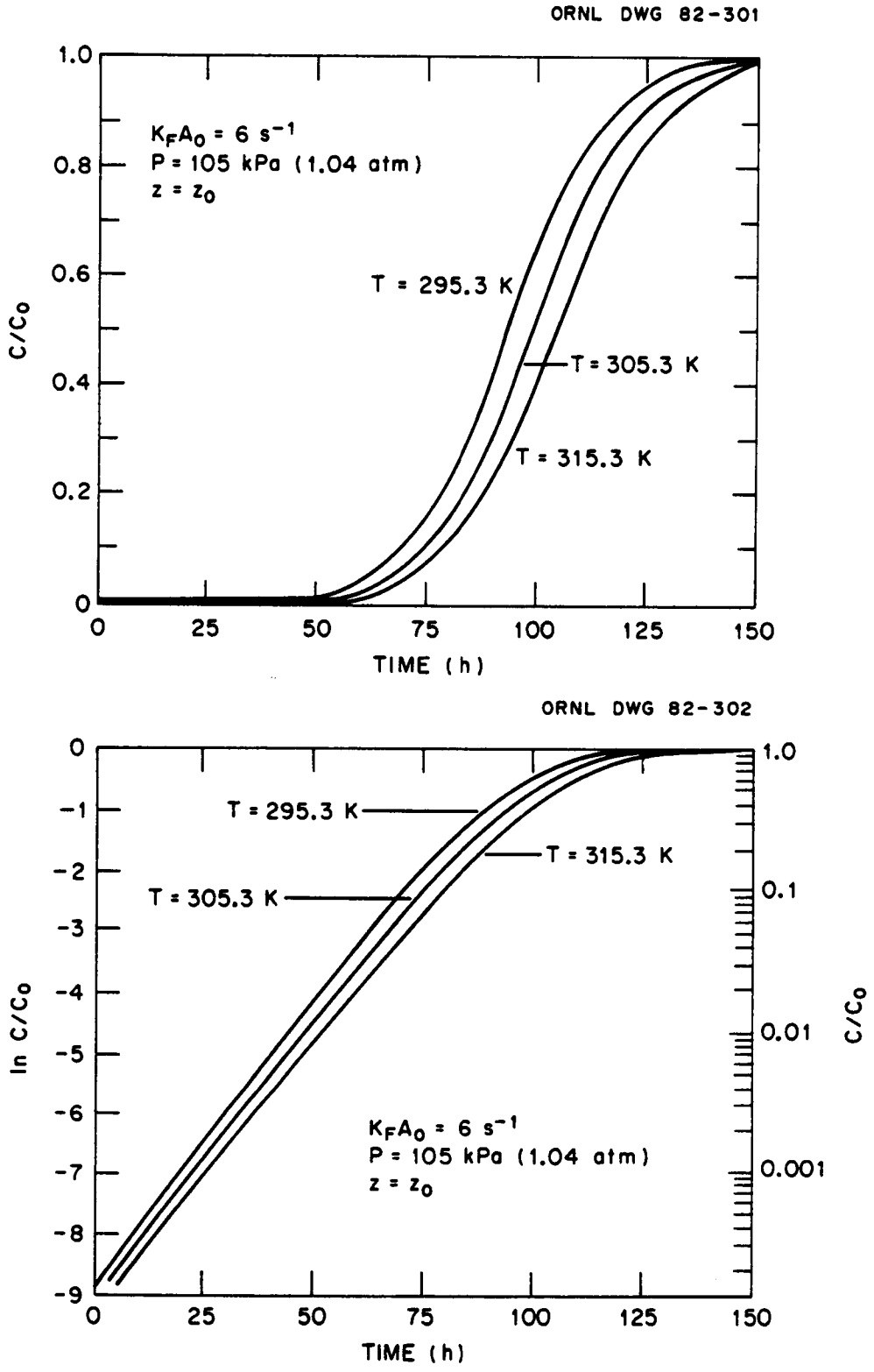


Figure 3.26. The effect and the natural logarithm of the effect of temperature upon the developed breakthrough profile.

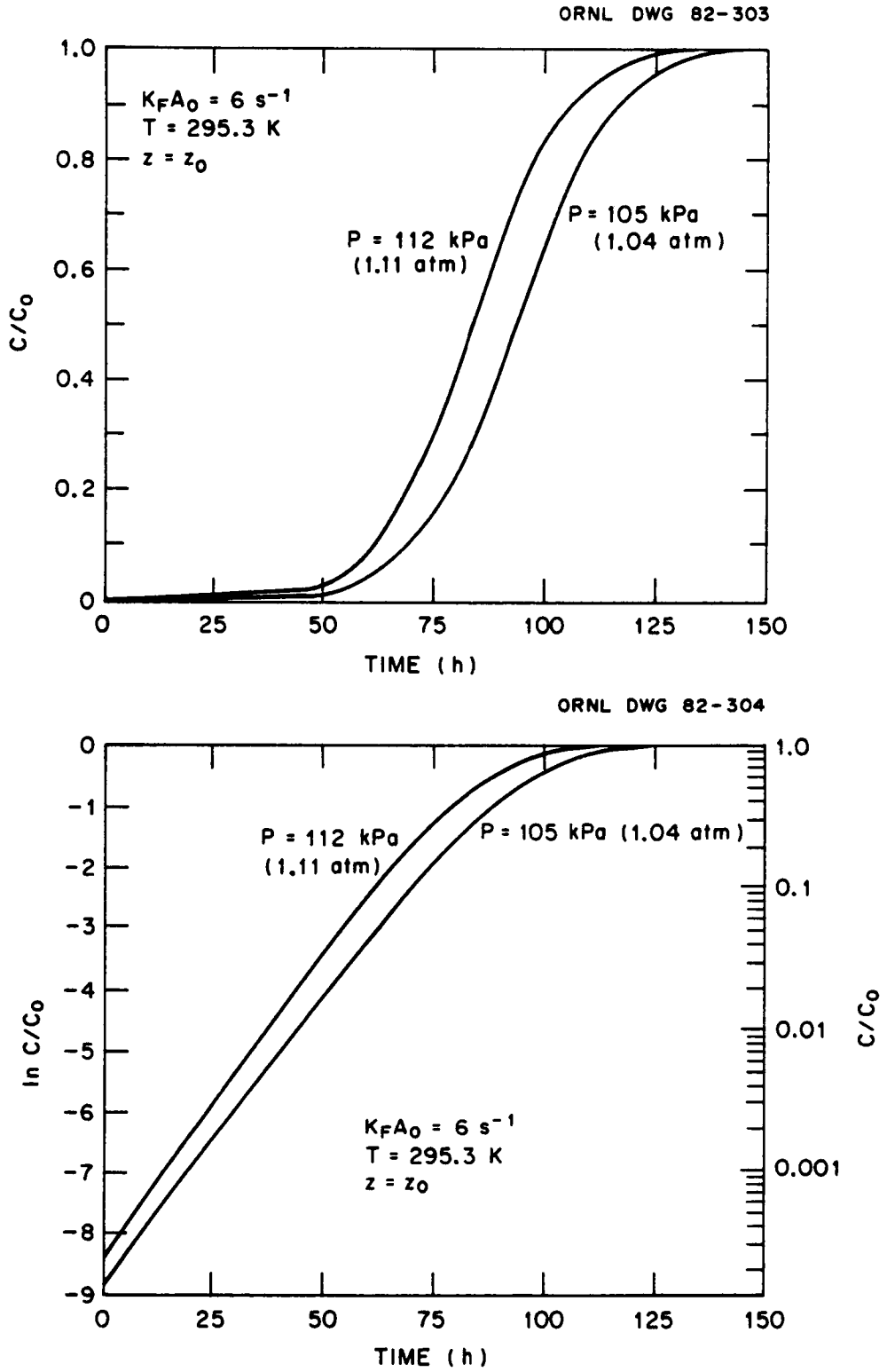


Figure 3.27. The effect and the natural logarithm of the effect of pressure upon the developed breakthrough profile.

Specifications for the $Ba(OH)_2 \cdot 8H_2O$ flakes indicated a bulk density of 1.04 g/cm^3 and a reactant stoichiometry of $Ba(OH)_2 \cdot 7.0H_2O$ to $Ba(OH)_2 \cdot 7.9H_2O$. Presented in Figure 3.28 are the effects of variations in the hydration stoichiometry (i.e., changes in reactant molecular weight) for a fixed bulk density. Little change is observed in the shape of the breakthrough curve; the major effect is a shift in the time of the breakthrough. Indications based upon mercury porosimetry studies (reported earlier in this chapter), show that upon hydration to $Ba(OH)_2 \cdot 8H_2O$, the molecular weight to bulk density values for various hydration stoichiometries would be approximately equal. In this case, no effect upon the shape or time of the breakthrough curve would be anticipated.

Values for the K_FA_o coefficients based upon the entire breakthrough curve were obtained by overlaying the model-predicted breakthrough curves on the actual experimental breakthrough curve and determining the modified mass transfer coefficient, K_FA_o, which best correlated the data. The experimental and model-predicted breakthrough curves are presented in Appendix N. In general, the fit was excellent. The data from this analysis are tabulated and presented in Table 3.14. Comparison of K_FA_o values obtained via the two techniques indicated the latter values to be ~10% greater than the values obtained when using only the linear portion of the breakthrough curve. It is speculated that the bias results from extension of the analyses in the former case into the nonlinear regime. The effect of process variables upon these data was evaluated in a manner similar to that use in the preceding section, and the results were very similar. The K_FA_o coefficients were determined to be weak functions of

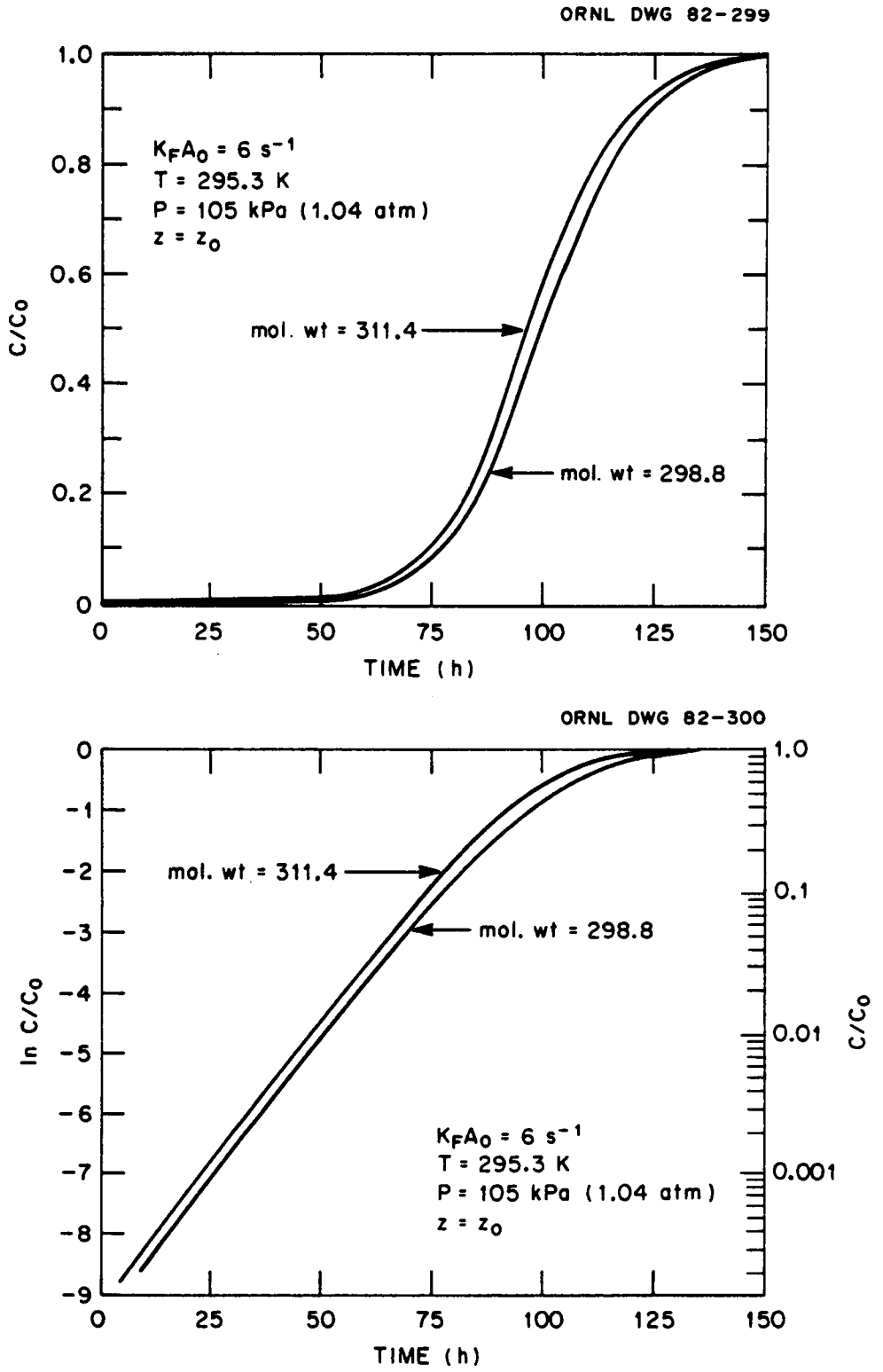


Figure 3.28. The effect and the logarithm of the effect of reactant molecular weight upon the developed breakthrough profile.

relative humidity, water vapor pressure, batch number, and temperature. When modeling the data for superficial velocities up to 15 cm/s, the correlation was also very similar to that obtained in the preceding section (Figure 3.29),

$$K_F A_o = K_1 \frac{P_0}{P} V_0^{1.11} \quad . \tag{3.53}$$

The dispersion of the data from the fitted value was essentially independent of gas velocity (Figure 3.30) over the velocity range examined. The researcher also cited greater confidence in the analysis technique at the lower gas velocities.

Determination of $K_F A_o$ via the conversion profile. To develop a better understanding of the process, a typical fixed-bed run was terminated after the development of the concentration and conversion profiles, but prior to breakthrough. Samples were taken at 2.5-cm (1-in.) intervals in the bed, and the extent of conversion was determined via acid-base titration and $Ba(OH)_2 \cdot 8H_2O$ thermal decomposition (data shown earlier in this section). Using the model-predicted conversion profiles, a mass transfer coefficient was determined (Figure 3.31). Although the predicted $K_F A_o$ of 5 s^{-1} is less than expected, the result is not unreasonable because of the dispersion observed in determining mass transfer coefficients at similar conditions.

Pressure drop during fixed-bed operation.

Introduction. Knowledge of the pressure drop associated with the flow of a fluid through a packed bed is beneficial in determining acceptable operating conditions and in developing a better understanding of

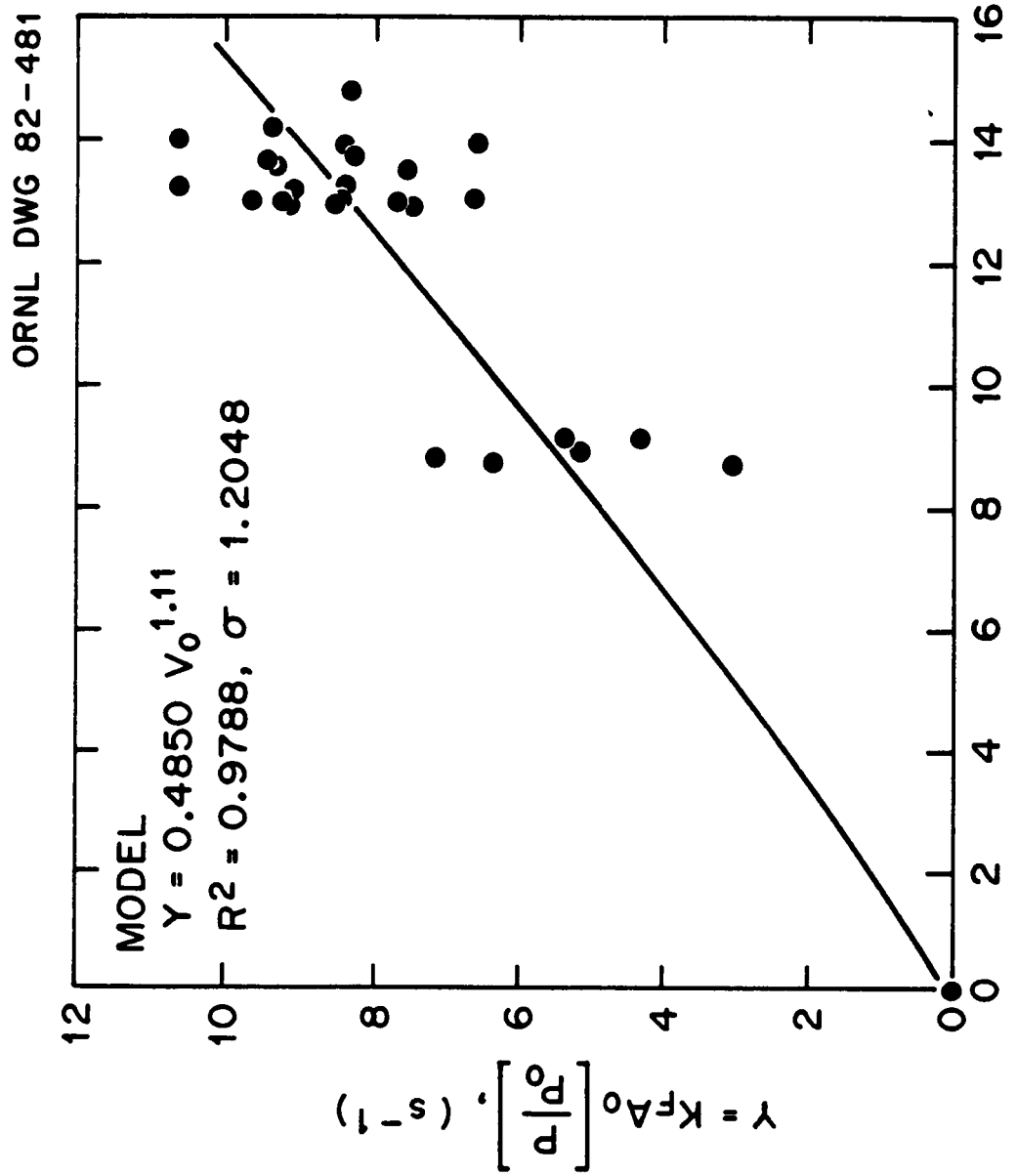


Figure 3.29. Correlation of $K_F A_o$ data obtained via technique No. 2 with model, $K_F A_o = K_1 P_o V^{1.11}/P$.

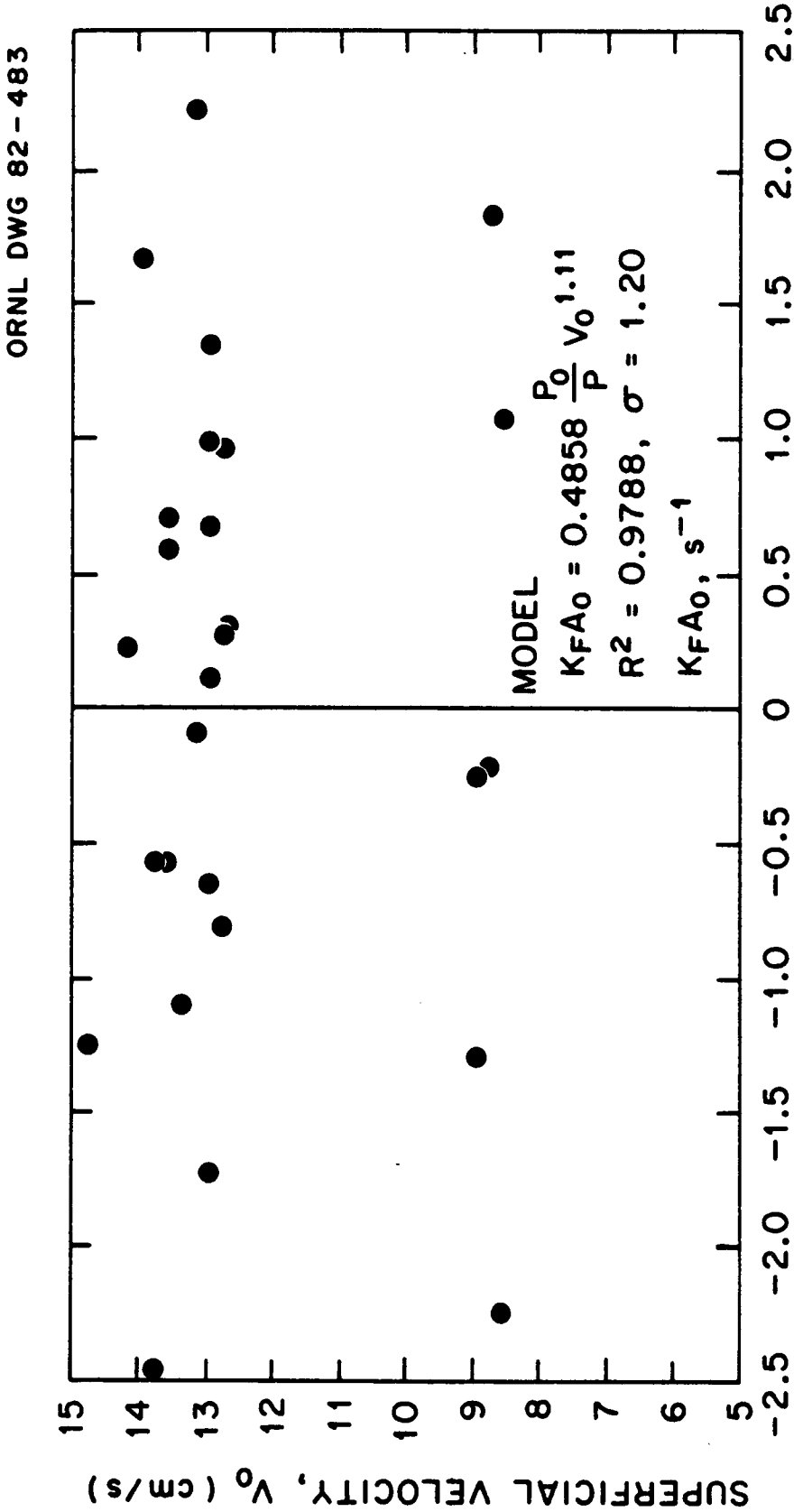


Figure 3.30. Residuals from model correlation of data obtained via technique No. 2.

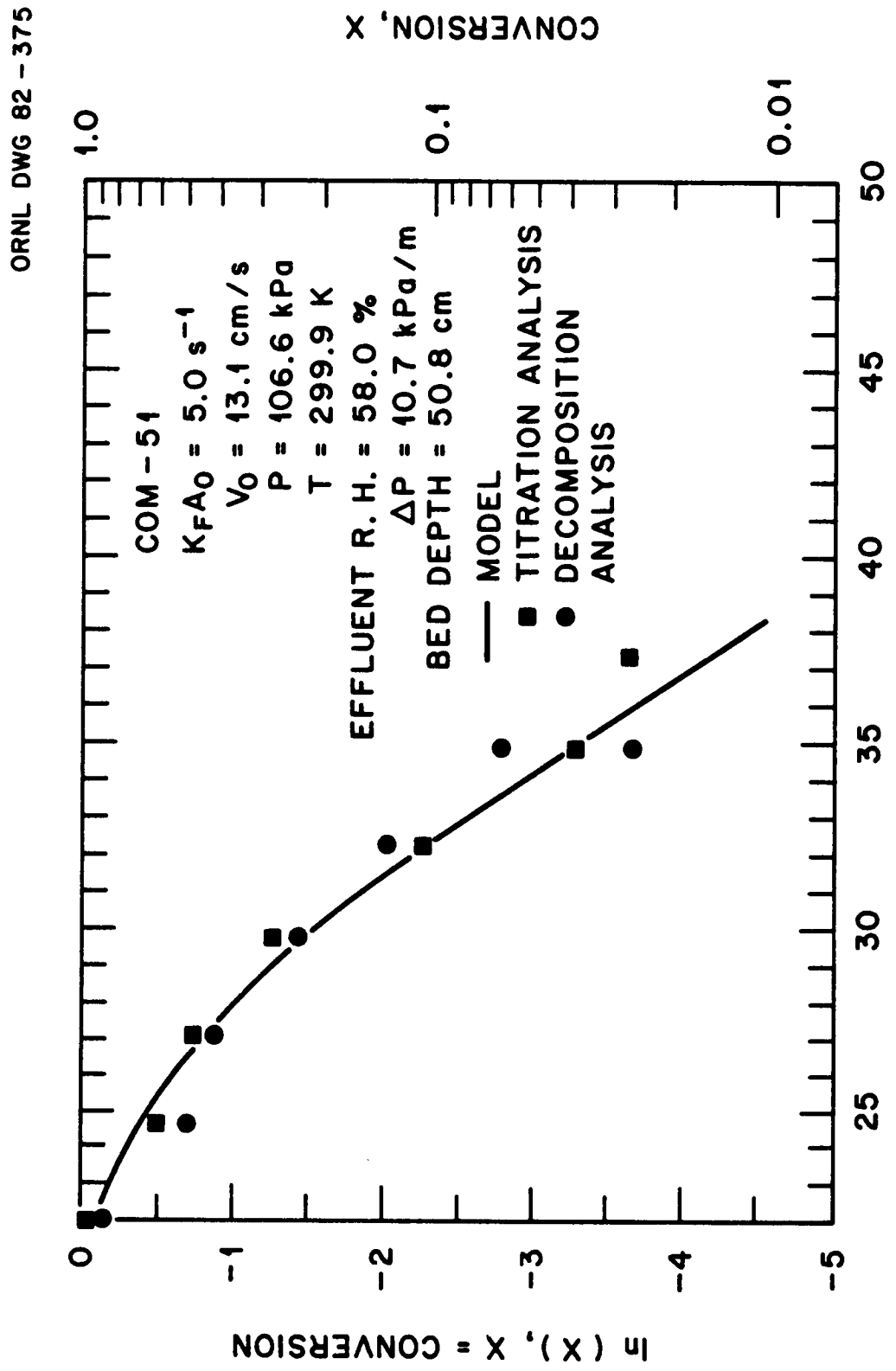


Figure 3.31. Conversion and model-predicted conversion profiles.

the transfer processes. The first portion of this section will be directed toward the determination of suitable operating conditions for the fixed-bed system and to develop correlations for predicting pressure drop as a function of system parameters. The second portion will address the significance of the analogy between momentum and mass transfer in the system of interest.

Pressure drop—operational characteristics. In the development of this fixed-bed process, it was observed that for a given mass throughput, certain process conditions resulted in a greater pressure drop than others. In several instances, the increase in pressure drop during a run behaved in an autocatalytic manner and necessitated discontinuation of the run. The increase in pressure drop appeared to result from two phenomena: (1) a slow gradual increase that was a function of bed conversion, and (2) a rapid increase that was a function of relative humidity. The magnitude of the latter often overshadowed the former. The observed pressure drop plotted as a function of relative humidity at two temperatures, 295 and 305 K, and a superficial velocity of ~13 cm/s is presented in Figure 3.32. It is significant that the data are consistent at the two temperatures since the saturation vapor pressures differed by a factor of 1.8. The dependency upon relative humidity indicates the presence of a surface adsorption phenomenon. Physical adsorption on surfaces (addressed extensively earlier and to be discussed again in Appendix G) is dependent upon the extent of saturation, P/P_0, or in the case of water, the relative humidity. Furthermore, the fact that the pressure drop becomes more severe at ~60% relative humidity indicates that capillary condensation is likely present. Because no hysteresis was observed during nitrogen

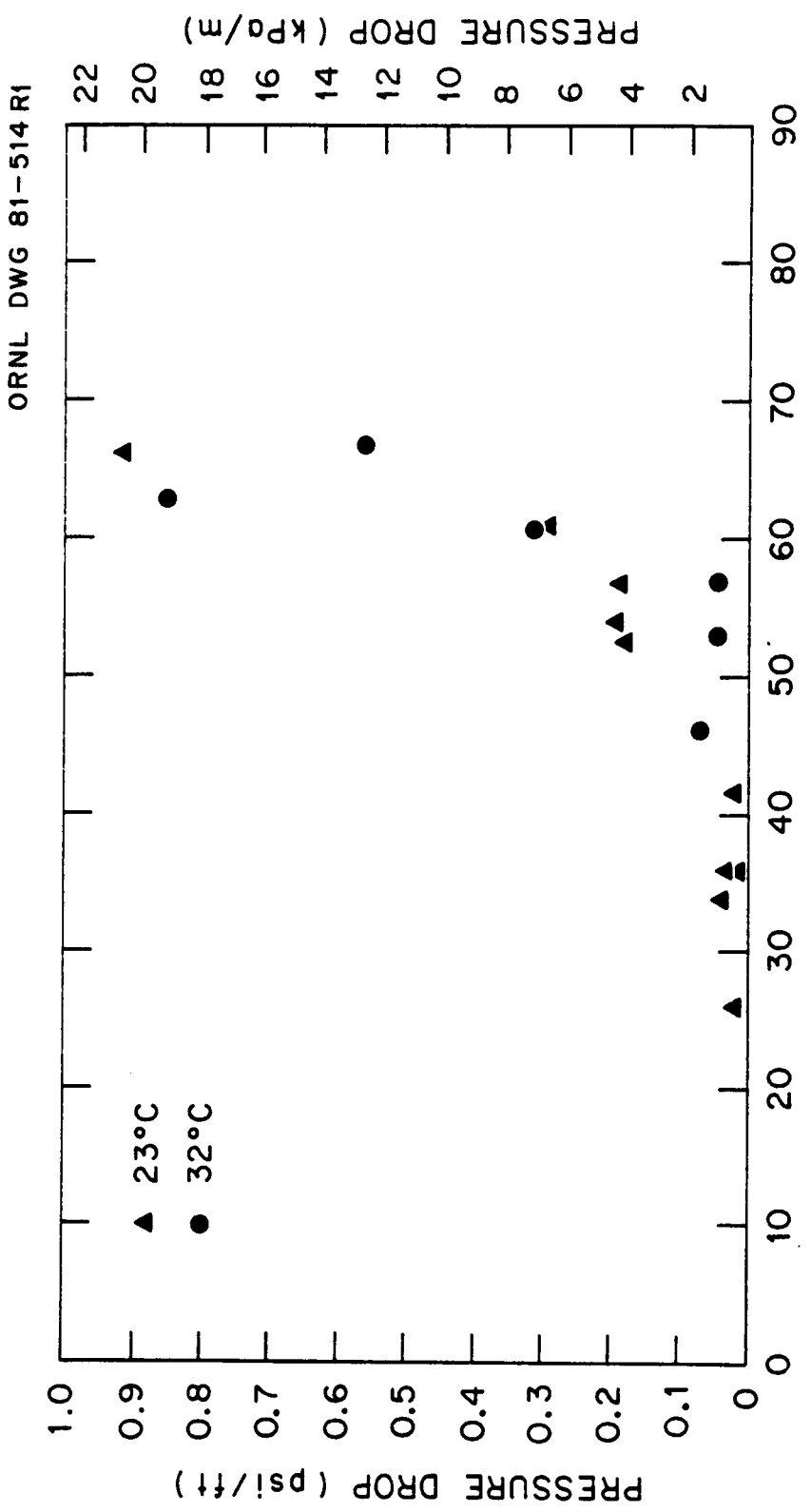


Figure 3.32. Pressure drop as a function of relative humidity during fixed-bed studies on *commercial* $Ba(OH)_2 \cdot 8H_2O$ flakes, reference superficial gas velocity of ~13 cm/s.

adsorption studies, it is speculated that the condensation occurs in V-shaped contact points or pores (Appendix G, Figure G.2). The presence of the condensed water then provides sites of rapid recrystallization. Since the flaked reactant was prepared by the rapid cooling of a magma that was substoichiometric in octahydrate (7.0 to 7.9 waters of hydration), the rate of recrystallization is likely enhanced by a need to reduce the energy locked up within the flake. This energy may be present as defects within the crystallites or surface energy, resulting from the small size of the crystallites and the presence of the $Ba(OH)_2 \cdot 3H_2O$—$Ba(OH)_2 \cdot 8H_2O$ eutectic. Photographs of *commercial* $Ba(OH)_2 \cdot 8H_2O$ flakes before and after recrystallization at a relative humidity in excess of 60% are presented in Figures 3.2 and 3.4. For rehydration at lower humidities, external changes of the flake were small.

The dependency of pressure drop upon relative humidity also explains the autocatalytic pressure drop behavior observed at high relative humidities. For a fixed influent water vapor concentration, any increase in system pressure at constant temperature will result in an increase in the water vapor pressure and likewise the relative humidity, P/P_0. Therefore, as the pressure drop across the bed increases, so does the relative humidity within the bed; each value continues to increase until the run must be terminated. At lower relative humidities, the rate of increase in pressure drop as a function of relative humidity is not sufficient to autocatalyze the process.

The dependence of pressure drop upon relative humidity also restricts the upper flow rate that the process may treat. Increased gas flows result in greater pressure drops across the bed (i.e., a greater pressure

at the entrance to the bed). Therefore, the relative humidity at the entrance of the bed must be <60%, but the influent water vapor pressure must be greater than the dissociation vapor pressure of $Ba(OH)_2 \cdot 8H_2O$.

Upon the completion of many of the fixed-bed runs, the pressure drop across the bed was determined as a function of superficial velocity over the range 0 to 22 cm/s (7 data points). Attempts were then made to correlate the pressure drop as a function of system parameters. Two correlation techniques were used. The first was the standard friction factor approach, and the second was the widely used Ergun equation.

The friction factor method for pressure drop correlation. The standard friction factor approach defines the friction factor, f, via the following equation:[88]

$$\Delta P/L = \frac{fA}{2} \rho_G \langle V \rangle^2 , \qquad (3.54)$$

where

$\Delta P/L$ = pressure drop/unit bed length,

A = external surface area exposed to fluid (i.e. wetted surface)/unit volume,

ρ_G = gas density, and

$\langle V \rangle$ = average stream velocity or free stream velocity (dependent upon the definition).

Using the experimental data cited in the preceding paragraph, the pressure drop was correlated as a power function of the superficial gas velocity at system conditions, V:

$$\Delta P/L = 0.01 \, BV^n \qquad (3.55)$$

The results of this analysis are presented in Table 3.16. From this data, the exponent, n, is reasonably constant and has an average value of

Table 3.16. Application of model, $\Delta P/L = 0.01BV^n(kPa/m)$, for correlating pressure drop across converted beds of *commercial* $Ba(OH)_2 \cdot 8H_2O$ flakes. V has units of cm/s.

CDM Run No.	Relative humidity (%)	Superficial velocity V (cm/s)	Temperature	n[a]	ln(B)	Correlation coefficient
54	47.8	13.65	317.5	1.35	2.05	0.992
50	48.5	8.73	296.3	1.40	2.62	0.997
53	53.1	8.89	303.9	1.46	2.68	0.998
52	54.2	8.66	296.2	1.38	2.38	0.993
56	54.8	14.16	316.2	1.35	3.02	0.997
49	54.9	13.94	305.3	1.48	2.96	0.998
55	59.1	9.08	304.0	1.34	4.85	0.999
48	60.2	8.65	296.3	1.42	4.83	0.998
46	61.2	17.50	299.7	1.48	2.93	0.998
57	62.6	9.08	304.0	1.41	4.27	0.999
40	63.3	13.88	305.2	1.44	4.29	0.999
45	66.4	18.50	296.1	1.29	5.66	0.999
47	69.6	8.93	296.0	1.41	5.02	0.999

[a] $n(average) = 1.40$; $\sigma = 0.058$.

1.40. However, the value of B is a very strong function of relative humidity. Presented in Figure 3.33 is a plot of ln(B) versus relative humidity. In a manner very similar to Figure 3.32, the value remains small and relatively constant up to a relative humidity of ~60%. Again, there are definite indications of capillary condensation and flake restructuring. The phenomenon does not appear to be a strong function of temperature. Similarly, the correlation of the data as a function of superficial velocity indicates that over the regime studied, the phenomenon is a weak function of gas velocity. Therefore, for prediction purposes, Figure 3.33 and Equations (3.56) and (3.57) should provide reasonable estimates of anticipated pressure drops across the fixed beds.

ORNL-DWG 82-377

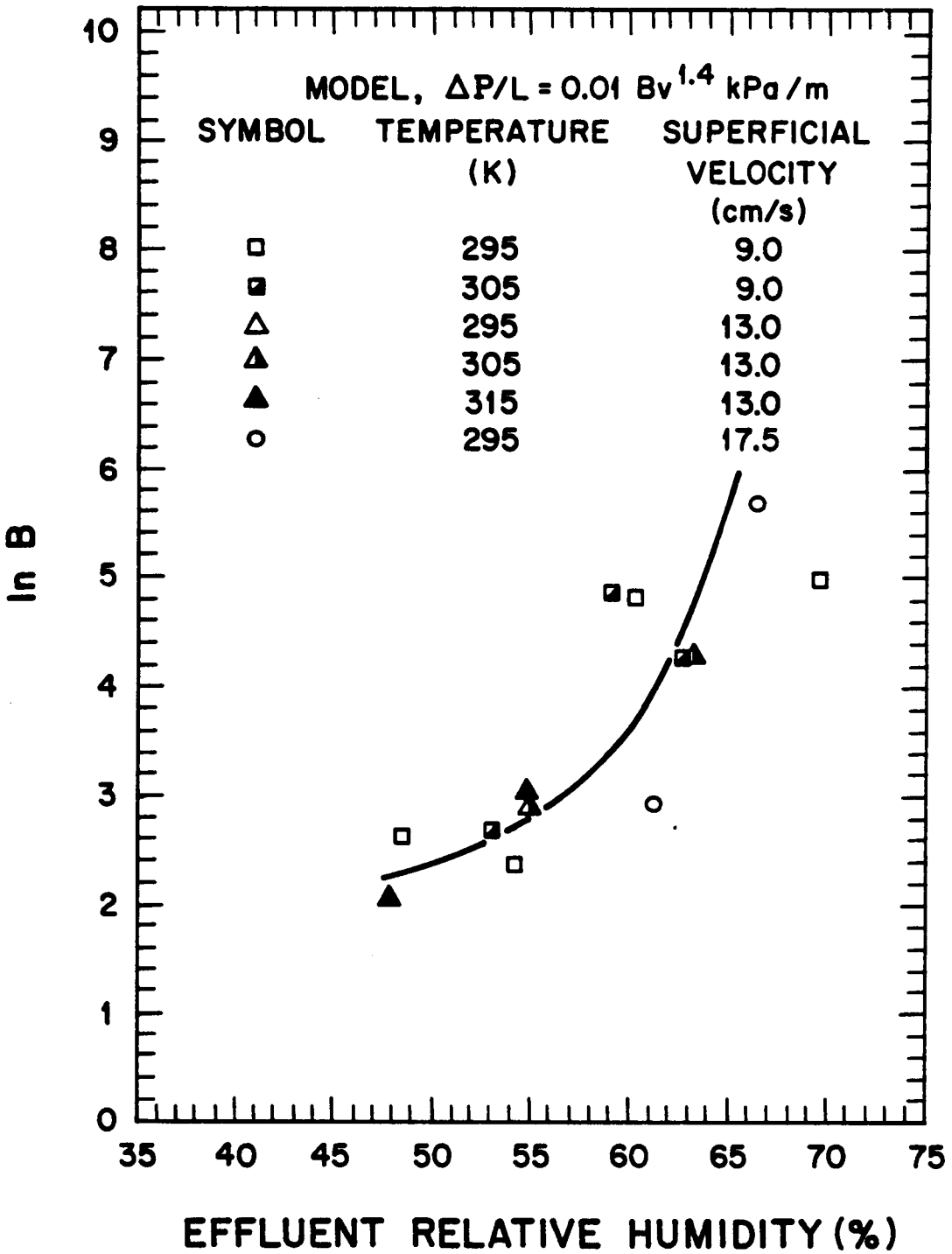


Figure 3.33. The effects of effluent relative humidity on the "B" term in the pressure-drop model, $\Delta P/L = 0.01BV_0^{1.4}$ (kPa/m).

$$\frac{\Delta_P}{L} = 0.01BV^{1.4} \quad , \text{ kPa/m; and} \tag{3.56}$$

$$\frac{\Delta_P}{L} = 4.42 \cdot 10^{-4} BV^{1.4}, \text{ psi/ft;} \tag{3.57}$$

where V has units of cm/s at system conditions.

Applying a force balance upon the system and defining the friction factor in the standard way for flow around particles, one obtains the following:

$$\frac{\Delta_P}{L} = \tau A = \frac{fA}{2} \rho_G V_\infty^2 \ , \tag{3.58}$$

where

τ = shear force,

A = area/volume,

f = friction factor,

V_∞ = free stream velocity.

It will be assumed that the free stream fluid velocity, V_∞, may be approximated by the superficial velocity, V, divided by the bed voidage, ε. Rearranging and eliminating the term $\Delta p/L$ via Equation (3.52), one obtains the following friction factor expression for flow-through fixed beds of *commercial* $Ba(OH)_2 \cdot 8H_2O$ product (B values are for c-g-s unit system).

$$fA = \frac{2B\varepsilon^2}{\rho_G^{0.6}} \tag{3.59}$$

Attempts were also made to correlate the initial pressure drop across fixed beds of *commercial* $Ba(OH)_2 \cdot 8H_2O$ flakes. The results are presented in Table 3.17. The correlation was not as good as for the converted beds because the smaller pressure drop at the lower flow rates were near the sensitivity of the D/P cell and the overall analytical technique. The unreacted beds did demonstrate a greater functional dependency of pressure drop upon flow rate than their reacted counterparts.

Table 3.17. Application of model, $\Delta P/L = 0.01BV^n(kPa/m)$, for correlating pressure drop across fixed beds of *commercial* $Ba(OH)_2 \cdot 8H_2O$

Sample No.	n	ln(B)	Correlation coefficient
1	1.59	+0.3806	0.971
2	1.74	-0.1458	0.995

The Ergun Equation for Pressure Drop Correlation. The Ergun equation has received widespread application for predicting and modeling pressure drops associated with liquid or gas flow across packed beds of spheres.[77,88,89] The Ergun equation is actually a combination of two fixed-bed equations — the Blake-Kozeny equation developed to model laminar flow where shear forces dominate the pressure drop, and the Blake-Plummer equation developed to model turbulent flow, where inertial forces dominate the pressure-drop term. Application to other particle geometries has been demonstrated by defining an effective particle diameter, d_p, and a sphericity factor, ϕ, and substituting the term ϕd_p, in place of d_p in the Ergun equation for spheres. The effective

diameter, d_p, is defined as the diameter of a sphere of equal volume to that of the particle. The sphericity factor is the ratio of the surface area of a sphere with diameter d_p divided by the actual surface area of the particle. The resulting Ergun equation is

$$\frac{\Delta_P}{L} = 150 \frac{(1-\varepsilon)^2}{\varepsilon^3} \frac{\mu V}{(\phi d_p)^2} + 1.75 \frac{(1-\varepsilon)}{\varepsilon^3} \frac{\rho_G V^2}{\phi d_p}, \tag{3.60}$$

where

L = bed length parameter,

ε = void fraction,

μ = viscosity,

V = superficial gas velocity at system conditions,

ϕ = sphericity, surface area of sphere of equal volume to the particle/particle area,

d_p = effective diameter, diameter of sphere of equal volume to the particle,

ρ_G = gas density.

The preceding equation may be rearranged in the following manner:

$$\frac{\Delta_P}{L} = \left[\frac{150(1-\varepsilon)}{\frac{\phi_p \rho V}{\mu}} + 1.75\right] \frac{(1-\varepsilon)}{\varepsilon^3 \phi d_p} \rho_G V^2, \tag{3.61}$$

$$= \left[\frac{150(1-\varepsilon)}{Re} + 1.75\right] \frac{(1-\varepsilon)}{\varepsilon \phi r_p} \frac{\rho_G \langle V \rangle^2}{2},$$

where

r_p = effective particle radius,

$\langle V \rangle$ = average interparticle fluid velocity, V/ε,

Re_p = particle Reynolds number.

From this equation, a particle friction factor may be defined.[89]

$$f_p = \frac{150(1-\varepsilon)}{Re_p} + 1.75 \tag{3.62}$$

The particle surface area per unit bed volume may be represented by:

$$A = \frac{1-\varepsilon}{3\varepsilon^2 \phi r_p} \tag{3.63}$$

The rearranged Ergun equation is now of similar for to the standard friction factor definition.

$$\frac{\Delta_P}{L} = f\ A\ \rho_G \frac{\langle V\rangle^2}{2}$$

$$= \frac{1}{3\varepsilon}\left[\frac{150(1-\varepsilon)}{Re_p} + 1.75\right] \frac{3(1-\varepsilon)}{r_p} \frac{\rho_G \langle V\rangle^2}{2} \tag{3.64}$$

$$= \frac{1}{3\varepsilon} f_P\ A \frac{\rho_G \langle V\rangle^2}{2}$$

The functional dependancy of the friction factor upon the Reynolds number is readily apparent in the preceding equations.

The pressure drop data were correlated as a function of velocity with the following equation.

$$\Delta P/L = A'V + B'V^2 \ . \tag{3.65}$$

The results of the least-squares analysis are presented in Appendix L. From the values of A' and B', values for ε and Φd_p were determined. As may be seen in Appendix E, the values of these parameters were not consistent with the actual physical system. Handley and Heggs argued in a

1968 paper that the constants used in the Ergun equation, 150 and 1.75, are not constants but rather are functions of the geometry and size of the particles composing the system.[90] For simple systems, they proposed that the pressure drop be modeled by an equation of the form of Equation (3.59). Therefore, attempts were made to correlate the parameters A' and B' as a function of system parameters, most notably relative humidity. No simple correlation was obtained, and this approach was abandoned.

Application of the Chilton-Colburn Analogy. Because of the similarities in the partial differential equations for momentum, heat, and mass transfer and their respective boundary conditions, Reynolds in 1928 speculated that for turbulent flow in a pipe, an analogy between the transfer of momentum, heat, and mass should exist.[88,91] Therefore, he proposed the following analogy:

$$\frac{f}{2} = \frac{h}{C_p G} = \frac{K_F \rho_G}{G} \tag{3.66}$$

where

f = friction factor,

h = heat transfer coefficient,

C_p = specific heat of fluid,

G = superficial mass velocity per unit area,

K_F = mass transfer coefficient,

ρ_G = density of fluid.

Hence with experimental knowledge of either pressure drop, heat transfer, or mass transfer data, the analogy would enable one to predict the magnitude of the other transfer coefficients in similar systems. Subsequent

application of this analogy indicated that an additional correction factor was required to account for the effects of molecular diffusion upon heat and mass transfer since no analogous phenomenon exists for momentum transfer. In a 1938 paper, Chilton and Colburn presented their semiempirical Chilton-Colburn analogy:[91]

$$\frac{f}{2} = \frac{h}{C_p G}\left[\frac{\mu}{\rho_G D}\right]^{2/3} = \frac{K_F}{G}\rho_G\left[\frac{\mu}{\rho D}\right]^{2/3} \qquad (3.67)$$

or

$$\frac{f}{2} = j_H = j_M ,$$

where

μ = viscosity,

D = molecular diffusivity,

j_H = j factor for heat transfer,

j_M = j factor for mass transfer.

For relatively simple systems, the preceding equations have received widespread applications. Furthermore as f is frequently a function of the Reynolds number, j_H and j_M must also be. However, extension of the Reynolds-Colburn analogies to fixed-bed systems must be approached with caution since the flow patterns may be extremely complex and may vary from turbulent to laminar to stagnant within a small spatial regime. Furthermore, bed voidage, particle geometry, particle surface area, and entrance and wall effects may also affect the monentum, heat, and mass transfer properties of the system. Form drag may contribute significantly to the transfer of momentum, but an analogous transfer process does not exist for either heat or mass transfer. The use of boundary layer theory is usually impractical because of the effects of surrounding particles upon the flow

patterns. Therefore, analogies between momentum and mass or heat transfer for a fixed-bed system are often constrained to a particular particle size and geometry. Correlation between the j factors for heat and mass transfer are generally much better because of the increased similarity in the physical transfer mechanism. Gamson[80] correlated heat and mass transfer data obtained on spheres and found $j_H/j_M = 1.076$.

For the system of interest, this study has indicated $K_F A_o$ to be a weak function and $\Delta P/L$ to be a strong function of relative humidity. Hence rigorous application of the Chilton-Colburn analogy may not be possible. However, since mass throughput or the superficial velocity at reference conditions (101.3 kPa, 294.3 K, or 1 atm, 70°F, noted by subscript o) is a key process parameter, an indication of the functional effect of superficial velocity upon the mass transfer coefficient as predicted by the Chilton-Colburn analogy from friction factor data may be very beneficial. Combining the experimental friction expression obtained in the preceding section with the Chilton-Colburn analogy, one obtains the following expressions for j_M and $K_F A_o$:

$$j_M = \frac{K_F \rho_G}{G}\left[\frac{\rho}{\rho_G D}\right]^{2/3} = \frac{K_F}{V}\left[\frac{\rho}{\rho_G D}\right]^{2/3} = \frac{1}{2} f \ ,$$

$$fA = \frac{2B\varepsilon^2}{\rho_G V^{0.6}} \ ,$$

$$j_M = \frac{B\varepsilon^2}{A\rho_G V^{0.6}} = \frac{B\varepsilon^2}{A\rho_G}\left[\frac{T_0 P}{T P_0}\right]^{0.6} V_0^{-0.6} \ , \qquad (3.68)$$

$$K_F A \propto \left[\frac{\rho_G D}{\mu}\right]^{2/3} \frac{B\varepsilon^2 V 0.4}{\rho_G} = \left[\frac{\rho_G D}{\mu}\right] \frac{B\varepsilon^2}{\rho_G} \left[\frac{T}{T_0} \frac{P_0}{P}\right]^{0.4} V_0{}^{0.4} \quad .$$

Assuming A to be equal to A_o the initial surface area, the calculated $K_F A_o$ values were 2 to 3 orders of magnitude greater than the experimental values. Based upon the work of Handley and Heggs, this differential is not surprising because their study on simple fixed-bed systems of spheres, ordered plates, cylinders, etc., indicated an order of magnitude variation between the experimental values and the Chilton-Colburn predicted values.[90] Therefore, the wide deviation between predicted theory and experimental data for the present system could result from the highly disordered nature of the packing within the bed, considerable contribution to the pressure drop from form drag, and the fact that the pressure drop was obtained on completely converted beds. These effects could also account for the lack of a functional dependency of relative humidity upon the $K_F A_o$ data.

A key process parameter is the effect of gas throughput upon the mass transfer coefficient or the j_M factor. The Chilton-Colburn analogy has indicated the J_M factor to be proportional to $V_0{}^{-0.6}$. Data concerning j factors for flake or slab geometry are lacking. However, numerous j factor correlations[66,77,80,87–101] on spheres or cylinders have indicated j $\propto$ $V_0{}^{-0.2} \rightarrow V_0{}^{-0.7}$. Hence some significance might be assigned to this analysis.

Realizing that for most fixed-bed systems the predicted j_D factor based upon friction factor data was significantly greater than the experimental j_D factor, Handley and Heggs attempted to break the pressure

drop into two parts via the Ergun equation.[90] They found that for simple systems, the pressure drop resulting from inertial forces, the V^2 term, was an indication of the tortuosity of the flow pattern and hence the efficiency of the gas-solid contacting process. However, application of this technique in the present study was not possible because of the failure of the Ergun equation to correlate the data as a function of system parameters.

Conclusion — fixed-bed studies.

Correlation of the model predicted and experimental breakthrough curves were excellent. The observation that the area available to mass transfer may be modeled as a linear function of conversion is not totally surprising due to the variation in the thickness and surface area of the flakes. Contributions to this term may also result from deviations from the assumptions in the model development, most notably negligible gas dispersion and channeling and negligible resistance to mass transfer through the product layer.

Although the correlation of the model with the data was excellent, the dispersion in the data at the two superficial velocities studied in detail was much greater than expected. As the dispersions about the least-squares fit were similar for the two procedures of data analyses, the dispersion appears to be an inherent property of this fixed-bed process and effectively masks out the effects of other process variables. A possible cause of the deviations in the $K_F A_o$ coefficient would be differing flow patterns (i.e., the presence of channeling) in the fixed bed. Based upon the modified Reynolds number as defined by Gamson and the information cited earlier, it is possible that the experimental data were

obtained in the transition range from laminar to turbulent flow.[80] In the experimental studies, no special precautions were taken in the loading of the fixed bed as the *commercial* $Ba(OH)_2 \cdot 8H_2O$ flakes were loaded in a random manner. Examination of the data indicated no correlation between reactant batch number and the $K_F A_o$ coefficient. Therefore, the randomness associated with the modified mass transfer coefficient appears to be a property of the process. It is interesting to note that Sherwood et al. reported similar difficulties in correlating mass transfer data obtained on fixed beds of spheres and cylinders.[95] Their analysis was based upon 15 papers. According to Sherwood et al., "The agreement between the several investigators is poor, but the experimental difficulties are considerable and the spread of the lines is perhaps not much greater than the experimental error." Based upon these correlations and assuming the data discrepancy to result from experimental error, one might expect a factor of ~2 variation in experimental mass transfer coefficients at a given mass throughput. This variation is consistent with the present observations on the fixed beds of *commercial* $Ba(OH)_2 \cdot 8H_2O$ flakes.

A second unique aspect of the process and of particular interest in process design is the greater-than-anticipated functional dependency of the $K_F A_o$ coefficient upon velocity. The preceding analyses have indicated $K_F A_o$ to be proportional to velocity to the 1.1 power. This aspect will now be addressed in greater detail.

Historically, the reference system for the determination of heat or mass data has been fixed beds of spheres. With uniform spheres, one need not worry about the packing geometry provided the ratio of the bed

diameter to the particle diameter is sufficiently large. Typically, the j factor correlation is of the following form:

$$j = A' Re^{n} , \tag{3.69}$$

where

A' = constant,

Re = Reynolds number, $\frac{d_p G}{\mu} \alpha \frac{d_p V_o}{\mu}$,

n = arbitrary exponent.

Reported values[66,77,87–101] of the exponent n vary from $-0.2 \rightarrow -0.7$. Thus one would predict $K_F \alpha V_0^{0.3} \rightarrow V_0^{0.8}$. Several empirical heat transfer correlations[102] have indicated h, the heat transfer coefficient, $\alpha V_o^{.9}$. Thus employing the analogy between heat and mass transfer, one might expect $K_F \alpha V_0^{0.9}$. Based upon boundary layer theory, one would predict $K_F \alpha V_o^{0.5}$. The correlation of Rowe and Claxton[77] for mass transfer from spheres into air is of the form

$$Sh = 2.0 + 0.69\ Re^{1/2} Sc^{1/3} , \tag{3.70}$$

where

Sh = Sherwood number,

Re = Reynolds number,

Sc = Schmidt number.

In the regime of interest, the equation predicts $K_F \alpha V_0^{0.5}$. Earlier in this chapter, the j factor correlation developed by Gamson for particles of widely differing geometries was presented. This correlation[80] indicated $K_F \alpha V_0^{o}$ to $V_0^{0.6}$.

The greater-than-anticipated dependency of the $K_F A_o$ coefficient upon gas velocity, $K_F A_o \alpha V_0^{1.1}$, indicates that the initial area available for mass transfer, A_o, may be a function of velocity. Although bed expansion

was nominal, it is speculated that the number of planar contact points between neighboring flakes is reduced by the upward shear force of the gas flowing through the bed. The shear force causes the particles to realign in a geometry parallel to the direction of gas flow and the resulting re-reduction in planar contact points provides greater area for mass transfer. For the smaller particles, localized fluidization may occur. The extent to which the points are realigned and localized fluidization occurs is dependent upon the shear force exerted on the flakes. Pressure drop studies presented earlier indicated the shear force to be proportional to the superficial velocity to the 1.4 power. Assuming the realignment and increase in surface area to be a function of the shear force, the functional dependance of the gas film mass transfer coefficient would then correlate more closely with the published values. In essence, the shape factor as defined by Gamson appears to be a function of velocity. It should be noted that for packing arrangements in which particle reallignment is restricted, a reduction in A_o from the predicted value would be observed. This variation in A_o would then contribute to the larger than anticipated dispersion in the experimental $K_F A_o$ coefficients.

In the j-factor correlation developed by Gamson, the portion of the surface area available for mass transfer was assumed to be dependent upon the particle geometry through the shape factor, and the extent of fluidization through the bed voidage term. With respect to the Gamson correlation, Gupta and Thodos[98] argued that the correlation was inconsistent for

$$j_M = \frac{A' \psi Re_M^{\,n}}{(1-\varepsilon)^{0.2}} \quad . \tag{3.71}$$

large bed voidages as $j_M \to \infty$, and therefore $K_F \to \infty$. They argued that a better correlation for uniform packing, based upon the actual area available for mass transfer and the bed voidage, could be developed. In the development of their correlation, they assumed the available surface area for mass transfer to be dependent upon the particle geometry and the packing arrangement. In this way, they were able to account for the surface area lost to mass transfer because of interparticle contact. Their correlation based upon data obtained from fixed and fluidized beds of uniform spheres, cylinders, cubes, partition rings, Raschig rings, and Berl saddles, but which excluded flakes, was of the following form:

$$j = \frac{0.300\ f'}{\varepsilon(Re^{0.35} - 1.90)} \quad , \tag{3.72}$$

where

f' = area availability factor,

ε = voidage,

$Re = A_p G/\mu$,

A_p = particle area/particle.

Presented in Table 3.18 are the predicted and experimental area availability factors for uniform packing in fixed and fluidized beds. In general, the correlation between predicted and experimental values is excellent. The factor of concern in the present study is the change in the area availability factor from one extreme, a fixed bed, to the other extreme, a fluidized bed. In the transition range, one would expect area availabil-ity factors between the extremes, that is the presence of some localized fluidization, and spread or dispersion in the values obtained at a given superficial velocity. Therefore, for nonuniform packing such

as flakes of differing sizes, it is speculated that the change in the area availability factor from one extreme to the other would be of greater magnitude and a stronger function of velocity, $f' \alpha V_0^n$. These speculated observations are consistent with the present experimental results. It also appears that for the present system and superficial velocities >15 cm/s, a rather dramatic change may occur and this would

Table 3.18. Comparison of the calculated area availability factor, f', with experimental data

	Area availability factor, f'			
	Calculated		Experimental	
Particle shape	Packed	Fluidized	Packed	Fluidized
Spheres	1.000	1.000	1.000	1.000
Cylinders	0.952	1.144	0.865	1.16
Cubes	0.820	1.24	0.825	
Partition rings	1.25	1.40	1.24	
Raschig rings	1.22	1.37	1.34	
Berl saddles	1.48	1.98	1.36	

account for the extremely large dispersion observed in the rather limited data base at these conditions.

CHAPTER 4

CONCLUSIONS AND RECOMMENDATIONS

Conclusions

Extensive studies have been conducted upon $Ba(OH)_2$ hydrates, their reaction with CO_2, and the operation of a fixed-bed process for CO_2 removal. Microscale studies indicated (1) the published vapor pressure data for $Ba(OH)_2 \cdot 8H_2O$ to be valid, (2) the rate of dehydration or rehydration to be proportional to the amount of free water on the surface (i.e., a function of relative humidity), and (3) the reactivity of $Ba(OH)_2 \cdot 8H_2O$ for CO_2 to be 3 orders of magnitude greater than that of either $Ba(OH)_2 \cdot 3H_2O$ or $Ba(OH)_2 \cdot H_2O$. Macroscale studies on 10.2-cm-ID fixed beds of *commercial* $Ba(OH)_2 \cdot 8H_2O$ flakes indicated that the pressure drop across the bed increased dramatically as 60% relative humidity in the effluent gas was approached. It is speculated that this phenomenon results from the capillary condensation of water in V-shaped contact points or pores and that this effect facilitates the subsequent recrystalization of the flake. Although the resulting flakes have greater external surface area, they are more fragile and degrade more readily upon conversion to $BaCO_3$; thus resulting in increased pressure drop across the fixed beds.

Experimental studies indicated the transfer of the reactant gas through the gas film to be the major resistance to mass transfer. Values of the $K_F A_o$ coefficient (gas film mass transfer coefficient multiplied by the initial surface area) were determined from the initial portion of the

breakthrough profile. For a given mass throughput, considerable dispersion in the values of the $K_F A_o$ coefficient was observed. However, attempts to correlate the dispersion with system parameters were fruitless. A model, assuming gas film control, was then developed and exact numerical solutions were obtained. Excellent correlations between the model-predicted breakthrough curves and the experimental breakthrough curve were achieved when the area available for mass transfer was modeled as a linear function of conversion [i.e., $A = A_o(1-X)$]. The dispersion in the determined $K_F A_o$ coefficient was again greater than expected and appears to be an inherent aspect of the process. Indications are that the dispersion resulted from differences in the actual area available for mass transfer and the possible presence of localized channeling. Based upon published correlations for the K_F coefficient, the correlation for the $K_F A_o$ coefficient possessed a greater functional dependancy upon velocity than expected. Because the studies were conducted on flaked material with considerable interparticle contact, it is speculated that the amount of surface area available for mass transfer increased as a function of gas velocity, thus resulting in the greater-than-anticipated functional dependancy of $K_F A_o$ upon velocity. This factor may also account for the greater-than-anticipated dispersion in modified mass transfer coefficients since some localized packing arrangements would be more conducive to restructuring. Such dispersion in mass transfer data has been observed by others.

Based upon the experimental data obtained during this study and its subsequent analyses, a window or regime of optimal process operation was determined to exist for the isothermal operation of this fixed-bed

process. The window is bounded on the lower side by the dissociation vapor pressure of $Ba(OH)_2 \cdot 8H_2O$ and on the upper side by the onset of appreciable capillary condensation and subsequent pressure drop problems (~60% relative humidity). An operating envelope is presented in Figure 3.34 for the treatment of 330 ppm_v CO_2 gas stream at a system pressure of 0.5 psig. The relative humidity of the influent gas must fall within the envelope for optimal gas throughput. If changes are made in either (1) the CO_2 concentration, thus affecting the amount of water vapor produced, or (2) the system pressure, thus affecting the partial pressure of the water vapor and subsequently the relative humidity (P/P_0), the operating envelope will change. Additionally, the operating envelope demonstrates why operational problems at 22 and 32°C were not severe, yet considerable difficulty was encountered when trying to operate the process at 42°C.

Successful operation at higher relative humidities (>60%) is possible by significantly reducing the gas throughput. The effect of operating the bed at conditions of water vapor saturation, whereby the water product would remain in the bed and the reaction would become exothermic, was not examined in detail. However, the reaction does proceed readily at these conditions, and the $BaCO_3$ product is insoluble.

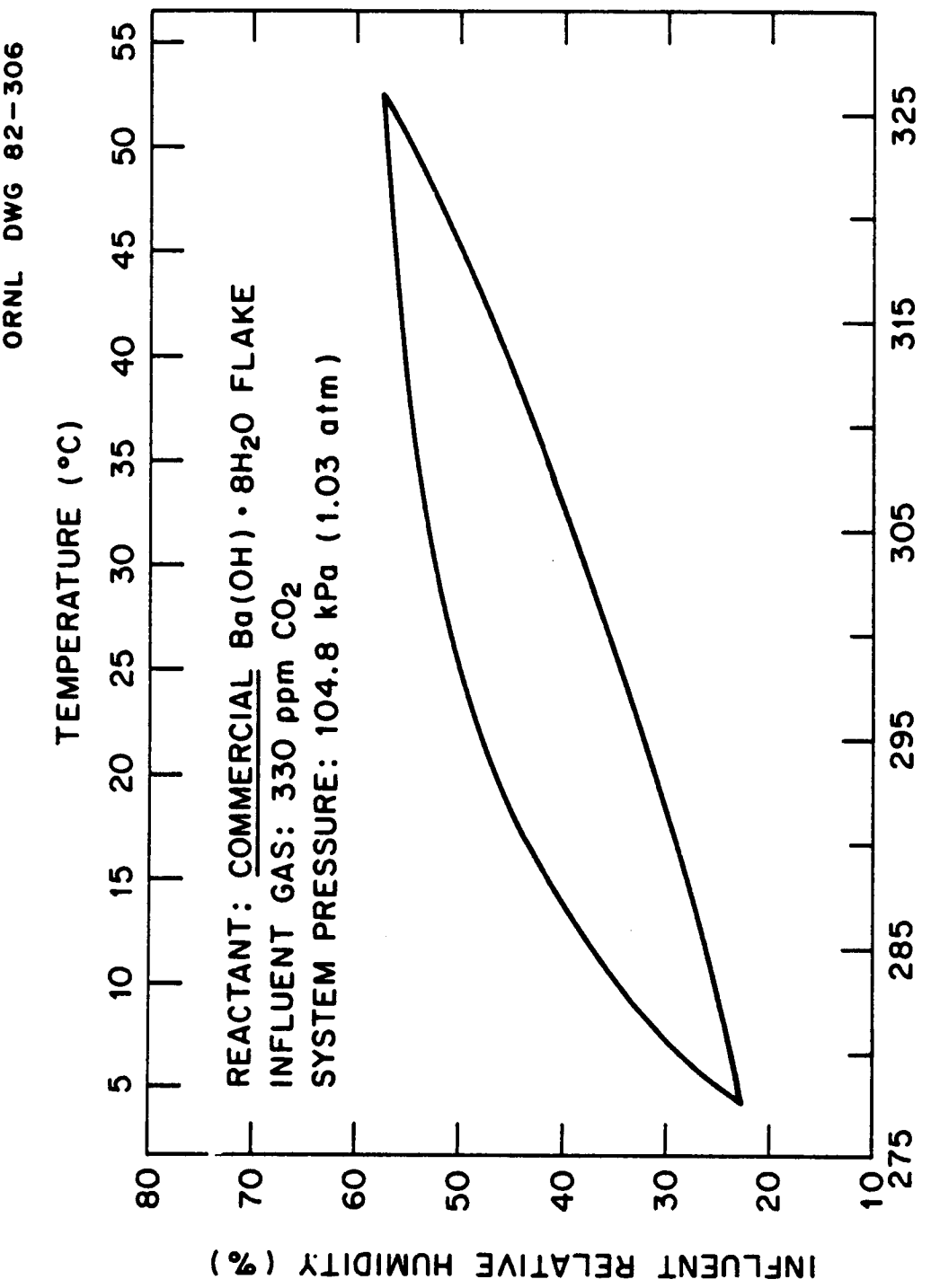


Figure 3.34. Operating window for the contacting of a 330 ppm_v CO_2 gas stream with fixed beds of *commercial* $Ba(OH)_2 \cdot 8H_2O$ flakes.

Recommendations

The CO_2—$Ba(OH)_2 \cdot 8H_2O$ gas-solid reaction offers a unique system for future mass transfer studies because few ambient temperature reactions exist in which there is a factor of ~3 reduction in molar volume upon conversion of the reactant to the product. As previously cited, the product is ~73% porous, and for thin flakes, diffusional resistance of the gaseous reactant through the product layer is small. With respect to the present studies, areas requiring additional investigation include the (1) evaluation of the effects of different CO_2 concentrations in the feed gas, (2) operation of the process at 10 and 50°C, and (3) conduction of studies with a different carrier gas (i.e., helium or argon rather than the O_2-N_2 mixture in air). This latter change would greatly affect the physical properties of the off-gas stream.

The pressure drop was determined to be a function of relative humidity and the rehydration of the water-deficient *commercial* $Ba(OH)_2 \cdot 8H_2O$ to $Ba(OH)_2 \cdot 8H_2O$. Additional studies are needed to determine if operation at effluent relative humidities >60% is possible by prior hydration of the bed at effluent humidities <60% with a CO_2-free gas.

As previously cited within the text, the reactant appears to possess the scrubbing capabilities of a caustic solution. Therefore, because of this observation and the favorable molar volume ratio of the reactant to the product, one would predict that the reaction should proceed with other acid gases and vapors (such as NO, NO_2, SO_2, HCl, acetic acid, etc). Initial scoping studies with NO_2 have indicated this prediction to be the case. However, further process studies are required to better

characterize the reactivity of this unique material toward other acid gases and vapors.

Since this study was oriented toward process development, additional fixed-bed studies are required to develop a more basic understanding of phenomena associated with a flaked reactant. Additional heat and mass transfer information is required to supplement published information and thus develop a better understanding of the operational characteristics of fixed beds of uniform flakes. What are the effects of flake thickness and geometry? For deep beds, at what particle length do dispersion effects become appreciable? Is a conventional sphericity factor or shape factor approach really sufficient to correlate data obtained on flaked reactant with more conventional data obtained on spherical reactant? For fixed-bed operation, can more easily obtainable heat transfer data be used in lieu of mass transfer data via the Chilton-Colburn analogy for heat and mass transfer? Can mass or heat transfer coefficients be estimated with confidence from pressure drop data via the Chilton-Colburn analogy? Finally, how does this information extend to the present system, a fixed bed of nonuniform flakes?

LIST OF REFERENCES

LIST OF REFERENCES

1. H. Bonka et al., "Contamination of the Environment by Carbon-14 Produced in High-Temperature Reactors," *Kernetechnik* 15(7), 297 (1973).

2. W. Davis, Jr., *Carbon-14 Production in Nuclear Reactors*, ORNL/NUREG/TM-12 (February 1977).

3. C. O. Kunz, W. E. Mahoney, and T. W. Miller, "Carbon-14 Gaseous Effluents from Boiling Water Reactors," *Trans. Am. Nucl. Soc.* 21, 91 (1975).

4. C. O. Kunz, W. E. Mahoney, and T. W. Miller, "C-14 Gaseous Effluent from Pressurized Water Reactors," pp. 229-234 in *Proceedings of the Health Physics Society 8th Midyear Symposium*, CONF 741018 (1974).

5. M. J. Kabat, "Monitoring and Removal of Gaseous Carbon-14 Species," *Proceedings of the 15th DOE Nuclear Air Cleaning Conference*, CONF-780819 (1978).

6. H. Schuttelkopf, *Releases of $^{14}CO_2$ from Nuclear Facilities with Gaseous Effluents*, Kernsforschungszentrum Karlsruhe KFK 2421, June, 1977 (translated from German) ORNL-tr-4527 (1978).

7. Program Strategy Document for the Management of Radioactive Airborne Wastes - Draft, Exxon Nuclear Idaho Company, Inc., prepared for Department of Energy, Idaho Operations Office (December 1981).

8. P. J. Magno, C. B. Nelson, and W. H. Ellett, "A Consideration of the Significance of Carbon-14 Discharges from the Nuclear Power Industry," p. 1047 in *Proceedings of the Thirteenth AEC Air Cleaning Conference*, CONF-740807 (1974).

9. G. G. Killough et al., *Progress Report on Evaluation of Potential Impact of ^{14}C Releases from an HTGR Reprocessing Facility*, ORNL/TM-5284 (July 1976).

10. L. Machta, "Prediction of CO_2 in the Atmosphere," *Carbon and the Biosphere*, G. M. Woodwell and E. V. Pecan, eds., Technical Information Center, Office of Information Services, U.S. Atomic Energy Commission (August 1973).

11. G. G. Killough, *A Diffusion-Type Model of the Global Carbon Cycle for the Estimation of Dose to the World Population from Releases of Carbon-14 to the Atmosphere*, ORNL/TM-5269 (1977).

12. J. W. Snider and S. V. Kaye, "Process Behavior and Environmental Assessment of ^{14}C Releases from an HTGR Fuel Reprocessing Facility," *Proceedings of the ANS-AIChE Topical Meeting*, Sun Valley, Idaho, Aug. 5-6, 1976.

13. L. Pauling, "Genetic and Somatic Effects of Carbon-14," *Science 128*, 1183 (1958).

14. J. Schwibach, H. Riedel, and J. Bretschneider, *Studies on the Emission of Carbon-14 from Nuclear Facilities (Nuclear Power Plants and Reprocessing Plants): Its Measurement and the Radiation Exposure Resulting from Emissions*, Series of the Institute for Radiation Hygiene of the Federal Health Office, No. 20 (translated from German) OLS-80-233 (1979).

15. *Radiological Significance and Mangement of Tritium, Carbon-14, Krypton-85, Iodine-129 Arising from the Nuclear Fuel Cycle*, Nuclear Energy Agency, Organization for Economic Cooperation and Development, Paris, France (1980).

16. A. G. Croff, *An Evaluation of Options Relative to the Fixation and Disposal of ^{14}C-Contaminated CO_2 as $CaCO_3$*, ORNL/TM-5171 (April 1976).

17. A. G. Evans, W. E. Prout, J. T. Buckner, and M. R. Buchner, *Management of Radioactive Waste Gases from the Nuclear Fuel Cycle* — Vol. 1, *Comparison of Alternatives*, NUREG/CR-1546, DPST-NUREG-80-5, Vol. 1. (1980).

18. D. W. Holladay, *Experiments with a Lime Slurry in a Stirred Tank for the Fixation of Carbon-14 Contamianted CO_2 from Simulated HTGR Fuel Reprocessing Off-Gas*, ORNL/TM-5757 (1978).

19. D. W. Holladay, *An Experimental Investigation of the Distribution of Krypton from Simulated HTGR Fuel Reprocessing Off-Gas During the Removal and Fixation of CO_2 by the CO_2-$Ca(OH)_2$ Slurry Reaction*, ORNL/TM-6539 (in preparation).

20. D. W. Holladay and G. L. Haag, "Removal of ^{14}C-Contaminated CO_2 from Simulated LWR Fuel Reprocessing Off-Gas by Utilizing the Reaction Between CO_2 and Alkaline Hydroxides in Either Slurry or Solid Form," pp. 548-69 in *Proceedings of the 15th DOE Nuclear Air Cleaning Conference*, CONF-780819 (1979).

21. K. J. Notz, D. W. Holladay, C. W. Forsberg, and G. L. Haag, "Processes for the Control of $^{14}CO_2$ During Reprocessing," paper presented at the International Symposium on Management of Gaseous Wastes from Nuclear Facilities, Vienna, Austria, Feb. 18-22, 1980.

22. *Handbook of Chemistry and Physics*, 52nd ed., The Chemical Rubber Co., Cleveland, Ohio, 1972, pp. 13-70.

23. W. F. Linke and A. Seidell, *Solubilities of Inorganic and Metal Organic Compounds*, 4th ed., American Chemical Society, Washington, D.C., 1958.

24. M. M. Markowitz, *Foote Prints 34, 9 (1965).*

25. D. A. Boryta and H. J. Maas, "Factors Influencing Rate of Carbon Dioxide Reaction with Lithium Hydroxide," *Ind. Eng. Chem. Process Des. Develop. 10(4), 489 (1971).*

26. D. D. Williams and R. R. Miller, *The Effect of Water Vapor on the LiOH-CO_2 Reaction, Part 1 — Dynamic Isothermal System,* NRL Report 6937 (October 1969).

27. *Closed Circuit Respiration/Ventilation System, Phase 1,* WADD Technical Report 60-33; prepared by Air Reduction Company for U.S. Air Force (January 1960).

28. T. C. Wang, "Decompression Cycling Effects on the Shelf Life of Lithium Hydroxide," *MTS Journal* 9(4), 36 (April 1975).

29. J. G. Smith, "Low Temperature Performance of CO_2 Scrubber Systems," 1973 Diver's Gas Purity Symposium, November 1973, published as Report AD-769 118 by Battelle Laboratories for Supervisor of Diving (Navy).

30. R. B. Cook, *Temperature and Pressure Effects on Sodasorb and Baralyme,* U.S. Naval Academy, TSPR No. 25 (1972).

31. L. J. Nuhn, "Acid-Gas Absorbent," U.S. patent 2,997,445, Aug. 22, 1961.

32. T. C. Wang, "Temperature Effects on Baralyme, Sodasorb, and Lithium Hydroxide," *Ind. Eng. Chem. Process. Dev.* 14(2) 191 (1975).

33. J. Adriani and D. H. Bolten, "The Efficiency of Mixtures of Barium and Calcium Hydroxides in the Absorption of Carbon Dioxide In Rebreathing Appliances," *Anesthesiology* 3(1), 1 (1942).

34. D. H. Batten and J. Andriani, "Clinical and Experimental Studies of Barium and Hydroxide Mixtures (Baralyme) for Carbon Dioxide Adsorption in Anethesic," *Anesth. and Analg.* May-June, 151 (1942).

35. J. W. Mellor, *A Comprehensive Treatise on Inorganic and Theoretical Chemistry,* vol. III., Longman, Green and Co., New York, 1923, p. 817.

36. R. Engle and B. Decken, Claus (Brown Boveri/Krupp Reaktorvbau G.m.b.H.), "Removing Carbon Dioxide and Water from a Gas Stream," U.S. Patent 3,519,384, July 7, 1970.

37. D. W. Holladay and G. L. Haag, "Methods of Immobilizing Carbon Dioxide from Gas Streams," U.S. patent 4,162,298, July 24, 1979.

38. G. L. Haag, "Carbon-14 Immobilization Via the CO_2—$Ba(OH)_2$ Hydrate Gas-Solid Reaction," ORNL/TM-7693 (1981).

39. *Encylopedia of Industrial Chemical Analysis,* vol. 18, Interscience Publishers, Wiley, New York, 1973.

40. B. A. Kondakov, P. V. Kovtunenko, and A. A. Bundel, "Equilibria Between Gaseous and Condensed Phases in the Barium Oxide—Water System," *Russ. J. Phys. Chem.* 38(1), 99-102 (1964).

41. M. Michaud, "Contribution to the Study of the Hydroxides of Potassium and Barium," *Revue de Chimie Mienrale,* t.5, 89 (1968).

42. M. Michaud, "Inorganic Chemistry - Study of the Binary WAter-Barium Hydroxide System," *C. r. hepd. Se'anc. Acad. Sci. Paris* 262.CV, 1143 (1966).

43. *JANAF Thermochemical Data,* calculated and compiled by the Dow Chemical Company, Thermal Laboratory, Midland, Mich. (updated November 1979).

44. F. D. Rossini, D. D. Wagman, W. H. evans, S. Levine, and I. Jaffe, *Selected Values of Chemical Thermodynamic Properties,* Circular 500, U.S. Dept. of Commerce/NBS (February 1952).

45. D. D. Wagman, W. H. Evans, V. B. Parker, I. Halow, S. M. Bailey, and R. H. Schumm, *Selected Values of Chemical Thermodynamic Properties — Tables for the First 34 Elements in the Standard Order of Arrangement,* U.S. Dept. of Commerce/NBS Technical Note 270-3 (January 1968).

46. V. B. Parker, D. D. Wagman, and W. H. Evans, *Selected Values of Chemical Thermodynamic Properties — Tables for the Alkaline Earth Elements,* U.S. Dept. of Commerce/NBS Technical Note 270-6 (November 1971).

47. O. Kubaschewski and E. L. Evans, *Metallurgical Thermochemistry,* Pergamon, London, 1958.

48. P. I. Barin and O. Knacke, *Thermochemical Properties of Inorganic Substances,* Springer-Verlag, New York, 1973.

49. P. B. Danckwerts, *Gas-Liquid Reactions,* McGraw-Hill, New York, 1970.

50. E. L. Fuller, Jr., M. H. Eager, R. W. Smithwick III, and N. R. Smyrl, *Surface Chemistry and Structure of Beryllium Oxide,* Y/DL-282 (1982).

51. Fuller, E. L. Jr., J. B. Condon, M. H. Eager, and L. L. Jones, *Sorption Analyses in Materials Science: Selected Oxides,* Y-DK-264 (1981).

52. Fuller, E. L. Jr., Yoos, T. R. III, and Walia, D. S., *Physiochemical Characterizations of Limestone for Fluidized-Bed Coal Conversion,* ORNL/TM-7292 (1981).

53. E. L. Fuller, Jr., and P. A. Agron, *The Reaction of Atmospheric Vapors with Lunar Soil,* ORNL-5129 (1976).

54. A. W. Czanderna, and S. P. Wolsky, eds., *Methods and Phenomenom 4, Microweighing in Vacuum and Controlled Environments,* Elsevier Scientific, Amsterdam, 1980.

55. J. F. O'Hanlon, *A Users Guide to Vacuum Technology,* Wiley, New York, 1980.

56. *SAS Users Guide-1979 Edition,* SAS Institute, Raleigh, N.C., 1979.

57. P. K. Warme, *Curve Fitter,* Interactive Microware, Inc., State College, Pa., 1980.

58. P. K. Warme, *Scientific Plotter,* Interactive Microware, Inc., State College, Pa., 1981.

59. M. C. Flemings, *Solidification Processing,* McGraw-Hill, New York, 1974.

60. R. E. Reed-Hill, *Physical Metallurgy Principals,* D. Von Nostrand, Princeton, N.J., 1972.

61. Jim Nillis, Sherwin Williams Company, Coffeeville, Kansas, personal communication, 1981.

62. J. F. Rouguerol, *"Texture Study of Divided Solids by Gas Adsorption: Application to Beryllia, Alumina, and to Gels and Oxides,"* Report CEA-R2947, Nuclear Research Center, Sarclay, France, English translation ORNL-tr-1443 (1965).

63. S. J. Gregg, and K. S. Sing, *Adsorption, Surface Area, and Porosity,* Academic Press, London, 1967.

64. S. Lowell, *Instruction Manual for the Quantasorb Sorption System,* Quantachrome Corp., Syosset, N.Y., 1975.

65. E. Robens, and G. Walter, "Determination of Specific Surface Area and Prorsity of Solids," *Analytical Methods 1(B),* Academic Press, New York, 1974, p. 678.

66. J. J. Carberry, *Chemical and Catalytic Reaction Engineering,* McGraw-Hill, New York, 1976.

67. H. Manohar and S. Ramaseshan, "The Crystal Structure of Barium Hydroxide Octahydrate—$Ba(OH)_2 \cdot 8H_2O$," *Zeitschrift fur Kristallographic* Bd. 119, 357 (1964).

68. V. M. Bhatnager, *Clathrate Compounds,* S. Chand and Co., New Delhi, India (1968).

69. A. F. Wells, *Structural Inorganic Chemistry,* Clarendon Press, Oxford (1975).

70. W. J. Moore, *Physical Chemistry,* Prentice-Hall, Englewood Cliffs, N.J., 1972.

71. T. E. W. Schumann, "Heat Transfer: A Liquid Flowing Through a Porous Prism," *J. Franklin Inst.* 208, 405 (1929).

72. C. C. Furnas, "Heat Transfer from a Gas Stream to a Bed of Broken Solids," *Ind. Eng. Chem.* 22, 26 (1930).

73. E. Wicke, "Empirical and Theoretical Studies of the Sorption Rate of Gases in Porous Substances, Part II," *Kolloid-Zeitschrift* 86,295. English translation ORNL-OLS-81-167 (1939).

74. J. B. Rosen, *A Mathematical Investigation of the Fixed Bed Single Solute Chemical System,* Ph.D. dissertation, Columbia University, Columbia, N.Y., 1952.

75. A. Rasmuson, "Exact Solution of a Model for Diffusion and Transient Adsorption in Particles and Longitudinal Dispersion in Packed Beds," *AIChE Journal* 27(6), 1032 (1981).

76. O. Levenspiel, *Chemical Reaction Engineering,* Wiley, New York, 1977.

77. J. Szekely, J. W. Evans, and H. Y. Sohn, *Gas-Solid Reactions,* Academic Press, New York, 1976.

78. O. Levenspiel, and K. B. Bischoff, "Patterns of Flow in Chemical Process Vessels," *Advances in Chemical Engineering,* vol. 4, Academic Press, New York (1963).

79. M. F. Edwards, and J. F. Richardson, "Gas Dispersion in Packed Beds," *Chem. Eng. Sci.* 23, 109 (1968).

80. B. W. Gamson, "Heat and Mass Transfer, Fluid-Solid System," *Chem. Eng. Prog.* 47(1), 19 (1951).

81. R. C. Reid, J. M. Prausnitz, and T. K. Sherwood, *The Properties of Gases and Liquids,* McGraw-Hill, New York, 1966.

82. N. Standish, and G. McGregor, "The Average Shape of a Mixture of Particles in a Packed Bed," *Chem. Eng. Sci.* 33, 618 (1978).

83. D. Kunii, O. Levenspiel, *Fluidization Engineering,* Robert E. Krieger Publishing Co., Huntington, N. Y., 1977.

84. H. Schlicting, *Boundary Layer Theory,* McGraw-Hill, New York, 1955.

85. C. H. Liaw, J.S.P. Wang, R. A. Greenkorn, and K. C. Chao, "Kinetics of Fixed-Bed Adsorption: A New Solution," *AIChE J.* 25(2), 376 (1979).

86. Lapidus, L., *Digital Computations for Chemical Engineers,* McGraw-Hill, New York.

87. L. K. McCune, and R. H. Wilhelm, "Mass and Momentum Transfer in Solid-Liquid System — Fixed and Fluidized Beds," *Ind. Engineering Chemistry* 41(6) 1124 (1949).

88. R. B. Bird, W. E. Stewart, and E. N. Lightfoot, *Transport Phenomenom,* Wiley, New York, 1960.

89. W. L. McCabe, and J. C. Smith, *Unit Operations in Chemical Engineering,* McGraw-Hill, New York (1976).

90. D. Handley, and P. J. Heggs, "Momentum and Heat Transfer Mechanisms in Regular Shaped Packings," *Trans. Inst. Chem. Eng.* 46, T251.

91. T. H. Chilton, and A. P. Colburn, "Mass Transfer (Absorption) Coefficients, Prediction from Data on Heat Transfer and Fluid Friction," *Ind. Eng. Chem.* 26 1183 (1934).

92. F. Yoshida, D. Ramaswami, and O. A. Hougen, "Temperature and Partial Pressure at the Surface of Catalyst Particles," *AIChE J.* 8(1), (1962).

93. G. Langer, A. Roethe, K. P. Roethe, and D. Gelbin, "Heat Mass Transfer in Packed Beds — III. Axial Mass Dispersion," *Int. J. Heat Mass Transfer* 21 751-759 (1978).

94. R. E. Trebal, *Mass Transfer Operations,* McGraw-Hill, New York, 1980.

95. T. K. Sherwood, R. L. Pigford, and C. R. Wilke, *Mass Transfer,* McGraw Hill, New York, 1975.

96. C. D. Scott, *Oxidation of Hydrogen and Carbon Monoxide in a Helium Stream by Copper Oxide, Analysis of Combined Film and Pore Diffusion with Rapid Irreversible Reaction for Two Components in A Fixed-Bed Process,* ORNL/TM-1540 (1966).

97. A. Y. Tan, B. D. Prasher, and J. A. Guin, "Mass Transfer in Nonuniform Packing," *AIChE J.* 21(2), 396 (1975).

98. A. S. Gupta, and G. Thodos, "Mass and Heat Transfer Through Fixed and Fluidized Beds," *Chem. Eng. Prog.* 58 (1962).

99. A. V. Bradshaw, A. Johnson, N. H. McLachlan, and Y-T Chiu, "Heat Transfer Between Air and Nitrogen and Packed Beds of Non-Reacting Solids," *Trans. Inst. Chem. Eng.* 48 T77 (1970).

100. J. G. Sandoval-Robles, J. P. Riba, and J. P. Couderc, "Mass Transfer Around a Sphere," *Trans. Inst. Chem. Eng.* 58 132 (1980).

101. P. F. Y. Wong, N. W. M. Ko, and P. C. Yip, "Mass Transfer from Large Diameter Vibrating Cylinders," *Trans. Inst. Chem. Eng.* 56 214 (1978).

102. M. Leva, and M. Grummer, "Heat Transfer to Gases Through Packed Tubes," *Ind. Chem. Eng.* 40(3), 315 (1948).

103. H. Lescoeur, *Compt. Rend.* 96, 1578 (1883).

104. W. Muller-Erzbach, *Ber.* 10, 1628 (1887).

105. O. Bauer, *Z. Angew. Chem.* 15, 341 (1903).

106. J. Johnston, "Dissociation Pressures of Some Metal Hydroxides and Carbonates," *Z. Phys. Chem.* 68, 83 (1910).

107. S. Tamaru and K. Siomi, "Redetermination of Thermal Dissociation Equilibria of Inorganic Compounds," *V. Z. Phys. Chem.* 171A, 229 (1934).

108. F. B. Marti and M. E. Clavel, "Thermogravimetric Study of Hydrated Strontium and Barium Oxides and Their Reactions with Ammonium Sulfate," *Congr. Interm. Chim. Pure et Appl., 16e, Mem. Sec. Chium. Mienrale* 861 (1958). Translated from French by Ralph McElroy Co., Austin, Tex.

109. M. D. Judd and M. I. Pope, "Monohydrates of Strontium and Barium Hydroxides - Their Preparation and X-ray Powder Patterns," *J. Thermal Anal.* 3, 397 (1971).

110. G. M. Habashy and G. A. Kolta, "Thermal Decomposition of the Hydrates of Barium Hydroxide," *J. Inorg. Nucl. Chem.* 34, 57–67 (1972).

111. H. D. Lutz, R. Heider, and R. A. Becker, "Polymorphism of Barium Hydroxide," *J. Naturforschg.* 24b, 1657 (1969).

112. H. Baernighausen, "Lattice Constants and Space Group of the Isotopic Compounds $Eu(OH)_2 \cdot H_2O$, $Sr(OH)_2 \cdot H_2O$, and $Ba(OH)_2 \cdot H_2O$," *Z. Anorg. Allgem. Chem.* 342, 233 (1966).

113. *Structural Reports for 1952,* vol. 16, p. 324, published for International Union of Crystallography by N.V.A. OOSTHOEK'S UITGEVERS MIJ, UTRECHT, (1952).

114. W. G. Vaux, "Calculating Flow Through Gas Rotameters," *Chem. Eng.* 87(24), 119 (1980).

115. R. E. Sonntag, and G. J. Van Wylen, *Fundamentals of Statistical Thermodynamics,* Wiley, New York, 1966.

APPENDIXES

APPENDIX A.

VAPOR PRESSURE DATA FOR $Ba(OH)_2$ HYDRATES

The vapor pressure of $Ba(OH)_2$ hydrates and even the existence of certain hydrates have been areas of considerable controversy. The existence of $Ba(OH)_2$ compounds with 1, 2, 3, 3.3, 4, 7, 8, 9, and 16 waters of hydration have been cited. However, only two of these, $Ba(OH)_2 \cdot H_2O$ and $Ba(OH)_2 \cdot 8H_2O$, have been commonly observed.[36-46] In this section, a literature review of published $Ba(OH)_2$ hydrate dissociation pressures will be presented in a chronological manner.

Due to the similarity of barium and strontium hydroxide hydrates, the two have often been studied together. One of the earliest studies of $Ba(OH)_2$ hydrates was that of Lescour[103] in 1883. The results of this vapor pressure study presented in Table A.1, indicate two stable hydrates, the mono- and the octahydrate.

Table A.1. $Ba(OH)_2$ hydrate vapor pressure data

Temperature, °C	13.5	20	35.5	58	70	74.5	100
Dissociation pressure							
$Ba(OH)_2 \cdot 8H_2O$, mm Hg	4.5	5.5	20.5	84	124	213	530
$Ba(OH)_2 \cdot H_2O$, mm Hg	<1	1	1	1	1	14	15

Source: H. Lescour, *Compt. Rend.* 96, 1578 (1883).

Muller-Engbach[104] in 1887 also reported the existence of two hydrates; a dihydrate and an octahydrate. The reported dissociation vapor pressure at 15°C for the dihydrate was 1.33 mm Hg and that of the octahydrate was

11.4 mm Hg. In 1903, Bauer[105] reported that $Ba(OH)_2 \cdot 3H_2O$ could be precipitated from a saturated $Ba(OH)_2$ solution at 105°C.

Johnston[106] in 1908 conducted a thorough study of strontium and barium hydroxide hydrates and compared his results with previously published values. From dissociation vapor pressure studies, he reported three stable hydrates: $Ba(OH)_2 \cdot 16H_2O$, $Ba(OH)_2 \cdot 8H_2O$, and $Ba(OH)_2 \cdot 1H_2O$. The vapor pressures for the first two were found to be represented by:

$$t' = t_w + 2.0, \text{ and} \qquad (A.1)$$

$$t' = 0.84\ t_w + 23. \qquad (A.2)$$

In the above equations, t' (°C) is the temperature of the $Ba(OH)_2$ hydrate solid and t_w (°C) is the temperature of water whose vapor pressure is equivalent to the dissociation vapor pressure of the solid. For t' = 54.3°C, t_w = 36.7°C and the vapor pressure of water at 36.7°C is 45.9 mm Hg. He concluded the Muller-Engbach vapor pressure data for $Ba(OH)_2 \cdot 8H_2O$ to be valid for $Ba(OH)_2 \cdot 16H_2O$ and questioned the validity of Lescour's data, particularly in the higher vapor pressure regime.

In 1934, Tamaru and Siomi[107] published the results of a study on the hydrates of $Sr(OH)_2$ and $Ba(OH)_2$. They concluded that the presence of $Ba(OH)_2 \cdot 3H_2O$ and $Ba(OH)_2 \cdot 16H_2O$ could not be confirmed from vapor pressure studies. Also, the water vapor dissociation pressure for conversion of the monohydrate to the anhydrous form could not be determined because of the slow kinetics. The dissociation vapor pressure for the octahydrate was found to be represented by an equation of the form

$$\log P = \frac{-13600}{4.575T} + 10.840\ , \qquad (A.3)$$

where

P = water vapor pressure, mm Hg,

T = temperature, K.

In the opinion of this author, the most comprehensive and credible study conducted to date on the dissociation vapor pressure of $Ba(OH)_2$ hydrates was that of Kondakov, Kovtunenko, and Bundel.[40] The results were published in 1964. In this study, the water vapor pressures of $Ba(OH)_2 \cdot xH_2O$ samples with x values of 0.3896, 1.342, 2.260, 3.282, 4.196, 5.042, 5.882, and 6.763 were determined. When the results were plotted (log P vs 1/T), three distinct lines were obtained, as shown in Figure A.1. The lines correspond to $Ba(OH)_2$ hydrate samples in which the monohydrate, the trihydrate, and the octahydrate were the contributing species to the system's water vapor pressure. The controlling decomposition steps and equations used to predict the dissociation vapor pressure were found to be:

$$Ba(OH)_2 \cdot H_2O(s) \rightleftarrows Ba(OH)(s) + H_2O(g), \qquad (A.4)$$

$$\log P = \frac{-61353}{19.155T} + 12.421; \qquad (A.5)$$

$$Ba(OH)_2 \cdot 3H_2O(s) \rightleftarrows Ba(OH)_2 \cdot 1H_2O(s) + 2H_2O(g), \qquad (A.6)$$

$$\log P = \frac{-62618}{19.155T} + 13.823; \qquad (A.7)$$

$$Ba(OH)_2 \cdot 8H_2O(s) \rightleftarrows Ba(OH)_2 \cdot 3H_2O(s) + H_2O(g), \qquad (A.8)$$

$$\log P = \frac{-58230}{19.155T} + 13.238; \qquad (A.9)$$

where

$P = nt/m^2$, Pa,

T = temperature of the system, K.

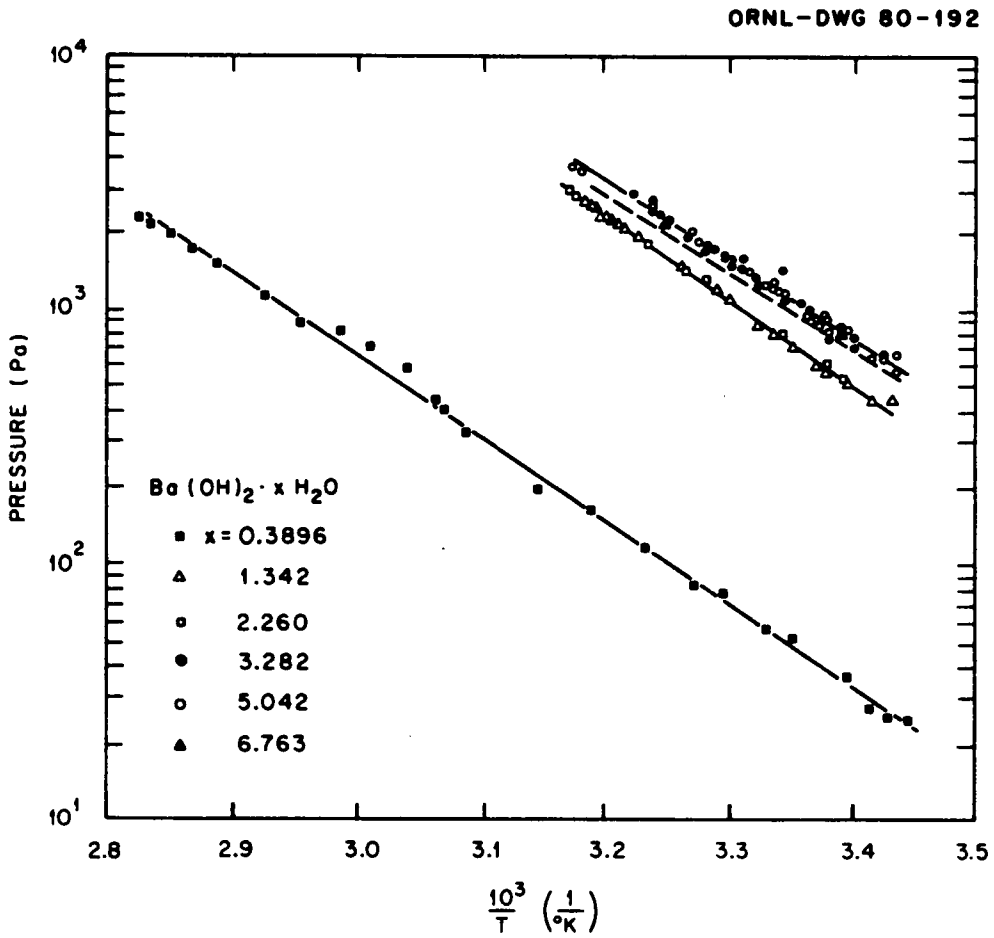


Figure A.1. Dissociation vapor pressure for $Ba(OH)_2$ hydrates. Source of data: B. A. Kondakov, P. V. Kovtunenko, and A. A. Bundel, "Equilibria Between Gaseous and Condensed Phases in the Barium Oxide — Water System," *Russ. J. Phys. Chem.* 38(1), 99-102 (1964).

Using the Van't Hoff equation, the data were analyzed for thermodynamic consistency with the results presented in Table A.2. Based upon the entropy changes for the formation of the trihydrate, they concluded that the trihydrate may be less stable than the other crystalline hydrates.

Table A.2 Vapor pressure analysis for thermodynamic consistency.

Reaction	$\Delta H°_{298}$ (kJ·mol^{-1}) Results	$\Delta H°_{298}$ (kJ·mol^{-1}) Standard tables	Relative error (%)	$\Delta G°_{298}$ (kJ·mol^{-1}) Results	$\Delta G°_{298}$ (kJ·mol^{-1}) Standard tables	Relative error (%)	$S°_{298}$ (kJ·mol^{-1}·K^{-1}) Results	$S°_{298}$ (kJ·mol^{-1}·K^{-1}) Standard tables	Relative error (%)
$Ba(OH)_2 \cdot H_2O(s)$	-1253.500	-1251.900	0.1	-1133.900			171.24		
$Ba(OH)_2 \cdot 3H_2O(s)$	-1862.700			-1616.000			211.01		
$Ba(OH)_2 \cdot 8H_2O(s)$	-3363.700	-3347.300	0.5	-2826.000	-2791.800	0.87	366.76		
$Ba(OH)_2(s)$	-949.980	-947.050	0.3	-886.140	-855.360 -857.040 -836.150	3.37	124.35	103.83	19.7
$Ba(OH)_2$ (aq.)	-965.060	-998.890	3.3	-848.660	875.880	3.1			
BaO(s)		-539.260			528.790			70.338	
$H_2O(g)$		-242.000			228.750			188.82	

Source: B. A. Kondakov, P. V. Kovtunenko, and A. A. Bundel, "Equilibria Between Gaseous and Condensed Phases in the Barium Oxide — Water System," *Russ. J. Phys. Chem.* 38(1), 99-102 (1964).

For comparative purposes, Figure A.1 includes a dashed line which represents the dissociation vapor pressure for $Ba(OH)_2 \cdot 8H_2O$ as determined by Johnston.[106] A review of $Ba(OH)_2$ hydrate vapor pressures at several temperatures, as reported by various researchers, is presented in Table A.3.

Table A.3. Published dissociation vapor pressures for $Ba(OH)_2$ hydrates

Investigator	Reference number	Year published	Temperature (°C)	Pressures of dissociating species, $Ba(OH)_2 \cdot xH_2O$				
				$\cdot H_2O$ (mm Hg)	$\cdot 2H_2O$ (mm Hg)	$\cdot 3H_2O$ (mm Hg)	$\cdot 8H_2O$ (mm Hg)	$\cdot 16H_2O$ (mm Hg)
Lescour	103	1883	20	1			5.5	
Muller-Erzbach	104	1887	15		1.33		11.4	
Johnson	106	1908	17.7				3.6	13.4
Tamaru and Siomi	107	1934	20.0				5.01	
Kondakov et al.	40	1964	20.0	0.234		3.52	5.54	

APPENDIX B.

THE BINARY WATER-$Ba(OH)_2$ SYSTEM

Studies cited thus far have concentrated on the gas-solid system and have attempted to determine from vapor pressure measurements the presence of distinct $Ba(OH)_2$ hydrate species. In 1966, Michaud[41,42] published the results of a study conducted on the liquid-solid equilibria of the binary H_2O-$Ba(OH)_2$ system. After a thorough review of the literature, he concluded that his study was to be the first conducted on this system. In his work, the solubility of $Ba(OH)_2$ and its hydrates in water were determined as a function of system temperature. Where required, the experiments were conducted under pressure to maintain a liquid or liquid-solid system. Thermal analyses, using a calorimeter, were conducted on the precipitated solid to determine the invariant plateaus. The compositions of the precipitants were confirmed by x-ray diffraction analysis. The patterns obtained for the trihydrate were the first reported and are referenced in the ASTM file. The resulting phase diagram is presented in Figure B.1.

Michaud's results indicated the presence of the monohydrate, trihydrate, and octahydrate, which is in agreement with the results of Kondokov, et al.[40] However, he observed a phenomenon that researchers conducting gas-solid studies would likely not observe and which might help to explain prior difficulties in confirming the existence of $Ba(OH)_2 \cdot 3H_2O$. Thermal analysis revealed a plateau between $Ba(OH)_2 \cdot 8H_2O$ and $Ba(OH)_2 \cdot 3H_2O$, signifying the existence of a eutectic phase consisting of $Ba(OH)_2 \cdot 3H_2O$ and $Ba(OH)_2 \cdot 8H_2O$. The eutectic composition was found to

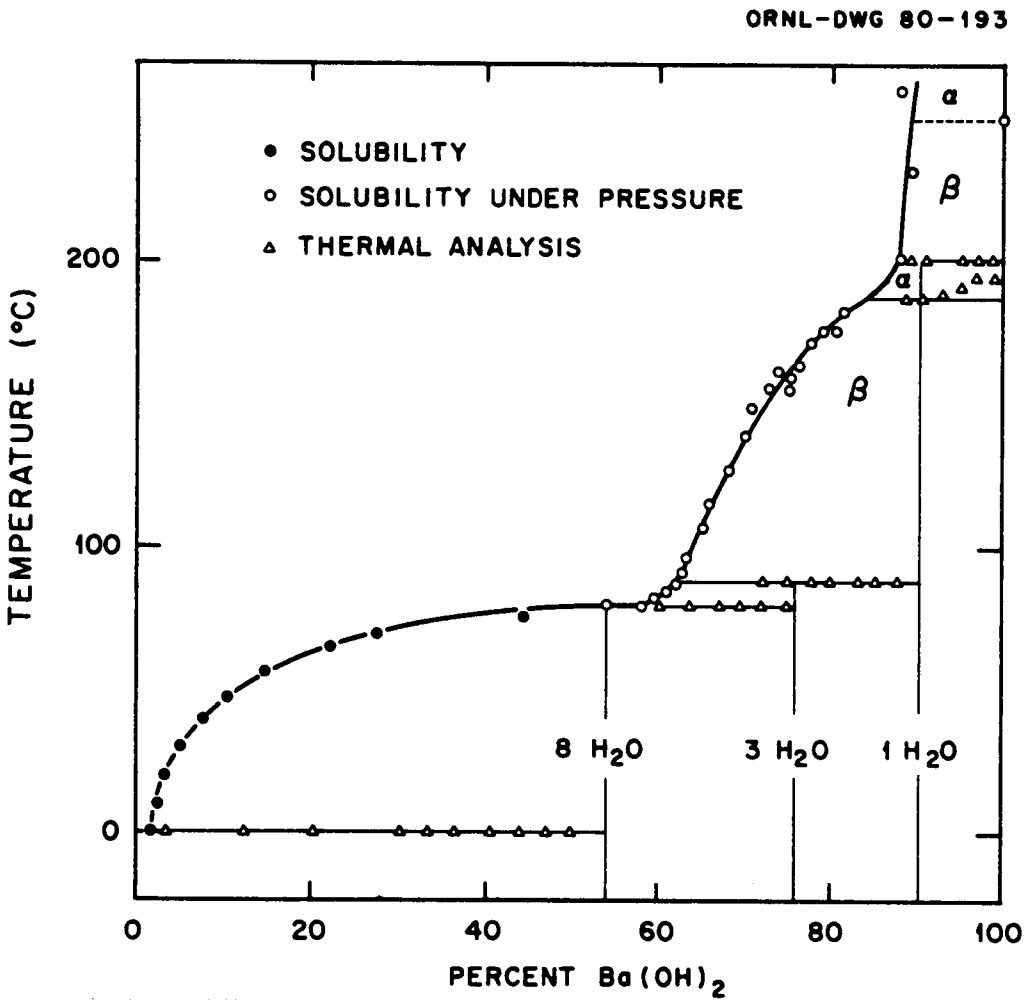


Figure B.1. H_2O-$Ba(OH)_2$ liquid-solid phase diagram. Source: M. Michaud, "Inorganic Chemistry — Study of the Binary Water-Barium Hydroxide System," *C. r. hepd. Se'anc, Acad. Sci.*, Paris 262.CV, 1143 (1966).

consist of 16 mol percent $Ba(OH)_2 \cdot 3H_2O$ and to have a stoichiometric composition of $Ba(OH)_2 \cdot 7.19H_2O$.

APPENDIX C.

THERMAL STUDIES OF $Ba(OH)_2$ HYDRATES

Considerable research has been conducted on the thermal decomposition of alkaline earth hydroxides in the preparation of oxides with favorable electron emission properties. In the course of this work, data obtained via thermo-gravimetric analyses (TGA), thermal or calorimetric analyses, differential thermal analyses (DTA), and evolved gas analyses (EGA) have been published on the hydrates of barium hydroxide. However, these results have often been of questionable quality, since the equipment and experimental objectives were directed toward studies at higher temperatures (i.e., is the decomposition of the hydroxide to the oxide). A major disadvantage of thermal studies, in contrast to vapor pressure and solubility studies, is that they are dynamic in nature. Vapor pressure and solubility studies are conducted in a gas-solid or liquid-solid system at equilibrium, while thermal analyses typically try to locate points of equilibrium by studying the response of a system to dynamic change. Care must be taken to ensure that the response being observed, usually a change in temperature or weight of the sample, is not masked by other phenomena within the system.

In 1958, Marti and Clavel[108] reported the results of a study on hydrates of strontium hydroxide and barium hydroxide. The intent of their study was to distinguish between waters of adsorption, waters of coordination, and constitutional water. Experimental techniques used included differential thermal analysis, chemical analysis, and thermogravimetry under isothermal and temperature ramp conditions. Although the rate of temperature increase was given, the size of the samples was not. Marti

and Clavel reported the existence of two stable hydrates of $Ba(OH)_2$, the mono- and the octahydrate, and they believed the seven waters of hydration released during the reaction $Ba(OH)_2 \cdot 8H_2O \rightarrow Ba(OH)_2 \cdot H_2O$, to be equally volatile.

A similar study in 1971 by Judd and Pope,[109] who have published extensively in the field of thermoanalytical techniques and decomposition modeling, reached the same conclusions. Their sample size was 500 mg, and the presence of the final product, $Ba(OH)_2 \cdot H_2O$, was confirmed by x-ray diffraction analysis. The material was prepared by evacuating samples of $Ba(OH)_2 \cdot 8H_2O$ to 0.1 mm Hg at 25°C for 5 h.

A study by Habashy and Kolta[110] on the thermal decomposition of the hydrates of barium hydroxide, published in 1972, utilized thermogravimetric, differential thermal, x-ray diffraction, and infrared spectral analysis. A unique aspect of this work was that two types of $Ba(OH)_2 \cdot 8H_2O$ samples were used. One type was prepared by precipitating $Ba(OH)_2 \cdot 8H_2O$ crystals from a saturated solution, while the second was prepared by dehydrating the $Ba(OH)_2 \cdot 8H_2O$ crystals at 80°C under a dynamic vacuum to form $Ba(OH)_2 \cdot H_2O$, followed by rehydration in moist air to form $Ba(OH)_2 \cdot 8H_2O$.

Their results, presented in Figure C.1., indicate the presence of three hydrates: $Ba(OH)_2 \cdot H_2O$, $Ba(OH)_2 \cdot 2H_2O$, and $Ba(OH)_2 \cdot 8H_2O$. However, the preparation of $Ba(OH)_2 \cdot 2H_2O$ was possible only under specially controlled conditions. When recrystallized $Ba(OH)_2 \cdot 8H_2O$ was subjected to a vacuum at temperatures ranging from 30 to 150°C for several hours, the dehydrated product was β-$Ba(OH)_2 \cdot H_2O$. A similar product was obtained when the dehydration took place in air at 150°C; however, when the

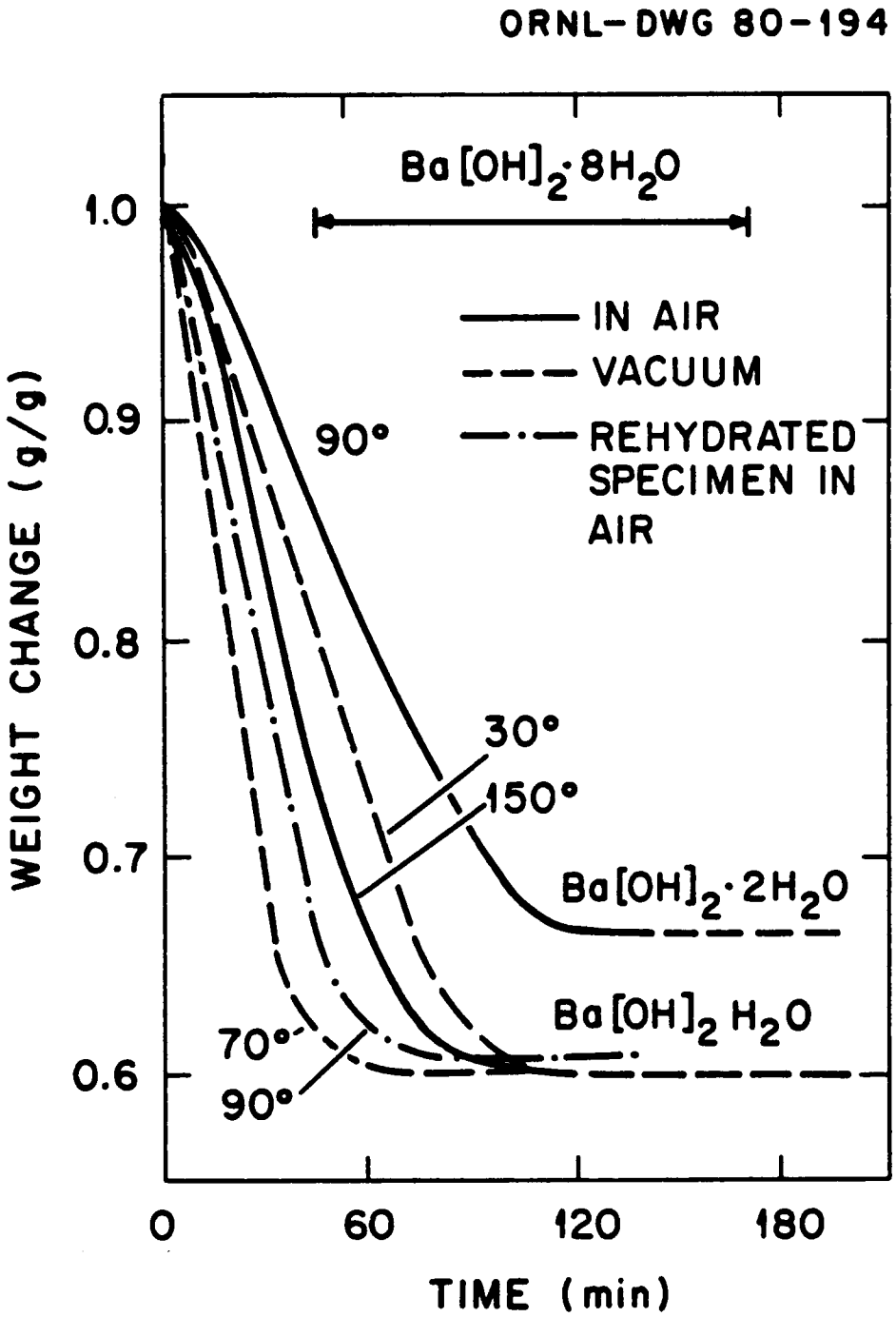


Figure C.1. Thermogravimetric study of $Ba(OH)_2 \cdot 8H_2O$ samples prepared by different techniques. Source: G. M. Habashy and G. A. Kolta, "Thermal Decomposition of the Hydrates of Barium Hydroxide," *J. Inorg. Nucl. Chem.* 34, 57-67 (1972).

material was dehydrated in air at temperatures less than 90°C for several hours, the resulting product was $Ba(OH)_2 \cdot 2H_2O$. Formation of this compound was subsequently verified by a separate endothermic peak during differential thermal analysis, a distinctive infrared spectrum, and by an x-ray diffraction pattern that was distinct from those published for α- and β-$Ba(OH)_2 \cdot H_2O$, $Ba(OH)_2 \cdot 3H_2O$, and $Ba(OH)_2 \cdot 8H_2O$. However, the dihydrate was not observed during similar studies on the rehydrated $Ba(OH)_2 \cdot 8H_2O$. Habashy and Kolta concluded that the formation of the dihydrate was dependent upon the rate of water removal from the decomposition interface. They speculated that the two lower hydrates are formed by one of the following mechanisms:

$$Ba(OH)_2 \cdot 8H_2O(s) \rightleftharpoons \text{amorphous product} + H_2O(g) \xrightarrow{\text{rehydration}} Ba(OH)_2 \cdot 2H_2O(s)$$

or

$$Ba(OH)_2 \cdot 8H_2O(s) \rightleftharpoons \text{amorphous product} + H_2O(g) \xrightarrow{\text{activated diffusion}} Ba(OH)_2 \cdot H_2O \qquad \text{(C.2)}$$

They concluded that when a dynamic vacuum was applied to the system, the rate of diffusion was increased or activated, resulting in more rapid water removal at the decomposition interface. The formation rate of the dihydrate would likely be dependent upon a kinetic rate constant and the water vapor partial pressure, thus it would be impaired by vacuum application, so that the reaction would likely proceed via the mechanism of Equation C.1. They also speculated that the rehydrated sample would possess a more open structure as a result of the prior dehydration and subsequent rehydration, causing the diffusion of water molecules from the structure to be more rapid than that from the precipitated octahydrate.

Hence, the reaction mechanism of Equation C.2 would control the dehydration process. These results were cited to parallel those of earlier studies conducted by Habashy on $BeSO_4$ and $CaSO_4$, where the existence of monohydrate and hemihydrate phases were confirmed.

APPENDIX D.

CRYSTAL PROPERTIES OF $Ba(OH)_2$ HYDRATES AND $BaCO_3$

The crystalline structure of $Ba(OH)_2 \cdot 8H_2O$ has been determined to be monoclinic[67] and a member of the C^5_{2b}—$P2_1/n$ space group, having a unit cell with four formula units of a = 9.35 Å, b = 9.28 Å, c = 11.87 Å, and $\beta = 99°$. The calculated crystal density is 2.06 g/cm^3; the measured density is 2.18 g/cm^3. The barium cation is coordinated by eight water oxygens in the form of a slightly distorted Archimedian prism at a distance of 2.69 to 2.77 Å. The unit cell has been shown to consist of 4 barium cations, 8 hydroxyl ions, and 32 water molecules. Studies[67] have indicated that each hydroxyl ion is surrounded by five water molecules and one hydroxyl ion as closest neighbors, a factor of potential significance in the overall reaction mechanism with an acid gas.

Relatively little information is available on the crystalline structure of $Ba(OH)_2 \cdot 3H_2O$, although it does possess a unique x-ray diffraction pattern. Bauer[105], in some studies published in 1903, stated that crystalline $Ba(OH)_2 \cdot 3H_2O$ could be prepared from a saturated $Ba(OH)_2$ solution maintained at 105°C. He determined the structure to be rhombic with an a:b:c ratio of 0.58905:1:0.7803.

In 1969, Lutz, Heider, and Becker[111] published the results of an infrared absorption study on $Ba(OH)_2$ and $Ba(OH)_2 \cdot H_2O$. Their results indicated that $Ba(OH)2 \cdot H2O$ exists in two stable forms designated beta (β) and gamma (γ). The β phase is more stable and is commonly prepared by the room temperature evacuation of $Ba(OH)_2 \cdot 8H_2O$. The γ form is unstable at room temperature, but it may be prepared at 60°C by evacuating a $Ba(OH)_2 \cdot 8H_2O$ sample to a pressure of 10^{-4} mm Hg. It may also be prepared by contacting β-$Ba(OH)_2$ with a moist stream of nitrogen or by the hydrolysis of barium alcoholates. Because of a lack of data, uncertainty exists as to whether the γ-$Ba(OH)_2 \cdot H_2O$ is identical to the α-$Ba(OH)_2 \cdot H_2O$ observed by Michaud[41,42] in his phase diagram studies (Appendix B). A second factor of interest in the study by Lutz et al.[111] is the difficulty that was cited in interpreting the infrared-sorption spectrum. They attributed this to the presence of amorphous compounds. However, they were uncertain as to whether these compounds were stable species or reaction intermediates. The most common monohydrate, β-$Ba(OH)_2 \cdot H_2O$, is a member of the $P2_1/am$ space group.[113] It has an orthorhombic structure with unit cell lengths of a = 6.9522 Å, b = 6.3657 Å, and c = 3.8947 Å. The crystal density is 3.65 g/cm^3.

The final product of interest in the present investigation, $BaCO_3$, may exist in one of three stable crystalline forms: gamma, beta, and alpha.[113] The gamma form, sometimes referred to as witherite and the most common, is orthorhombic, with cell dimensions of a = 8.8345 Å, b = 6.549 Å, and c = 5.2556 Å. The crystal density is 4.43 g/cm^3. The gamma transforms to the beta form and finally to the alpha form at 811 and 982°C, respectively. Decomposition of $BaCO_3$ occurs at ~1450°C.

APPENDIX E.

SPECIFICATIONS FOR COMMERCIAL $Ba(OH)_2 \cdot 8H_2O$

SHERWIN WILLIAMS CHEMICALS

Specifications

Barium Octahydrate

$Ba(OH)_2 \cdot 8H_2O$

Grade: 065

For General Application

Chemical Analysis	Specifications
Total Barium (weak acid soluble) as BaO %	49.0 - 51.0
$BaSO_4$ (acid insoluble) %	0.1 max.
$BaCO_3$ %	0.8 max.
Cl %	0.02 max.
S (as sulfide) %	0.02 max.
Fe %	0.002 max.
Other Properties	
Appearance	White dry flakes
Apparent Packed Bulk Density, lb/ft^3	65

This information is believed reliable; however, all recommendations are made without guarantee, since the conditions of use are beyond our control. All products are sold without warranty, expressed or implied, and on the condition that purchasers shall make their own tests to determine the suitability of such products for their purposes and that all risks are assumed by the user. Statements contained herein shall not be construed to be a recommendation to infringe any patent.

The Sherwin-Williams Company, Chemicals Division, P.O. Box 6520, Cleveland, Ohio 44101.

© 1977 The Sherwin-Williams Company

277

APPENDIX F.

CALCULATION OF CORRECTION FOR THE BUOYANCY EFFECT IN MICROBALANCE STUDIES

One must remember that a balance-beam microbalance operating outside a vacuum measures an apparent weight or force, rather than mass. Therefore, buoyancy effects must often be accounted for to insure that a real mass measurement is obtained. This is particularly true when the sample being weighed is at the temperature of liquid nitrogen (~77 K) and the counter-balance weight is at ambient temperature.

For the following derivation of a buoyancy effect correction factor, the reasonable assumption of gas ideality will be used. Applying Archimedes' principle, that the decrease in weight caused by the buoyancy effect is equal to the weight of the displaced gas, the net weight change for a balance-beam microbalance is then the difference between the buoyancy effects for the sample-side and for the counterbalance-side. Therefore,

$$\Delta W = \rho_{(gas-s)}\, V_s - \rho_{(gas-c)} \cdot V_c, \qquad (F.1)$$

where

$\rho_{(gas)-s}$ gas density at sample-side conditions,

V_s = volume of sample-side items,

$\rho_{(gas)-c}$ = gas density at counterbalance-side conditions,

V_c = volume of counterbalance-side items.

The sample volume is related to the sample mass and density by the following expression:

$$V_i = \frac{m_i}{\rho_i} , \tag{F.2}$$

where

V_i = volume of sample i,

m_i = mass of sample i,

ρ_i = density of sample i.

Assuming an ideal gas,

$$\rho_{gas-i} = MW \frac{P}{RT_i} , \tag{F.3}$$

where

MW = molecular weight of gas,

P = pressure,

R = ideal gas constant,

T_i = absolute temperature of i.

Combining Equations (F.1), (F.2), and (F.3), one obtains:

$$\Delta W = \frac{MW}{R}\left[\frac{m_s}{\rho_s T_s} - \frac{m_c}{\rho_c T_c}\right] P . \tag{F.4}$$

To be totally accurate, the buoyancy effects resulting from the sample, the counter-balance weight, the sample pans, and the suspension wires at their respective temperatures, as well as the unsymmetrical properties of the balance beam must be accounted for. However, the approach used in this study was to place on the sample-side a weight of known mass

and density and to experimentally determine the correction factor that would account for buoyancy effects and other system factors. Buoyancy corrections between other samples and this reference weight could then be calculated, using the preceding equations. A 150-mg, class-M weight, constructed of tantalum with a density of 16.6 g/cm^3 was used as the reference weight. The sample side with the reference weight was placed in a liquid nitrogen bath, and the ΔW effect as a function of N_2 pressure was determined. This is represented by the lower line in Figure F.1. As expected, no curvature was observed, indicating negligible surface adsorption and other nonlinear effects. (Surface adsorption did occur, but the effect was negligible because of the small surface area.) A linear, least-squares analysis provided the following equation, with a correlation coefficient of 0.9999.

$$\Delta W = -0.00052896\ P - 0.0754817\ , \qquad \text{(F.5)}$$

where

ΔW = apparent weight change, mg,

P = absolute pressure, mm Hg.

As the absolute pressure approaches zero, one would expect the bouyancy effect also to approach zero. It is speculated that the nonzero intercept in the preceding equation results from thermomolecular effects on the sample-side hangdown wire as the temperature changes from 77 K to ambient.[63]

Equation (F.4) may be rearranged in the following manner:

$$\Delta W = \frac{MW}{R}\left[\frac{m_s}{\rho_s T_s} - \frac{m_R}{\rho_R T_R} + \frac{m_R}{\rho_R T_R} - \frac{m_c}{\rho_c T_c}\right] P\ , \qquad \text{(F.6)}$$

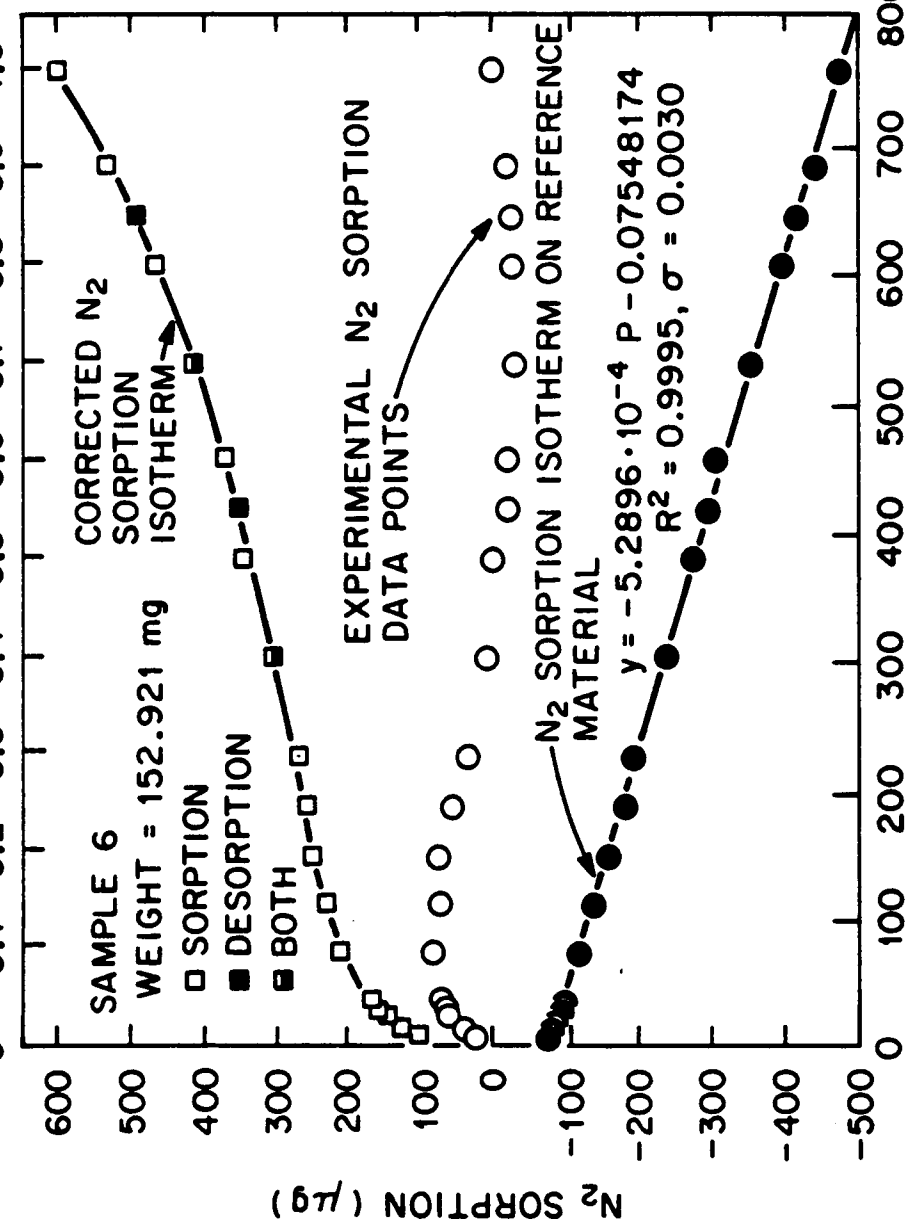


Figure F.1. Adsorption isotherm data obtained with a balance-beam microbalance.

or

$$\Delta W = \frac{MW}{R}\left[\frac{m_s}{\rho_s T_s} - \frac{m_R}{\rho_R T_R}\right] + \frac{MW}{R}\left[\frac{m_R}{\rho_R T_R} - \frac{m_c}{\rho_c T_c}\right] P \ , \qquad \text{(F.7)}$$

where subscript R refers to the 150-mg tantulum reference weight. From the microbalance system, the last term in Equation (F.7) was experimentally determined to be represented by Equation (F.5). Furthermore, both the reference and the sample mass are at ~77 K, and the buoyancy effects from the sample wire, pan, and other items cancel. Therefore, the mass and density terms are those of the actual reference and sample materials. Rearrangement of Equation (F.7) gives a true correction factor for the microbalance system:

$$\Delta W_{CF} = \frac{MW}{RT}\left[\frac{m_s}{\rho_s} - \frac{m_R}{\rho_R}\right] P + 0.00052896P + 0.0754817 \qquad \text{(F.8)}$$

where ΔW_{CF} = correction factor, mg. For nitrogen adsorption studies at 77 K, the preceding equation reduces to:

$$\Delta W_{CF} = 5.81938 \times 10^{-3}\left[\frac{m_s}{\rho_s} - \frac{0.150}{16.6}\right] P + 0.00052896\ P + 0.0754817 \ , \qquad \text{(F.9)}$$

where

m_S = mass of the sample, g,

ρ_S = density of the sample, g/cm^3,

P = system pressure, mm Hg, and

ΔW_{CF} = apparent weight change, or buoyancy factor.

A true mass reading is then obtained by subtracting Eq. (F.9) from the indicated microbalance weight of a sample:

$$M = W - \Delta W_{CF} \ , \qquad \text{(F.10)}$$

where

M = true mass, mg, and

W = indicated microbalance weight, mg.

Presented in Figure (F.1) are the observed weight changes for a nitrogen isotherm (middle data points), and the final isotherm obtained from Equation (F.10) (upper curve). This isotherm was obtained from a $BaCO_3$ sample.

APPENDIX G.

SORPTION THEORY

The BET Adsorption Theory

In the development of the BET adsorption theory, the following assumptions are made:

1. Equilibrium exists between each layer of adsorbate and the adsorbate vapor pressure.
2. The solid is nonporous.
3. The bonding energy between the adsorbent and the adsorbate is much greater than between the adsorbate layers.
4. The bonding energy between subsequent layers is constant.
5. The ratio of adsorption-desorption kinetic terms for the second and subsequent layers is constant.

This derivation of the BET adsorption equation will follow an approach similar to that presented by Carberry.[66] As stated in assumption 1, equilibrium is assumed to exist between each layer of adsorbate and the adsorbate vapor pressure. At equilibrium, the rate of molecules adsorbing on a given layer must equal the number of molecules escaping. From a statistical perspective, the energy of the adsorbed molecules may be represented by the Boltzman Distribution Law.[70,115]

$$N_j = g_j \exp(-\alpha) \exp(-\varepsilon_j/kT) , \qquad (G.1)$$

where

N_j = number of molecules in state j,

g_j = degeneracy of state j,

α = constant,

ε_j = molecular energy of state j ,

k = Boltzman constant,

T = absolute temperature.

If we assume that there are many molecules and that the distinct energy levels may be approximated by a continuous function, the following equations may be developed.

$$\underset{j=o}{\overset{j=A}{N_j}} = \frac{\sum_{j=0}^{j=A} N_j \Delta\varepsilon_j}{\sum_{j=0}^{j=A} \Delta\varepsilon_j} = \frac{\int_0^{\varepsilon_A} N_j d\varepsilon}{\int_0^{\varepsilon_A} d\varepsilon} = \frac{g \exp(-\alpha) \int_0^{\varepsilon_A} \exp\left(\frac{\varepsilon}{-kT}\right) d\varepsilon}{\int_0^{\varepsilon_A} d\varepsilon} \qquad (G.2)$$

The fraction of molecules with energy $\leq \varepsilon_A$ is then:

$$\frac{N\ \varepsilon \leq \varepsilon_A}{N\ \varepsilon = \infty} = \frac{\left(N\ \varepsilon \leq \varepsilon_A\right)}{N_{Total}} = \frac{\int_0^{\varepsilon_A} \exp\left(\frac{\varepsilon}{-kT}\right) d\varepsilon}{\int_0^{\infty} \exp\left(\frac{\varepsilon}{-kT}\right) d\varepsilon}$$

$$= \frac{\exp\left(\frac{-\varepsilon_A}{kT}\right) - 1}{-1} \qquad (G.3)$$

$$= 1 - \exp\left(\frac{-\varepsilon_A}{kT}\right)$$

Therefore, the fraction of molecules with energy in excess of ε_A is:

$$\frac{N\left(\varepsilon > \varepsilon_A\right)}{N_{Total}} = \exp\left(\frac{-\varepsilon_A}{kT}\right). \qquad (G.4)$$

The surface area covered by a layer of molecules may be represented by

$$s_i = A_o N_i \ , \tag{G.5}$$

where

s_i = surface area covered by layer i,

A_o = specific area per molecule,

N_i = number of molecules on layer i.

Therefore for a given layer of adsorbates, substitution of Equation (G.4) into Equation (G.5) results in the surface fraction of that layer with molecules of $\varepsilon > \varepsilon_A$, or

$$\frac{s\left(\varepsilon>\varepsilon_A\right)}{s_i} = \exp\left(\frac{-\varepsilon_A}{kT}\right). \tag{G.6}$$

Multiplying the denominator and numerator of the exponential term by the Avogadro number, one obtains:

$$\frac{s\left(E>E_A\right)}{s_i} = \exp\left(\frac{-E_A}{RT}\right), \tag{G.7}$$

where

E_A = activation energy,

R = gas constant.

The meaning of E_A may now be clarified. For bonding between the adsorbate and adsorbent, it is a measure of bond strength and is frequently termed the heat of adsorption. For bonding between adsorbate molecules in subsequent layers, the activation energy (E_A) is assumed to be equal to the latent heat of liquifaction or condensation for the adsorbate[63]

(~5.65 kJ/mol for N_2 at 77 K). For equilibrium to exist, the rate of adsorption must equal the rate of desorption, as represented by the following equation.

$$a_1 s_0 P = b_1 s_1 , \tag{G.8}$$

where

a_1 = kinetic adsorption factor,

s_0 = unoccupied surface,

P = adsorbate pressure,

b_1 = proportionality factor,

s_1 = surface area of first layer possessing sufficient energy for desorption.

Substitution of Equation (G.8) into Equation (G.7) results in the following equation:

$$a_1 s_0 P = b_1 s_1 \exp\left(\frac{-E_1}{RT}\right) . \tag{G.9}$$

For subsequent layers, one obtains:

$$a_i s_{(i-1)} P = b_i s_i \exp\left(\frac{-E_i}{RT}\right) . \tag{G.10}$$

The total surface area, S, of the solid may be expressed as

$$S = \sum_{i=0}^{i=\infty} s_i . \tag{G.11}$$

The assumption of a nonporous solid enables the upper limit of the summation to be infinity. The volume of gas adsorbed on the monolayer per unit surface area is

$$Q = \frac{V_M}{S} , \tag{G.12}$$

where V_M = volume of molecules on monolayer. Therefore, the total volume of gas adsorbed is given by

$$V = Q \sum_{i=0}^{i=\infty} s_i = \frac{V_M}{S} \sum_{i=0}^{i=\infty} i s_i \ , \qquad (G.13)$$

Rearranging,

$$\frac{V}{V_M} = \frac{\sum_{i=0}^{i=\infty} i s_i}{\sum_{i=0}^{i=\infty} s_i} \ . \qquad (G.14)$$

Upon rearrangement of Equations (G.9) and (G. 10), one obtains:

$$s_1 = \frac{a_1}{b_1} P s_0 \quad \exp\left(\frac{E_1}{RT}\right) \ , \qquad (G.15)$$

$$s_2 = \frac{P}{g} s_1 \exp\left(\frac{E_2}{RT}\right), \text{ and} \qquad (G.16)$$

$$g = \left(\frac{b}{a}\right)_{i>1} . \qquad (G.17)$$

The energy of activation for the monolayer, E_1, is assumed to be much greater than that of the subsequent layers. Furthermore, the activation energies of subsequent layers are assumed to be equal to the heat of liquifaction (E_L). The preceding equations may be combined such that Equation (G.17) is a direct function of s_0, the free surface area:

$$s_2 = \left(\frac{a}{b}\right)_1 \frac{P^2}{g} \exp\left[\frac{E_1}{RT}\right] \quad \exp\left[\frac{E_L}{RT}\right] s_0 \ . \qquad (G.18)$$

The ratio of kinetic terms for the second and subsequent layers, $\left(\frac{a}{b}\right)_{i>1}$, is also assumed to be a constant which results in the following general equation:

$$s_i = \left(\frac{a}{b}\right)_1 g \exp\left[\frac{E_1 - E_L}{RT}\right] \left(\frac{P}{g}\right)^i \exp\left[\frac{iE_L}{RT}\right] s_0 \ . \qquad \text{(G.19)}$$

The following definitions are now made.

$$y = \left(\frac{a}{b}\right)_1 P \exp\left[\frac{E_1}{RT}\right] , \qquad \text{(G.20)}$$

$$x = \frac{P}{g} \exp\left[\frac{E_L}{RT}\right] , \text{ and} \qquad \text{(G.21)}$$

$$c = \frac{y}{x} = \left(\frac{a}{b}\right)_1 g \exp\left[\frac{E_1 - E_L}{RT}\right] . \qquad \text{(G.22)}$$

Combining Equations (G.19) and (G.22), one obtains:

$$s_i = c\left(\frac{P}{g}\right)^i \exp\left[\frac{iE_L}{RT}\right] s_0 \qquad \text{(G.23)}$$

This equation may be further simplified via Equation (G.21),

$$s_i = cx^i s_0$$

Upon substitution into Equation (G.14), one obtains:

$$\frac{V}{V_M} = \frac{\sum_{i=0}^{i=\infty} i s_i}{\sum_{i=0}^{i=\infty} s_i} = \frac{\sum_{i=0}^{i=\infty} ic\, x^i\, s_0}{\sum_{i=0}^{i=\infty} s_i} \qquad \text{(G.24)}$$

$$= \frac{\sum_{i=0}^{i=\infty} ic\, x^i s_0}{s_0 + \sum_{i=0}^{i=\infty} cx^i\, s_0} \qquad \text{(G.25)}$$

$$= \frac{c\sum_{i=0}^{i=\infty} ix^i}{1 + c\sum_{i=1}^{i=\infty} x^i} \qquad (G.26)$$

It can be shown that:

$$(1 - x)\sum_{i=1}^{i=n} x^i = x - x^{(n+1)} \qquad (G.27)$$

For $x<1$, the physical meaning of $x<1$ to be demonstrated in a subsequent step and $n \to \infty$, this equation reduces to

$$\sum_{i=1}^{i=n} x^i = \frac{x}{1 - x} . \qquad (G.28)$$

Also, the following identity may be shown to be valid.

$$\sum_{i=1}^{i=n} ix^i = x\frac{d}{dx}\sum_{i=1}^{i=n} x_i . \qquad (G.29)$$

Combining the two preceding equations,

$$\sum_{i=1}^{i=n} ix^i = x\frac{d}{dx}\left[\frac{x}{1 - x}\right] = \frac{x}{(1 - x)^2} . \qquad (G.30)$$

Equations (G.28) and (G.30) are now substituted into Equation (G.23) to obtain

$$\frac{V}{V_M} = c\frac{x}{(1 - x)^2}\frac{1}{1 + c\frac{x}{(1 - x)}} = \frac{cx}{(1 - x)(1 - x + cx)} . \qquad (G.31)$$

Previously, we defined x in the following manner:

$$x = \frac{P}{g}\exp\left(\frac{E_L}{RT}\right) . \qquad (G.32)$$

At $P = P_0$, the saturation vapor pressure, the term $\frac{V}{V_M}$ must approach infinity. For this to occur, x must approach 1.0;

$$x_{P \to P_0} = \frac{P_0}{g} \exp\left(\frac{E_L}{RT}\right) = 1.0 \; ; \tag{G.33}$$

or

$$P_0 = g \exp\left(\frac{-E_L}{RT}\right) . \tag{G.34}$$

Thus,

$$x = \frac{P}{P_0} < 1.0 \tag{G.35}$$

Equation (G.31) now reduces to:

$$\frac{V}{V_M} = \frac{c \; P/P_0}{[1 - (P/P_0)][(1 - P/P_0) + (cP/P_0)]} \tag{G.36}$$

$$= \frac{cP}{(P_0 - P)[1 + (c-1) \; P/P_0]}$$

After further rearrangement, one obtains the widely used BET equation,

$$\frac{P}{(P_0 - P)V} = \frac{1}{cV_M}\left[1 + (c-1)\frac{P}{P_0}\right] = \frac{1}{cV_M} + \frac{(c-1)}{cV_M}\left(\frac{P}{P_0}\right) . \tag{G.37}$$

Plotting the term $P/[V(P_0 - P)]$ on the ordinate axis and P/P_0 on the abscissa, a straight line would be expected for systems with constant V_M and c. With knowledge of the slope and intercept, the monolayer volume (V_M) and the c value may be determined. Generally, the BET equation is assumed applicable over the range of $0.05 < P/P_0 < 0.35$. However, this range is dependent upon the properties of the solid and the

extent of deviation from the original assumptions. As has been pointed out by Fuller,[50–54] the adsorption properties of the solid over the entire pressure range, $0 < (P/P_0) < 1.0$, must be used in establishing the validity of the BET equation over any range. This topic will be discussed more fully in the section entitled "Polarization Theory and the Sorption Potential Model."

Using the microbalance data presented in Appendix F, the adsorption isotherm, Figure F.1, was linearized via Equation (G.37) and the results are presented in Appendix H (Sample 6). Since mass was the dependent variable rather than volume, Equation (G.34) was modified by replacing the volume terms, V and V_M, with mass terms, Γ and Γ_M, and using the data for nitrogen adsorbate presented in Table III.B.1 (3480 m^2/g adsorbate at monolayer coverage). The saturation vapor pressure, P_0, was experimentally determined to be ~757 mm Hg. For Sample 6, the surface area was determined to be 4.44 m^2/g and the correlation coefficient of the straight line was 0.9946. The value of c was found to be 263. Since c was defined in Equation (G.22) as:

$$c = \left(\frac{a}{b}\right)_1 g \exp\left(\frac{E_1 - E_L}{RT}\right),$$

this value for c leads to the conclusion that the adsorbent–adsorbate bonding is very strong and is much greater than the bonding in subsequent layers ($E_1 >> E_L$). This phenomenom is commonly observed for adsorption on oxides, hydrated oxides,[63] and carbonates.[50–53]

For such systems, the BET surface area may be estimated via a single-point method.[64] For large values of c, Equation (G.37) reduces to:

$$\frac{P}{(P_0 - P)V} = \left(\frac{1}{V_M}\right)\left(\frac{P}{P_0}\right) \qquad (G.38)$$

$$(P_0 - P)V = P_0 V_M \tag{G.39}$$

$$V = \left(\frac{P_0 - P}{P_0}\right) V \tag{G.40}$$

The choice of the adsorbate partial pressure for the single-point method is important. Adsorbate partial pressures generally must fall within the linear range of the BET equations (typically 0.05 to 0.35). Analytical accuracy is usually improved at the higher gas concentrations because of the greater adsorption.

Analysis of Porous Solids

When the assumptions implicit in the development of the BET equation are no longer valid, care must be exercised in the interpretation of adsorption isotherm data. Such a situation exists when pores are present within the solid.[50–54, 62–66] The presence of pores reduces the upper summation limits in Equation (G.14) from infinity to a finite number. Furthermore, when extremely small micropores (diam <2 nm) exist within the solid, the adsorbate may be bonded to more than one surface, causing experimental data to indicate an excessively large heat of adsorption. Such physical adsorption is often difficult to distinguish from chemisorption in which a chemical bond is formed. Its presence may often be detected through the use of several adsorbates of differing diameters. Pores are usually classified by their mean width, d, as presented in Table G.1.

For these reasons, application of the BET equation is often limited to the regime, $0.05 < P/P_0 < 0.35$. A typical BET isotherm is presented in

Table G.1. Pore classification

Pore type	Pore width (nm)	Relative pressure range for adsorption
macropores	>50	>0.95
mesopores	2–40	0.35–0.95
micropores	<2	<0.35

Source: E. Robens, and G. Walter, "Section 9.7 Determination of Specific Surface Area and Porosity of Solids," *Analytical Methods* 1(B), 678, Academic Press, New York, 1974.

Figure G.1, along with the associated adsorption and desorption phenomena which may occur as a function of P/P_0.

The hysteresis shown in Figure G.1 is indicative of either a nonrigid solid or the presence of meso- and macropores. At ~77 K, the solid is usually assumed to be rigid, and the hysteresis likely results from pore filling and emptying.

Lord Kelvin[66] observed that the vapor pressure of a liquid in a small diameter capillary was less than the normal free surface vapor pressure. He attributed the difference to surface tension forces between the liquid and the capillary wall. For the evaporation of a liquid at a given temperature, the Helmholtz free energy change per unit mass is a state function and is equivalent to the negative of the energy available from the system as work, external work, and PdV work under reversible conditions. For the case of evaporation from a free surface in a closed isothermal system with no external work (assuming gas ideality), the following equations are applicable:

$$n(\Delta A_v) = n[-SdT - PdV] = n[-PdV] = nRT \ln(P_0/f_L) = 0.0 , \qquad (G.41)$$

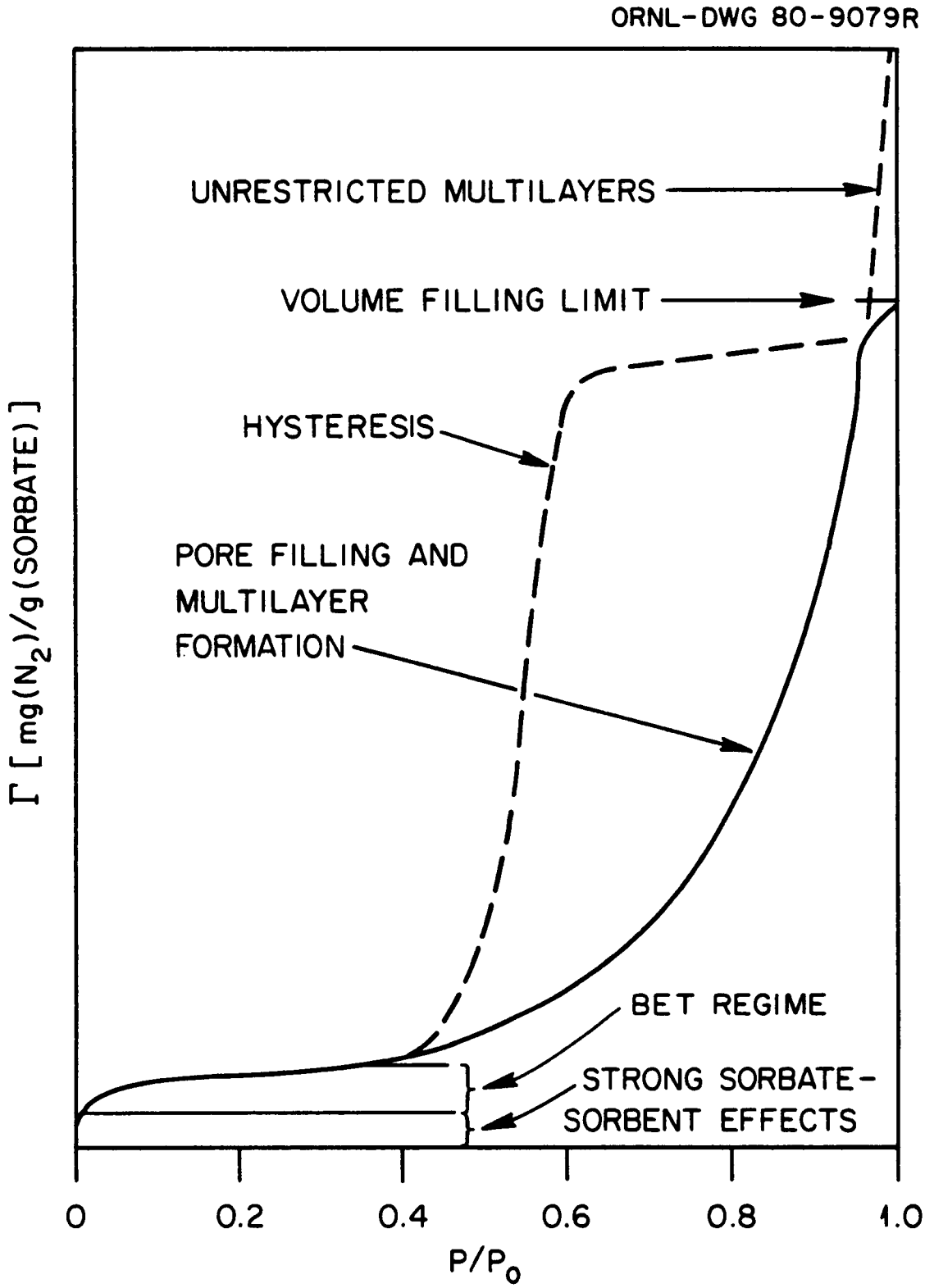


Figure G.1. Representative adsorption isotherms and associated sorption phenomenon.

where

n = moles evaporated

ΔA_v = Helmholtz free energy of vaporization,

S = entropy,

W = work done by the system,

V = volume,

P = pressure,

R = gas constant,

T = absolute temperature,

P_0 = saturation vapor pressure,

f_L = liquid fugacity.

Assuming that equilibrium is maintained in the isothermal system, the entire work energy is available as PdV energy. However, for the evaporation of a liquid in a capillary, a portion of the total free energy is required to move a force, surface tension times perimeter, through a distance. Mathematically, the equations are represented by

$$n\Delta A_v = nRT \ln(P/f_L) = -\sigma \mathrm{Cos}\Theta dA \ , \qquad (G.42)$$

where

P = vapor pressure,

σ = surface tension,

A = area,

Θ = angle of contact.

Combining Equations (G.41) and (G.42) and assuming the angle of contact to be ~0°,

$$nRT \ln(P/P_0) = -\sigma dA \ . \qquad (G.43)$$

Assuming cylindrical pores, one may now make the following substitutions:

$$dA = 2\pi r dl \ , \qquad (G.44)$$

where r = pore radius, and l = pore length; and

$$n = \frac{dV}{V_M} = \frac{\pi r^2 dl}{V_M} , \qquad (G.45)$$

where V_M = molar volume. Upon combining Equations (G.43), (G.44), and (G.45), one obtains:

$$\ln (P/P_0) = - \frac{V_M \, 2\pi r dl}{\pi r^2 RT dl} \sigma = - \frac{2\sigma V_M}{rRT} , \qquad (G.46)$$

or, in exponential form,

$$P/P_0 = \exp\left(\frac{-2\sigma V_M}{rRT}\right) . \qquad (G.47)$$

Hysteresis is observed because the pores fill and empty via different mechanisms. Physical adsorption is accompanied by the radial filling of pores as subsequent adsorbate layers are added, resulting in a continuing decrease of the effective pore diameter. Therefore, the area and volume terms in the preceding equations are functions of r, as represented by

$$dA = 2\pi l dr ,$$

$$dV = 2\pi r l dr .$$

Upon substitution into Equation (G.43) and subsequent integration and rearrangement, the following equation is obtained:

$$\frac{P_A}{P_0} = \exp\left(- \frac{\sigma V_M}{rRT}\right) , \qquad (G.48)$$

where P_A = adsorption vapor pressure.

The desorption step has been shown to proceed via the mechanism assumed in the development of Equation (G.47), an axial emptying of the pores:

$$\frac{P_D}{P_0} = \exp\left(-\frac{-2V_M\sigma}{rRT}\right) , \qquad (G.\ 49)$$

where P_D = desorption vapor pressure.

Upon combining Equations (G.48) and (G.49) for a given pore radius, one obtains:

$$\left(\frac{P_A}{P_0}\right)^2 = \frac{P_D}{P_0} , \qquad (G.50)$$

or expressed in the nomenclature of Figure G.2, $A^2 = D$. Also, presented in Figure G.2 are the respective sorption isotherms for pores of various configurations and the observed relationships between A and D.[52] Nitrogen adsorption isotherm studies have indicated pore sizes down to 2 nm will exhibit hysteresis.[51] When pore sizes are <2 nm (a P/P_0 of <0.30 for nitrogen), the validity of the Kelvin equation is suspect, and the physical sorption forces dominant for both sorption and desorption mechanisms.[64]

For systems with adsorption and desorption isotherms consistent with Equation (G.50), methods have been proposed and successfully used for determining the pore size distribution from desorption data. When vapor pressure conditions are such that a pore of radius r is emptied, layers of physically adsorbed sorbate of a thickness consistent with adsorption on a smooth surface at the same P/P_0 still remain upon the surface. The average thickness of this adsorbed layer for nitrogen as a function of P/P_0 is presented in Table G.2. The Halsey equation may be used for estimating the thickness, t, of the sorbed layer:

$$t = 3.54\left[\frac{5}{\ln(P_0/P)}\right]^{1/3} , \qquad (G.51)$$

where t has units of Å. (A nitrogen monolayer has a thickness of

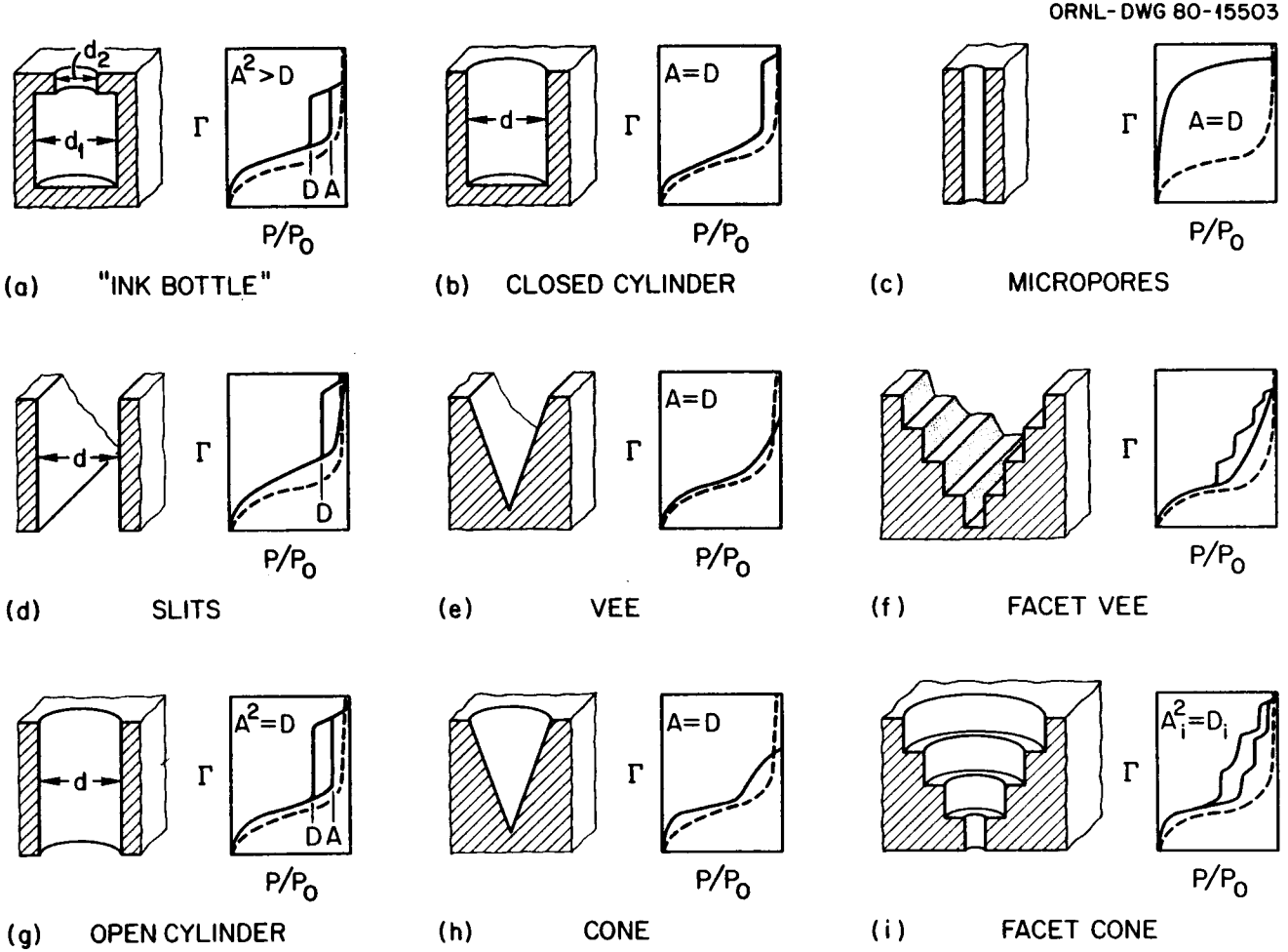


Figure G.2. Representative adsorption isotherms for porous solids with differing pore geometries. Source: Fuller, E. L. Jr., Yoos, T. R. III, and Walia, D. S., *Physiochemical Characterizations of Limestone for Fluidizied-Bed Coal Conversion*, ORNL/TM-7292 (1981).

Table G.2. Thickness of adsorbed layer at various relative pressures

P/P_o	t,Å	P/P_o	t,Å	P/P_o	t,Å	P/P_o	t,Å
0.3	5.6	0.62	7.7	0.75	9.1	0.87	11.5
0.35	5.9	0.64	7.8	0.76	9.2	0.88	11.9
0.40	6.2	0.66	8.0	0.77	9.4	0.89	12.2
0.425	6.3	0.67	8.1	0.78	9.5	0.90	12.7
0.45	6.5	0.68	8.2	0.79	9.7	0.91	13.1
0.475	6.6	0.69	8.3	0.80	9.9	0.92	13.7
0.50	6.8	0.70	8.5	0.81	10.1	0.93	14.4
0.52	6.9	0.71	8.6	0.82	10.3	0.95	16.2
0.54	7.0	0.72	8.7	0.83	10.5	0.96	17.3
0.56	7.2	0.73	8.8	0.84	10.7	0.97	19.2
0.58	7.3	0.74	8.9	0.85	11.0	0.98	22.1
0.60	7.5			0.86	11.2	0.99	27.8

Source: S. Lowell, *Instruction Manual for the Quantasorb Sorption System*, Quantachrome Corp., Syosset, New York, 1975.

where t has units of Å. (A nitrogen monolayer has a thickness of ~3.54. For desorption data, Wheeler[62] suggested the following equation for estimating the pore size distribution:

$$V_0 - V = \pi \int_{r_c}^{\infty} (r-t)^2 L(r)dr \ , \qquad (G.52)$$

where

V_0 = pore volume at saturation,

V = volume remaining upon desorption to P_A/P_0,

r = radius,

t = thickness of adsorbed layers,

$L(r)$ = pore length distribution function,

$L(r)dr$ = length of pores with radii of r to (r + dr).

For desorption, the Kelvin equation may be used to determine the respective pore radius for a given P/P_0. For nitrogen desorption,

$$r_k = \frac{2\sigma V_m \cos \Theta}{RT \ln(P_0/P)} \ , \qquad (G.53)$$

where

$r_k = r - t$, Å,

$R = 8.31 \times 10^7$ ergs/mol k ,

$T = 77$ K,

$\theta = 0°$,

$\sigma = 8.85$ ergs/cm^2,

$V_M = 34.7$ cm^3/mol.

Substituting the respective values into the preceding equation,

$$r_k = \frac{4.146}{\log (P_0/P)} \ . \qquad (G.54)$$

In analyzing desorption data, Wheeler[62] assumed a density distribution function, such as Gaussian, for the pore radii, L(r), and determined the characteristics and goodness of fit for that particular distribution function when substituted into Equation (G.52).

Rather than specifying a given density distribution function, Barret, Joyner, and Holenda[62] simplified Equation (G.52) by using a summation to approximate the integral expression:

$$V_o - V = \pi \sum_{r_c}^{\infty} r - t \, {}^2L(r) \Delta r \, . \qquad (G.55)$$

The desorption curve was then evaluated in a stepwise manner and the distribution function determined. For additional information concerning the two techniques for estimating pore size distribution, the doctoral thesis by Rouquerol[62] is recommended.

Polarization Theory and the Sorption Potential Model

Whereas the BET Model assumes a distinct sorbent-sorbate bonding energy and identical sorbate-sorbate bonding energies for the formation of subsequent adsorbate layers, polarization theory and the resulting sorption potential model assumes that the bonding energy varies as a function of the number of sorbed layers.[50-54,62-63] An excellent review of the sorption potential model and its application in the analyses of sorption data is presented in papers by Fuller et al.[50-53] These papers will be referenced extensively in the ensuing paragraphs.

The sorption potential, E, as defined by Polangi[52,63] is the reversible work performed on the system, the change in free energy, required

to isothermally compress the adsorbate from the system pressure to its saturation vapor pressure. Thus for an ideal gas,

$$E = dA = -PdV - SdT = - RT \ln \frac{V}{V_0} = RT \ln \frac{P}{P_0} , \qquad (G.56)$$

where

E = sorption potential,

A = Helmhotz free energy,

V = volume,

P = vapor pressure,

P_0 = saturation vapor pressure,

R = gas constant,

T = absolute temperature.

For the adsorption to occur on the surface, the sorption potential (actually the energy of sorption) must equal the energy of the sorbent-sorbate bond. Thus the extent of adsorption is a direct function of the corresponding energies:

$$\Gamma = f(E) , \qquad (G.57)$$

where

$$\Gamma = \frac{\text{g adsorbate}}{\text{g adsorbent}} :$$

As indicated by Fuller,[53-54] several functional forms for Equation (G.57) have been proposed (some from first principles) and tested. However, Fuller determined the relationship proposed by deBoer and Zwicker to be quite beneficial in the analyses of sorption isotherms. Their model is based upon the interaction of the sorbent and sorbate by mutual field-multipole forces. The functional form of the interaction equation is

$$E = E_0 e^{-\alpha\Gamma}, \qquad (G.58)$$

where

E_0 = initial (zero coverage) energy of interaction,

α = exponential decay factor,

Γ = amount adsorbed.

Equations (G.56) and (G.57) may now be used in analyzing the sorption isotherm. Determination of the monolayer coverage, Γ_M, is possible via application of the equipartition of energy theory.

Depending upon the energetics of the surface, the sorption potential for a given coverage will equal RT and this energy [see Equation (G.56)] will correspond to a unique value of P/P_0. The specific energy value, RT, corresponds to the loss of two degrees of translational freedom were used in forming a given layer, and the bonding energy must equal this. In a similar manner, a sorption potential exists for which only one degree of translational freedom was used. This layer would then contain only half the molecules present in a completed layer and would have a sorption potential of 0.5 RT. The monolayer coverage may then be calculated from the extent of adsorption at E = 0.5RT and E = RT or:

$$\Gamma_M = 2.0\,[\Gamma_2(E = 0.5\ RT) - \Gamma_1(E = RT)]. \qquad (G.59)$$

Since Equation G.56 shows that $E = -RT\ \ln(P/P_0)$, one may then obtain:

$$\Gamma_M = 2.0\,[\Gamma_2(P/P_0 = 0.6065) - \Gamma_1(P/P_0 = 0.3679)]. \qquad (G.60)$$

Thus the monolayer coverage may be estimated by the adsorption values at two values of P/P_0. As indicated by Fuller,[51] highly energetic surfaces will generally require Γ_2 and Γ_1 to be sorption values for the second and third adsorbate layer. For less energetic surfaces, the sorption potential quickly drops and is equal to RT and 0.5 RT for the first and second adsorbate layers, respectively.

In the analyses of sorption data, the term E_0, the energy of interaction at zero coverage, is extremely important as it provides an indication of the type and strength of the sorbate-sorbent bonding. This value may be obtained from isotherm data by rearrangement of Equation (G.58):

$$\ln\left(\frac{E}{RT}\right) = -\alpha\Gamma + \ln\left(\frac{E_0}{RT}\right). \qquad (G.61)$$

Combining Equations (G.56 and (G.61), one obtains the following linear equation:

$$\ln\left[-\ln\left(P/P_0\right)\right] = -\alpha\Gamma + \ln(E_0/RT) \qquad (G.62)$$

From adsorption data and a plot of $\ln\left[-\ln(P/P_0)\right]$ versus Γ, one can then determine E_0 from the intercept value. Fuller's study indicated that for a square or hexagonal crystal lattice array, 16 degrees of surface freedom would be lost upon adsorption (termed a moderately active surface). Thus for this case, $E_0/RT = 8.0$ ($E_0 = 5.1$ kJ at 77 K would be the minimal intercept value). In reality, values which are greater than and less than this value are commonly observed due to variations in the energetics of sorbent-sorbate interaction. Large positive deviations from this value usually result from chemisorption or the existence of neighboring surfaces with accompanying surface potentials.

A major advantage of the sorption potential model is that it may be applied over the entire P/P_0 range. As previously demonstrated by Eq. (G.61), the amount of adsorbed sorbent is ideally a linear function of $\ln(E/RT)$ or $\ln\left(-\ln\left(P/P_0\right)\right]$. Depending upon the properties of the solid, several linear regimes in the sorption potential plot may be observed which indicate changes in the energy of interaction (E_0) or the presence of other phenomena such as capillary condensation and hysteresis.

Typical sorption potential plots are presented in Appendix H. Analysis of the experimental data is presented in Chapter 3.

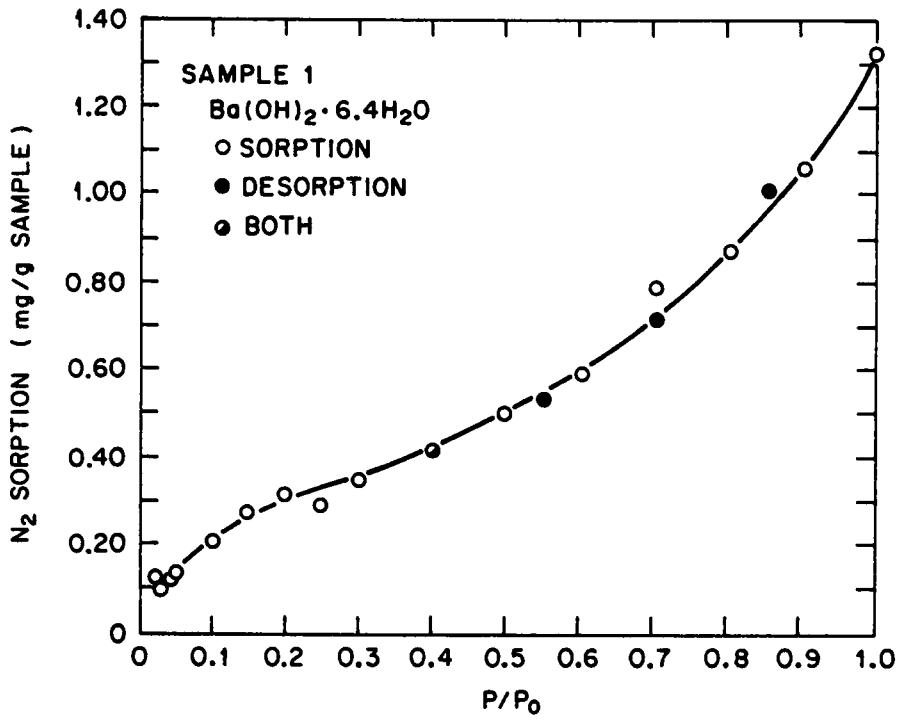
Conclusion

Information obtained via sorption potential model analysis, BET model analysis, sorption-desorption data analysis, chemistry studies on the solid, and through the experience of the researcher increases our understanding of the surface characteristics of solids. These research techniques are only tools, however, and the final information can only be reliable when these tools are correctly used in their regime of applicability and the resulting data are properly correlated and interpreted.

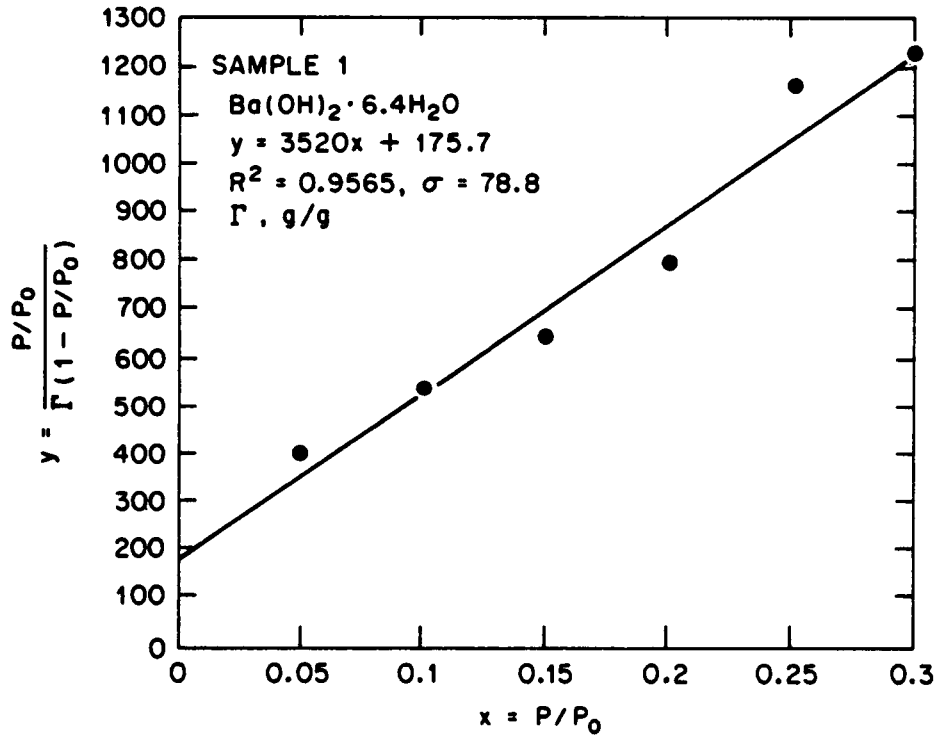
APPENDIX H

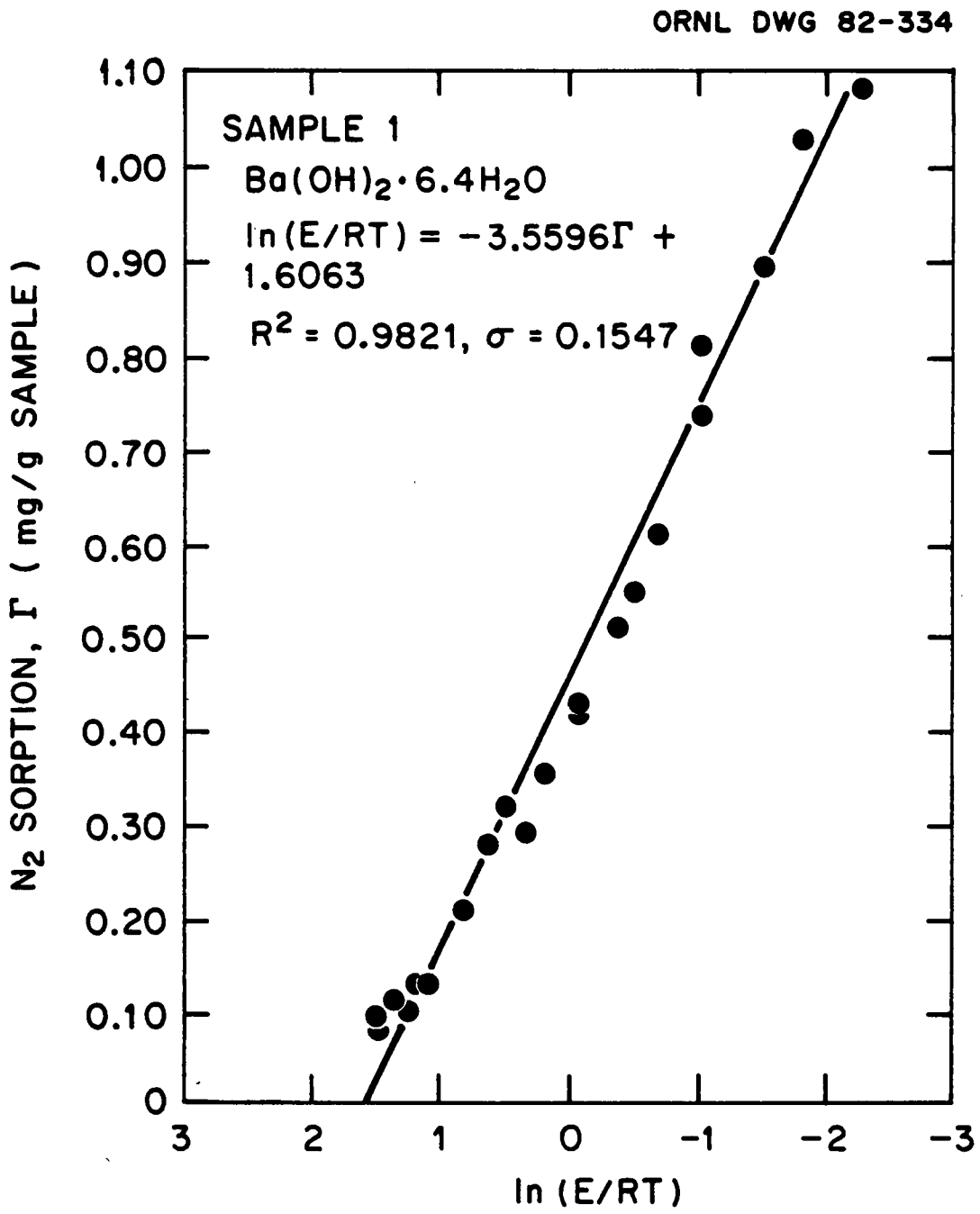
ADSORPTION ISOTHERMS, BET PLOTS, AND SORPTION POTENTIAL PLOTS

ORNL DWG 82-331

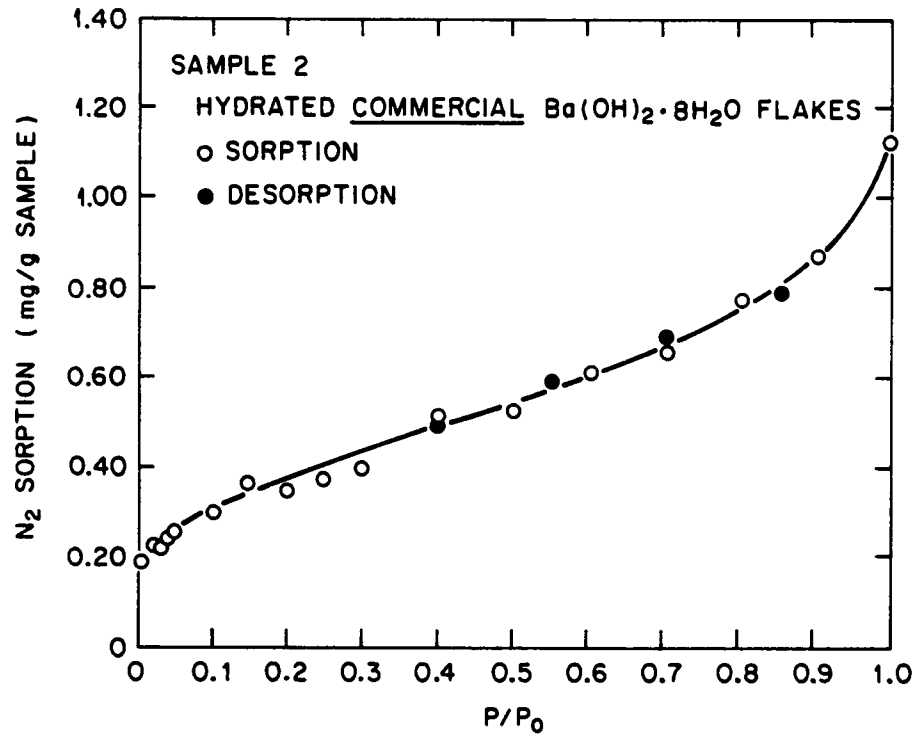


ORNL DWG 82-338

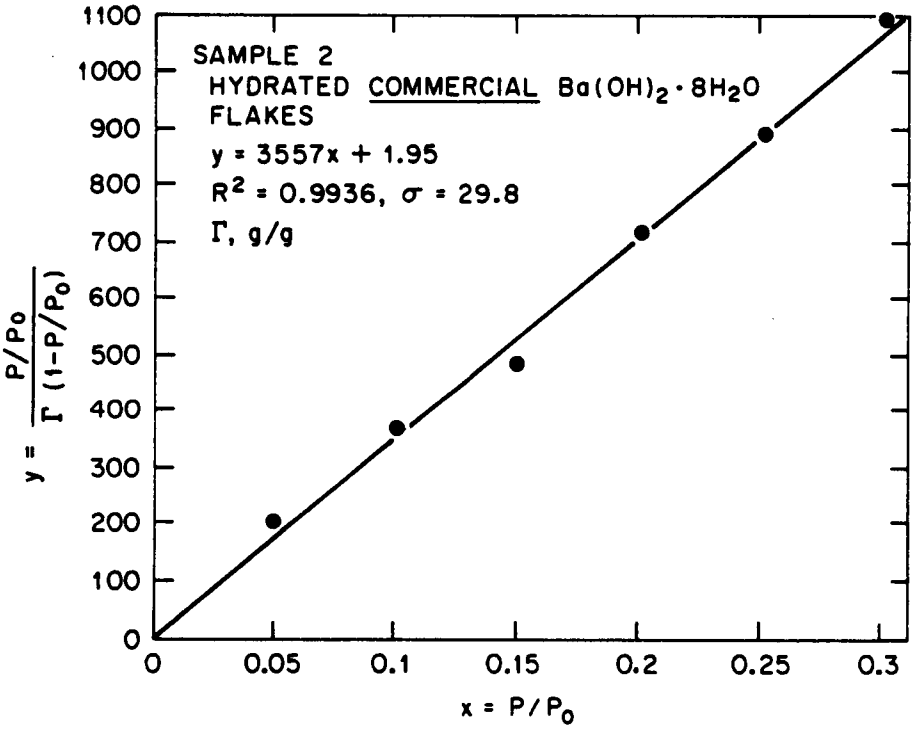


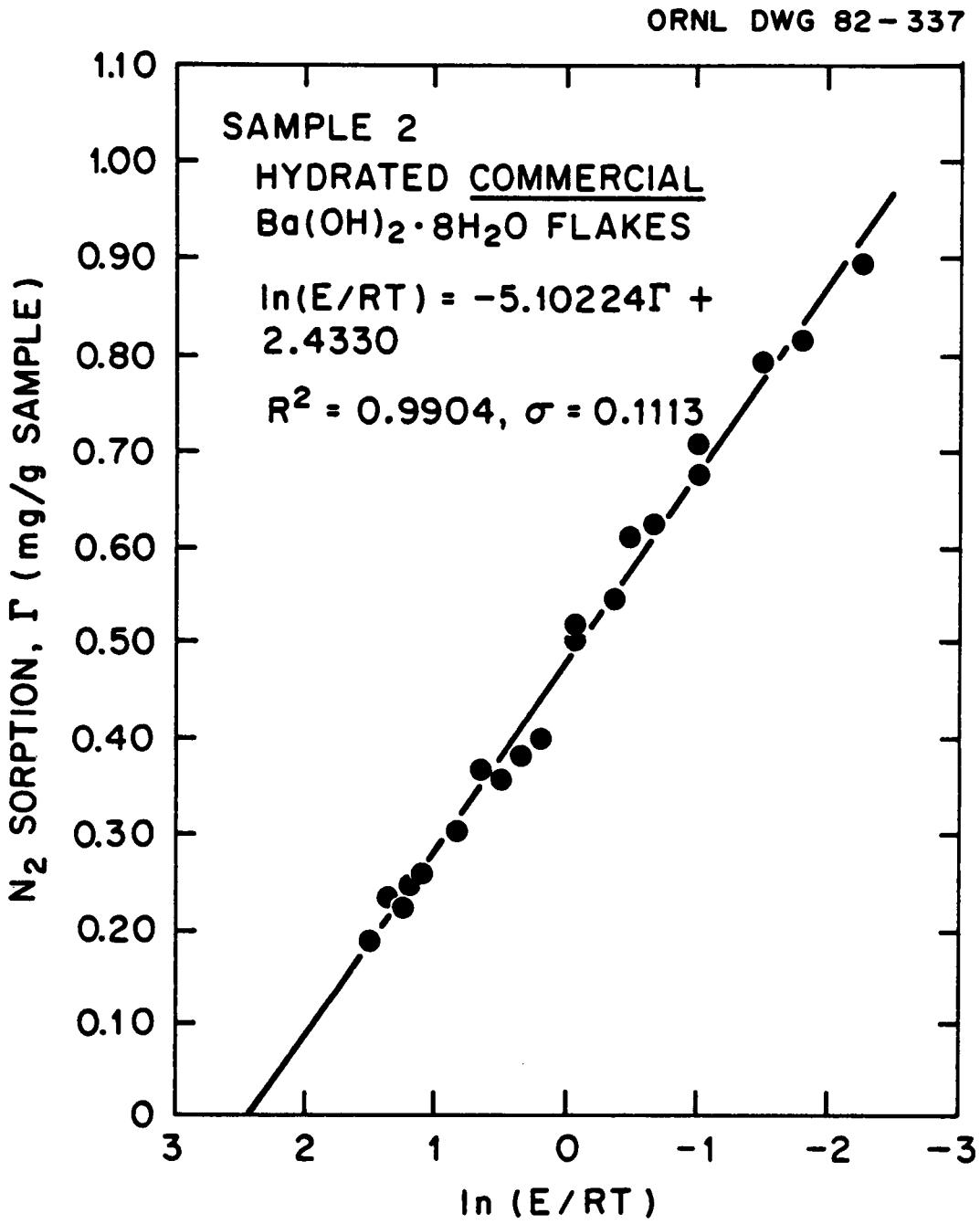

ORNL DWG 82-334
SAMPLE 1
$Ba(OH)_2 \cdot 6.4H_2O$
$\ln(E/RT) = -3.5596\Gamma + 1.6063$
$R^2 = 0.9821, \sigma = 0.1547$
N_2 SORPTION, Γ (mg/g SAMPLE)
1.10
1.00
0.90
0.80
0.70
0.60
0.50
0.40
0.30
0.20
0.10
0
3
2
1
0
-1
-2
-3
ln (E/RT)

ORNL DWG 82-332

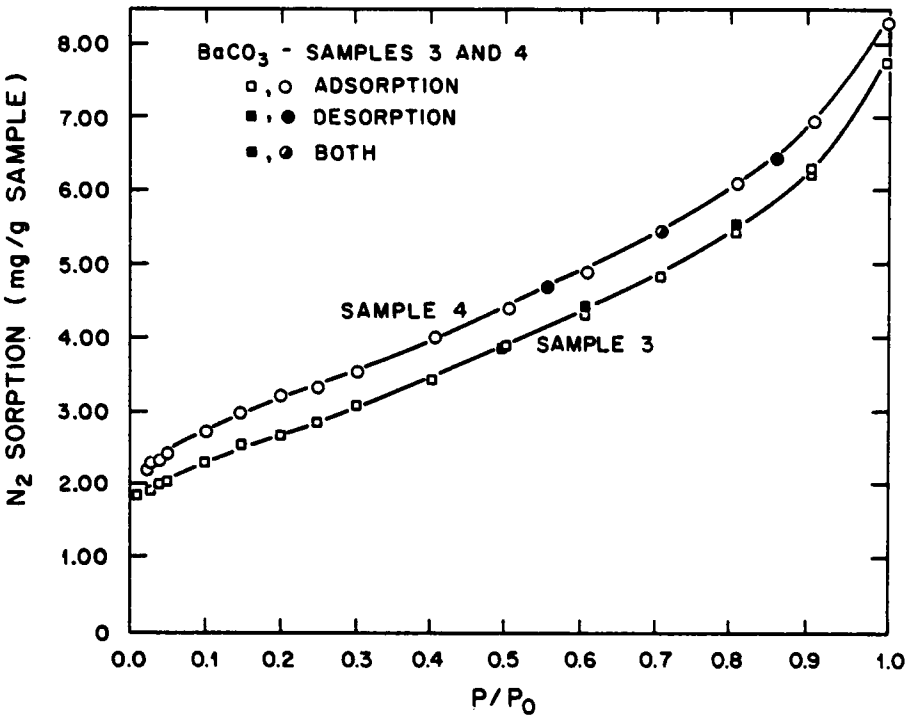


ORNL DWG 82-339

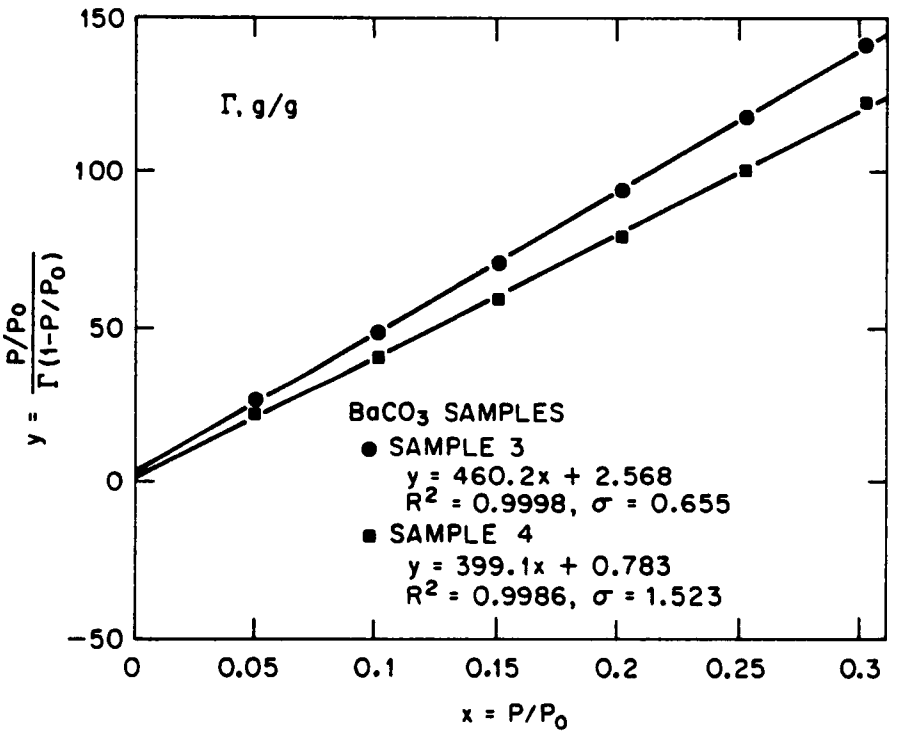


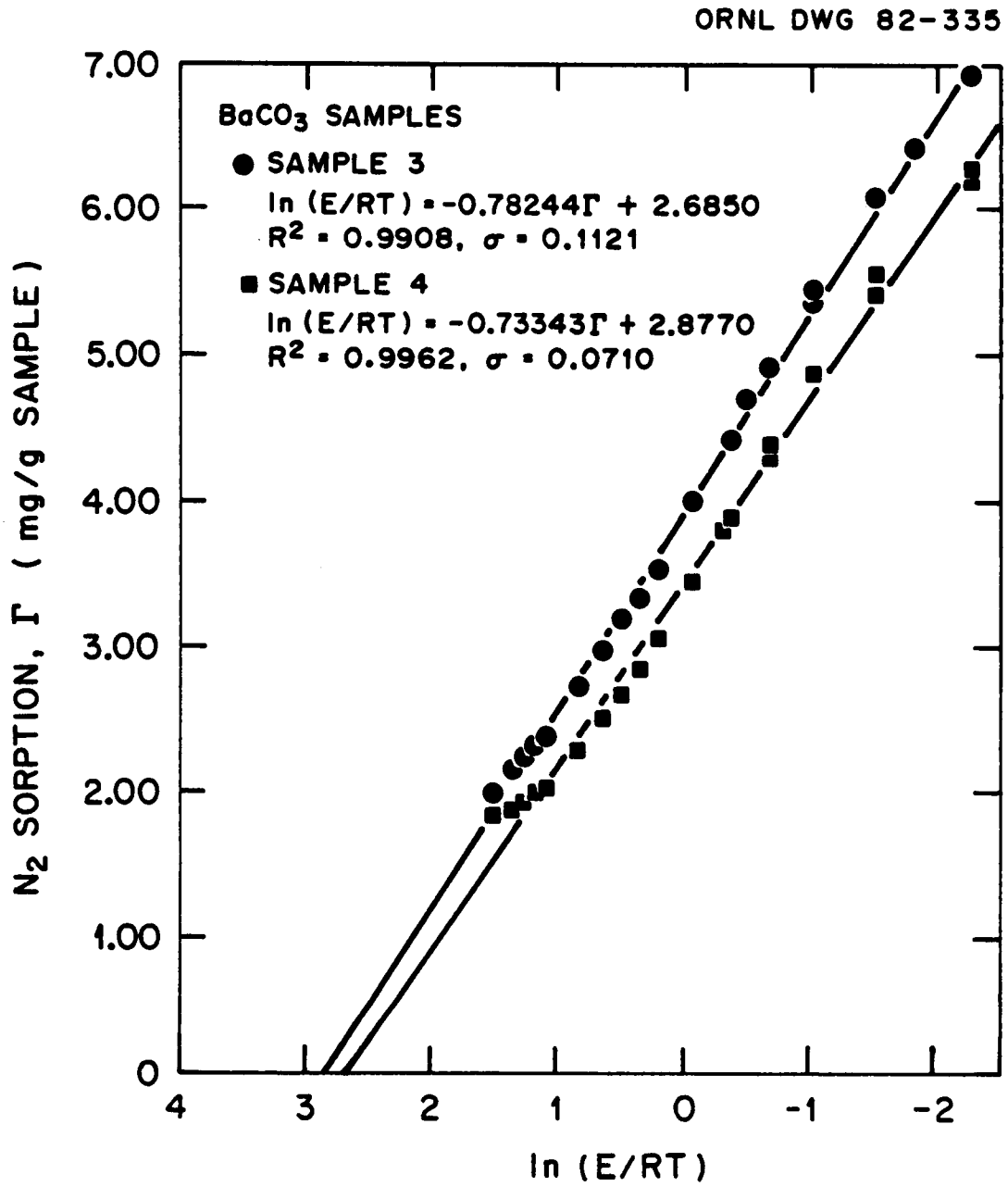

ORNL DWG 82-337
SAMPLE 2
HYDRATED COMMERCIAL
Ba(OH)2·8H2O FLAKES
ln(E/RT) = -5.10224Γ + 2.4330
R2 = 0.9904, σ = 0.1113
N2 SORPTION, Γ (mg/g SAMPLE)
ln (E/RT)
1.10
1.00
0.90
0.80
0.70
0.60
0.50
0.40
0.30
0.20
0.10
0
3
2
1
0
-1
-2
-3

ORNL DWG 82-330

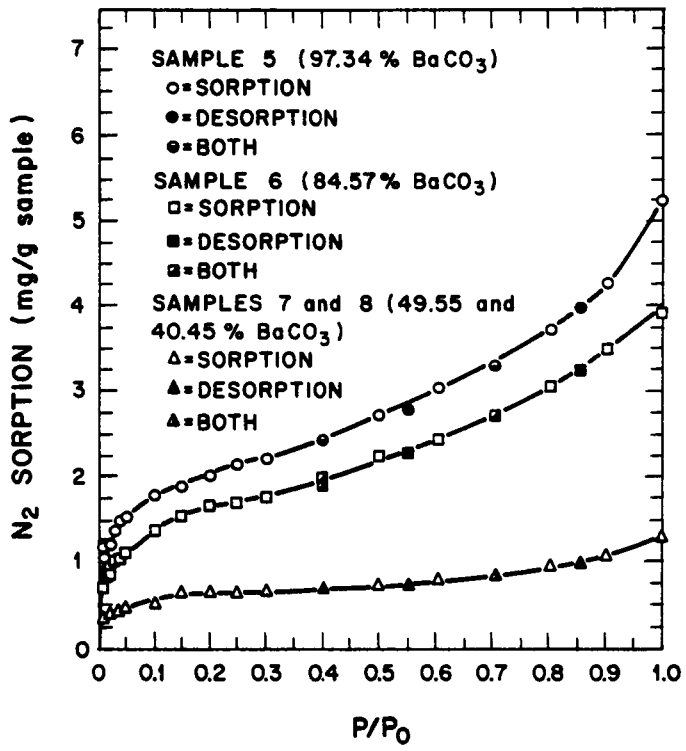


ORNL DWG 82-340

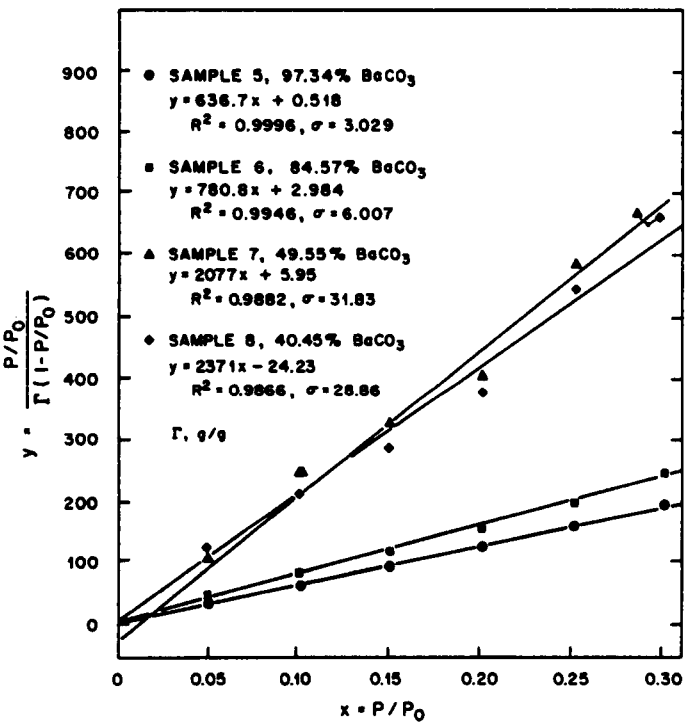



ORNL DWG 82-335
BaCO3 SAMPLES
SAMPLE 3
ln (E/RT) = -0.78244Γ + 2.6850
R2 = 0.9908, σ = 0.1121
SAMPLE 4
ln (E/RT) = -0.73343Γ + 2.8770
R2 = 0.9962, σ = 0.0710
N2 SORPTION, Γ (mg/g SAMPLE)
ln (E/RT)
7.00
6.00
5.00
4.00
3.00
2.00
1.00
0
4
3
2
1
0
-1
-2

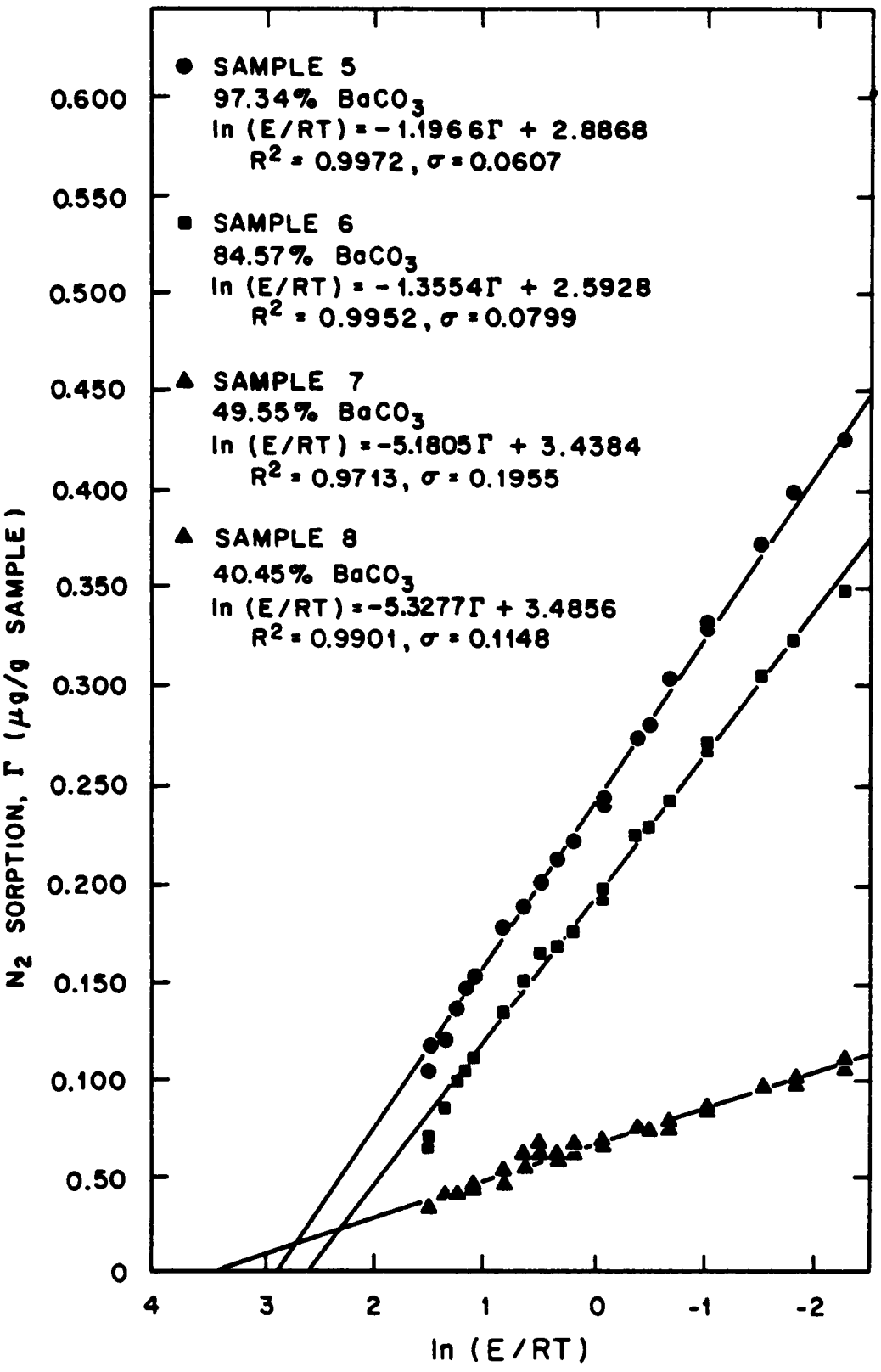
ORNL-DWG 82-333



ORNL DWG 82-341



ORNL DWG 82-336



APPENDIX I

MERCURY POROSIMETRY DATA SHEET

Table I.1. Mercury porosimetry data sheet

Mercury pressure (psig)	Pore diameter (μm)	Cumulative pore volume (mL)			
		$Ba(OH)_2 \cdot 7.0H_2O$ (2.0975 g)	$Ba(OH)_2 \cdot 7.5H_2O$ (2.4311 g)	$BaCO_3$ COM-35 (0.2793 g)	$BaCO_3$ COM-40 (0.2972 g)
0		0.0000	0.0000	0.0000	0.0000
5	35.0	0.0005	0.0006	0.0004	0.0010
10	17.5	0.0011	0.0016	0.0006	0.0029
15	11.7	0.0021	0.0030	0.0010	0.0059
20	8.75	0.0030	0.0051	0.0015	0.0080
30	5.83	0.0047	0.0088	0.0021	0.0115
40	4.38	0.0066	0.0124	0.0027	0.0144
50	3.50	0.0088	0.0199	0.0033	0.0175
75	2.33	0.0140	0.0256	0.0045	0.0225
100	1.75	0.0194	0.0358	0.0057	0.0225
125	1.40	0.0231	0.0427	0.0067	0.0276
175	1.00	0.0333	0.0562	0.0084	0.0309
250	0.700	0.0450	0.0682	0.0115	0.0345
350	0.500	0.0547	0.0787	0.0142	0.0384
500	0.350	0.0655	0.0887	0.0181	0.0477
600	0.291	0.0695	0.0946	0.0212	0.0575
700	0.250	0.0747	0.1001	0.0240	0.0715
900	0.194	0.0846	0.1109	0.0300	0.0974
1000	0.175	0.0861	0.1132	0.0315	0.1109
1500	0.117	0.1045	0.1396	0.0501	0.1350
2000	0.0875	0.1082	0.1421	0.0743	0.1541
2500	0.0700	0.1102	0.1438	0.0902	0.1631
3000	0.0580	0.1115	0.1456	0.1177	0.1654
4000	0.0438	0.1120	0.1459	0.1271	0.1663
5000	0.0350	0.1125	0.1471	0.1284	0.1667
6000	0.0292	0.1127	0.1476	0.1289	0.1670
8000	0.0219	0.1132	0.1476	0.1297	0.1670
10000	0.0175	0.1134	0.1482	0.1298	0.1673
12500	0.0146	0.1135	0.1484	0.1298	0.1673
15000	0.0112	0.1139	0.1482	0.1298	0.1676

APPENDIX J

GAS ROTAMETER CALIBRATION AND CORRECTION FACTORS

Gas flowrates for the fixed-bed studies were measured with Fischer-Porter Model 10A1755 rotameters. The rotameters were factory calibrated for air in the flowrate range of 1 to 6 ft^3/min at 70°F and 14.7 psia. Because of different operating conditions and to validate the factory calibration, the rotameters were recalibrated by the Physical and Electrical Standards Laboratory at the Y-12 Plant operated by Union Carbide Nuclear Division. The calibrations were conducted with air at 5 and 15 psig and 75°F. For this calibration, standard temperature and pressure were defined to be 70°F and 14.7 psia. The flowrate was found to vary linearly with the rotameter scale. However, a method was required to calculate gas flowrates at other than the calibrated system conditions. Using a technique patterned after that of Vaux, an equation was developed to account for differences in gas temperature, flowrate, and molecular weight.[114] Assuming that the annular space between the float or ball and the rotameter tube may be viewed as an orifice, one may apply the orifice equation for gases. This equation was developed by applying a momentum or force balance on the float.

$$Q\sqrt{\rho} = CYS\frac{2g_c\,\Delta P}{10\beta^4}, \qquad (J.1)$$

where

Q = volumetric flowrate,

ρ = gas density,

C = discharge coefficient,

Y = expansion factor,

S = orifice area,

g_c = Newton's law factor,

β = cross-section ratio, and

ΔP = pressure drop.

For a given float position, z, the terms on the right hand side of the preceding equation are constant. Thus:

$$Q\sqrt{\rho} = \text{constant} \quad . \tag{J.2}$$

$$z = \text{constant}$$

Therefore, for the same float position but at differing system conditions, the following equality must hold.

$$Q_1\sqrt{\rho_1} = Q_2\sqrt{\rho_2} \; . \tag{J.3}$$

For the gas conditions to be encountered, the reasonable assumption of gas ideality will be used, so that

$$\rho = \frac{PMW}{RT} \; , \tag{J.4}$$

where

P = pressure,

MW = molecular weight,

R = gas constant, and

T = absolute temperature.

Combining Equations (J.3) and (J.4), (with subscript 1 referring to calibration conditions for the rotameters and subscript 2 referring to actual rotameter flowrate reading and operating conditions), one obtains:

$$Q_1\sqrt{\frac{P_1 MW_1}{RT_1}} = Q_2\sqrt{\frac{P_2 MW_2}{RT_2}}$$

$$Q_1 = Q_2\sqrt{\frac{P_2\ MW_2\ T_1}{P_1\ MW_1\ T_2}} \tag{J.5}$$

However, the calibration curve provides referenced flowrates at 1 atm and 70°F as a function of pressure (5 psig or 15 psig) and float position or:

$$Q_c = f(P_1, z) \qquad (J.6)$$

Therefore, from the calibration curve for a given float position and at ambient temperatures, one can determine the flow rate at reference conditions, 1 atm and 70°F, for system pressures of either 5 or 15 psig. One may then use Equation (J.5) to correct for the effect of other rotameter pressures. In our system, the molecular weights of the gases for the two conditions were identical, and the changes resulting from differences in absolute temperature were negligible. Therefore,

$$Q_R = \frac{P_2}{P_1} Q_c \,, \qquad (J.7)$$

where

Q_R = flow rate at reference conditions, 1 atm and 70°F,

P_2 = system pressure at rotameter,

P_1 = rotameter pressure used for the calibration curve, and

Q_c = flow rate at reference conditions for given rotameter pressure, P_1.

As the rotameters were calibrated at 5 and 15 psig, Equation (J.7) was used to predict flow rates at 15 psig from the calibration data at 5 psig. For the two rotameters, maximum errors of 4.4 and 2.2% were calculated.

APPENDIX K.

FINITE DIFFERENCE SOLUTION TO THE FIXED-BED PARTIAL DIFFERENTIAL EQUATIONS

Computer Program Nomenclature

T = Temperature, K

P = Pressure, atm

AO = Surface area, area/volume, cm^2/cm^3

CO2FRAC = Volume fraction of CO_2 in feed

AMW = Molecular weight of reactant

CIN = Inlet CO_2 concentration, $g\text{-}mol/cm^3$

SDEN = Reactant bulk density, g/cm^3

AKF = Gas film mass transfer coefficient, cm/s

DELS = S increment where $S = z/V$, s

DELT = Θ increment where $\Theta = t - \varepsilon z/V$, s

TIME = Θ, h

S = S, s

X(NZ) = Fractional conversion of solid reactant

C(NZ) = Fractional conversion of gaseous reactant

NZ = Counter for total number of DELS increments

L = Counter for number of DELS increments since last output

KKK = Counter for number of DELT increments since last output

KK = Counter for increasing KKK Values

Computer Program Listing for the Finite Difference Solution of the Fixed-Bed Partial Differential Equations

```
      DIMENSION C(2000), X(2000)
    1 FORMAT (F15.8)
    2 FORMAT (3E20.10)
      T=295.3
      P=1.03881
      AO=6.0
      CO2FRA=.00033
      AMW=298.8
      CIN=P*CO2FRA/(82.06*T)
      SDEN=1.0
      AKF=1.0
      DELS=0.00700
      DELT=.00015
      TIME=0.0
      DO 100 NZ=1,2000
      X(NZ)=0.0
  100 C(NZ)=0.0
      C(1)=1.0
      N=0
      NN=2
      KK=0
      KKK=10
  140 K=0
      L=9
      N=N+1
      TIME=TIME+DELT/3600.0
      IF (N.NE.KKK) GO TO 160
      TYPE 1,TIME
  160 S=0
      DO 200 NZ=NN,2000
      NZM1=NZ-1
      C(NZ)=-DELS*AKF*AO*(1.0-X(NZ)**1.0)*C(NZM1)+C(NZM1)
      S=S+DELS
      IF (N.NE.KKK) GO TO 170
      L=L+1
      IF (L.NE.10) GO TO 170
      L=0
  165 TYPE 2,S,C(NZ),X(NZ)
  170 X(NZ)=X(NZ)+DELT*AMW*CIN**AKF*AO/SDEN*(1.0-X(NZ)**1.0
     C)*C(NZ)
      IF (C(NZ).LT.1.0E-06) GO TO 210
  200 CONTINUE
  210 IF (TIME.GT.5.0E-07) DELT=10.0
       IF (N.NE.KKK) GO TO 220
      IF (KK.NE.6) KK=KK+1
      N=0
      KKK=KK*500
  220 IF (TIME.GT.120) GO TO 300
      GO TO 140
  300 STOP
      END
```

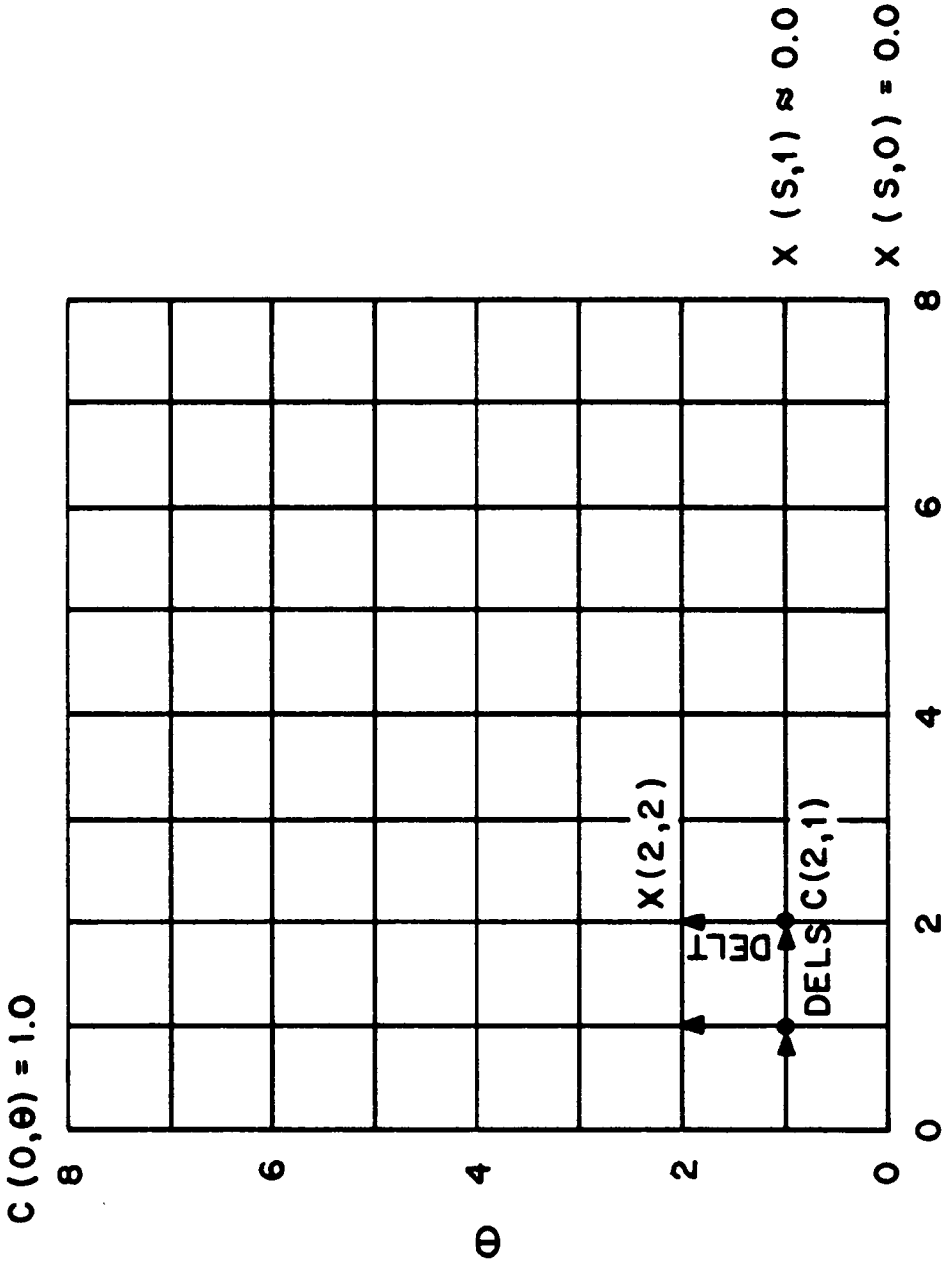
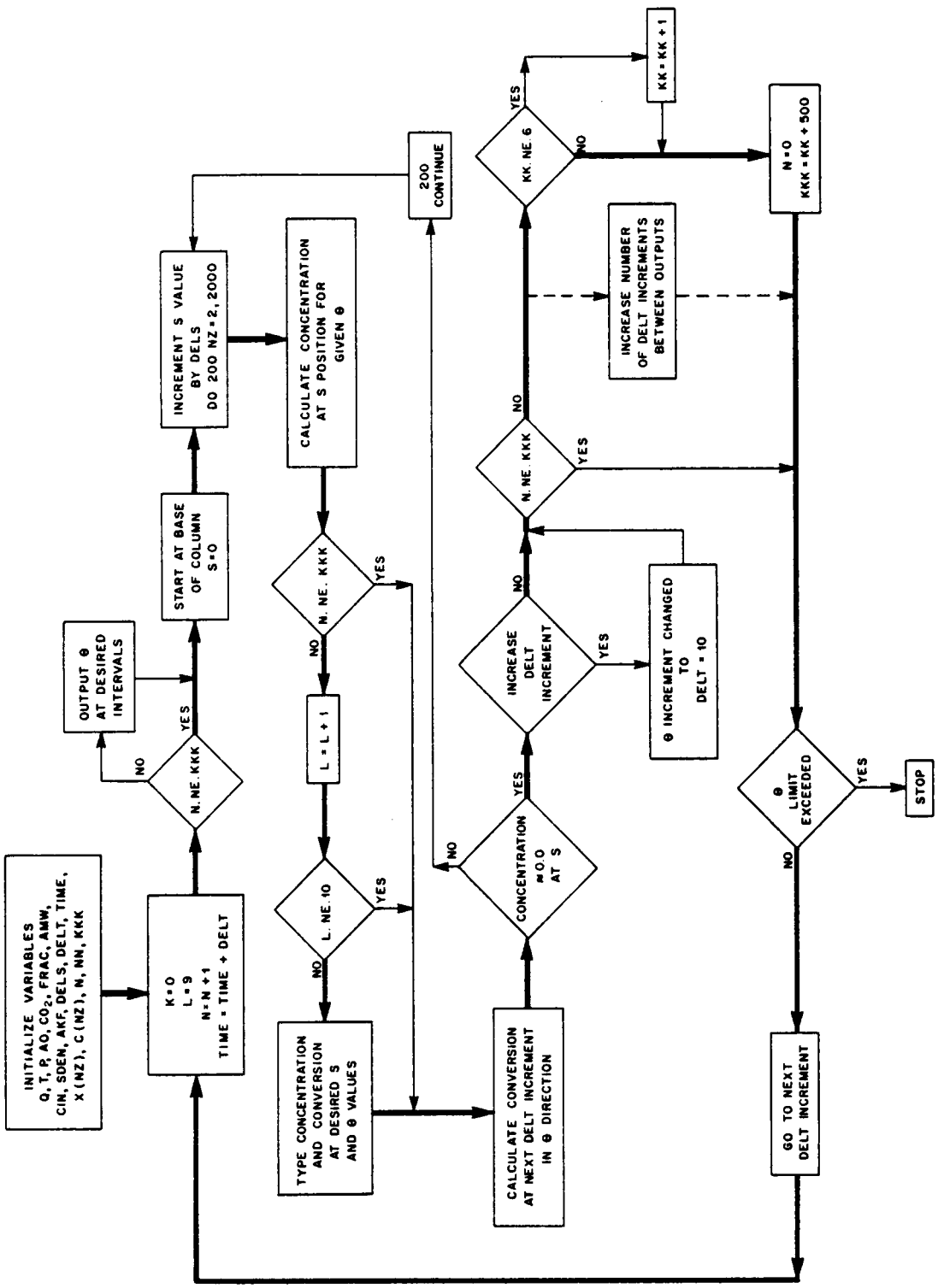


Figure K.1. Grid schematic for finite-difference solution of the controlling partial differential equations and their respective boundary conditions.

ORNL DWG 82-320



APPENDIX L

FITTED VALUES IN ERGUN EQUATION

Table L.1. Fitted values in Ergun Equation, $\Delta P/L = A'V + B'V^2$, and calculated values of ε and ϕd_p

COM Run No.	Effluent relative humidity (%)	Superficial velocity, V_o[a] (cm/s)	Temperature (K)	Constants A'	Constants B'	Voidage ε	ϕd_p (cm)
31	40.2	13.00	296.7	0.8904	0.4100	0.0934	5.6524
54	47.8	13.65	317.5	8.6862	0.7513	0.1332	1.0153
50	48.5	8.73	296.3	17.6362	1.5176	0.1056	1.0424
53	53.2	8.89	303.9	26.7312	1.7478	0.1104	0.7877
52	54.3	8.66	296.2	12.9348	1.1651	0.1136	1.0808
56	54.8	14.16	316.2	26.3669	1.7791	0.1086	0.8146
49	55.0	13.94	305.3	26.0630	2.6249	0.0835	1.1237
55	59.1	9.08	304.0	204.751	7.8009	0.2309	0.6392
48	60.2	21.90	296.3	3.3151	0.2032	0.0509	1.0488
46	61.2	17.50	299.7	25.3273	2.8154	0.7893	1.3861
57	62.6	9.08	304.0	114.166	6.5648	0.0735	0.7311
40	63.3	13.88	305.2	8.0672	0.3035	0.0655	0.8599
45	66.4	18.50	296.1	390.931	16.5176	0.0604	0.5372
47	69.6	8.93	296.0	222.632	15.644	0.0519	0.9013

[a] V_o = superficial velocity at reference conditions, 294.3 K and 101.3 kPa.

V = superficial velocity at system conditions.

APPENDIX M

MASS TRANSFER MODELS FOR SHRINKING-CORE SYSTEMS

In the modeling of gas-solid reactions, one often assumes that the reaction interface is reasonably sharp. Mass-transfer models based upon this assumption are often referred to as "shrinking-core models."[76,77] Factors which may affect or control the rate of mass transfer in these models are (1) mass transfer of gaseous reactant or product through the gas film surrounding each particle, (2) mass transfer of gaseous reactant or product through the solid product layer, and (3) a kinetically limited chemical reaction at the reaction interface. Models will be developed for the following reaction for the cases in which mass transfer of reactant through the gas film and the product layer is controlling and for the case of a kinetically controlled reaction: $aA(g) + bB(s) \rightarrow cC(g) + dD(s)$.

For these cases, the entire concentration gradient or driving force is applied to the step that is rate controlling, thus equations can be developed for predicting particle conversion as a function of time for planar, cylindrical, and spherical reactant geometry. For cases in which no single step is rate controlling, and the rate controlling steps are linear functions of concentration, the mass transfer resistance terms may be grouped and solved in a manner analogous to thermal resistances in heat transfer. The solutions to such problems are straightforward and will not be presented.

Gas-Film Controlled Mass Transfer

Gas film controlled: planar geometry. The mass transfer rate, $\bar{R}$, through the gas film may be expressed as:

$$\bar{R} = K_F A C_B \ , \qquad (M.1)$$

where

K_F = mass transfer coefficient,

A = area for mass transfer, and

C_B = bulk gas concentration of reactant.

The advancement of the reaction interfaces into the particle, with the center of the particle as the reference for the coordinate system, results in the following rate expression:

$$\bar{R} = \frac{b}{a} \rho \frac{dV}{dt} \ , \qquad (M.2)$$

or

$$\bar{R} = \frac{b}{a} \rho A \left(- \frac{dr}{dt}\right) , \qquad (M.3)$$

where

a = stoichiometric term,

b = stoichiometric term,

ρ = molar density,

r = distance from particle center,

V = volume, Ar.

Combining Equations (M.1) and (M.3) and using as boundary conditions, r = R at t=0, (where R is 1/2 the particle thickness), one obtains:

$$\frac{b}{a} \rho \left(- \frac{dr}{dt}\right) = K_F C_B$$

$$R - r = \frac{a}{b\rho} K_F C_B t$$

$$t = \frac{(R - r)b\rho}{K_F C_B a} \qquad (M.4)$$

The time, τ, required for complete particle conversion (i.e., $r = 0$) is given by:

$$\tau = \frac{Rb\rho}{K_F C_B a} . \qquad (M.5)$$

Dividing Equation (M.4) by Eq. (M.5), one obtains:

$$\frac{t}{\tau} = \frac{R - r}{R} = 1 - \frac{r}{R} . \qquad (M.6)$$

For planar geometry, the unreacted fraction of the solid is

$$X = \frac{Ar}{AR} = \frac{r}{R} . \qquad (M.7)$$

Upon substituting Equation (M.7) into Equation (M.6), the desired solution is obtained:

$$\frac{t}{\tau} = 1 - X . \qquad (M.8)$$

Gas-film controlled: cylindrical geometry. The derivation proceeds in a manner analogous to the preceding case for planar geometry.

$$\bar{R} = K_F A C_B ,$$

$$\bar{R} = \frac{b}{a} \rho \frac{dV}{dt} ,$$

$$V = \pi r^2 h ,$$

$$\bar{R} = \frac{b}{a} \rho \frac{d(\pi r^2 h)}{dt} = - \frac{b}{a} \rho \, 2\pi h \frac{d(r^2)}{dt} . \qquad (M.9)$$

Combining Equations (M.1) and (M.9), one obtains:

$$\frac{-b}{a}\,\rho 2\pi h\,\frac{d(r^2)}{dt} = K_F A C_B \ ,$$

$$R^2 - r^2 = \frac{aK_F A C_B}{bh\ 2\pi\rho}\,t \ ,$$

$$t = \left(\frac{bh2\pi\rho}{aK_F A C_B}\right)(R^2 - r^2) \ . \qquad \text{(M.10)}$$

At 100% conversion, $r = 0$ and $t = \tau$,

$$\tau = R^2\left(\frac{b\ h2\pi\rho}{a\ K_F A C_B}\right) = \frac{b\rho}{aK_F C_B}\,R \qquad \text{(M.11)}$$

Dividing Equation (M.10) by Equation (M.11), one obtains:

$$\frac{t}{\tau} = \frac{R^2 - r^2}{R^2} = 1 - \frac{r^2}{R^2} \ . \qquad \text{(M.12)}$$

The fraction of solid reactant remaining as a function of r is:

$$X = \frac{\pi r^2 h}{\pi R^2 h} = \left(\frac{r}{R}\right)^2 \ . \qquad \text{(M.13)}$$

Upon substitution of Equation (M.13) into (M.12), the desired result is obtained,

$$\frac{t}{\tau} = 1 - X \ . \qquad \text{(M.14)}$$

Gas film controlled: spherical geometry

Again proceeding in a manner analogous to the two prior derivations, one obtains:

$$\bar{R} = AK_F C_B$$

$$\bar{R} = \frac{b}{a} \rho \frac{dV}{dt}$$

$$V = 4/3\ \pi r^3$$

$$\bar{R} = \frac{b\rho\ d\left(\frac{4\pi r^3}{3}\right)}{a\ dt} = -\frac{4b\rho\pi\ d(r^3)}{3a\ dt} \qquad \text{(M.15)}$$

At boundary conditions for this differential equation, ($r = R$ at $t = 0$), the solution is:

$$R^3 - r^3 = \frac{3aAK_F C_B}{4b\rho\pi}\ t\ ,$$

$$t = \left(\frac{4b\rho\pi}{3aAK_F C_B}\right)\left(R^3 - r^3\right)\ . \qquad \text{(M.16)}$$

At 100% conversion, $r = 0$ and $t = \tau$, therefore:

$$\tau = \left(\frac{4b\rho\pi}{3aAK_F C_B}\right) R^3 = \frac{b\rho}{3aK_F C_B}\ R\ . \qquad \text{(M.17)}$$

Dividing Equation (M.16) by (M.17), one obtains:

$$\frac{t}{\tau} = \frac{R^3 - r^3}{R^3} = 1 - \frac{r^3}{R^3} \qquad \text{(M.18)}$$

The fraction of solid reactant remaining, X, is given by:

$$X = \frac{\frac{4\pi r^3}{3}}{\frac{4\pi R^3}{3}} = \frac{r^3}{R^3} \qquad \text{(M.19)}$$

Thus:

$$\frac{t}{\tau} = 1 - X \ , \qquad \text{(M.20)}$$

is a valid equation for the case of film diffusion controlled mass transfer in planar, cylindrical, and spherical geometry.

Diffusion Controlled Mass Transfer

For the case of diffusional control, the development of shrinking-core models requires several additional assumptions. Using the center of the particle as the reference point, the partial differential equation describing gas-phase mass transfer in planar geometry within the solid is

$$\varepsilon\frac{\delta C}{\delta t} + V\frac{\delta C}{\delta r} - D\frac{\delta^2 C}{\delta r^2} = 0.0 \ , \qquad \text{(M.21)}$$

where

ε = product voidage,

V = bulk gas velocity,

D = effective diffusivity.

Because of the difference in the molar densities of gases and solids, the movement of the reaction interface is extremely slow; therefore, contributions to the overall mass transfer rate from the term $\delta C/\delta t$

are extremely small. Assuming equimolal counterdiffusion, the bulk velocity term in Equation (M.20) is 0.0, thus:

$$D \frac{d^2C}{dr^2} = 0.0 \text{ , and}$$

$$D\frac{dC}{dr} = \text{constant} = \bar{R} \quad . \tag{M.22}$$

This equation may be integrated, rearranged, and equated to a rate term based upon movement of the reaction interface as in Equation (M.2):

$$\bar{R} = \frac{b}{a} \rho \frac{dV}{dt} .$$

Solution of the resulting differential equation provides an excellent estimate of the rate of conversion as a function of time. Although derived for planar geometry, Equation (M.22) is also applicable to cylindrical and spherical geometry where the radius is the variable of interest.

Diffusion controlled: planar geometry. Starting with Equation (M.22), we have:

$$\bar{R} = AD \frac{dC}{dr} .$$

Upon solving this equation with the boundary conditions, $C = C_B$ at $r = R$, and realizing that $C = 0$ at the reaction interface, r, one obtains:

$$\bar{R} = \frac{ADC_B}{R - r} . \tag{M.23}$$

This equation is now equated to the rate term based on movement of the interface, rearranged, and integrated with the boundary conditions, r = R at t = 0:

$$\bar{R} = \frac{b}{a} \rho \frac{dV}{dt} = - \frac{b\rho A}{a} \frac{dr}{dt} ,$$

$$(r - R)\frac{dr}{dt} = \frac{a}{b} \frac{DC_B}{\rho} ,$$

$$0.5r^2 + 0.5R^2 - Rr = \frac{aDC_B}{b\rho} t ,$$

$$t = \frac{b\rho}{aDC_B} (0.5r^2 + 0.5R^2 - Rr) . \qquad (M.24)$$

At complete reactant utilization, r = 0 and t = τ,

$$\tau = \frac{b\rho}{aDAC_B} (0.5R^2) . \qquad (M.25)$$

Dividing Equation (M.24) by Equation (M.25), one obtains:

$$\frac{t}{\tau} = \frac{r}{R}^2 + 1 - 2\frac{r}{R} . \qquad (M.26)$$

As previously shown in Equation (M.7), the fraction of unreacted solid in planar geometry is

$$X = \frac{Ar}{AR} = \frac{r}{R} .$$

Thus Equation (M.26) reduces to:

$$\frac{t}{\tau} = X^2 - 2X + 1 \ . \qquad \text{(M.27)}$$

Diffusion controlled: cylindrical geometry. As previously shown by a mass balance on the reactive gaseous species:

$$\bar{R} = AD\frac{dC}{dr} = 2\pi rh\ D\frac{dC}{dr} = \text{Constant} \ .$$

Upon integration with the boundary conditions, $C = C_B$ at $r = R$, one obtains:

$$\bar{R}\ln\left(\frac{r}{R}\right) = -2\pi hDC_B \ . \qquad \text{(M.28)}$$

The mass balance on the reacting solid provides the following equation.

$$\bar{R} = \frac{b}{a}\rho\frac{dV}{dt} = -\frac{b}{a}\rho\ 2\pi hr\frac{dr}{dt} \ . \qquad \text{(M.29)}$$

Combining and rearranging Equations (M.28) and (M.29) and integrating by parts, with the boundary conditions $r = R$ at $t = 0$, one obtains:

$$\frac{-b}{a}\rho 2\pi hr\frac{dr}{dt} = \frac{2\pi hDC_B}{\ln(r/R)} \ , \text{ and}$$

$$\ln\left(\frac{r}{R}\right) r\frac{dr}{dt} = \frac{aDC_B}{b\rho} \ ,$$

where the following definitions apply:

$$u = \ln\left(\frac{r}{R}\right) \qquad dv = rdr$$

$$du = \frac{dr}{r} \qquad v = 0.5r^2$$

$$0.5r^2 \ln\left(\frac{r}{R}\right)\Big|_R^r - \int_R^r 0.5r \, dr = \frac{aDC_B}{b\rho h} t$$

$$0.5r^2 \ln\left(\frac{r}{R}\right) - 0.25r^2 + 0.25R^2 = \frac{aDC_B}{b\rho h} t$$

$$t = \frac{b\rho}{aDC_B} \left(0.5r^2 \ln\left(\frac{r}{R}\right) - 0.25r^2 + 0.25R^2\right) . \qquad (M.30)$$

At complete conversion, $r = R$ and $t = \tau$, so

$$\tau = \left(\frac{b\rho}{aDC_B}\right) 0.25R^2 . \qquad (M.31)$$

Dividing Equation (M.30) by (M.31), one obtains:

$$\frac{t}{\tau} = 2\left(\frac{r}{R}\right)^2 \ln\left(\frac{r}{R}\right) - \left(\frac{r}{R}\right)^2 + 1 . \qquad (M.32)$$

The fraction of unreacted solid, X, in the cylindrical geometry is given by Equation (M.13):

$$X = \frac{\pi r^2 h}{\pi R^2 h} = \left(\frac{r}{R}\right)^2 .$$

Thus, Equation (M.32) reduces to:

$$\frac{t}{\tau} = X \ln X - X + 1.0 . \qquad (M.33)$$

Diffusion controlled: spherical geometry. The rate of gas-phase mass transfer through the product layer may be expressed by:

$$\bar{R} = AD\frac{dC}{dr} = 4\pi r^2 D\frac{dC}{dr} = \text{Constant} \qquad (M.34)$$

Upon integration with boundary conditions $C = C_B$ at $r = R$, and recognizing that $C = 0$ at the reaction interface, r, one obtains:

$$\bar{R} = 4\pi DC_B\left(\frac{1}{R} - \frac{1}{r}\right)^{-1} \qquad (M.35)$$

The rate of reaction based upon movement of the reaction interface is:

$$R = \frac{b\rho}{a}\frac{dV}{dt} = \frac{b\rho}{a}\frac{d}{dt}\left(\frac{4\pi r^3}{3}\right) = -\frac{b\rho 4\pi r^2}{a} \qquad (M.36)$$

Combining, rearranging, and integrating Equations (M.35) and (M.36) with the boundary conditions $r = R$ at $t = 0$, results in:

$$\left(\frac{1}{R} - \frac{1}{r}\right) r^2\frac{dr}{dt} = \frac{3aDC_B}{b\rho}$$

$$\frac{aDC_B}{b\rho}t = \frac{1}{3}\left[\frac{r^3}{R} - \frac{R^3}{R}\right] - \frac{1}{2}\left[r^2 - R^2\right]$$

$$t = \frac{b\rho R^2}{aDC_B}\left[\frac{1}{3}\left[\left(\frac{r}{R}\right)^3 - 1\right] - \frac{1}{2}\left[\left(\frac{r}{R}\right)^2 - 1\right]\right] \qquad (M.37)$$

At complete conversion, r = 0 and t = τ. The time required for complete conversion is then:

$$\tau = \left(\frac{b\rho R^2}{aDC_B}\right)\left(\frac{1}{6}\right) \qquad (M.38)$$

Dividing Equation (M-37) by (M.38), one obtains:

$$\frac{t}{\tau} = 2\left(\frac{r}{R}\right)^3 - 3\left(\frac{r}{R}\right)^2 + 1 \qquad (M.39)$$

For spherical geometry, the fraction of unreacted solid is given by Equation (M.18):

$$X = \frac{\frac{4\pi r^3}{3}}{\frac{4\pi R^3}{3}} = \left(\frac{r}{R}\right)^3$$

Equation (M.39) then reduces to:

$$\frac{t}{\tau} = 2X - 3X^{2/3} + 1 \qquad (M.40)$$

First Order Kinetically Controlled Mass Transfer

Reaction controlled: planar geometry. For the case of a controlling chemical reaction controlling step in planar geometry, the rate expression may be expressed by:

$$\bar{R} = AK_K C_B \ ,$$

where K_K = kinetic rate constant. This equation is now coupled with an

equation relating the movement of the solid interface and integrated with the boundary conditions, $r = R$ at $t = 0$. The resulting equations are

$$\bar{R} = \frac{b}{a} A\rho\left(\frac{-dr}{dt}\right)$$

$$\frac{-dr}{dt} = \frac{a}{b} K_K C_B$$

$$r - R = -\frac{a}{b\rho} K_K C_B t$$

$$t = \frac{b}{a} \frac{\rho}{K_K C_B} (R - r). \qquad (M.41)$$

At complete conversion, $r = 0$ and $t = \tau$. The time required for complete conversion is

$$\tau = \frac{b}{a} \frac{\rho}{K_K C_B} R \qquad (M.42)$$

Dividing Equation (M.41) by (M.42), one obtains:

$$\frac{t}{\tau} = 1 - \frac{r}{R} \qquad (M-43)$$

The fraction of unreacted solid is given by Equation (M.7):

$$X = \frac{Ar}{AR} = \frac{r}{R}$$

Upon substituting into Equation (M.42), the desired form is obtained.

$$\frac{t}{\tau} = 1 - X \qquad (M.44)$$

Reaction controlled: cylindrical geometry. The reaction rate may be expressed by:

$$\bar{R} = AK_K C_B = 2\pi rhK_K C_B \ .$$

This equation is now combined with the mass balance equation based upon the movement of the interface, rearranged, and integrated with boundary conditions, r = R at t = 0. The resulting equations are

$$\bar{R} = \frac{b}{a}\frac{dV}{dt} = \frac{b}{a}\frac{d(\pi r^2 h)}{dt} = -\frac{b}{a}\pi\rho\ 2rh\frac{dr}{dt} \ ,$$

$$\frac{dr}{dt} = -\frac{a}{b\rho}K_K C_B \ ,$$

$$R - r = \frac{aK_K C_B t}{b\rho} \ , \text{ and}$$

$$t = \frac{b\rho}{aK_K C_B}(R - r) \ . \qquad \text{(M.45)}$$

At complete conversion, r = 0 and t = τ. Therefore,

$$\tau = \frac{b\rho}{aK_K C_B} R \ . \qquad \text{(M-46)}$$

Dividing Equation (M.45) by Equation (M.46), one obtains:

$$\frac{t}{\tau} = 1 - \frac{r}{R} \ . \qquad \text{(M.47)}$$

The fraction of unreacted solid is found by Equation (M.13):

$$X = \frac{\pi r^2 h}{\pi R^2 h} = \left(\frac{r}{R}\right)^2 \ .$$

Upon substitution into Equation (M.47), the final solution is

$$\frac{t}{\tau} = 1 - X^{1/2} \quad . \tag{M.48}$$

Reaction controlled: spherical geometry. The reaction rate for spherical geometry may be expressed as:

$$\bar{R} = AK_K C_B = 4\pi r^2 K_K C_B \quad .$$

The rate of gaseous reactant consumption as a function of interface movement is

$$\bar{R} = \frac{b\rho}{a} \frac{dV}{dt} = \frac{b\rho}{a} \frac{4\pi}{3} \frac{d(r^3)}{dt} = - \frac{b\rho 4\pi r^2}{a} \frac{dr}{dt} \quad . \tag{M.49}$$

Upon combining, rearranging, and integrating the two preceding equations with the boundary conditions r = R at t = 0, one obtains

$$- \frac{dr}{dt} = \frac{a}{b\rho} K_K C_B \quad ,$$

$$R - r = \frac{aK_K C_B}{b\rho} t \quad ,$$

$$t = \frac{b\rho}{aK_K C_B} (R - r) \quad . \tag{M.50}$$

At complete conversion, r = 0 and t = τ, therefore the time required for complete conversion is

$$\tau = \frac{b\rho}{aK_K C_B} R \quad . \tag{M.51}$$

Dividing Equation (M.50) by (M.51), one obtains:

$$\frac{t}{\tau} = 1 - \frac{r}{R} . \qquad \text{(M.52)}$$

In spherical geometry, the fraction of unreacted solids, X, as a function of r is given by Equation (M.18):

$$X = \frac{\frac{4\pi r^3}{3}}{\frac{4\pi R^3}{3}} = \frac{r^3}{R^3} .$$

Upon substitution into Equation (M.52), the desired solution is:

$$\frac{t}{\tau} = 1 - X^{1/3} . \qquad \text{(M.53)}$$

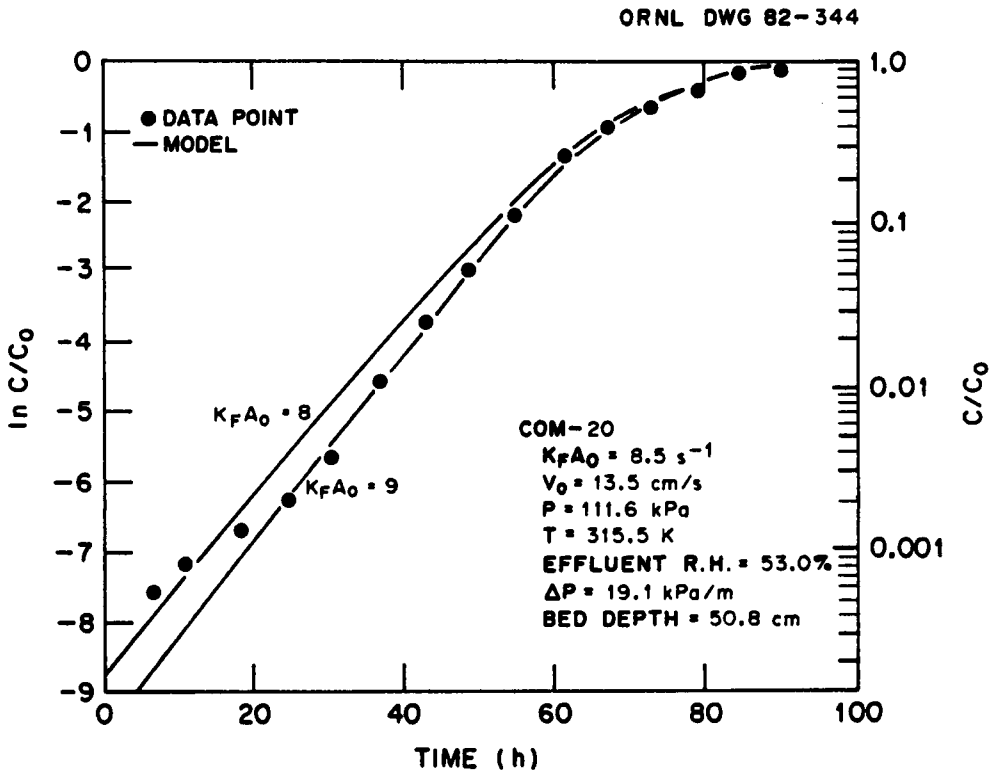
Table M.1. Shrinking core model predictions for limited mass transfer of gaseous reactant

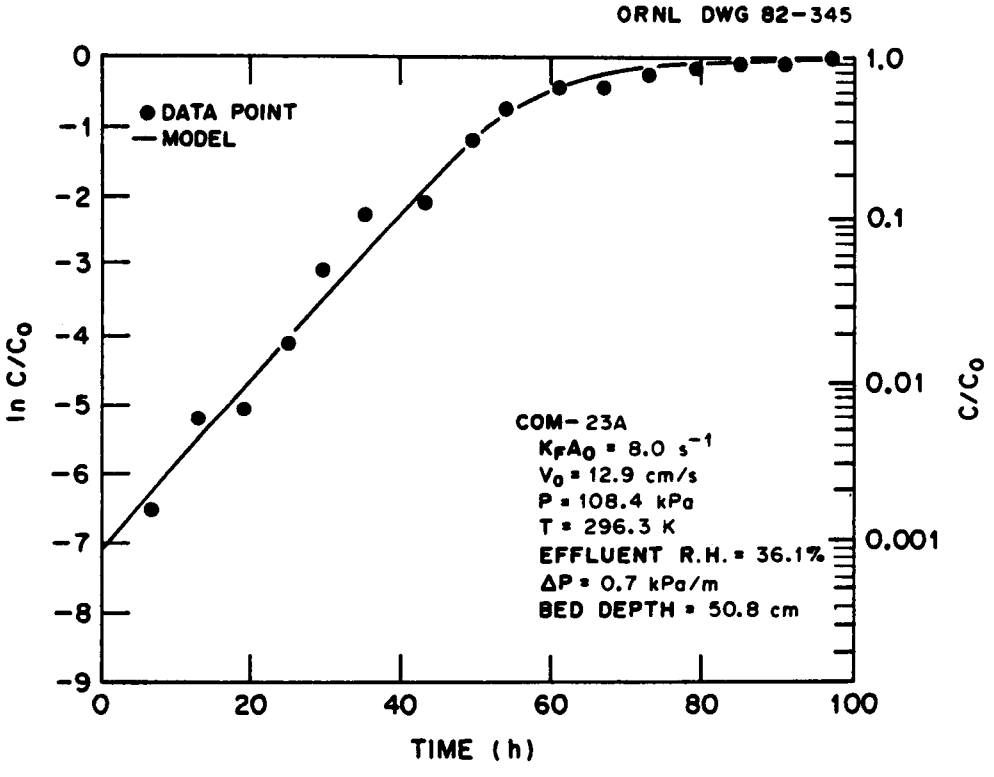
Controlling mechanism	Particle geometry	Reaction time[a]
Gas film	Planar	$\frac{t}{\tau} = 1 - X;\ \tau = \frac{bR\rho}{aK_F C_B}$
	Cylindrical	$\frac{t}{\tau} = 1 - X;\ \tau = \frac{bR\rho}{aK_F C_B}$
	Spherical	$\frac{t}{\tau} = 1 - X;\ \tau = \frac{bR\rho}{aK_F C_B}$
Diffusion through solid product	Planar	$\frac{t}{\tau} = X^2 - 2X + 1;\ \tau = \frac{bR^2\rho}{a2DC_B}$
	Cylindrical	$\frac{t}{\tau} = X\ \ln X - X + 1;\ \tau = \frac{bR^2\rho}{a4DCB}$
	Spherical	$\frac{t}{\tau} = 2X - 3X^{2/3} + 1;\ \tau = \frac{bR^2\rho}{a6DC_B}$
First-order, kinetically controlled reaction	Planar	$\frac{t}{\tau} = 1 - X;\ \tau = \frac{bR\rho}{aK_K C_B}$
	Cylindrical	$\frac{t}{\tau} = 1 - X^{1/2};\ \tau = \frac{bR\rho}{aK_K C_B}$
	Spherical	$\frac{t}{\tau} = 1 - X^{1/3};\ \tau = \frac{bR\rho}{aK_K C_B}$

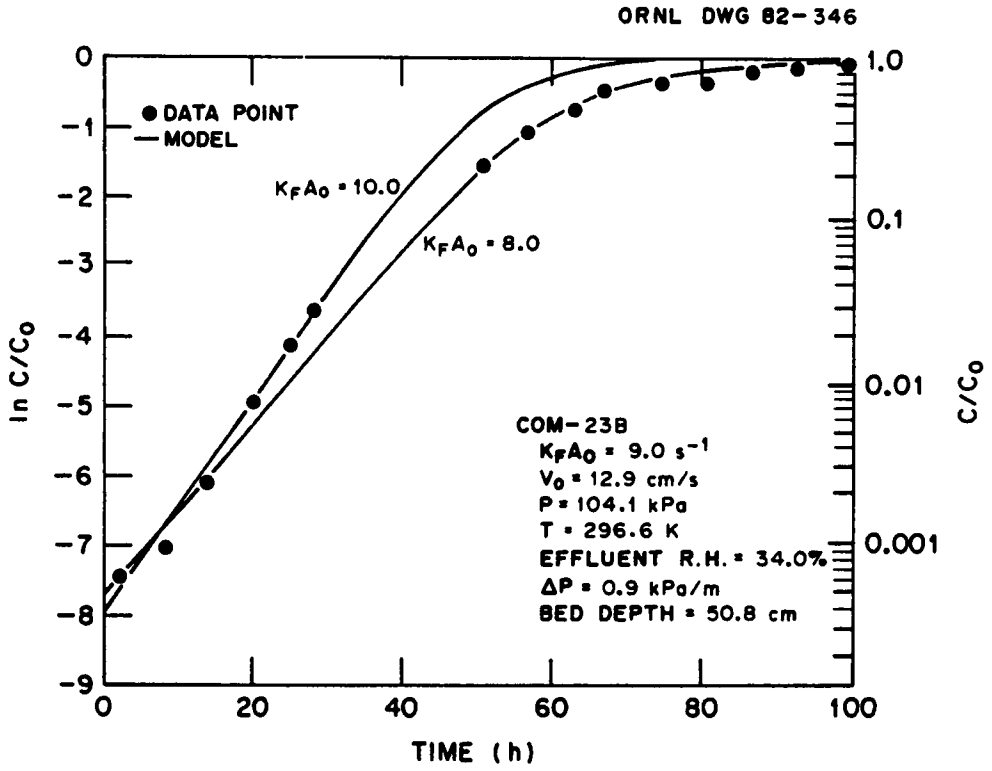
[a]Reaction time as a function of fractional conversion of reactant.

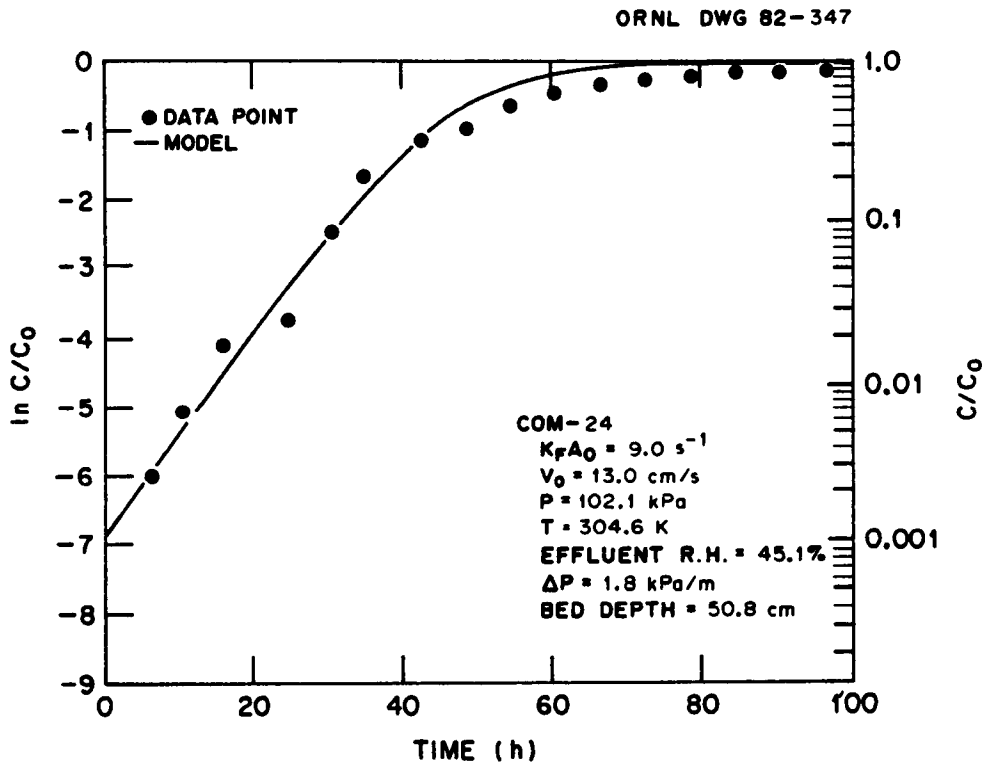
APPENDIX N

EXPERIMENTAL AND MODEL-PREDICTED BREAKTHROUGH CURVES FROM FIXED-BED STUDIES

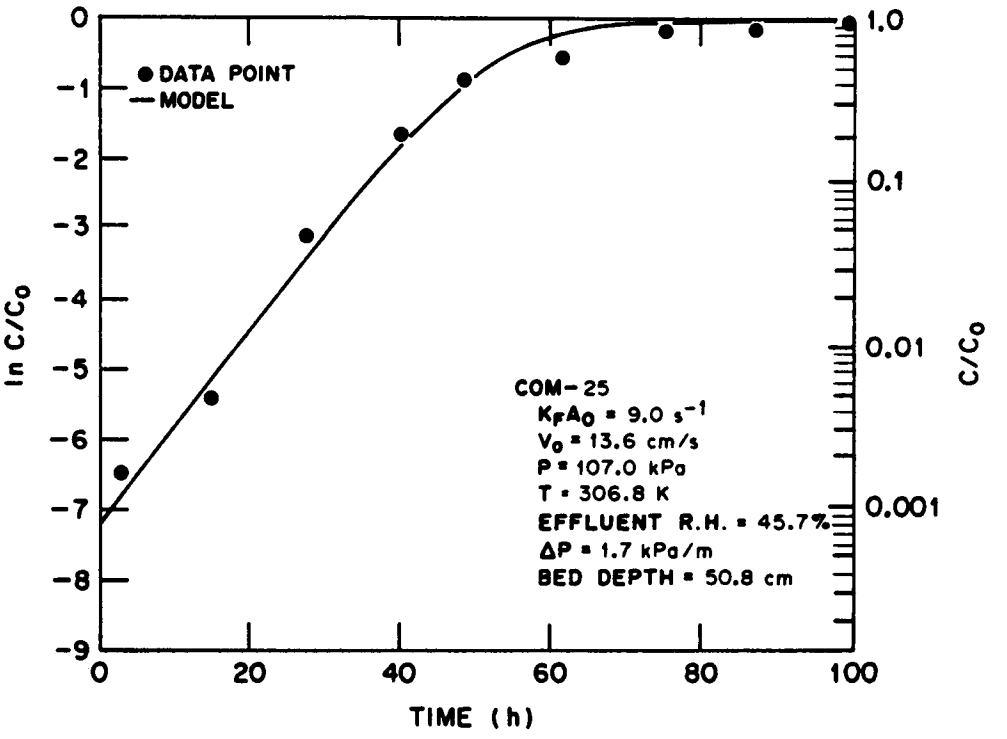

ORNL DWG 82-344
● DATA POINT
— MODEL
K_FA_o = 8
K_FA_o = 9
COM-20
K_FA_o = 8.5 s^{-1}
V_o = 13.5 cm/s
P = 111.6 kPa
T = 315.5 K
EFFLUENT R.H. = 53.0%
ΔP = 19.1 kPa/m
BED DEPTH = 50.8 cm
ln C/C$_o$
C/C$_o$
TIME (h)


ORNL DWG 82-345
● DATA POINT
— MODEL
COM-23A
K_FA_o = 8.0 s^{-1}
V_o = 12.9 cm/s
P = 108.4 kPa
T = 296.3 K
EFFLUENT R.H. = 36.1%
ΔP = 0.7 kPa/m
BED DEPTH = 50.8 cm
ln C/C$_o$
C/C$_o$
TIME (h)

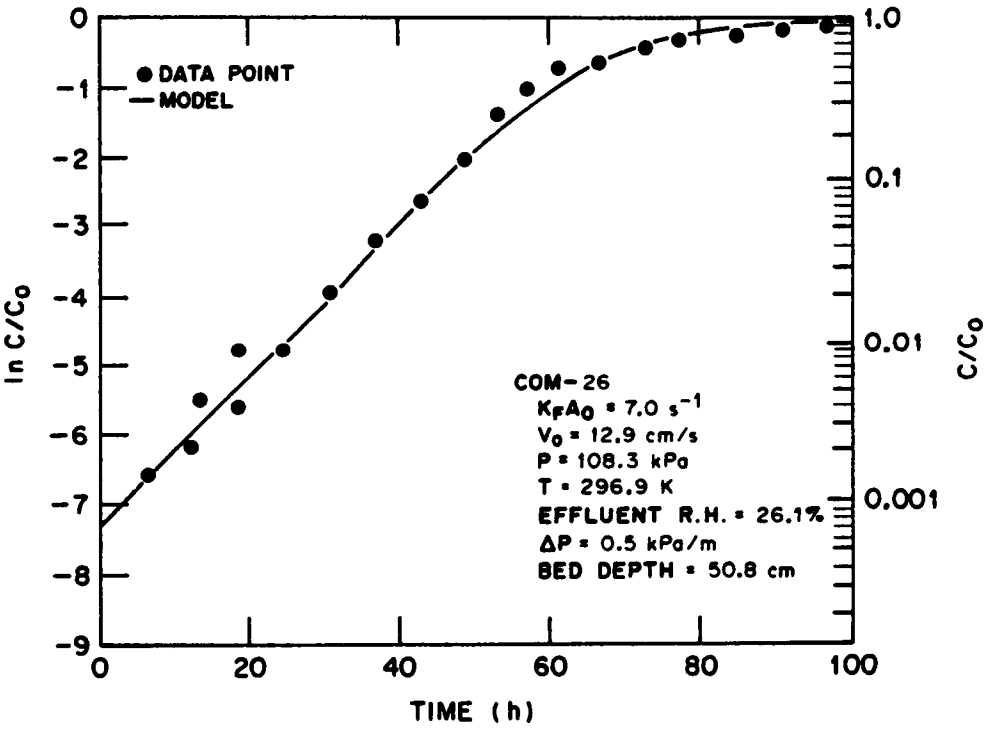

ORNL DWG 82-346
DATA POINT
MODEL
K_FA_o = 10.0
K_FA_o = 8.0
COM-23B
K_FA_o = 9.0 s^{-1}
V_o = 12.9 cm/s
P = 104.1 kPa
T = 296.6 K
EFFLUENT R.H. = 34.0%
ΔP = 0.9 kPa/m
BED DEPTH = 50.8 cm
ln C/C$_o$
C/C$_o$
TIME (h)

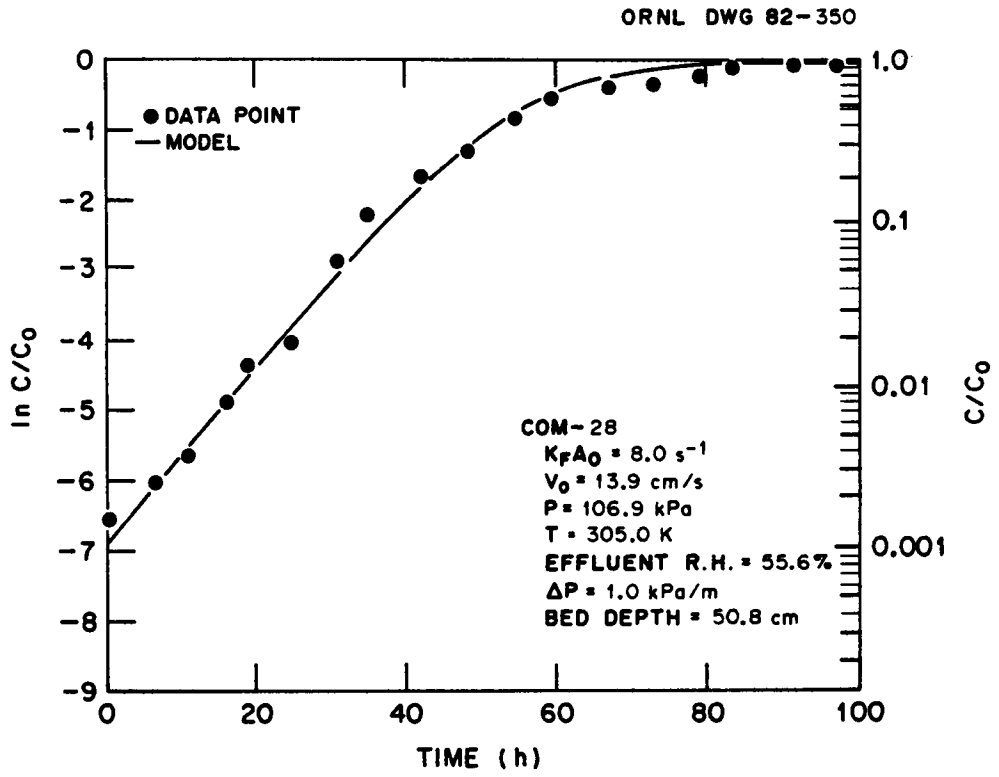

ORNL DWG 82-347
DATA POINT
MODEL
COM-24
K_FA_o = 9.0 s^{-1}
V_o = 13.0 cm/s
P = 102.1 kPa
T = 304.6 K
EFFLUENT R.H. = 45.1%
ΔP = 1.8 kPa/m
BED DEPTH = 50.8 cm
ln C/C$_o$
C/C$_o$
TIME (h)

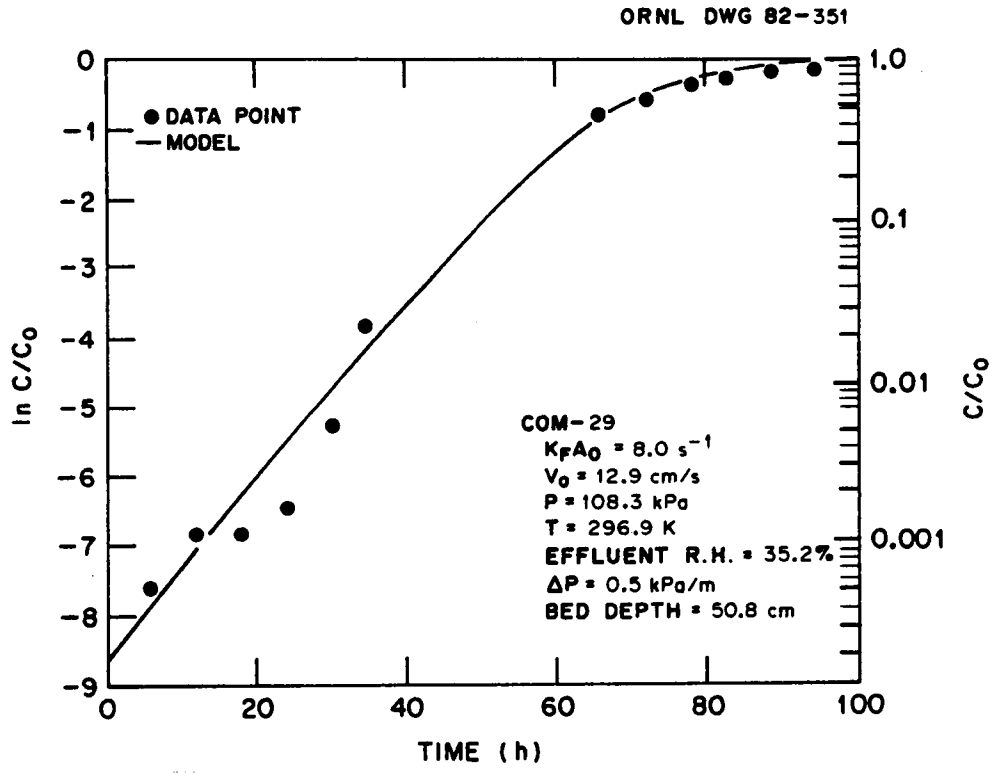
ORNL DWG 82-348

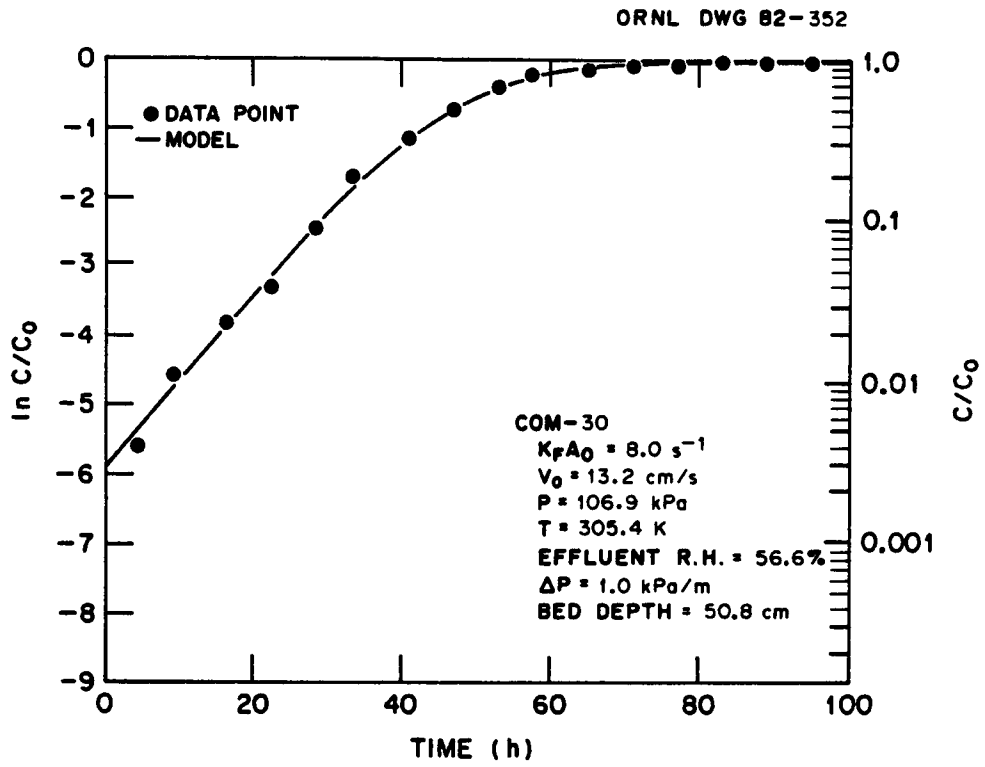


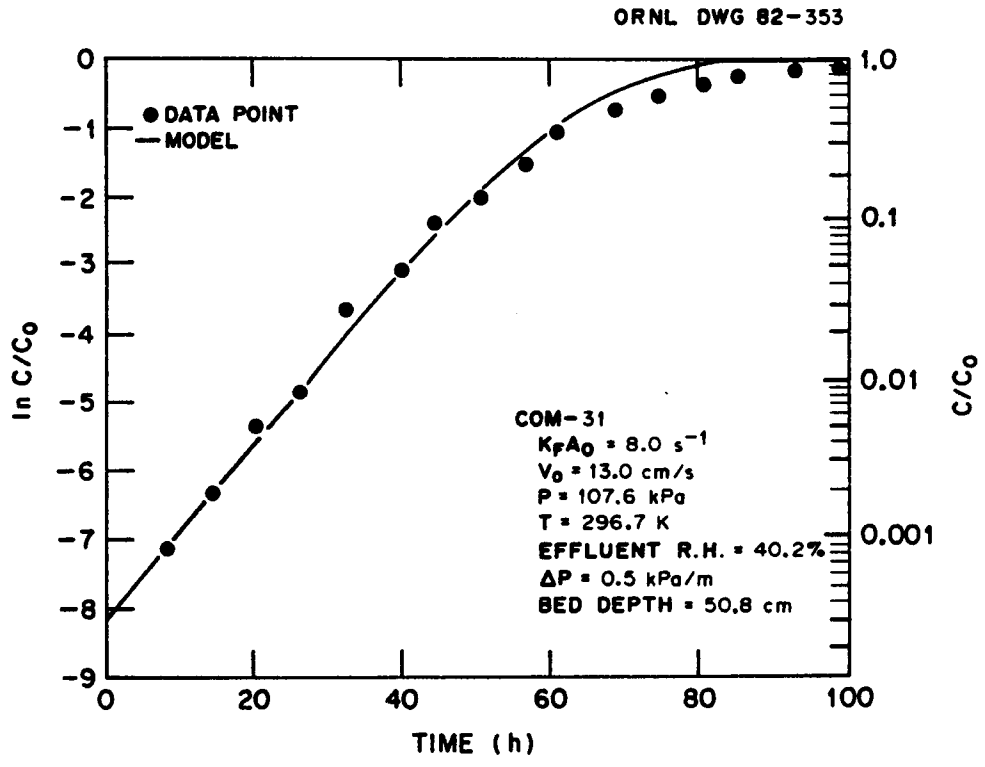
ORNL DWG 82-349



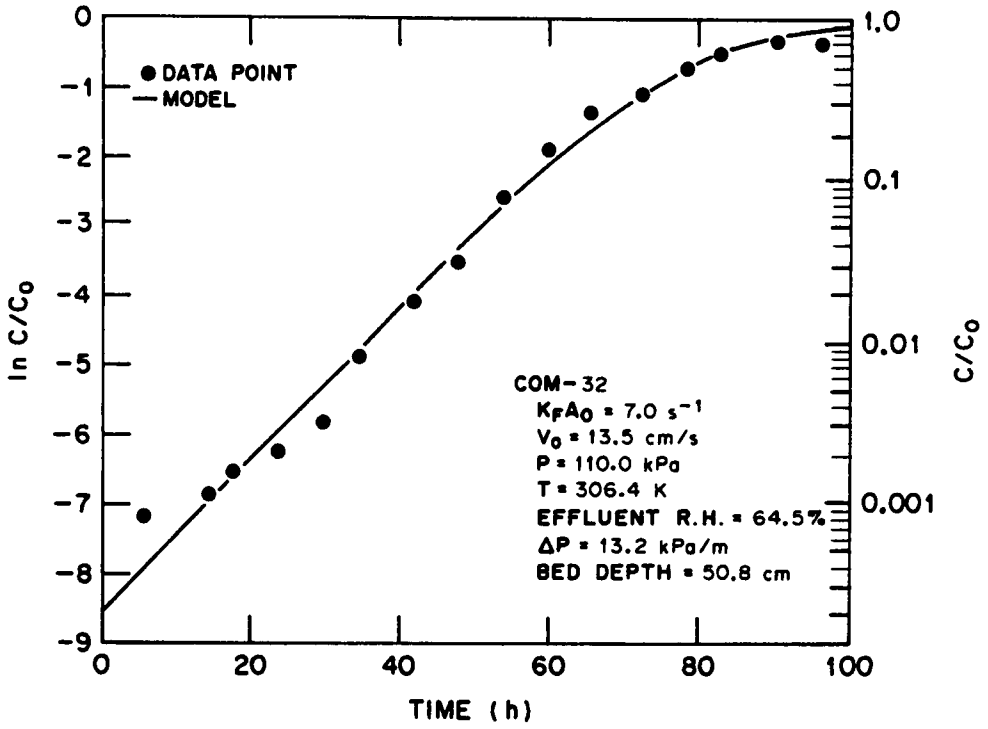

ORNL DWG 82-350
● DATA POINT
— MODEL
COM-28
K_FA_0 = 8.0 s^{-1}
V_0 = 13.9 cm/s
P = 106.9 kPa
T = 305.0 K
EFFLUENT R.H. = 55.6%
ΔP = 1.0 kPa/m
BED DEPTH = 50.8 cm
ln C/C₀
C/C₀
TIME (h)
0
-1
-2
-3
-4
-5
-6
-7
-8
-9
1.0
0.1
0.01
0.001
0
20
40
60
80
100


ORNL DWG 82-351
● DATA POINT
— MODEL
COM-29
K_FA_0 = 8.0 s^{-1}
V_0 = 12.9 cm/s
P = 108.3 kPa
T = 296.9 K
EFFLUENT R.H. = 35.2%
ΔP = 0.5 kPa/m
BED DEPTH = 50.8 cm
ln C/C₀
C/C₀
TIME (h)
0
-1
-2
-3
-4
-5
-6
-7
-8
-9
1.0
0.1
0.01
0.001
0
20
40
60
80
100

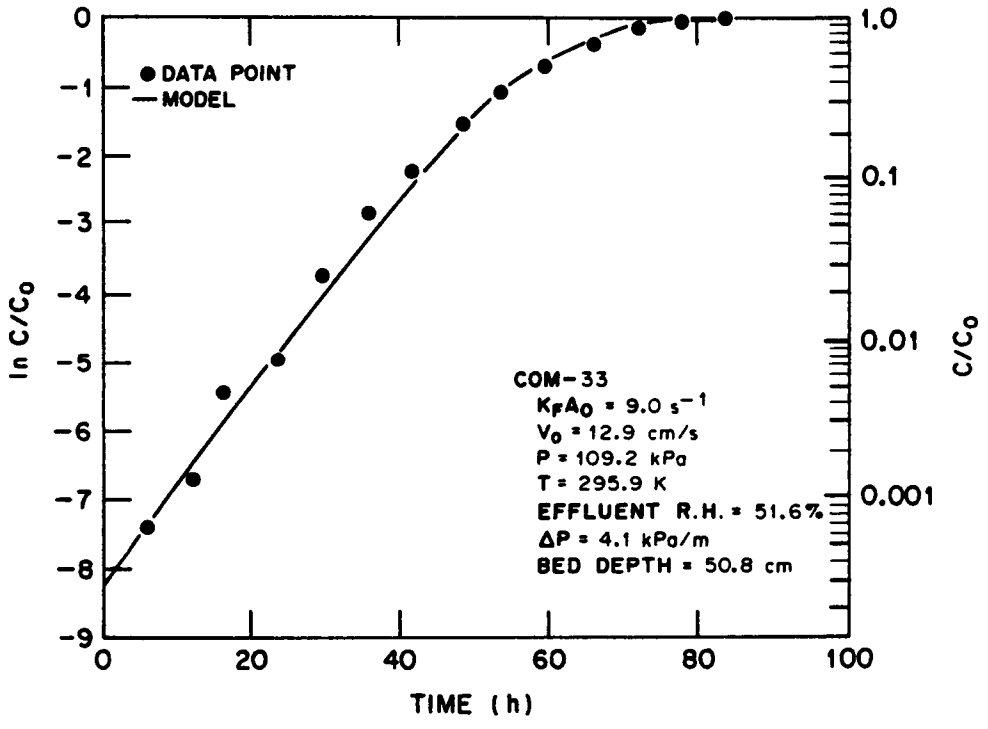

ORNL DWG 82-352
● DATA POINT
— MODEL
COM-30
K_FA_0 = 8.0 s^{-1}
V_0 = 13.2 cm/s
P = 106.9 kPa
T = 305.4 K
EFFLUENT R.H. = 56.6%
ΔP = 1.0 kPa/m
BED DEPTH = 50.8 cm
ln C/C$_0$
C/C$_0$
TIME (h)
0
-1
-2
-3
-4
-5
-6
-7
-8
-9
1.0
0.1
0.01
0.001
0
20
40
60
80
100

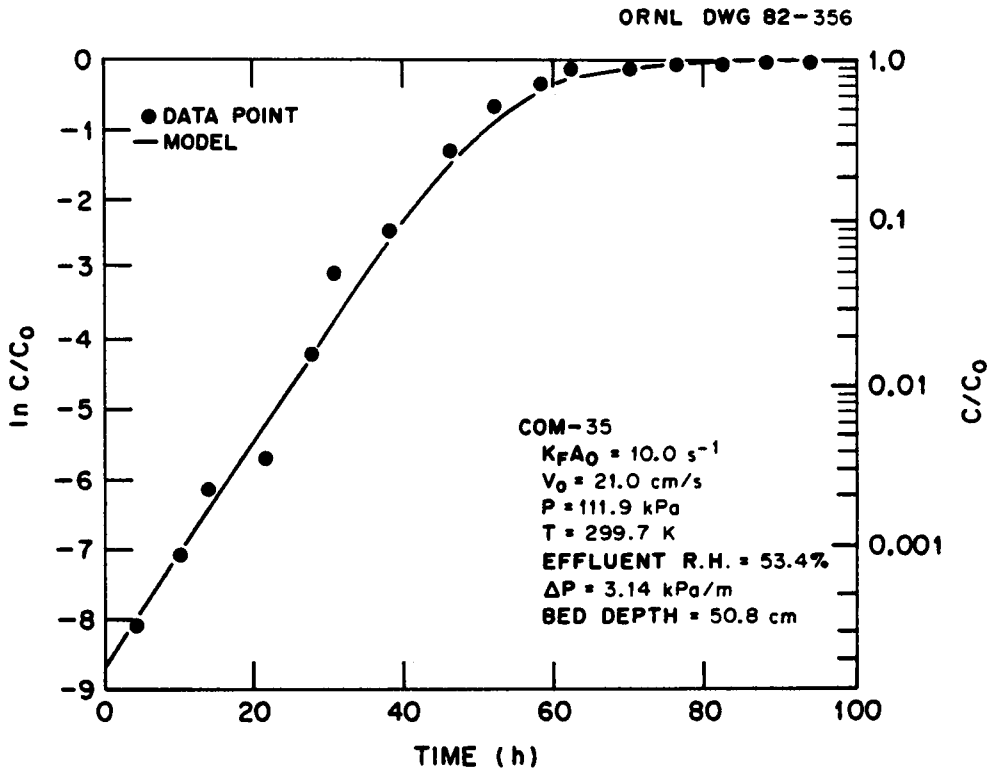

ORNL DWG 82-353
● DATA POINT
— MODEL
COM-31
K_FA_0 = 8.0 s^{-1}
V_0 = 13.0 cm/s
P = 107.6 kPa
T = 296.7 K
EFFLUENT R.H. = 40.2%
ΔP = 0.5 kPa/m
BED DEPTH = 50.8 cm
ln C/C$_0$
C/C$_0$
TIME (h)
0
-1
-2
-3
-4
-5
-6
-7
-8
-9
1.0
0.1
0.01
0.001
0
20
40
60
80
100

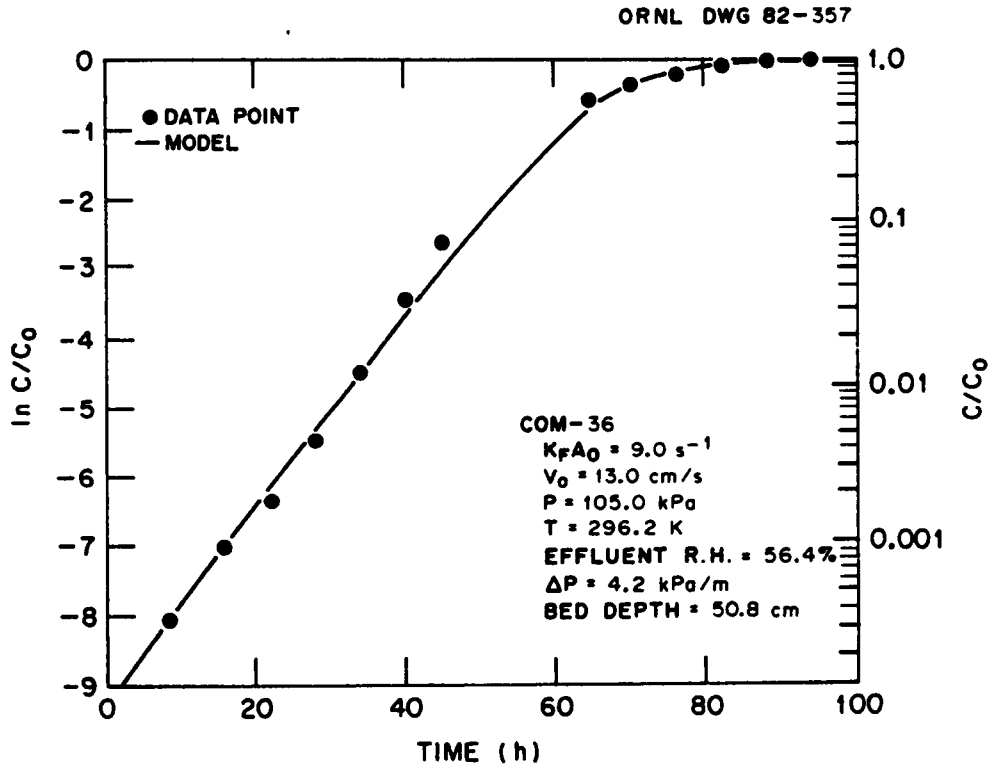
ORNL DWG 82-354

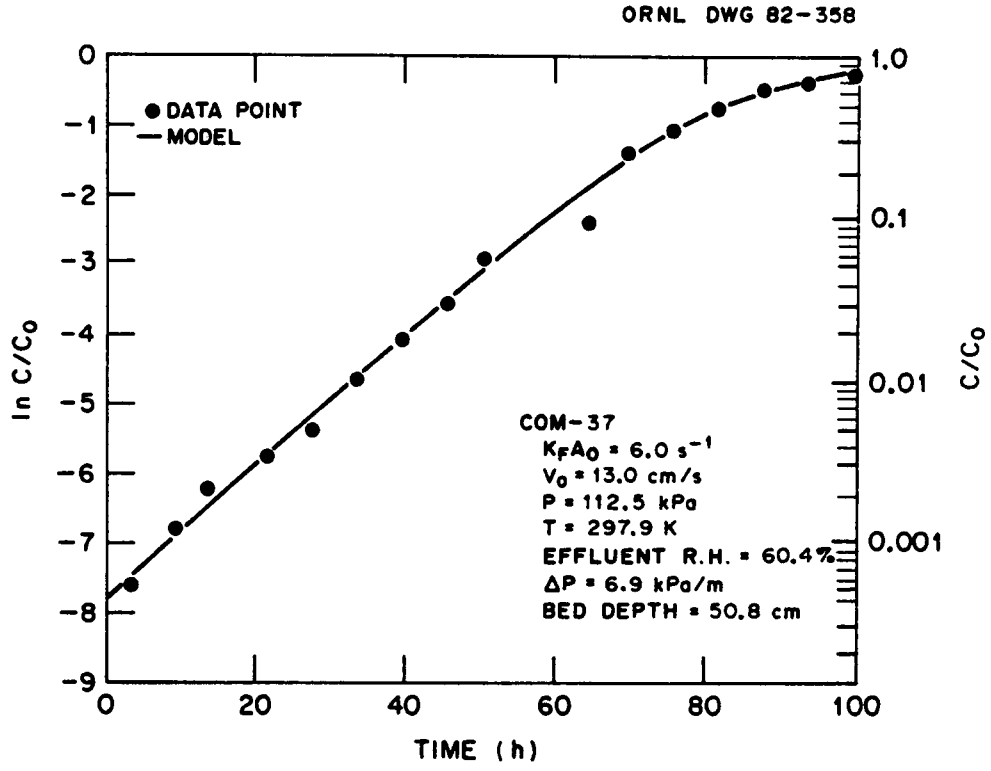


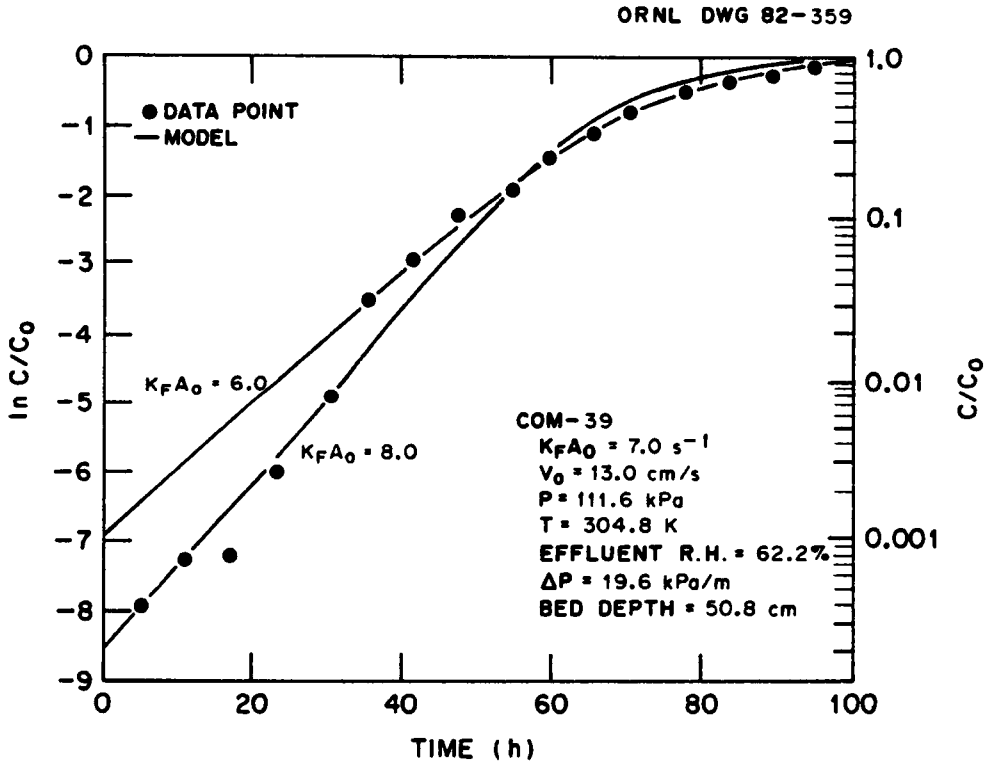
ORNL DWG 82-355



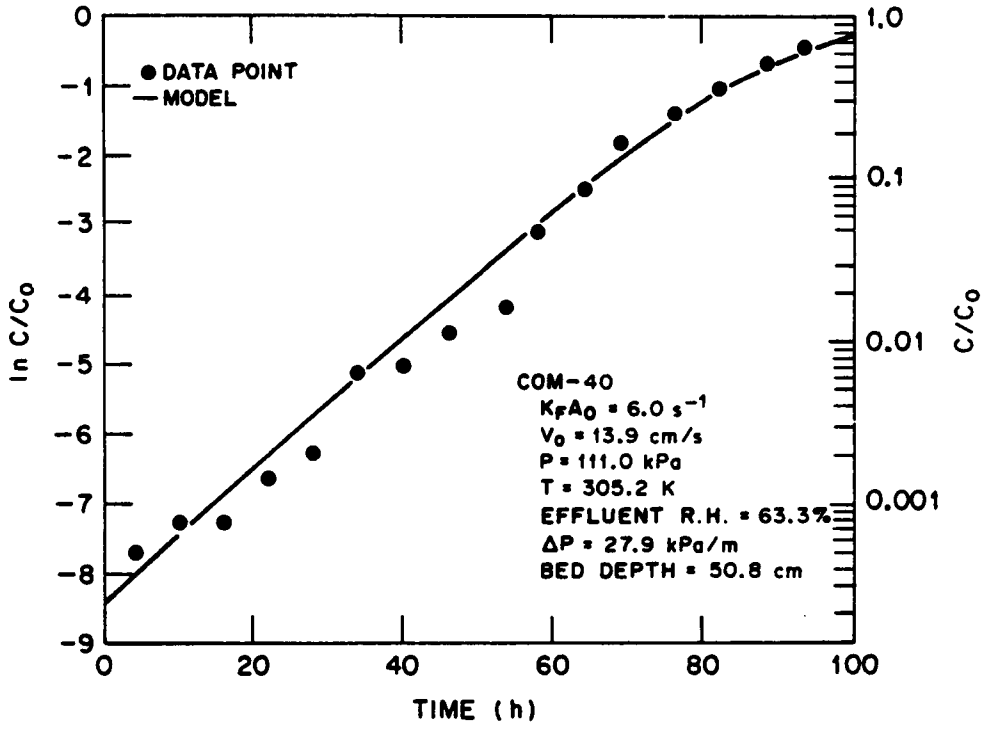

ORNL DWG 82-356
DATA POINT
MODEL
COM-35
K_FA_0 = 10.0 s^{-1}
V_0 = 21.0 cm/s
P = 111.9 kPa
T = 299.7 K
EFFLUENT R.H. = 53.4%
ΔP = 3.14 kPa/m
BED DEPTH = 50.8 cm
ln C/C$_0$
C/C$_0$
TIME (h)
0
-1
-2
-3
-4
-5
-6
-7
-8
-9
1.0
0.1
0.01
0.001
0
20
40
60
80
100


ORNL DWG 82-357
DATA POINT
MODEL
COM-36
K_FA_0 = 9.0 s^{-1}
V_0 = 13.0 cm/s
P = 105.0 kPa
T = 296.2 K
EFFLUENT R.H. = 56.4%
ΔP = 4.2 kPa/m
BED DEPTH = 50.8 cm
ln C/C$_0$
C/C$_0$
TIME (h)
0
-1
-2
-3
-4
-5
-6
-7
-8
-9
1.0
0.1
0.01
0.001
0
20
40
60
80
100

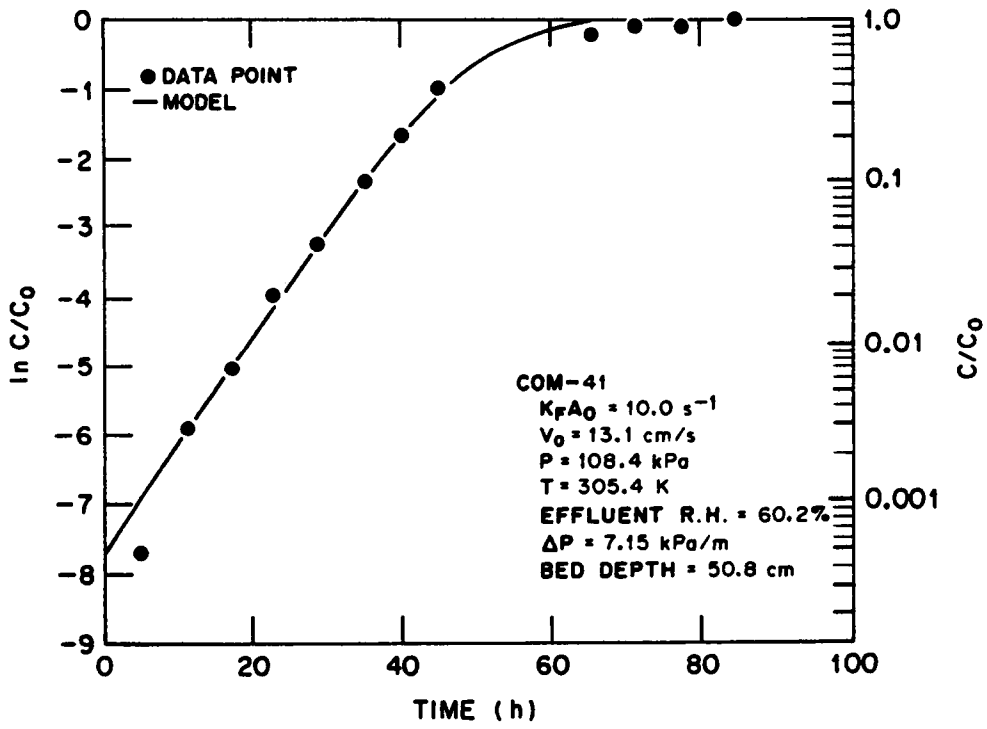

ORNL DWG 82-358
● DATA POINT
— MODEL
COM-37
K_FA_0 = 6.0 s^{-1}
V_0 = 13.0 cm/s
P = 112.5 kPa
T = 297.9 K
EFFLUENT R.H. = 60.4%
ΔP = 6.9 kPa/m
BED DEPTH = 50.8 cm
ln C/C$_0$
C/C$_0$
TIME (h)

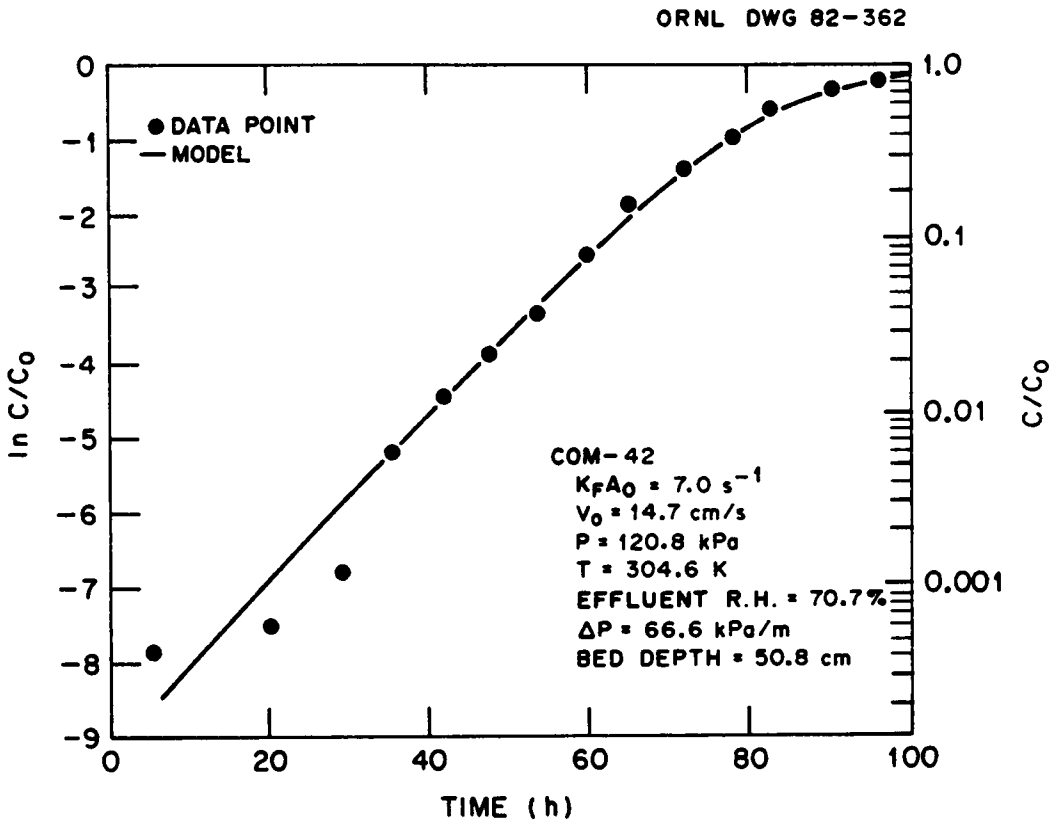

ORNL DWG 82-359
● DATA POINT
— MODEL
K_FA_0 = 6.0
K_FA_0 = 8.0
COM-39
K_FA_0 = 7.0 s^{-1}
V_0 = 13.0 cm/s
P = 111.6 kPa
T = 304.8 K
EFFLUENT R.H. = 62.2%
ΔP = 19.6 kPa/m
BED DEPTH = 50.8 cm
ln C/C$_0$
C/C$_0$
TIME (h)

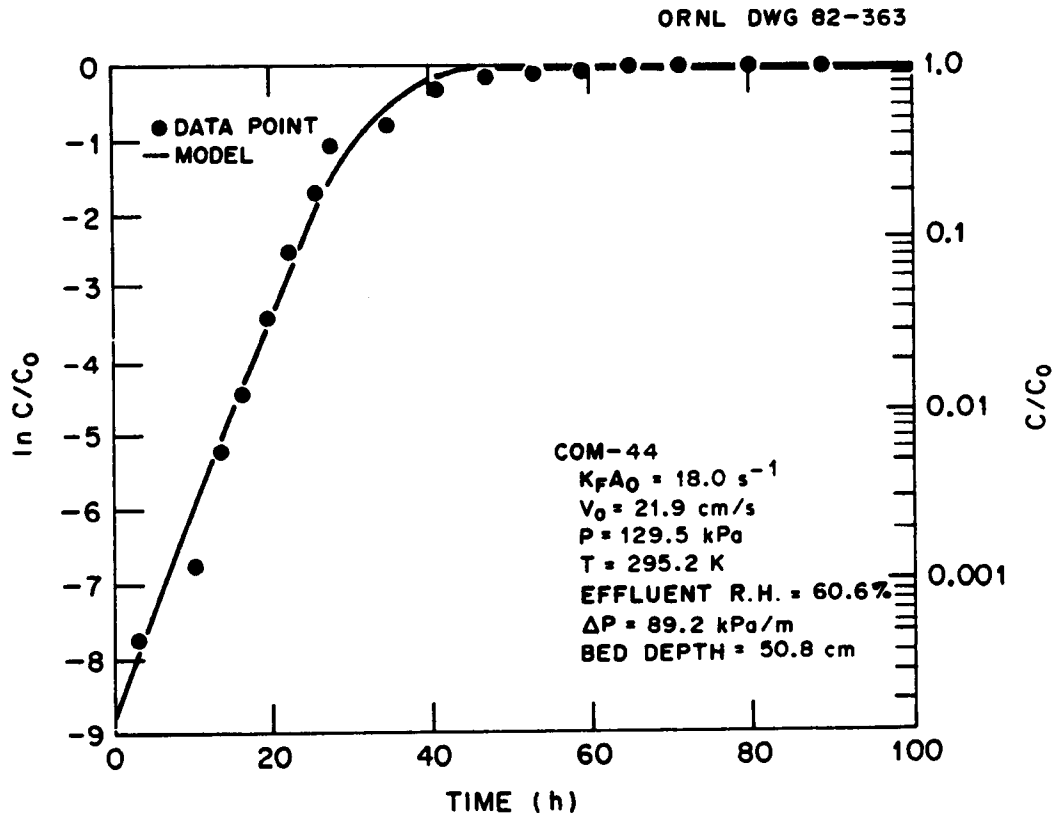
ORNL DWG 82-360

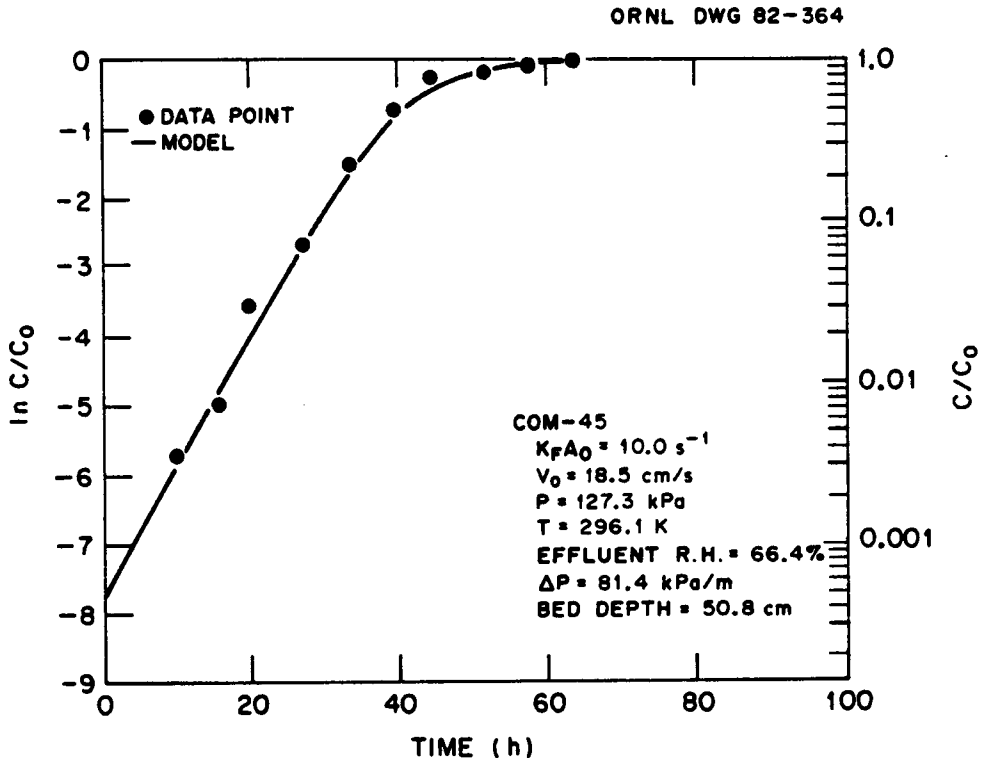


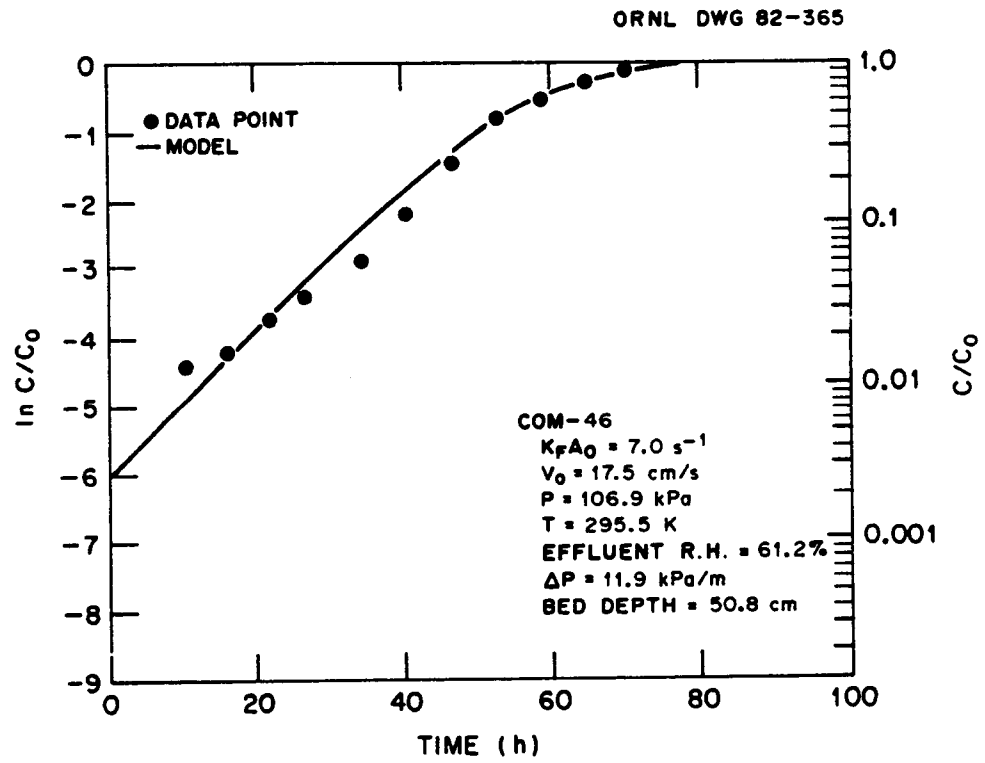
ORNL DWG 82-361



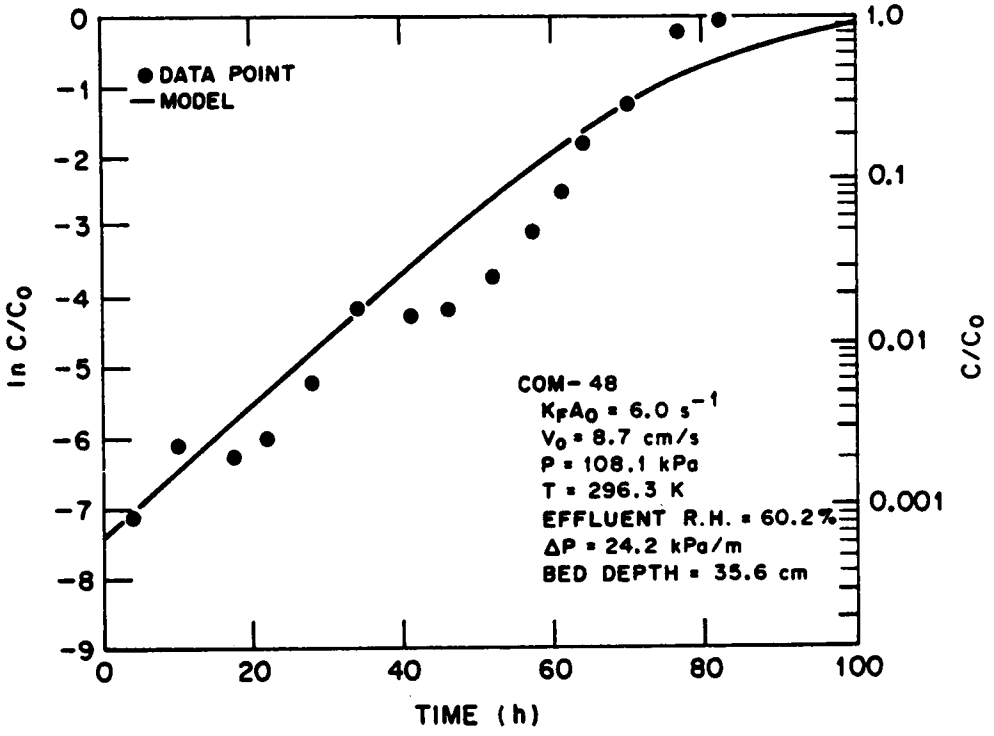

ORNL DWG 82-362
● DATA POINT
— MODEL
COM-42
K_FA_0 = 7.0 s^{-1}
V_0 = 14.7 cm/s
P = 120.8 kPa
T = 304.6 K
EFFLUENT R.H. = 70.7%
ΔP = 66.6 kPa/m
BED DEPTH = 50.8 cm
ln C/C$_0$
C/C$_0$
TIME (h)


ORNL DWG 82-363
● DATA POINT
— MODEL
COM-44
K_FA_0 = 18.0 s^{-1}
V_0 = 21.9 cm/s
P = 129.5 kPa
T = 295.2 K
EFFLUENT R.H. = 60.6%
ΔP = 89.2 kPa/m
BED DEPTH = 50.8 cm
ln C/C$_0$
C/C$_0$
TIME (h)

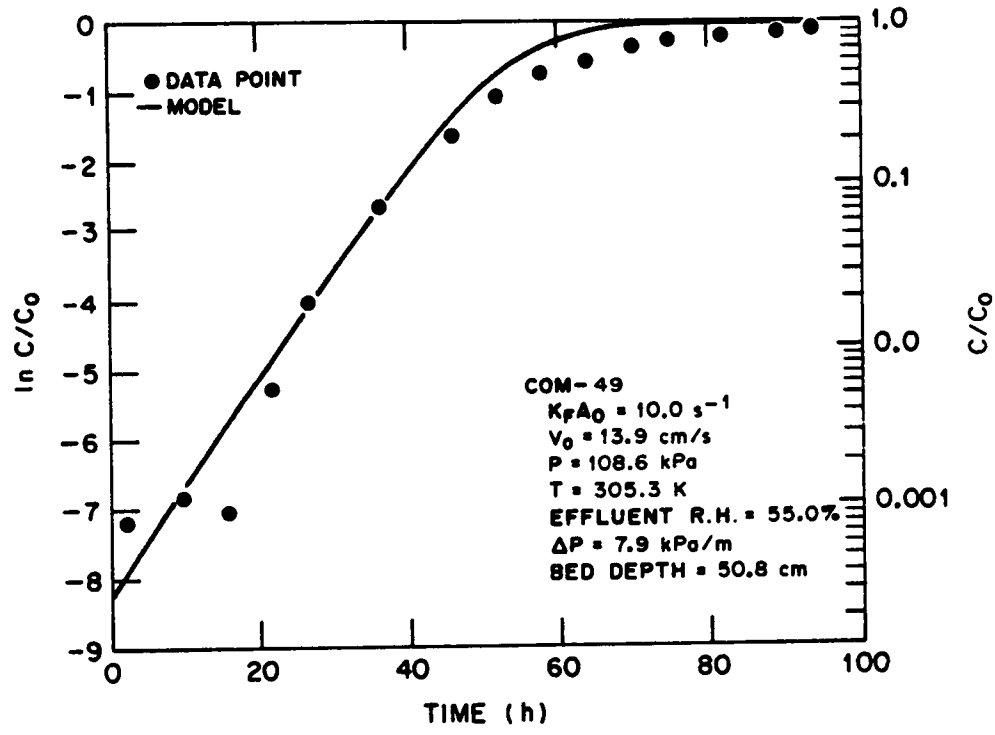

ORNL DWG 82-364
DATA POINT
MODEL
COM-45
K_FA_0 = 10.0 s^{-1}
V_0 = 18.5 cm/s
P = 127.3 kPa
T = 296.1 K
EFFLUENT R.H. = 66.4%
ΔP = 81.4 kPa/m
BED DEPTH = 50.8 cm
ln C/C0
C/C0
TIME (h)


ORNL DWG 82-365
DATA POINT
MODEL
COM-46
K_FA_0 = 7.0 s^{-1}
V_0 = 17.5 cm/s
P = 106.9 kPa
T = 295.5 K
EFFLUENT R.H. = 61.2%
ΔP = 11.9 kPa/m
BED DEPTH = 50.8 cm
ln C/C0
C/C0
TIME (h)

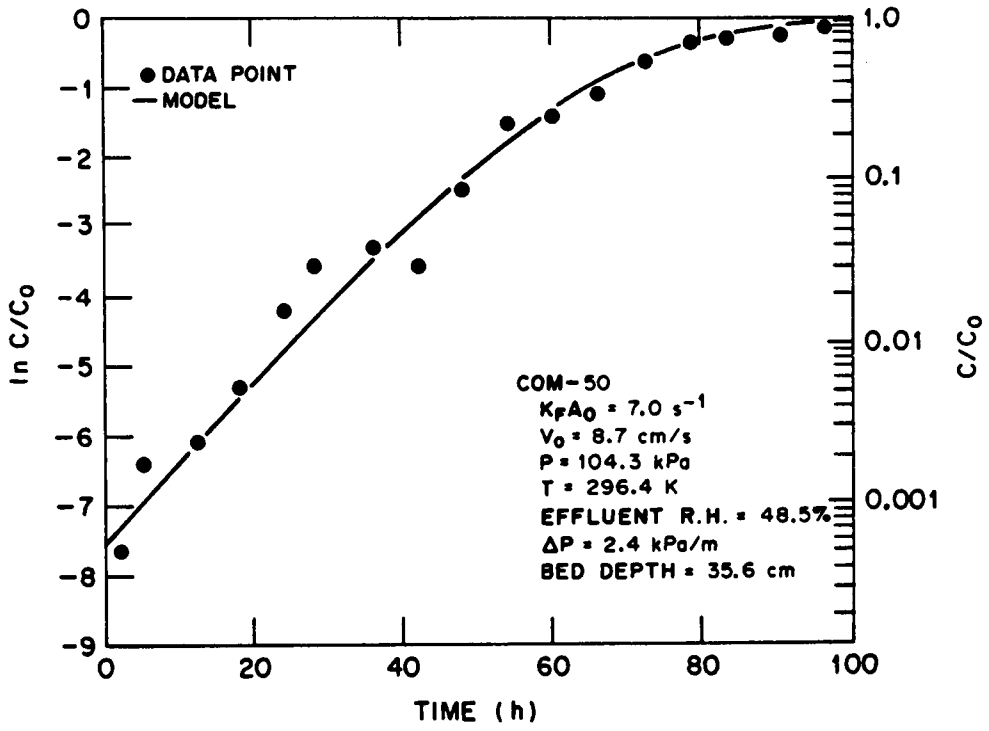
ORNL DWG 82-366



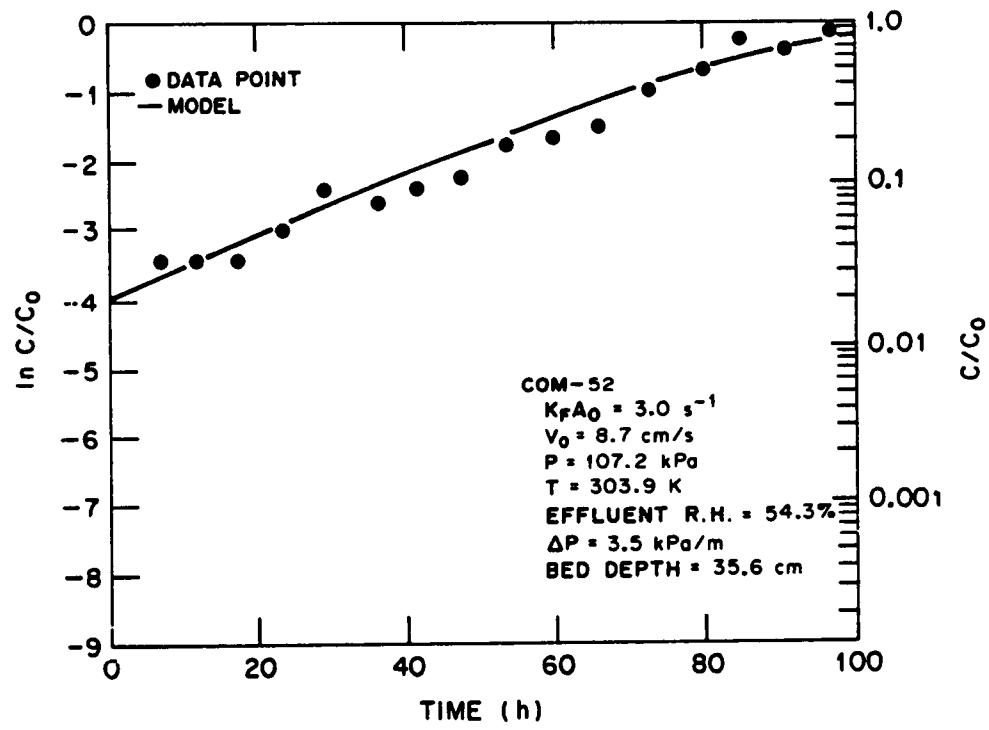
ORNL DWG 82-367

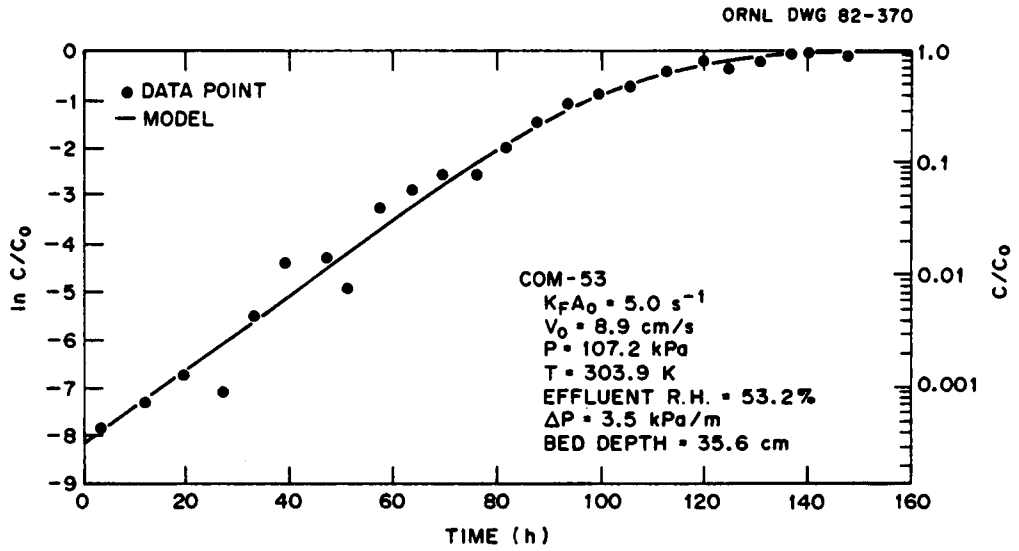


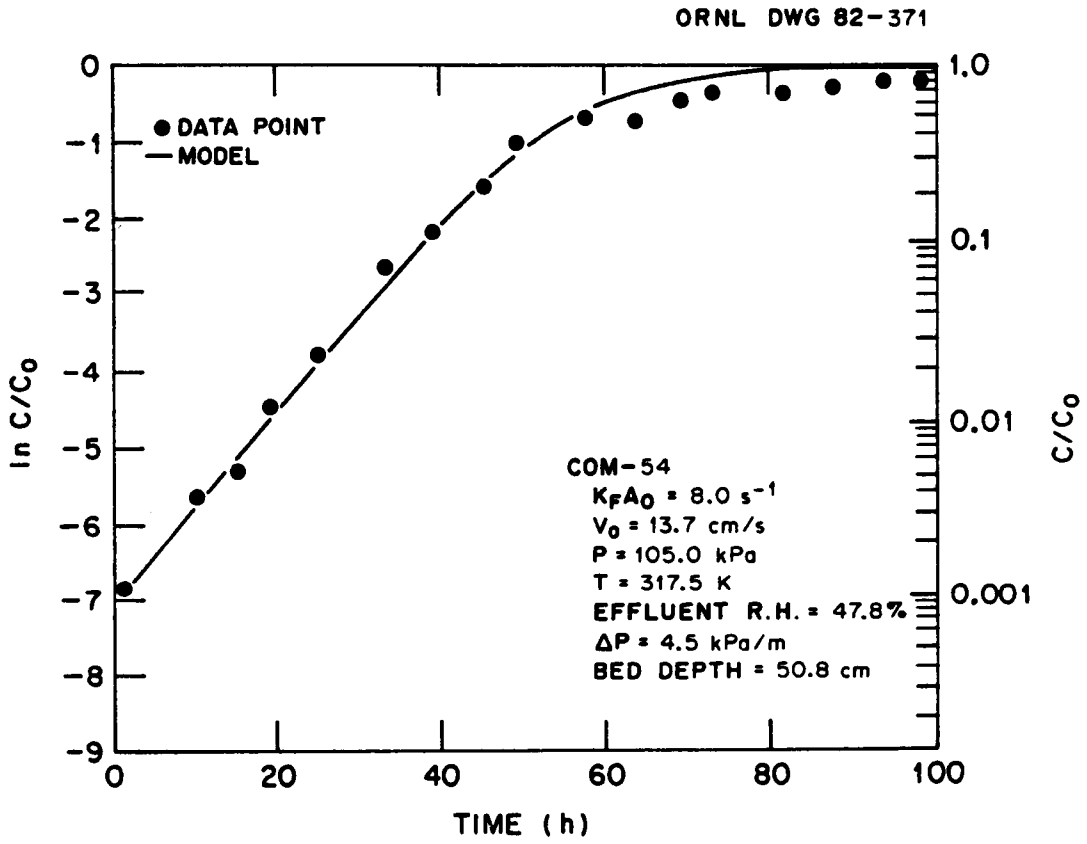
ORNL DWG 82-368

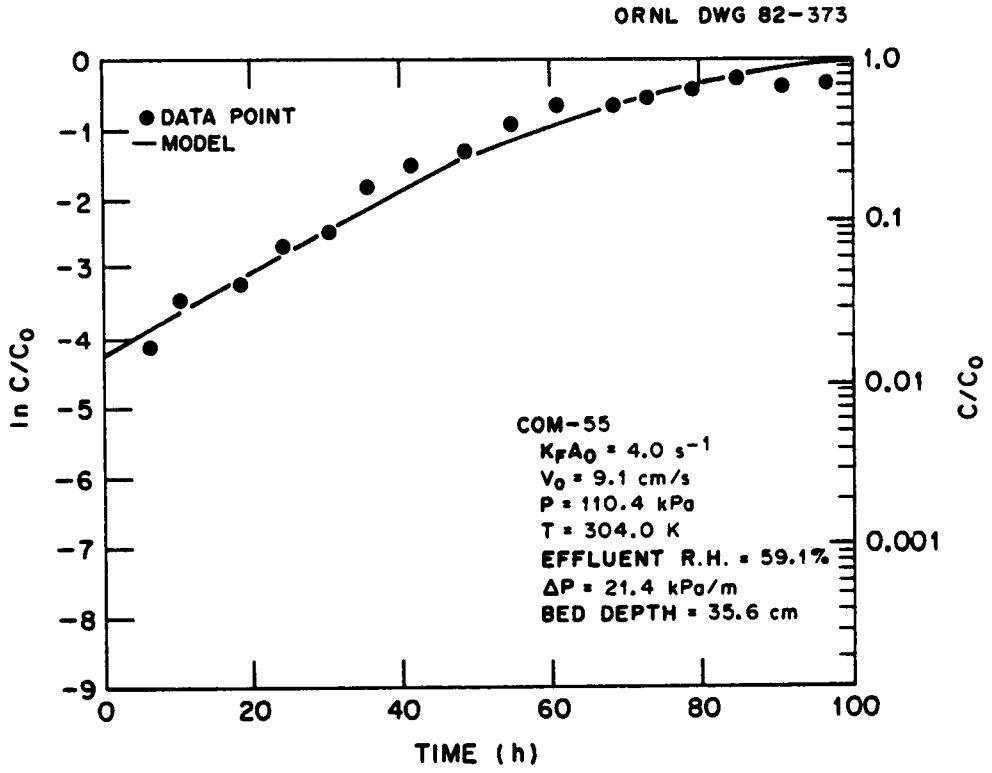


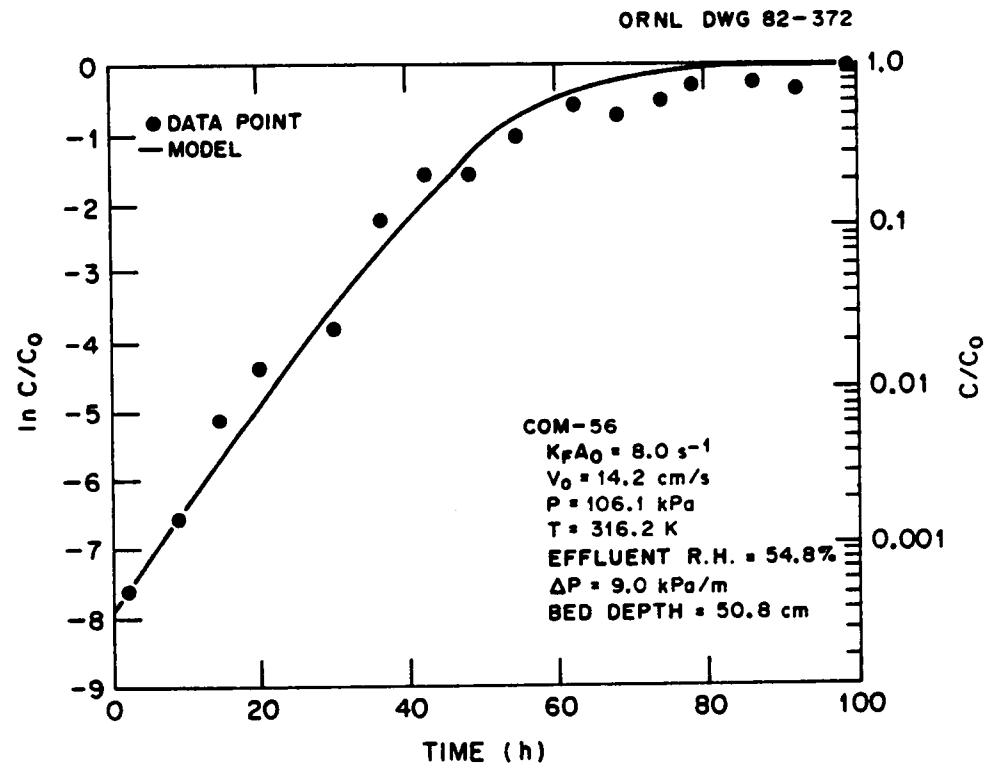
ORNL DWG 82-369

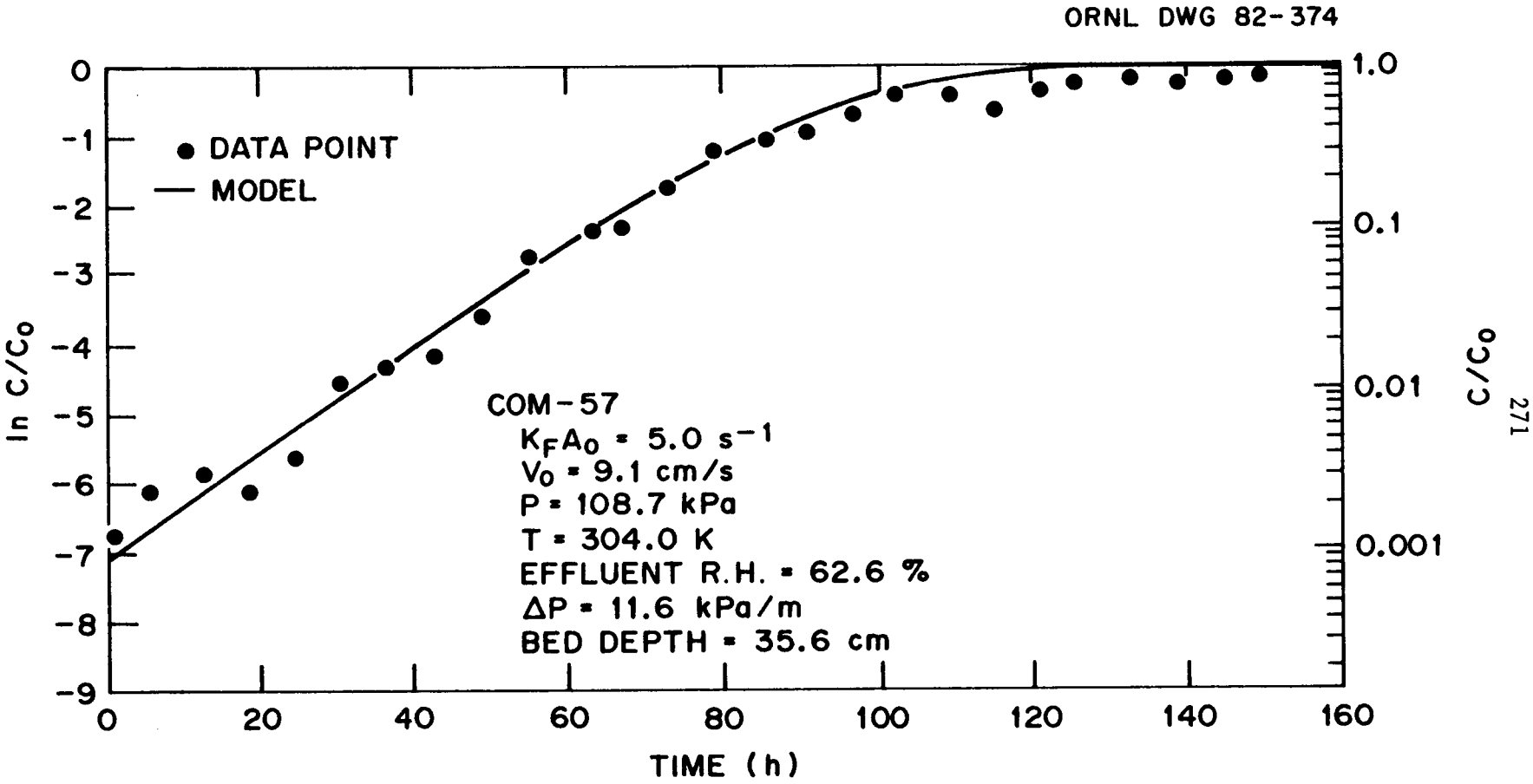



ORNL DWG 82-370
● DATA POINT
— MODEL
COM-53
$K_F A_0$ = 5.0 s^{-1}
V_0 = 8.9 cm/s
P = 107.2 kPa
T = 303.9 K
EFFLUENT R.H. = 53.2%
ΔP = 3.5 kPa/m
BED DEPTH = 35.6 cm
ln C/C₀
C/C₀
TIME (h)


ORNL DWG 82-371
● DATA POINT
— MODEL
COM-54
$K_F A_0$ = 8.0 s^{-1}
V_0 = 13.7 cm/s
P = 105.0 kPa
T = 317.5 K
EFFLUENT R.H. = 47.8%
ΔP = 4.5 kPa/m
BED DEPTH = 50.8 cm
ln C/C₀
C/C₀
TIME (h)


ORNL DWG 82-373
● DATA POINT
— MODEL
COM-55
K_FA_0 = 4.0 s^{-1}
V_0 = 9.1 cm/s
P = 110.4 kPa
T = 304.0 K
EFFLUENT R.H. = 59.1%
ΔP = 21.4 kPa/m
BED DEPTH = 35.6 cm
ln C/C$_0$
C/C$_0$
TIME (h)


ORNL DWG 82-372
● DATA POINT
— MODEL
COM-56
K_FA_0 = 8.0 s^{-1}
V_0 = 14.2 cm/s
P = 106.1 kPa
T = 316.2 K
EFFLUENT R.H. = 54.8%
ΔP = 9.0 kPa/m
BED DEPTH = 50.8 cm
ln C/C$_0$
C/C$_0$
TIME (h)


ORNL DWG 82-374
DATA POINT
MODEL
COM-57
$K_F A_0$ = 5.0 s^{-1}
V_0 = 9.1 cm/s
P = 108.7 kPa
T = 304.0 K
EFFLUENT R.H. = 62.6 %
ΔP = 11.6 kPa/m
BED DEPTH = 35.6 cm
ln C/C₀
C/C₀
TIME (h)
0
-1
-2
-3
-4
-5
-6
-7
-8
-9
1.0
0.1
0.01
0.001
0
20
40
60
80
100
120
140
160

APPENDIX O

INFRARED SPECTROMETER CALIBRATION CURVES

ORNL DWG 82-326

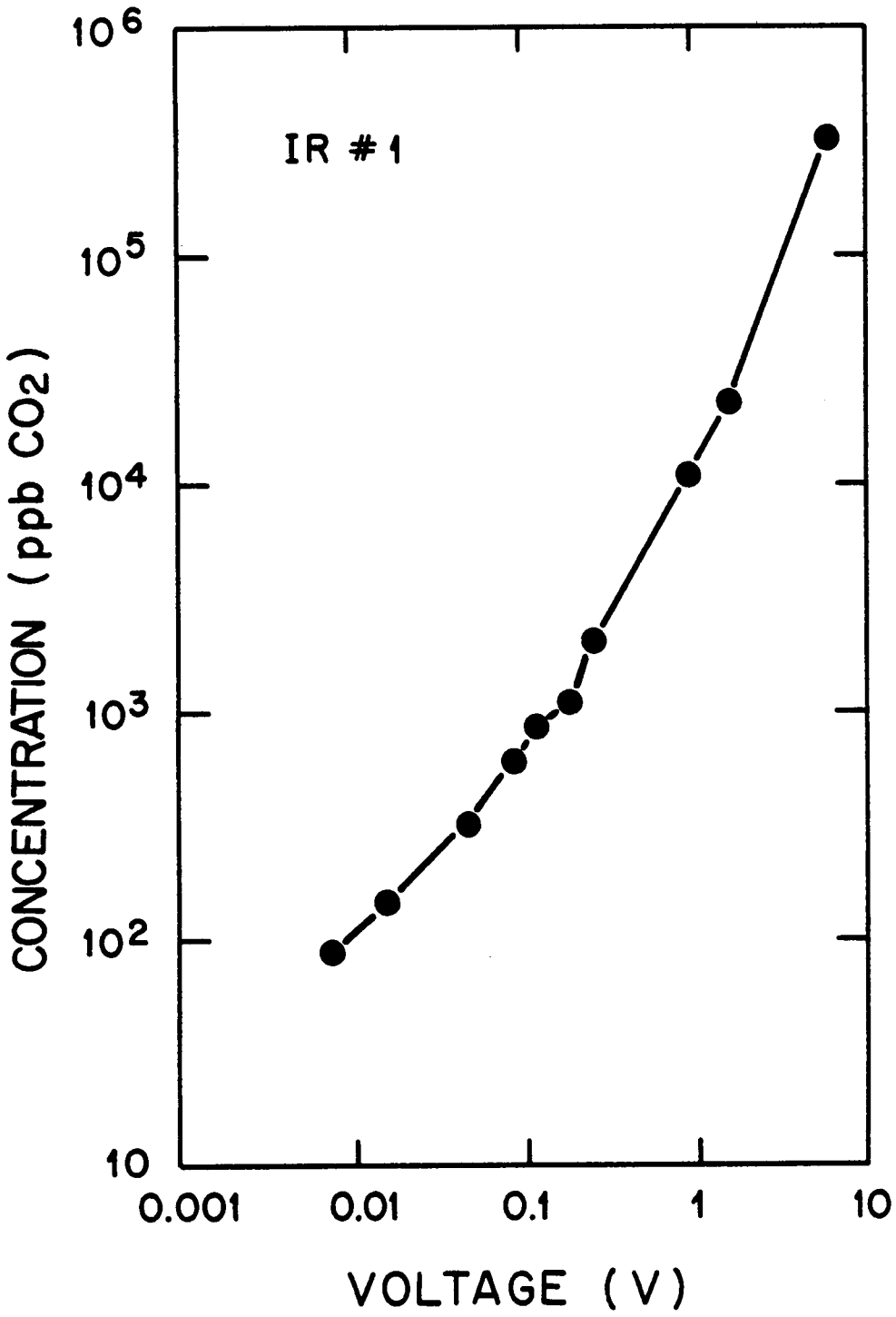


Figure 0.1. Calibration curve for IR No. 1.

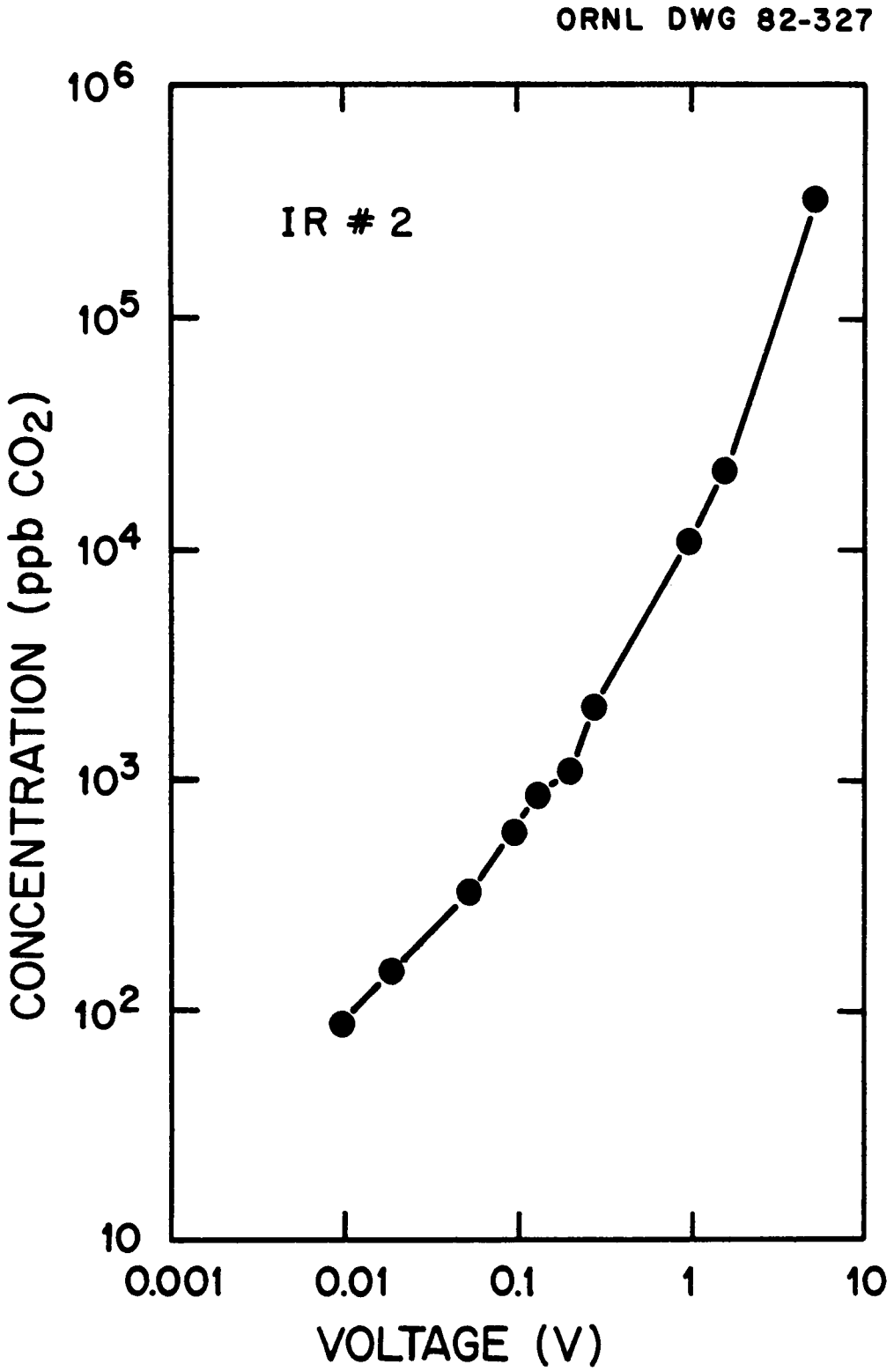


Figure 0.2. Calibration curve for IR No. 2.

VITA

Gary Lee Haag was born in McCook, Nebraska on March 6, 1953. He grew up on a farm near Bartley, Nebraska and attended Bartley Public and Bartley High School, graduating from high school in May 1971. He attended McCook Community College for one year and then transferred to the University of Nebraska-Lincoln where he received a B.S. degree in chemical engineering in May 1975. Upon accepting a research assistantship at Ames Laboratory, he attended Iowa State University-Ames and received an M.S. degree in Chemical Engineering in November 1976. He began employment at Oak Ridge National Laboratory in September 1976 and initiated schooling on part-time basis at The University of Tennessee, Knoxville. He received his doctorate degree in August 1982.

Gary is presently the principal investigator of the "Carbon-14 Immobilization" program and is the author or coauthor of eight publications and 1 patent. He is a registered Professional Engineer in the State of Tennessee and a member of AIChE and Phi Kappa Phi.

He is married to the former Cindy Burton of Bartley, Nebraska. They have two children, Blaine and Jessica.